THE EFFECT OF RADIO-FREQUENCY SELF BIAS ON ION ACCELERATION IN EXPANDING ARGON PLASMAS IN HELICON SOURCES

by

Matthew D. Wiebold

A dissertation submitted in partial fulfillment of

the requirements for the degree of

Doctor of Philosophy

(Electrical Engineering)

at the

UNIVERSITY OF WISCONSIN - MADISON

2011

Abstract

Large, time-averaged plasma potential differences, up to ΔV = 165 V evolving over several hundred Debye lengths, have been observed in low pressure (p_n < 1 mTorr) argon plasmas near the junction between the insulating, upstream glass source tube and grounded, large-diameter expansion chamber in the Madison Helicon Experiment. The potential gradient leads to ion acceleration exceeding $E_i \approx 7\ kT_e$ in some cases. A half-turn, double-helix antenna is driven at 13.56 MHz at up to 1 kW of RF power and a static magnetic field up to 1 kG in a nozzle profile (mirror ratio = 1.4) is imposed by six water-cooled electromagnets coaxial with the source tube. Retarding potential analyzers (RPAs) are used to measure the ion energy distribution function (IEDF) and a swept emissive probe is used to measure the plasma potential using the inflection point method. Single and double probes are used to measure the electron density and temperature. Two distinct antenna coupling mode hops are observed, the capacitive-inductive (E-H) and inductive-helicon (H-W) transitions, identified by jumps in electron density as RF power is increased at fixed magnetic field and neutral pressure. In the capacitive (E) mode, large amplitude ($V_{p-p} \gtrsim$ 140 V, $V_{p-p}/\overline{V_p} \approx$ 150%) fluctuations of the plasma potential are measured at the RF frequency and harmonics, leading to the formation of a self-bias voltage. The more mobile plasma electrons are able to fully respond to time-dependent gradients in the plasma potential on the RF timescale, however, the massive ions cannot, and only respond to the time-averaged plasma potential profile. The electrons can easily flow from the upstream region during an RF cycle, whereas the ions cannot, leading to an imbalance of flux. This imbalance is short-lived, however, as the steady state fluxes of electrons and ions must balance over an RF cycle (assuming no net current flow). A time-averaged (DC) potential difference, or self-bias voltage, builds to retard electron flux and increase ion flux, while the time-averaged plasma potential in the expansion chamber is held near the DC floating potential for grounded walls ($\overline{V_p} \approx 5kT_e/e$ for argon). Consequently, in the capacitive mode, the time-averaged plasma potential and ion density profile through the potential difference between the upstream, insulating source chamber and the grounded, downstream expansion chamber do not follow an ambipolar relation. The relatively long axial extent of the potential gradient as well as the observations of strong plasma potential oscillations at the RF frequency are inconsistent with formation of a classical, static double layer. The rate of decay of the accelerated ion population that is formed by the potential gradient is consistent with that predicted by charge-exchange collisions. If the current-free requirement of the flow between the source and expansion chambers is lifted by grounding the conducting upstream endplate of the source, a net current can flow through the source region while still maintaining global net zero current out of the plasma, since the upstream ground provides a current closure. The increased electron flux out of the plasma due to the grounded upstream endplate results in a higher time-averaged plasma potential in the source region and, therefore, a higher potential difference ($\approx$ 15%) between the source region and the expansion chamber than for the floating endplate case. In the inductive and helicon modes, the time-averaged plasma potential and ion density evolution more closely follow an ambipolar relation. This is a result of decreased RF-timescale plasma potential fluctuation amplitude from the reduced penetration of the RF electrostatic antenna fields as a result of the increased electron density in these modes. The scaling of the potential gradient with the argon flow rate (neutral pressure), magnetic field strength and RF power are investigated, with the highest potential gradients observed for the lowest flow rates and lowest magnetic fields in the capacitive mode. The magnitude of the self-bias voltage agrees well with that predicted for an RF sheath with the same plasma potential fluctuation amplitude. The exploitation of the self-bias effect for use in a plasma thruster is briefly explored, with possible use as a low thrust, high specific impulse mode in a multi-mode helicon thruster. Operation in the inductive and helicon modes leads to a lower specific impulse but higher thrust. This work could also explain the observations of larger-than-ambipolar and relatively long (several hundred Debye lengths) potential gradients in some expanding helicon plasmas that are ascribed to double layer formation in the literature.

Contents

List of Figures

Chapter 1

Introduction

Chemical propulsion has been the primary workhorse of the space program since its inception. Substantial thrust is generated as a result of combustion of propellant gases which expand in a nozzle. Thrust produced is sufficient to accelerate large payloads to low Earth orbit (LEO) and beyond. The Saturn V rocket, used extensively in the late 1960's, could launch a payload of 262,000 pounds (34 MN) into LEO. Chemical rockets, while delivering high thrust, are not particularly efficient at propellant utilization, requiring large amounts of propellant to be carried onboard. For instance, for the Saturn V rocket used on Apollo 13, the cargo (payload to LEO) was only 4% of the total vehicle mass, with the fuel and oxidizer accounting for 91.8% of the total vehicle mass [2]. Once a vehicle is in orbit, however, the thrust required for maneuvers is drastically decreased, and a more propellant-efficient source of propulsion is desired.

One technology that can deliver high propellant efficiencies is electric propulsion (EP). EP is a broad field of study with the main goal of achieving very high exhaust velocities, thus reducing the required initial mass of propellant and the launch mass of the system. EP is a mature field of study, with several hundred devices in operation on communication satellites [3]. These "flown" technologies have benefitted from the last several decades of research, and are often used for satellite station keeping and orbit control. Typical examples are Hall thrusters and gridded ion thrusters. High propellant efficiency, low thrust devices are of interest for station keeping of satellites and long duration missions.

One mission well-suited for an EP device would be to set Earth-Mars communication satellites in Non-Keplerian orbits to prevent communications blackout when the Sun is between Earth and Mars [4]. Calculations were performed requiring thrusts up to 300 mN, well within the range of EP devices. The Variable Specific Impulse Magnetoplasma Rocket (VASIMR) is a high profile example of an EP device, using a helicon source to create plasma and ion cyclotron heating (ICH) to increase the energy of ions which accelerate out of the device using a magnetic nozzle [5], which will soon be tested on the International Space Station [6].

Recent observation of accelerated ion populations in expanding helicon sources has led to increased interest their use as an EP device. Potential structures, including double layers and ambipolar (distributed) fields, have been observed in the expanding plume, which form without the aid of any biased grids. Ions traverse these potential structures and are accelerated, without interacting with a physical medium, increasing operational lifetime. In addition, these sources may not require the use of a neutralizer if there are sufficient electrons to neutralize the ion flow, further increasing operational lifetime.

The present work further increases the understanding of the RF power scaling of these devices for thruster use, as well as highlights the need for consideration of these devices as an RF source. This thesis is organized as follows. This introductory chapter gives the motivation for the research. Chapter 2 discusses helicon sources and their operating modes. Chapter 3 gives an overview of ion acceleration mechanisms in expanding helicon sources, particularly ambipolar electric fields and double layers and evidence of both in experiment. Chapter 4 details the experimental apparatus used for this work, and Chapter 5 discusses the diagnostics used. Chapter 6 gives an overview of the main experimental results of this work and Chapter 7 discusses these results. Conclusions and ideas for further work are discussed in Chapter 8, as well as a summary of the research results.

1.1 Propulsion Metrics

The thrust generated by any propulsion device is due to ejected propellant from the device. The thrust is equal to the rate of change of the momentum of the propellant:

$$T = \frac{\mathrm{d}p_p}{\mathrm{d}t} = v_p \frac{\mathrm{d}m_p}{\mathrm{d}t} \tag{1.1}$$

where p_p is the momentum of the propellant, v_p is the propellant exhaust velocity (assumed constant in time) and m_p is the propellant mass.

Chemical propulsion systems, using combustion of propellants for acceleration, typically have exhaust velocities from 3 km/s to 4 km/s [3]. Since electric propulsion systems accelerate using electric or magnetic fields, exhaust velocities can be much larger, on the order of 5 km/s up to 50 km/s. Even though the exhaust velocity is larger than that of chemical rockets, the propellant input rate is much lower and consequently the thrust generated is lower, since less mass per unit time is being ejected. Rockets with lower specific impulses and higher thrust typically burn for short periods of time followed by ballistic trajectories whereas high specific impulse, low thrust devices burn for long periods of time.

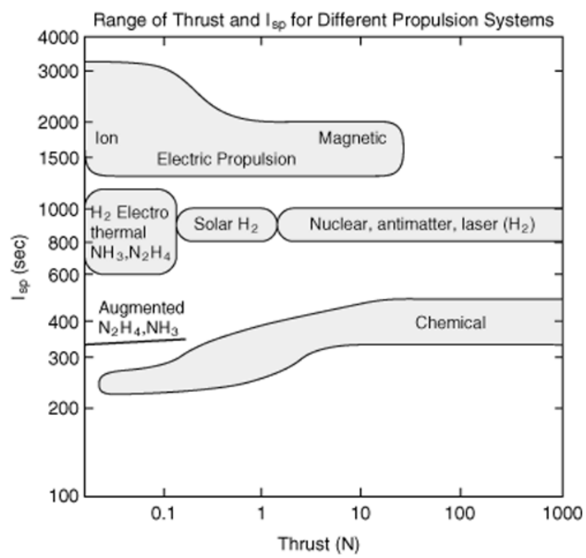

FIGURE 1.1: Specific impulse and thrust for several thruster classes [7].

The change in velocity gained by a payload is calculated from the rocket equation:

$$\Delta v = v_p \ln\left(\frac{M_1}{M_0}\right)$$

where M_1 is the mass of the rocket plus its fuel (wet mass) and M_0 is the mass of the rocket alone (dry mass). For a given Δv mission with a specified dry (delivered) mass, the wet mass (M_1) can be reduced if the exhaust velocity v_p is increased, leading to reductions in size and cost of the launch vehicle.

One metric used to determine efficiency of a thruster is specific impulse, which is the ratio of the thrust to propellant consumption (by weight) and is equal to the impulse delivered per unit propellant:

$$I_{sp} = \frac{T}{\frac{\mathrm{d}m_p}{\mathrm{d}t} g} = \frac{v_p}{g} \tag{1.2}$$

Specific impulse is measured in seconds. A higher specific impulse equates to a smaller amount of propellant required to gain a certain momentum. In more physical terms, if an engine's thrust could be adjusted such that it was equal to the initial weight of its propellant (in Earth's gravity), the specific impulse is how long the propellant would last. The specific impulse is an indicator of the mass efficiency of a propulsion system, and more efficient use of propellant means less is needed on the launch vehicle.

Since the thrust in an electric thruster is due to the accelerated ions, if the ions are accelerated through a voltage V, their velocity v_i will be (assuming a zero or small initial ion velocity):

$$v_i = \sqrt{\frac{2Vq}{m_i}} \tag{1.3}$$

where q is the ion charge and m_i is the ion mass. The thrust of an ion beam accelerated through a potential V is then, from Eq. 1.1 and Eq. 1.3:

$$T = v_p \frac{\mathrm{d}m_p}{\mathrm{d}t} = v_i \Gamma_i A m_i = v_i \frac{m_i I_b}{q} = I_b \sqrt{\frac{2Vm_i}{q}} \tag{1.4}$$

where I_b is the beam current. The thrust is proportional to the square root of the acceleration voltage and inversely proportional to the square root of the ion charge, so maximum thrust is achieved with singly ionized particles. If there is a significant possibility of multiply ionizing the propellant, it is important to determine the charge state of the ions to maximize thrust.

Specific impulse is a measure of propellant efficiency, but another important metric is the power efficiency, or the ability of a thruster to turn input power into useful thrust. One way of quantifying this efficiency is the ionization cost, or the energy needed to create ion-electron pairs. The ionization cost is defined as the input power divided by the total number of ions produced per time:

$$\epsilon = \frac{P_{RF}}{\Gamma_i A} \tag{1.5}$$

where P_{RF} is the RF input power, Γ_i is the ion flux and A is the area through which the ions are traveling, and has the units eV/ion. This metric gives an indication of how much energy is required to create *and* accelerate each ion. The total efficiency is the ratio of the beam power $P_b = I_b V_b$ to the total power input to the system, which encapsulates both production and acceleration of the ions as well:

$$\eta = \frac{P_b}{P_{in}} = \frac{I_b V_b}{I_b V_b + P_o} \tag{1.6}$$

where P_o is the "other power" required to create the ions and that is lost by other mechanisms such as thermal or optical radiation, and this should be kept to a minimum. The beam power can be written as:

$$P_b = \frac{1}{2}\dot{m}_p v_p^2 \tag{1.7}$$

Using this in Eq. 1.6 gives

$$\eta = \frac{P_b}{P_{in}} = \frac{T^2}{2\dot{m}_p P_{in}} \tag{1.8}$$

since $T = \dot{m}_p v_p$. This is a commonly accepted equation for thruster efficiency.

1.2 Electric Propulsion Technology

Electrothermal

Electrothermal propulsion devices heat the propellant electrically, which then expands thermally through a nozzle and provides thrust. Examples include the arcjet, which heats the propellant using an electric arc driven through it, or the resistojet, which heats propellant in a resistivelyheated chamber. Some of the restrictions on chemical propellants can be lifted, as propellant combustion chemistry doesn't need to be considered. Propellants such as ammonia or hydrazine are common, due to their dissociation to low-molecular-weight components and high specific heat.

Electromagnetic

Electromagnetic propulsion devices use the the interaction of a current in the propellant and a magnetic field to accelerate charged particles. There are a wide variety of electromagnetic propulsion devices, both pulsed and steady-state. Magnetoplasmadynamic (MPD) thrusters use the Lorentz force to accelerated particles, while Hall thrusters are a hybrid of an electromagnetic and electrostatic device.

Electrostatic

Electrostatic propulsion devices directly accelerate charged particles via an applied electric field. Ions are generated by an upstream source (RF, DC or microwave, for instance) and accelerated by an applied electric field. The simplest example is a gridded ion thruster, a diagram of which is shown in Fig. 1.2. Ions are produced upstream and extracted from the source with a negatively biased grid. A neutralizing source of electrons is required in the plume to avoid spacecraft charging and subsequent reduction of thrust. Gridded ion thrusters are a mature technology, with several devices having been flown on Russian spacecraft. Gridded thrusters provide up to a few hundred millinewtons of thrust with specific impulses of several thousand seconds with high efficiency, and are commercially produced.

The grids and neutralizer in an ion thruster can be lifetime-limiting components. If the accelerating electric field could be generated without the use of a physical medium in contact with the plasma, thruster lifetime could be improved. In addition, if the plume could be self-neutralized, there would be no need for a neutralizing source of electrons, also improving operational lifetime. Fig. 1.3 shows a schematic of such an arrangement. Plasma electrons and ions are generated in the source region, often by an RF or microwave source, which expands into a larger volume. The expanding plasma creates a self-consistent axial electric field, similar to a sheath, to retard mobile

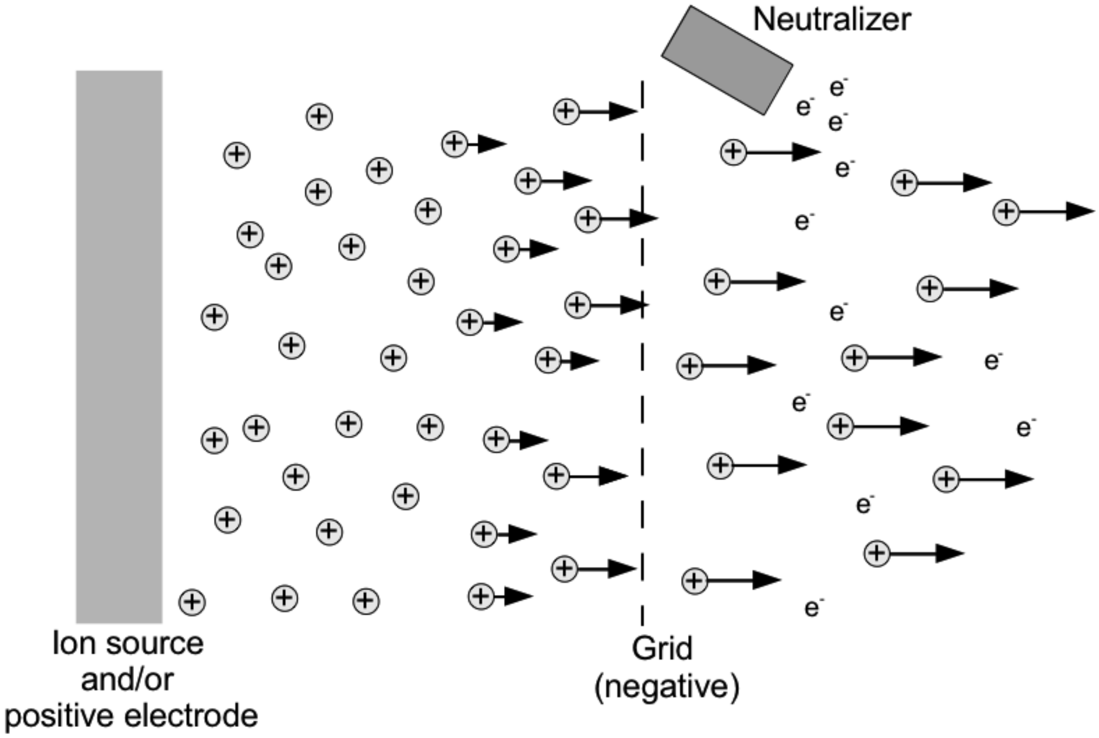

FIGURE 1.2: Representation of a gridded ion thruster. Plasma ions are extracted from a source upstream (left) and accelerated through a permeable grid (dashed line). Other grids may be used to tailor the potential profile. An electron source acts as a neutralizer to avoid charging of the spacecraft and limiting of the ion current.

electrons and accelerate ions [8]. Double layers, non-neutral regions of separated charge over a short distance (on the order of sheath dimensions), can also form create the required potential drop. Again, these devices have no grids or cathodes to erode, and therefore can have long operating lifetimes. Examples of gridless plasma thrusters include the helicon double layer thruster and the microwave (ECR) thruster.

The Variable Specific Impulse Magnetoplasma Rocket (VASIMR), shown in Fig. 1.4, is a project under development by the Ad Astra Rocket Company. Plasma is produced by a helicon source and the ions are heated by ion cyclotron resonant heating (ICRH). A magnetic nozzle accelerates the ions axially using classical conservation of magnetic moment. There have been several iterations of this device, and the current model is VX-200, which includes more than 200 kW RF power (48 kW helicon, 165 kW ICRH) and uses superconducting magnets with up to 2 Tesla peak field.

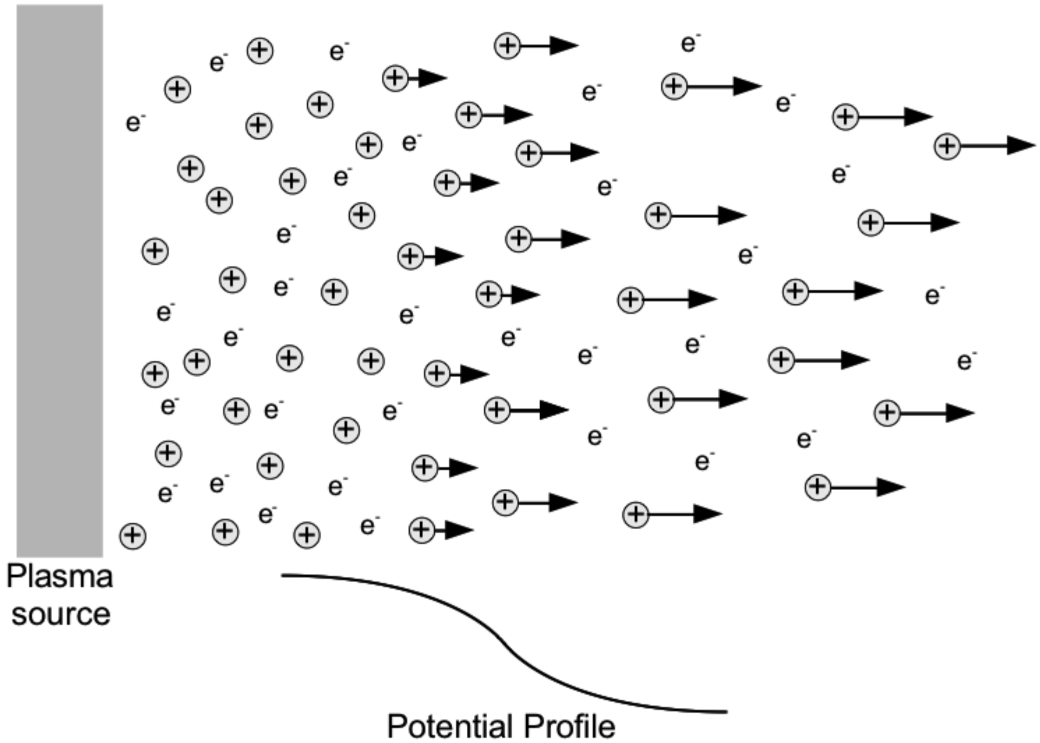

FIGURE 1.3: Gridless ion thruster. A plasma potential profile is imposed, perhaps by a double layer, on electrons and ions generated in the source.

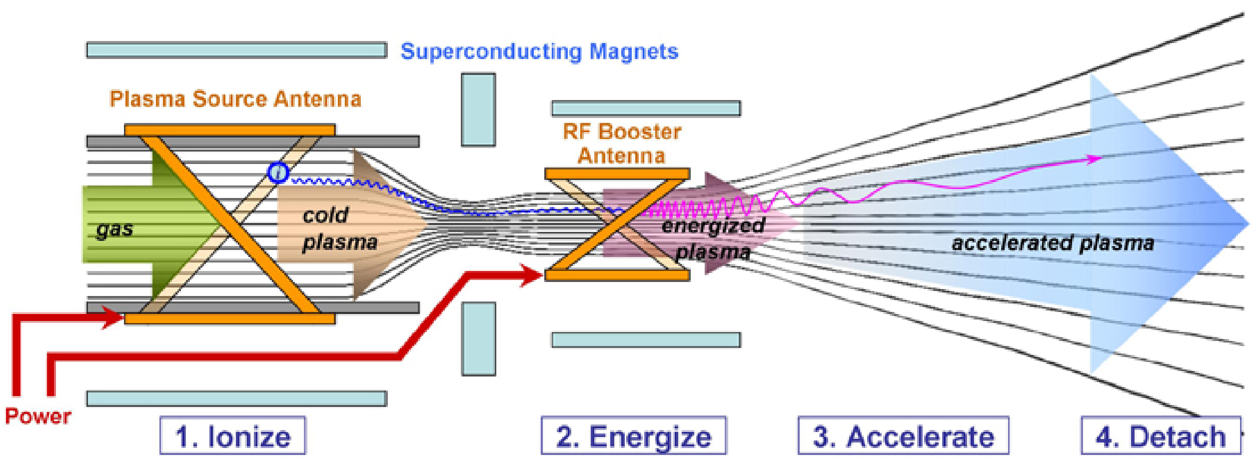

FIGURE 1.4: VASIMR engine design [9].

A prototype will be placed in the International Space Station and use stored energy to operate. Exhaust velocities up to 150 km/s have been measured, corresponding to $I_{sp} > 15000$ seconds

[10]. Recently, operation of the VASIMR system with only the helicon source powered at 30 kW have shown the simple plasma expansion results in a 20 eV ion beam with a significant upstream plasma density (up to 10^{14} cm^{-3}), but no double layer was observed [11].

1.3 Research Goals

Observation of double layers and accelerated ions in expanding helicon sources has led to an increased experimental, computational and analytical effort to understand their formation. Ion acceleration has been observed in several experimental devices, some of which are detailed in Sections 3.2.1 and 3.3.6. In order to use accelerated ions from a helicon source as a propulsion device, it is necessary to determine the optimum operating parameters for the desired application. In devices that claim to contain double layers, scaling studies of varying completeness have been performed for neutral pressure, magnetic field, geometry, RF frequency and RF power, as detailed by Charles [12]. For ambipolar acceleration from helicon devices, scaling studies have also been done for most of these operating parameters.

The cursory RF power scaling studies that have been performed claim there is no significant variation in the potential drop ΔV for a wide range of RF powers, from 20 W to over 1 kW [12]. However, general power scaling studies conducted in helicon sources have shown there are large, discontinuous changes in plasma potential and electron density as RF power is increased, known as mode hops, where the antenna coupling changes significantly (see Chapter 2). A largely ignored aspect of ion acceleration in helicon sources in the literature is the operating mode of the source when the acceleration is observed. At least three modes of antenna coupling are possible in helicon sources; capacitive, inductive and helicon (wave) coupling. At the lowest plasma densities, capacitive coupling dominates due to strong penetration of the RF electrostatic fields into the plasma. At slightly higher densities, inductive coupling dominates where induced currents can shield the RF fields. Helicon (wave) mode is only attainable when the dispersion relation for helicon waves can be satisfied in the source. In the literature, beam formation is more pronounced (higher energies) at the lowest neutral pressures and disappears at higher neutral pressures, and most studies are conducted at low or moderate powers (100 W - 800 W) and magnetic fields (< 500 G). It is likely that some helicon sources that exhibit ion acceleration are not operating in the classical wave-coupled helicon mode, but are helicon sources operated in the capacitive or inductive coupling modes.

To that end, there are consequences of operating in a mode where the RF nature of the source has non-negligible effects, and it is imperative to examine these effects on the ion acceleration. The scaling of the RF power allows a study of the effect of the antenna coupling mode on the potential difference ΔV, which is the primary goal of the present research. The magnitude of potential gradients observed in expanding helicon sources have been shown to scale with the electron temperature T_e for both double layer acceleration as well as the ambipolar (Boltzmann) acceleration (see Chapter 3). As RF power is increased, it has been shown that the electron temperature increases monotonically in the helicon mode in our experimental device [13]. Therefore, we predict that the observed potential difference ΔV should increase with increasing RF power (increasing electron temperature). However, the presence of mode hops will likely result in discontinuous jumps in ΔV as well as the density n_e and electron temperature T_e.

Summary

Low thrust, high specific impulse electric thrusters (Hall, gridded ion thrusters) have been successfully flown, but have lifetime-limiting elements such as grids and cathodes. Gridless plasma thrusters such as the helicon double layer thruster (HDLT) or VASIMR are being explored for high reliability operation, but many questions remain about ion acceleration in such devices. Ion acceleration in expanding helicon sources has been observed as a result of double layers or ambipolar plasma expansion, but the scaling of the acceleration with RF input power is not fully understood. Helicon sources typically exhibit discontinuous mode transitions, but the effect of the operating mode on the ion acceleration has not been explored. This work aims to further the understanding of the RF power scaling of these devices and to highlight their RF nature.

Chapter 2

Helicon Sources

Helicon plasma sources are noted for their ionization efficiency. These sources can produce electron densities an order of magnitude larger than other sources at comparable input powers and pressures [14], with typical densities ranging from 10^{11} cm^{-3} to 10^{14} cm^{-3}. These high density sources have applications ranging from materials processing [15], etching of semiconductors [16], ion sources for inertial confinement fusion [17], thrusters [18] to wave propagation studies [19]. The geometry of a helicon is typically cylindrical with a coaxial magnetic field, although helicon waves have been launched in toroidal [20] and annular geometries [21]. A radio frequency antenna, typically driven at 13.56 MHz, launches helicon waves along the axis of the cylindrical chamber. Several types of antennas have been studied, including the Nagoya Type III and various types of helices, loops and saddle coils. Input powers typically range from tens of watts to up to several tens of kilowatts in the literature. Axial magnetic fields usually range between 20 G to 4 kG or more. Neutral pressures in these sources range from as low as 10^{-6} Torr up to several tens of millitorr [22]. Instead of neutral pressure, which can vary across a flowing system, mass flow rate is used to uniquely specify the fill condition in such systems.

2.1 Operating Modes

Helicons (and other RF plasma sources) can operate in one or more of three modes, depending on the antenna, geometry, source conditions and other source characteristics. These three modes are the capacitive (E), inductive (H) and helicon (W) mode, and distinct transitions can be observed between these modes in the same source, often exhibiting hysteresis. A review of the three mode types are given in [23–25] and references therein.

2.1.1 Capacitive (E) Mode

In the capacitive (E) mode, the RF power from the antenna is transmitted to the mobile plasma electrons directly by the RF electrostatic electric field imposed by the antenna. In the E mode, the skin depth for the RF fields in the plasma is a significant fraction of the plasma dimensions, therefore the antenna fields can penetrate far into the plasma and couple to the electrons directly. The plasma electrons oscillate around the positive space charge cloud of ions (provided $\omega_{pe}^2 \ll \omega_{RF}^2[1+\frac{\nu_{en}^2}{\omega_{RF}^2}]$, where ν_{en} is the electron-neutral collision frequency, ω_{pe} is the electron plasma frequency and ω_{RF} is the RF frequency), and since the ions are much more massive, they can only respond to the time-averaged electric fields (provided $\omega_{pi}^2 \ll \omega_{RF}^2$, see Section 3.1.2). If electron-neutral collisions are rare within an RF cycle ($\nu_{en}^2 \ll \omega_{RF}^2$, $p_n < 25$ mTorr in argon at 13.56 MHz), the skin depth is given by:

$$\delta_p = \frac{1}{\alpha_p} = \sqrt{\frac{m_e}{e^2 \mu_0 n_e}} \tag{2.1}$$

where δ_p is the skin depth (meters), α_p is the attenuation constant, m_e is the electron mass, n_e is the electron density and μ_0 is the vacuum permeability.

Energy transfer occurs due to stochastic heating in the sheaths and ohmic heating in the bulk plasma [23]. Stochastic heating is the result of the plasma electrons colliding with the oscillating sheath potential, similar to a ball bouncing from a moving wall, transferring energy from the wall to the ball in the process. Ohmic heating is due to collisions between the accelerated electrons and neutrals in the bulk plasma.

Time-averaged plasma potentials in the capacitive mode can be as high as the RF driving voltage (V_{RF}). Large fluctuations in the sheath (and plasma) potential are observed, due to the high penetration of the RF electrostatic fields. Confinement of plasma electrons is provided by the electric field in the sheaths at the walls. Ions are continuously accelerated towards the walls through the sheaths, but electrons are only able to escape the bulk when the instantaneous plasma potential reaches the wall potential. This allows sufficient electrons to escape the bulk plasma to account for the ions lost throughout the rest of the RF cycle. In the presence of plasma potential fluctuations, a self-bias voltage forms to equalize the electron and ion fluxes from the plasma, and this phenomenon is discussed further in Section 3.1.3.

Typical plasma densities in the E mode are typically less than 10^{11} cm^{-3}, and densities near 10^{10} cm^{-3} have been measured for the E-H transition in (magnetized) helicon sources [26]. The large, asymmetric electric fields in the plasma can drive anomalous cross-field diffusion in magnetized plasma columns, as suggested by Degeling [26] and Perry [27].

2.1.2 Inductive (H) Mode

As the plasma density rises, the skin depth decreases and approaches the chamber diameter, the plasma starts to generate currents that shield those imposed by the antenna. A positive feedback occurs between the skin depth and power deposition, and often a discontinuous jump in density is observed across the E-H transition. The induced currents, generated within a few skin depths of the surface of the plasma, heat the plasma. Both stochastic and ohmic heating exist, with stochastic heating dominating at lower pressures where electron-neutral collisions may be rare. The induced electric fields in the plasma are non-propagating. The plasma potentials are much lower than those in the capacitive mode, since the power transfer is no longer directly from the antenna electric fields but due to the induced currents. The plasma density is higher than that of the capacitive mode, often on the order of 10^{11} cm^{-3} to 10^{12} cm^{-3}.

At low electron densities in the inductive mode, where the skin depth is not necessarily small compared to the plasma dimensions ($\delta_p \sim$ R,L), the absorbed power scales as [23]:

$$P_{abs} \propto n_e I_{rf}^2 \tag{2.2}$$

where I_{rf} is the RF antenna current and P_{abs} is the absorbed power by the plasma. At higher electron densities, when the skin depth is much smaller than the plasma dimensions ($\delta_p \ll$ R,L), the absorbed power scales as the square root of the density:

$$P_{abs} \propto \sqrt{n_e} I_{rf}^2 \tag{2.3}$$

This results in a maximum in the absorbed power when the skin depth is on the order of the plasma dimensions. The absorbed power for two different antenna currents I_{rf} is shown in Fig. 2.1, as well as the power loss vs. electron density n_o. The loss power P_{loss} is linear with the electron density assuming a constant loss area and energy loss per electron. There exists a minimum antenna current I_{min} such that a stable inductive discharge equilibrium is possible. Below this threshold current, an inductive discharge is not possible, but a capacitive discharge can form (dotted line in Fig. 2.1).

The inductive mode is reached after passing through the capacitive mode in most cases. When RF power is applied to the antenna, the high RF electrostatic fields break down the fill gas and the electron density rises and a capacitive-mode discharge forms. When the density increases enough to reach the inductive mode (where the skin depth is on the order of the plasma dimensions), the discharge transitions to the inductive mode.

2.1.3 Helicon (W) Mode

Helicon waves are propagating wave modes in a finite diameter, axially magnetized plasma column. Helicon waves satisfy $\omega_{LH} \ll \omega \ll \omega_{ce}$ and $\omega_{pe}^2 \gg \omega\omega_{ce}$, where ω_{LH} is the lower hybrid frequency, ω_{ce} is the electron cyclotron frequency, ω_{pe} is the electron plasma frequency, and ω is

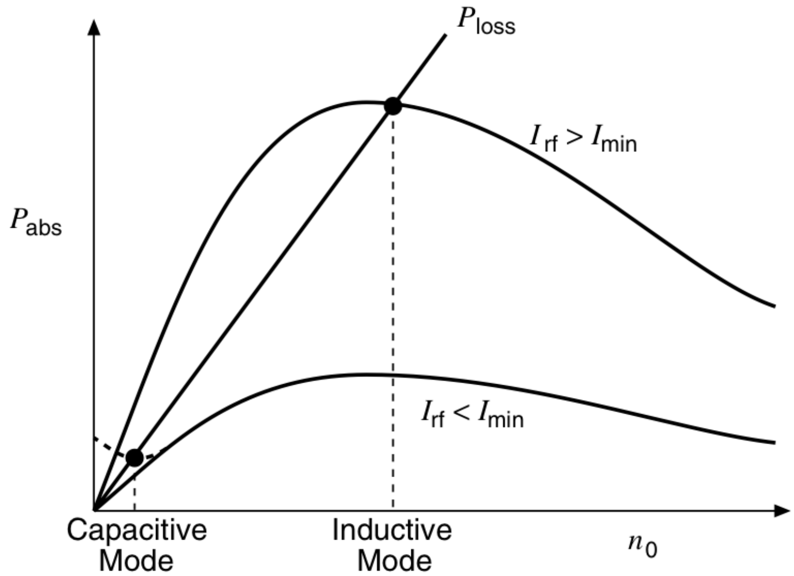

FIGURE 2.1: Inductive source absorbed power vs. electron density n_o for two RF antenna currents (I_{rf}), above and below the threshold current I_{min} for stable inductive operation [23]. The intersection of the loss curve and the absorbed power curves indicates the equilibrium point. For $I_{rf} < I_{min}$, there is no solution for inductive operation, however a capacitive discharge (dashed line) can still exist.

the driving frequency.

The helicon waves are excited with an RF antenna which couples to the helicon mode structure through an insulating chamber wall. The mode propagates along the column, and the mode energy is absorbed by the plasma through collisionless and collisional damping. The exact physical process that causes such efficient ionization is an active area of research, however. Several mechanisms have been suggested [28], including Landau damping, collisional processes, mode conversion, helicon wave penetration, non-linear trapping of fast electrons, parametric instabilities, and antenna localized acceleration.

Helicon waves are essentially bounded Whistler waves, and the helicon dispersion relation is derived below in Section 2.3. The RF antenna *k*-spectrum is often able to excite several helicon modes that satisfy the wave dispersion relation, and discontinuous jumps in the electron density may occur, even within the W mode. The plasma potentials for helicons are often much lower than the inductive and capacitive mode, whereas the density can be much higher, up to 10^{14} cm^{-3}.

2.2 Mode Transitions

Capacitive to inductive mode transitions have been observed in several types of sources, and have a rich history in both low pressure (mTorr) and higher pressure (several Torr) plasma sources. Transitions between the three modes, including hysteresis, have been observed in helicon sources when the RF power is increased [25]. In the capacitive mode, the ionization is localized under the high-voltage leads of the antenna, and the density is low, with a centrally peaked radial density profile. When the electron density is sufficient, there is a transition to the inductive mode. In the inductive mode, there exists a radial density depression due to the power deposition in the edges of the discharge from the skin effect, depending on the skin depth and the amount of losses to the walls. The density increases due to the improved power transfer. As the density increases, the helicon wavelength shortens and is able to “fit” within the plasma column, and a helicon wave is able to propagate. The radial density profile again becomes peaked, due to the interaction of the helicon wave with the plasma electrons in the bulk.

Franck [29] gives clear evidence of the mode transitions in a typical helicon source operating in capacitive, inductive and helicon modes. Some authors, including Franck, have seen transitions directly from E to W mode, bypassing the H mode as power is increased. However, it is shown that the H mode can be reached when the power is *decreased* from the power level in W mode, as shown in Fig. 2.2.

As mentioned above, Degeling [26] observed the E-H transition in their helicon for an electron density of 10^{10} cm^{-3}, which was independent of the static magnetic field value and the fill gas pressure, except through the effect of these parameters on the electron density. They observed the E-H transition when the skin depth $\delta_p \sim \frac{R}{2}$.

Perry [27] measured the modulation of the plasma potential in a helicon source operating in the capacitive and inductive modes. They observed a sharp decrease in both the modulation (Fig. 2.3(a)) and value (Fig. 2.3(b)) of the time-averaged plasma potential during the E-H transition. Modulations on the order of the plasma potential ($\Delta V \sim V_p$) were observed in the capacitive

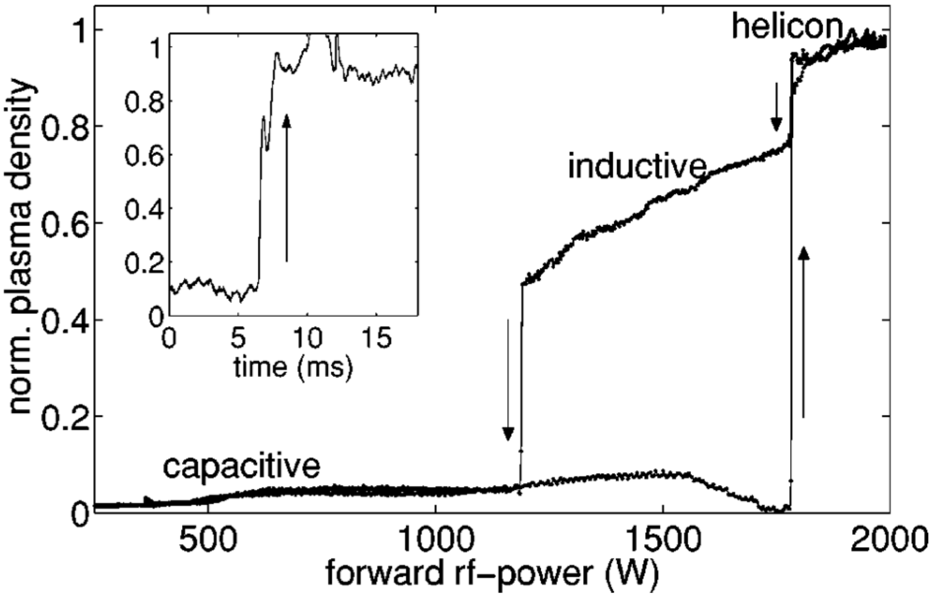

FIGURE 2.2: Electron density vs. RF power in a helicon source showing mode transitions as well as hysteresis [29].

mode, with a peaked radial profile of the modulation amplitude. The authors suggest that in the E mode, anomalously high cross-field diffusion is present, due to the large radial RF fields present in the plasma bulk. In the H mode, much smaller radial electric fields are present, and cross-field diffusion is reduced, contributing to the density jump observed.

The physical appearance of the discharge can indicate the mode of operation. Photos of our experiment in each mode are shown in Fig. 2.4. For the capacitive mode, a diffuse pink glow exists under the antenna, with some extension of the plasma downstream (to the right in the image). The pink glow is a result of excitation (and decay through optical emission) of neutral argon. In the inductive mode, a brighter glow exists, with a more uniform distribution of light output. In the helicon mode, there is a bright, blue core in the center of the column, due to excitation of ionized argon by the wave-interacting electrons. In some cases, at high magnetic fields and RF powers but still in the inductive mode, a weak blue core can be observed in the center of the discharge. The blue core, in either type of discharge is a result of excitation of ionized argon.

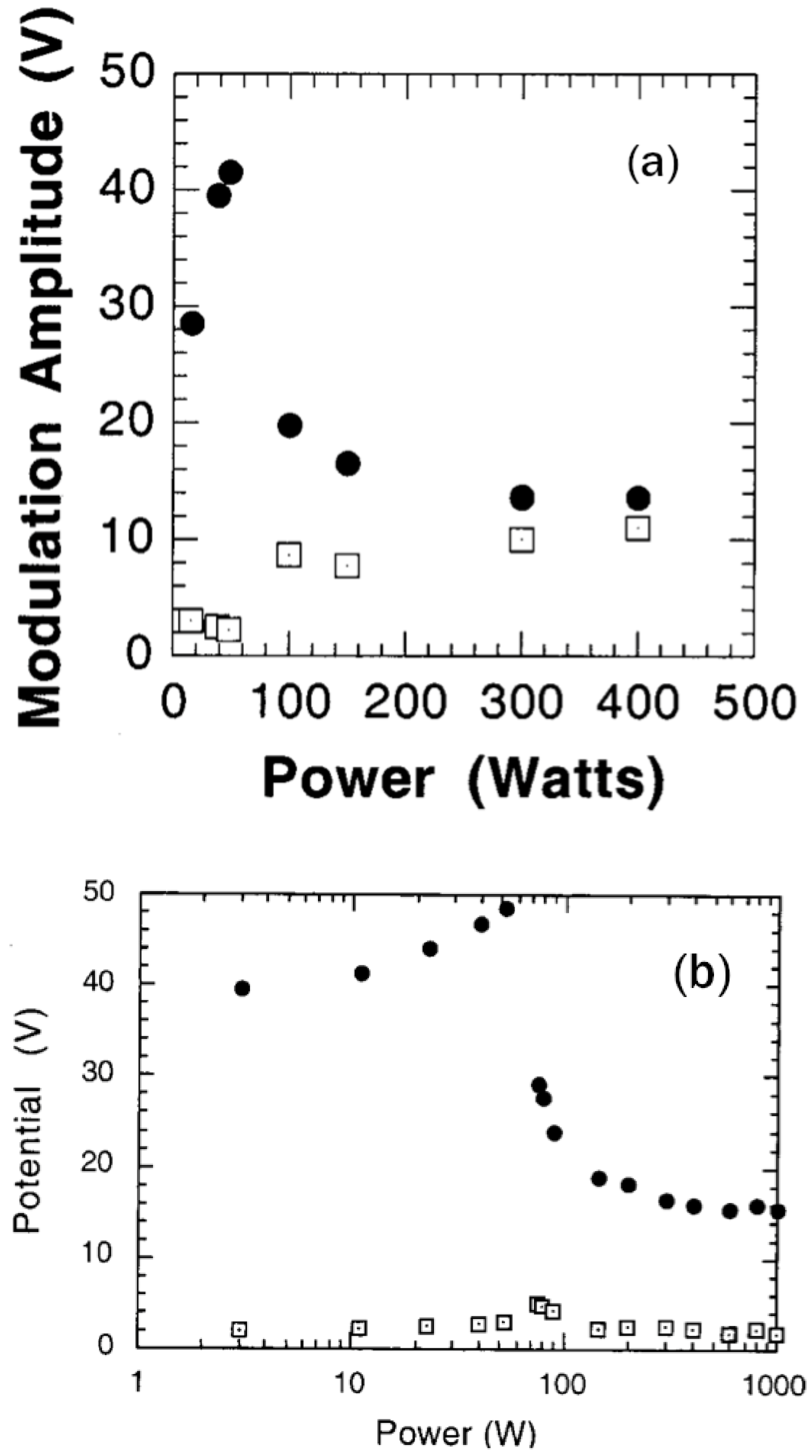

FIGURE 2.3: (a) Modulation of the plasma potential vs. RF power measured with an emissive probe. A decrease in the modulation is observed during the E-H transition (b) Decrease in plasma potential vs. RF power, measured with a floating emissive probe [27].

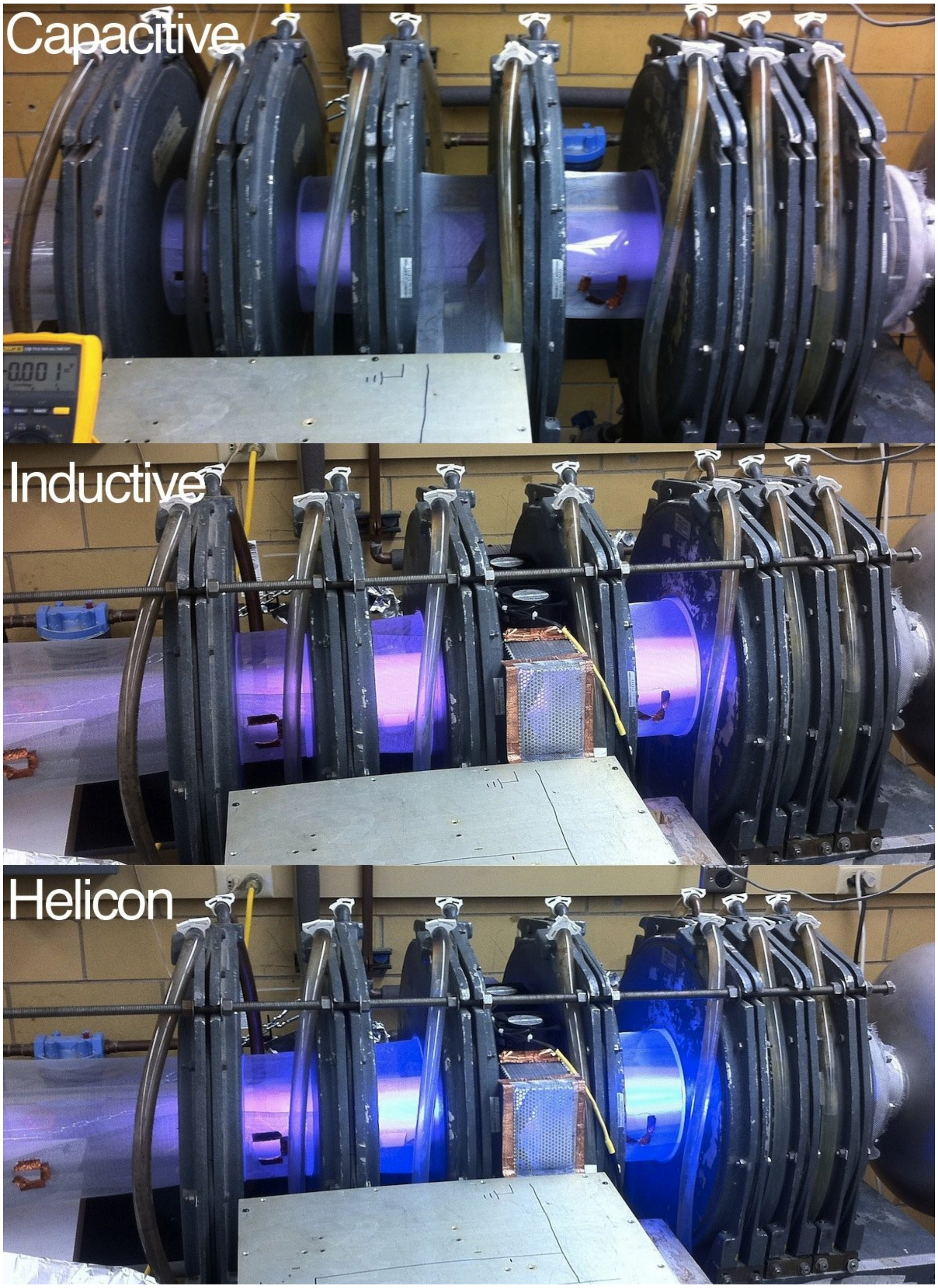

FIGURE 2.4: Comparison of the appearance of the plasma in the capacitive, inductive and helicon modes in the MadHeX system.

2.3 Helicon Wave Propagation

The following is an abbreviated derivation based on that in Lieberman [23] of the basic wave dispersion relation for helicon waves, which will be helpful for the analysis of the source operation in conjunction with the observed ion acceleration. Helicon waves are bounded Whistler waves with $\omega_{ci} \ll \omega \ll \omega_{ce}$ and $\omega_{pe}^2 \gg \omega\omega_{ce}$. The dispersion relation for unbounded Whistler waves is given by:

$$N^2 = R = 1 - \frac{\omega_{pi}^2}{\omega(\omega + \omega_{ci})} - \frac{\omega_{pe}^2}{\omega(\omega - \omega_{ce})} \approx \frac{\omega_{pe}^2}{\omega\omega_{ce}} = \frac{kk_z}{k_0^2} \tag{2.4}$$

where $N = kc/\omega$ and k_z is the z component of the wavevector (along B) and $k_0 = \omega/c$. k can be decomposed into:

$$k = \sqrt{k_\perp^2 + k_z^2} \tag{2.5}$$

where $k_\perp$ is the radial component of the wavevector. The helicon modes are mixtures of electromagnetic and quasistatic fields of the form:

$$\vec{E}, \vec{H} \sim e^{j(\omega t - k_z z - m\theta)} \tag{2.6}$$

where m is the azimuthal mode number. The boundary conditions for the wave propagation in a insulating or conducting cylinder is given by Chen [30], assuming a uniform plasma density and the total radial current density amplitude $\tilde{J}_r = 0$:

$$mkJ_m(k_\perp R) + k_z J'_m(k_\perp R) = 0 \tag{2.7}$$

Using Eqns. 2.4, 2.5 and 2.7 it is possible to solve for $k_\perp$,k_z and k for a given ω, n_e and B_0, giving the dispersion relation.

The antenna in our experiment primarily launches an $m = 1$ mode number, which results in a helical variation of the fields in space. The transverse electric field for $m = 1$ is shown in Fig. 2.5 for five axial locations. The antenna couples to these transverse electric (and magnetic) fields.

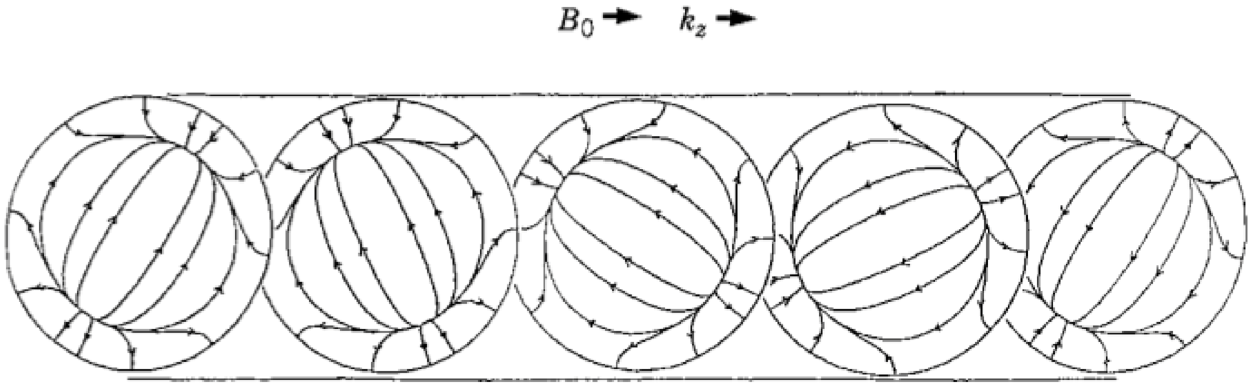

FIGURE 2.5: Transverse electric fields in the helicon (m = 1) mode [23].

The dispersion relation Eq. 2.4 can be rewritten as:

$$kk_z = \frac{e\mu_0 n_0 \omega}{B_0} \tag{2.8}$$

from which there are two limits, $k_z \ll k_\perp$ and $k_z \gg k_\perp$. The transition point between these two limits is when $n_0 = n_0^*$, where $k_z = k_\perp$ for the $m = 1$ mode. For typical source parameters R = 5 cm, f = 13.56MHz and B_0 = 200 G, $n_0^* \approx 4.0 \times 10^{12}$ cm^{-3}. For densities $n_0 \ll n_0^*$, the dispersion relation is approximately:

$$\lambda_z = \frac{2\pi}{k_z} = \frac{3.83}{R}\frac{B_0}{e\mu_0 n_0 f} \tag{2.9}$$

and for $n_0 >> n_0^*$:

$$\lambda_z = \sqrt{\frac{2\pi B_0}{e\mu_0 n_0 f}} \tag{2.10}$$

Both limits have their drawbacks for practical helicon design, so most helicon antennas are designed for operation near n_0^*. Typically, $k_\perp$ is chosen to be larger than k_z, such that the low density relation in Eq. 2.9 is appropriate, and it has been shown to roughly follow that relation. As mentioned earlier, RF antennas designed for helicon sources may couple to a range of λ_z, leading to operation in a range of densities.

Helicon Wave Damping

Both collisional and collisionless damping of the helicon wave have been suggested as heating mechanisms for the plasma electrons. Collisional damping primarily heats the thermal electron population, while collisionless (Landau) damping heats the tail of the electron population near where the electron phase velocity is close to that of the helicon wave. The collision frequency ν_c in the discharge is the sum of the electron-neutral and electron-ion collision frequencies, and the Landau damping frequency is [23]:

$$\nu_{LD} \approx 2\sqrt{2}\omega\zeta^3 e^{-\zeta^2} \quad \zeta \gg 1 \tag{2.11}$$

$$\nu_{LD(max)} \approx 1.45\omega \quad \zeta \approx 1.2 \tag{2.12}$$

where $\zeta = \omega/(k_z\sqrt{2}v_{th})$ where $v_{th} = \sqrt{eT_e/m_e}$, the thermal electron velocity. The axial decay constant for the helicon wave damping in the low density limit (see above) is:

$$\alpha_z^{-1} \approx \frac{\omega_{ce}}{k_\perp \nu_T} \tag{2.13}$$

where $\nu_T = \nu_c + \nu_{LD}$, and for the high density limit:

$$\alpha_z^{-1} \approx \frac{2\omega_{ce}}{k_\perp \nu_T} \tag{2.14}$$

The damping length α_z^{-1} should be less than the source chamber length to maximize energy transfer between the wave and the plasma.

Summary

Helicon sources, noted for their high densities and ionization efficiency at moderate powers, use bounded Whistler waves to accelerate electrons which ionize neutrals. Helicon sources exhibit three (or more) distinct modes of operation which are a result of changes in the power coupling between the RF antenna and the plasma. In the capacitive (E) mode, the RF fields imposed by the antenna can penetrate the plasma due to the long skin depth in the system. Plasma potentials are typically high (up to V_{RF}) and large modulation in the plasma potential on the RF timescale are observed. Densities are low ($n_e \approx 10^{10}$ cm^{-3}), and the plasma is unable to shield out the imposed RF fields. The inductive (H) mode, usually reached after passing through the E mode, occurs when the plasma is able to shield out the imposed RF fields with self-generated currents which heat the plasma. Densities are higher than E mode ($n_e \approx 10^{11}$ cm^{-3}) and plasma potentials are considerably lower than the E mode. The helicon mode, which can be reached when the helicon wave dispersion relation can be satisfied in the system (the helicon wavelength “fits” in the system), results in improved coupling and a large density increase. Densities are typically greater than 10^{11} cm^{-3}, up to 10^{14} cm^{-3} in some systems, and plasma potentials are quite low.

CHAPTER 3

Expanding Plasmas in Helicon Sources

In systems with a high aspect ratio ($L \gg R$), as plasma expands from a small cross section to a larger cross section, a potential structure forms to ensure that electron and ion fluxes from the small cross section region are equal to maintain quasineutrality. The potential structure that forms can be interpreted as opposing the electron pressure gradient $p_e = n_e k T_e$. This phenomenon is well known and is discussed in several works (see Lieberman [23] or Manheimer [31] for example). The spatial scale for this expansion is long compared to sheath dimensions, and Debye shielding by the electrons is satisfied throughout the expansion. It is also possible for a structure called a double layer (DL) to form, which is a sharp potential gradient over a short distance (on the order of sheath dimensions, tens of Debye lengths) that is a result of charge separation occurring in space, where Debye shielding from the electrons does not hold. The following is an overview of these two potential structures, which have both been observed in expanding plasmas in helicon sources, and have been suggested as mechanisms for developing thrust.

3.1 Sheath Theory

In order to understand these potential structures in expanding plasmas, a brief discussion of DC and RF sheaths as well as self-biasing in RF discharges is helpful in understanding the processes at work.

3.1.1 DC Collisionless Sheaths

Sheaths form in order to balance ion and electron flux from a plasma to its boundaries and maintain neutrality in the bulk plasma. For electropositive discharges, such as those considered here, the mobile electrons are able to leave the discharge much more readily than the ions due to their mass difference, which would cause a charge imbalance. An electric field forms in the sheaths at the plasma boundaries to retard and confine the mobile electrons and accelerate the ions to maintain quasineutrality, which results in the plasma charging positive relative to the wall potential. The ion and electron densities and the potential profile are shown in Fig. 3.1 for a collisionless DC sheath at a floating wall [23].

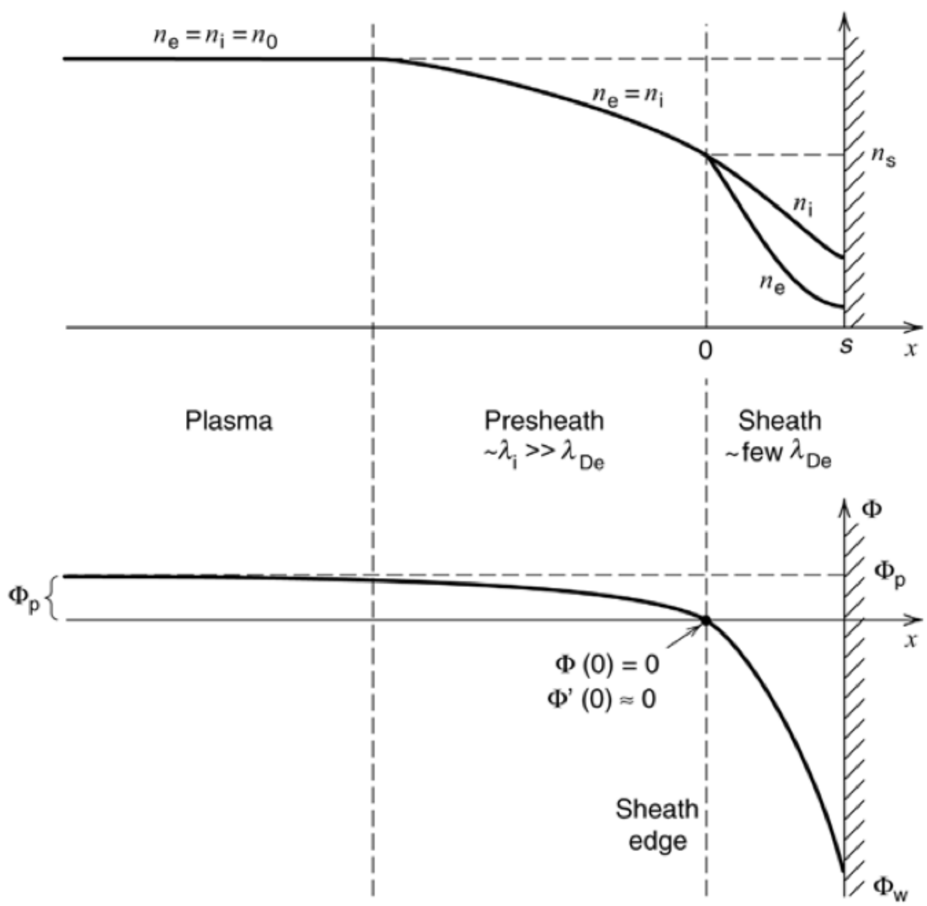

FIGURE 3.1: Ion and electron densities (top) and potentials (bottom) in a typical collisionless DC sheath [23].

The ion density in these wall sheaths is much larger than the electron density, thus they are referred to as “ion-rich”. The strength of this positive sheath is found by equating the ion and electron fluxes at the boundary (floating wall boundary condition), and is given by

$$|V_s| = \frac{kT_e}{e} \ln \sqrt{\frac{M_i}{2\pi m_e}} \tag{3.1}$$

where T_e is the (Maxwellian) electron temperature, M_i is the ion mass and m_e is the electron mass. For argon, this potential drop is 4.7 kT_e/e. The floating potential is referenced from the plasma potential, therefore the plasma potential will be larger than the floating potential by $|V_s|$.

The stable solution to the governing equations for the sheath potential and particle densities dictate there must also be a potential gradient that accelerates ions to at least the Bohm velocity, $v_B = c_s = \sqrt{kT_e/M_i}$, and the region of this potential gradient is called the “presheath”. In the presheath, the ion flow is subsonic ($v_i < c_s$) and the ions are accelerating through the presheath potential gradient. At the sheath-presheath boundary, the ions become sonic ($v_i = c_s$) and then supersonic ($v_i > c_s$) into the sheath, where charge neutrality must break down. Physically, since total ion flux ($\Gamma_i = n_i v_i$) in the sheath must be conserved, the ion density will decrease through the sheath. If the decrease in density is too great, the electrons that diffuse into the sheath region due to their finite temperature will leave a net negative charge and the ions will be further accelerated. Conversely, if the density gradient is not large enough, the ions will be slowed. The stable solution, the Bohm criterion, results in the ions attaining at least the Bohm velocity c_s across the presheath, which has a potential drop $\Delta\phi \approx \frac{kT_e}{2e}$. Thus the total potential drop from bulk plasma to a floating wall is $|V_s| \approx 5.2kT_e/e$ in argon plasmas. Any potential imposed on the floating wall will increase or decrease the plasma potential.

The width of a DC sheath is typically on the order of few Debye lengths, calculated using parameters measured at the plasma-sheath boundary. For high-voltage (Child’s law) sheaths like those in a capacitively driven discharge such that $eV_s \gg kT_e$, $n_e \approx n_s e^{-eV_s/kT_e} \to 0$, the sheath width can be much larger, up to tens or hundreds of Debye lengths. The sheath width s in this case is given by [23]:

$$s = \frac{\sqrt{2}}{3}\lambda_D\left(\frac{2eV_s}{kT_e}\right)^{\frac{3}{4}} \tag{3.2}$$

where λ_D is the Debye length.

3.1.2 RF Collisionless Sheaths

Since helicon sources operating in the capacitive or inductive modes can support non-zero RF plasma potential fluctuations [27], it is necessary to understand the effect of the RF fields on the sheath. When a plasma is created using an RF source there can be significant fluctuations of the plasma potential in time due to the coupling of the RF fields to the plasma electrons and the inability of the plasma to shield out the RF fields. These fluctuations can result in a growth of the sheath width as well as the DC sheath voltage drop (self-biasing), which can reach several hundred volts [32], on the order of typical RF driving voltages. The nonlinearity of the sheath impedance results in a rectification of the RF voltage, which leads to the growth in width and voltage drop of the sheath as well as non-sinusoidal fluctuations in the plasma potential.

Several models of RF sheaths have been developed, with those by Lieberman ([23] and references therein) and Godyak [32] being well accepted. The sheath dynamics can be understood with the following assumptions:

– The ions can only respond to time-averaged electric fields, which is a good approximation if:

$$\frac{\omega_{pi}^2}{\omega_{RF}^2} \ll 1 \tag{3.3}$$

which is equivalent to the assumption that the response time of the ions $\tau_i \approx \omega_{pi}^{-1}$ is much longer than an RF period (see Eq. 3.6).

– The electrons can respond to the RF-timescale fluctuations, which is a good approximation if:

$$\frac{\omega_{pe}^2}{\omega_{RF}^2} \gg \sqrt{1 + \frac{\nu_{en}^2}{\omega_{RF}^2}} \tag{3.4}$$

where ν_{en} is the electron-neutral collision frequency. In argon at 13.56 MHz, $\nu_{en} \approx \omega_{RF}$ for p_n = 25 mTorr, therefore for the neutral pressures considered here, this assumption is justified. If the neutral pressure is too high, electrons suffer collisions during an RF cycle and cannot fully respond to changes in the plasma potential. Equivalently, the electron response time $\tau_e \approx \omega_{pe}^{-1}$ is much shorter than an RF period.

– The sheath drop is much larger than the electron temperature, which leads to a near-zero electron density in the sheath region.

These assumptions are appropriate for the plasmas investigated here, as will be discussed further in Chapter 7. The particle densities in the sheath under these assumptions are shown in Fig. 3.2. Note that the sheath width $S(t)$ is a function of time, and the sheath width fluctuates between S_1 and S_2. The time-averaged electron density is shown as a dashed line. The sheath width is increased in this case by a factor of $\approx$ 1.36 above the width of a Child law sheath due to the reduction in space charge in the sheath, compared to a DC sheath, provided by the non-zero time-averaged electron density [23].

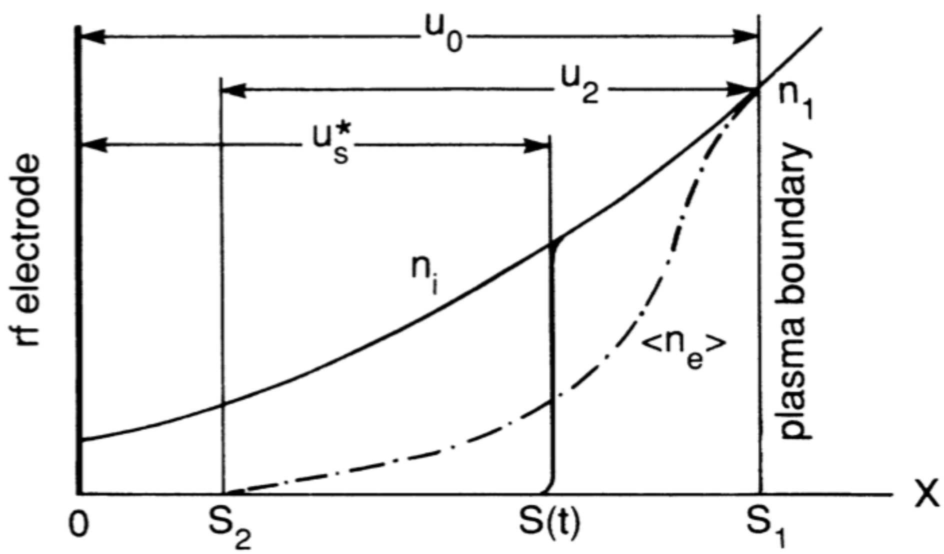

FIGURE 3.2: Ion and electron densities in a typical collisionless RF sheath where $eV_{RF} \gg kT_e$. n_i is the ion density, $\langle n_e \rangle$ is the time averaged-electron density, $S(t)$ is the instantaneous sheath location, and S_1 and S_2 are the maximum and minimum sheath excursions [32].

The inability of the plasma ions to respond to the RF fields can be seen by examining the ions as oscillators driven by an RF field on the order of that present in an RF sheath as done in Chabert [33]. The ions, in the presence of an RF electric field on the order of a sheath field, respond according to:

$$\frac{\mathrm{d}^2 x}{\mathrm{d}t^2} = \frac{e}{M_i}\frac{kT_e}{e\lambda_D}\sin(\omega_{RF}t) \tag{3.5}$$

where x is the position, M_i is the ion mass, T_e is the electron temperature, λ_D is the Debye length and ω_{RF} is the driving frequency. The solution will have the form $x = x_0 \sin(\omega_{RF}t)$, where x_0 is given by:

$$\frac{x_0}{\lambda_D} = \frac{\omega_{pi}^2}{\omega_{RF}^2} = \frac{\tau_{RF}^2}{\tau_i^2} \tag{3.6}$$

The maximum excursion of the ion is proportional to the ion plasma frequency at a fixed RF frequency. If the density is low, such that the ion plasma frequency $\omega_{pi}^2 \ll \omega_{RF}^2$, the ion excursion around its undisturbed position is small with respect to the Debye length. For electrons, the above equation holds except with the ion mass M_i replaced by the electron mass m_e, and therefore ω_{pi} replaced by ω_{pe}. The ratio of the electron plasma frequency to the RF frequency is much larger (10^4 to 10^5 for the conditions in our experiment), so the electrons can fully respond to the fluctuations.

3.1.3 Self-Bias Effect

RF fluctuations of the plasma potential (and the sheath potential) can lead to an increased electron loss from the bulk plasma compared to a DC sheath. In a DC sheath, the sheath electric field builds to retard the mobile electrons and accelerate the ions from the plasma such that the fluxes are equal in steady state, resulting in the floating potential given in 3.1. However, RF fluctuations of the electrons' potential allow, for some non-zero duration of the RF cycle, the electrons to "leak" out of the plasma initially. Ions are continuously accelerated from the plasma by the time-averaged value of the fluctuating sheath voltage, which rises to accommodate the extra electron losses such that they are equal in steady state (for a floating boundary condition or for the total flux from the plasma). This increase in the time-averaged value of the sheath voltage is known as the self-bias effect. RF plasma processing reactors often exploit the self-bias effect to control incident ion energies on substrates, which can be much greater than ion energies in DC sheaths [23].

The magnitude of the self-bias voltage is a function of the particle balance in the discharge. For simple geometries, the physical area of the driven and grounded electrodes can be used to determine the self-bias voltage assuming the sheath areas correspond with the physical areas of the electrodes. In planar-electrode configurations, when the driven electrode is capacitively coupled to the generator, there is no path for the initial extra electron current from the plasma to dissipate. This results in the capacitively coupled electrode charging negatively with respect to the plasma in steady state, and is the "classical" formulation of the self-bias voltage, which is defined as the DC voltage of the electrode relative to ground. Figure 3.3 shows a circuit model for a capacitively coupled RF discharge. There are two sheaths, one at the driven electrode (a) and one at the grounded electrode (b). The self-bias voltage is simply the difference between the two sheath drops, a result of Kirchoff's Voltage Law ($\Sigma V = 0$):

$$V_{SB} = -(V_a - V_b) \tag{3.7}$$

where V_a and V_b are the time-averaged values of the sheath drops at a and b, respectively.

The driven, capacitively-coupled electrode floats to V_{SB}, and the potential difference between the bulk plasma and the driven electrode remains such that the particle fluxes to the driven electrode are equal over an RF cycle, but here the electrode voltage adjusts (instead of the plasma potential). If the sheath capacitances for sheath a and b are given by C_a and C_b, respectively, the self-bias voltage can be written as:

$$V_{SB} = \frac{C_a - C_b}{C_a + C_b} V_{RF} \tag{3.8}$$

where V_{RF} is the magnitude of the RF driving voltage. Note that C_B is an *external* capacitor whereas C_b is the sheath capacitance at sheath b. The time-averaged plasma potential $\overline{V_p}$, ne-

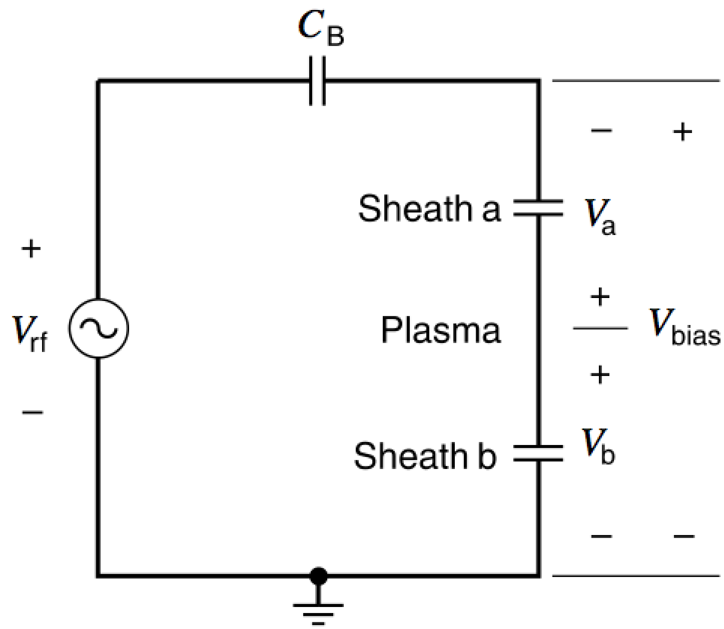

FIGURE 3.3: Circuit diagram for a capacitively coupled, RF discharge [23]. C_B is an external capacitor.

glecting the floating potential, is given by:

$$\overline{V_p} = \frac{C_a}{C_a + C_b} V_{RF} \tag{3.9}$$

The sheath capacitances are approximately proportional to the sheath areas, therefore the voltage drop across the sheath is inversely proportional to the electrode area and the electrode with the smaller area has the larger voltage drop. This can also be interpreted from a particle balance perspective. The electrode with the smaller area has a lesser effect on the global losses from the plasma, and therefore has a lesser effect on the time-averaged plasma potential. The difference between the time-averaged plasma potential $\overline{V_p}$ and the electrode potential then increases since the larger area electrode is “setting” the plasma potential. If the sheath capacitances are the same (a symmetric discharge), there is no self-bias voltage because the time-averaged sheath drops across both sheaths are the same [33, 34].

If the driven electrode has a DC path to ground, the time-averaged plasma potential will adjust such that the *total* particle flux (current) from the plasma is zero (electron and ion fluxes are equal), and a net current may flow to ensure equal fluxes. Figure 3.4 shows the plasma potential $V_p(t)$ and the driven electrode voltage for symmetric and asymmetric geometries for DC and capacitively-coupled electrodes.

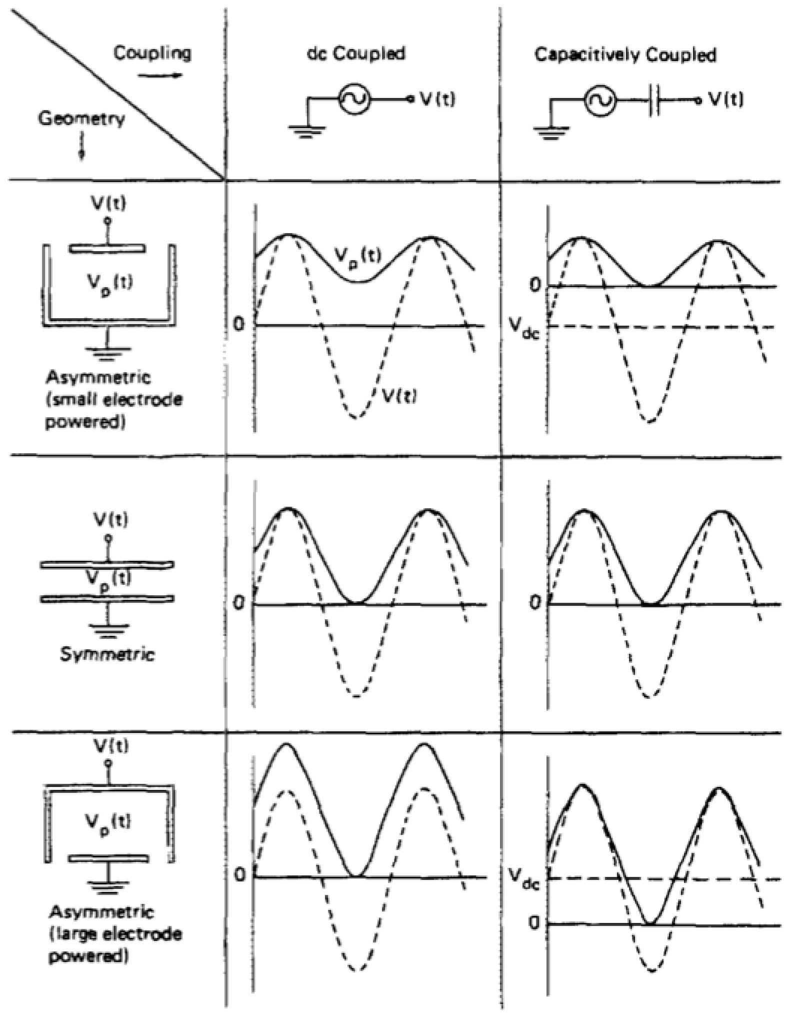

FIGURE 3.4: Plasma potential $V_p(t)$ and driven electrode voltage (dashed line), including DC and capacitively-coupled driven electrodes, for symmetric and asymmetric geometries [35].

In general, the self-bias voltage will be set self-consistently by particle balance in the discharge. In the presence of RF fluctuations, the DC floating potential (Eq. 3.1) for an undriven electrode is modified to include the effects of the electron oscillations. The net, time-averaged particle fluxes will be equal, which for sinusoidal potential fluctuations is written as [33, 34]:

$$\left\langle \frac{1}{4} n_s v_e \exp\left[\frac{e(V_1 \sin\omega t + \overline{V_p})}{kT_e}\right]\right\rangle = \langle n_s c_s \rangle \tag{3.10}$$

where n_s is the density at the sheath edge, v_e is the electron velocity, V_1 is the amplitude of the RF fluctuations, $\overline{V_p}$ is the RF floating potential (to be solved for) and c_s is the ion sound speed. Note that because it is assumed $\omega_{pi}^2 \ll \omega_{RF}^2$, the ion flux is unaffected by the plasma potential oscillations. The time-average in Eq. 3.10, denoted by $\langle\rangle$, is calculated using:

$$\langle f(t) \rangle = \frac{\omega}{2\pi} \int_0^{2\pi/\omega} f(t) \mathrm{d}t \tag{3.11}$$

The modified Bessel function of the first kind, defined as:

$$I_0(a) = \frac{\omega}{2\pi} \int_0^{2\pi/\omega} \exp\left[a \sin(\omega t)\right] \mathrm{d}t \tag{3.12}$$

will be helpful in calculating the RF floating potential due to the exponential dependence of the electron flux on the potential in Eq. 3.10. Carrying out the time-average,

$$\overline{V_p} = |V_{fl}| + \frac{kT_e}{e} \ln\left[I_0\left(\frac{eV_1}{kT_e}\right)\right] \tag{3.13}$$

where V_{fl} is given by Eq. 3.1 ($\approx 4.7kT_e$ in argon) and I_0 is the modified Bessel function of the first kind [33, 34]. For insulating walls, the plasma will float to a voltage $\overline{V_p}$ above the walls since the particle fluxes must be equal. For grounded conducting walls, the fluxes need not balance but the integrated fluxes (particle currents) must balance throughout the system [23]. For small plasma potential fluctuations, ($\frac{eV_1}{kT_e} \ll 1$), $\overline{V_p} \to |V_{fl}|$.

The RF floating potential from Eq. 3.13 is plotted in Fig. 3.5 versus the amplitude of the RF fluctuations, both normalized to the electron temperature. The magnitude of the self-bias voltage approaches the magnitude of the fluctuations of the plasma potential for large magnitude fluctuations.

It is important to note that because of the RF fluctuations, DC (time-averaged) sheath voltages

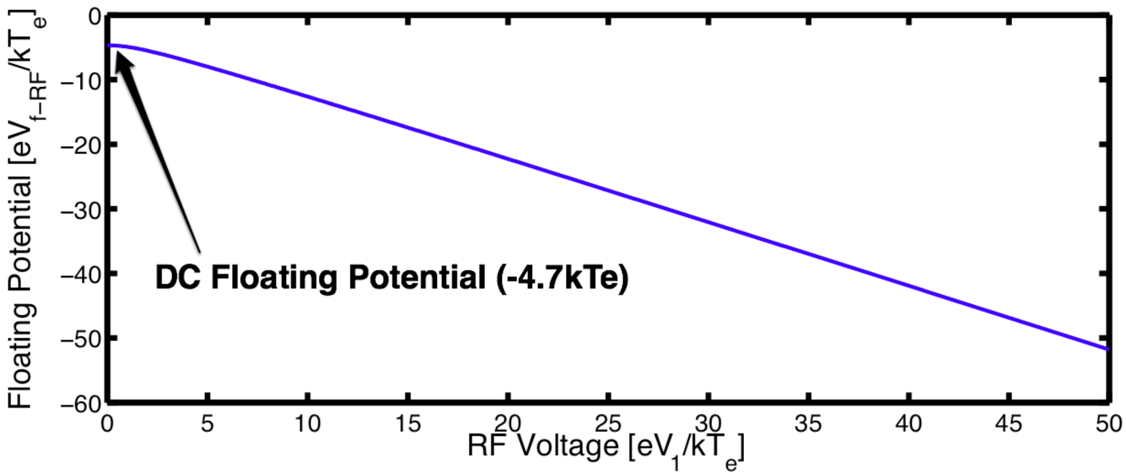

FIGURE 3.5: Modification of floating potential by fluctuations in the plasma potential.

(the self-bias) much higher than those in DC discharges can be supported while satisfying zero net (time-averaged) current flow since the plasma electrons are not confined for all times in the discharge. For low amplitude plasma potential fluctuations ($eV_1 \approx kT_e$), the difference between the RF and DC floating potentials is only $\overline{V_p} - |V_{fl}| \approx 0.25kT_e/e$. Only when the fluctuations reach $V_1 \approx 2.25kT_e/e$ do the RF and DC floating potentials differ by an electron temperature kT_e/e.

3.2 Ambipolar Plasma Expansion

Expansion of a plasma into a region of lower density plasma or vacuum can lead to ion acceleration, a phenomenon well known and well studied since the 1930s [8]. The expansion of plasma leads to an electron pressure gradient ($p_e = n_e kT_e$) and an electric field forms to retard mobile electrons and accelerate the massive ions, similar to a sheath at a plasma boundary. However, instead of at a boundary, this sheath-like potential structure forms from the expansion of plasma, in free space. This ambipolar potential is similar to a double layer, but occurs over a longer distance (a few ion-neutral mean free paths) and is not caused by charge separation that violates the Debye shielding condition. A beam of ions can be formed that is highly divergent at low pressures. If a constant electron temperature is assumed through the expansion, the resulting density profile will be [8]:

$$n_e(z) = n_{e0} exp\left[\frac{e(V_p(z) - V_{p0})}{kT_e}\right] \tag{3.14}$$

where n_{e0} is the initial density at the expansion point and V_{p0} is the plasma potential there. Ambipolar diffusion does not require separation of charge over larger than a few Debye lengths, which is what differentiates it from a double layer (see Section 3.3). The Debye length is the distance over which a separation of charge can occur in a uniform density and temperature plasma:

$$\lambda_D = \sqrt{\frac{\epsilon_0 T_e}{en_e}} \tag{3.15}$$

where T_e is the electron temperature and n_e is the electron density. In an ambipolar expansion, the electrons' density and potential follow the Boltzmann relation, and no violation of the Debye shielding criterion occurs. In magnetically expanding plasmas, a further calculation can be made under the assumption that the plasma is tied to the field lines so the density profile is known. If radial diffusion and collisions can be ignored through the expansion, the ions and electrons will follow the magnetic field lines. The physical picture is shown in Fig. 3.6.

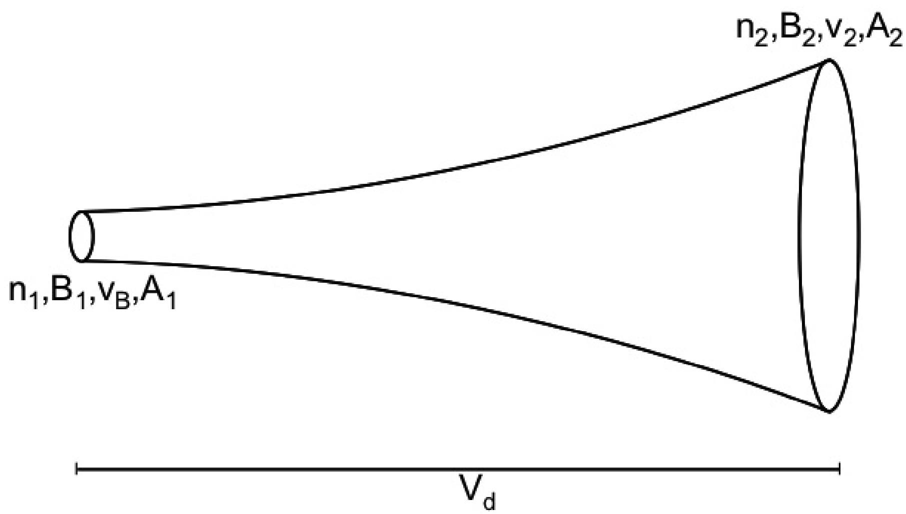

FIGURE 3.6: Expansion of a plasma along field lines. A is the cross sectional area, B is the magnetic field strength, v is the ion velocity and n is the plasma density. Subscripts *1* and *2* denote the upstream and downstream quantities, and v_B is the Bohm velocity. V_d is the distributed potential difference that arises from the plasma expansion.

The cross-sectional area of the expanding plume can be calculated from the magnetic field strength:

$$A_2 = A_1 \frac{B_2}{B_1} \tag{3.16}$$

where A and B are the cross sectional area and magnetic field, and the subscripts *1* and *2* denote the upstream and downstream quantities. The conservation of ion flux and energy lead to:

$$n_1 v_b A_1 = n_2 v_2 A_2 \tag{3.17}$$

$$\frac{1}{2} M v_b^2 + eV_d = \frac{1}{2} M v_2^2 \tag{3.18}$$

where n is the ion (and electron) density, v is the ion velocity (assumed to be the Bohm velocity $v_b = c_s$ upstream) and eV_d is the potential drop due to expansion. Eqns. 3.14, 3.16, 3.17 and 3.18 can be solved for eV_d/kT_e as a function of $A_2/A_1 = B_1/B_2$:

$$\frac{A_2}{A_1} = \frac{e^{eV_d/kT_e}}{\sqrt{1 + \frac{2eV_d}{kT_e}}} \tag{3.19}$$

This equation can be solved numerically, and the result eV_d/kT_e vs. A_2/A_1 is plotted in Fig. 3.7 for expansion ratios near those found in our experiment.

The potential drop approaches a few times kT_e/e for large expansion ratios, up to $V_d \approx 5kT_e/e$ for the highest expansion ratios in MadHeX. In this model, the potential gradient as well as the ion density ratio are "set" by the magnetic field profile, which is independent of the magnetic field strength, and the electron temperature. Therefore, if the expansion is collisionless and radial diffusion can be ignored, the potential and density gradient will be independent of the source parameters.

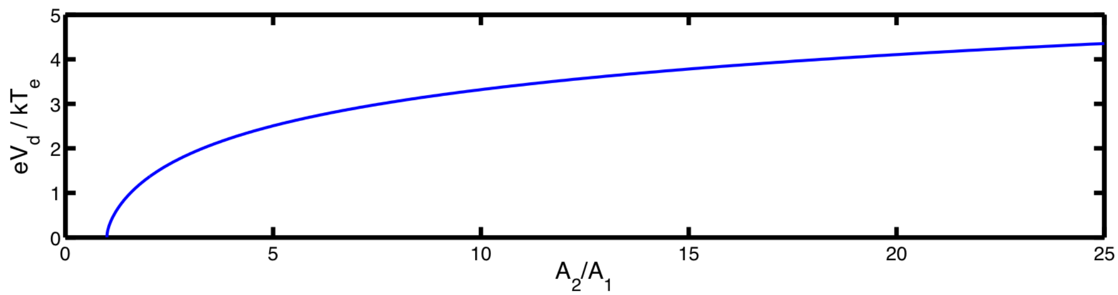

FIGURE 3.7: Normalized potential drop eV_d/kT_e vs. expansion area ratio $A_2/A_1 = B_1/B_2$ calculated from Eq. 3.19.

3.2.1 Experimental Evidence

Ion acceleration has been observed in expanding helicon plasmas, and the distinction between double-layer-containing acceleration and simple ambipolar expansion can be unclear. Some experiments observe acceleration over several hundred Debye lengths, but still claim double layer formation since the potential gradient is too large to be explained by ambipolar expansion. Other experiments clearly observe double layer formation, a few of which are highlighted in Section 3.3.6. The following is a summary of a few experiments that have seen ion acceleration but have not directly claimed double layer formation.

Corr et. al. [36, 37] observed ion beam formation in their geometrically expanding reactor below argon pressures of 3 mTorr. The *Bilby* reactor (see Fig. 3.8) consists of a 14 cm diameter, 28 cm long aluminum expansion chamber adjacent to a Pyrex source tube with varying diameters (2, 4.5, 6 cm) without a static magnetic field. They found that a lower ratio of source to expansion chamber radius results in a higher energy beam, due to the increase of plasma density and potential gradients between the source and expansion regions with the smaller tubes. An ion beam with energy of $E_b \approx 50$ eV in a plasma with $kT_e \approx 8$ eV is measured near the source-expansion chamber interface in the Bilby system with a 4.5 cm diameter source tube at 0.6 mTorr and 100 W RF power.

Lafleur et. al. [38] measured the plasma potential with a 4-grid RPA and an emissive probe (EP) in their *Piglet* helicon reactor (see Fig. 3.9), which consists of an 18 cm long, 13.6 cm inner

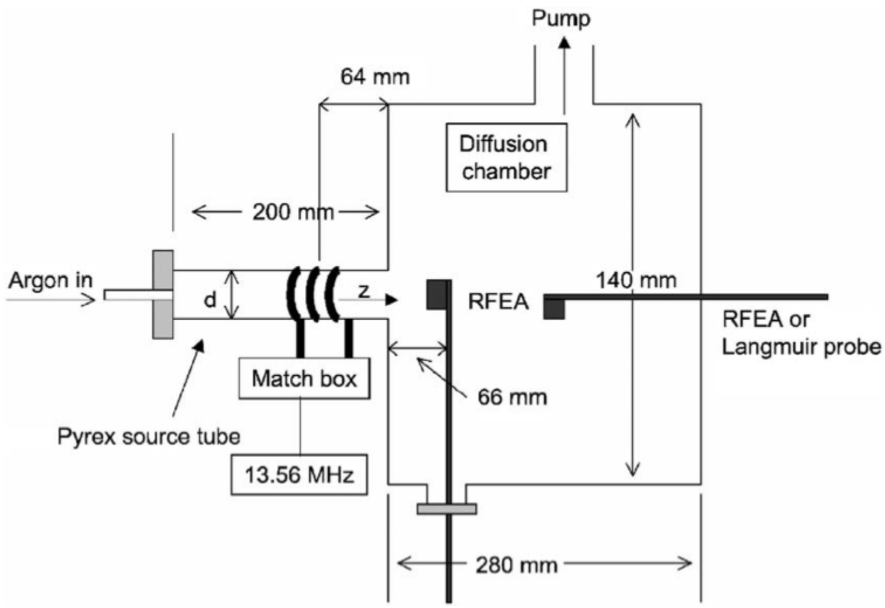

FIGURE 3.8: Inductive *Bilby* reactor at ANU [36].

diameter Pyrex tube connected to a 28.8 cm long, 30 cm diameter aluminum diffusion chamber with a static, expanding magnetic field of 160 G (maximum). A grounded metal grid is installed at the pump end (opposite the diffusion chamber) An ion beam with energy $E_b \approx 18$ eV was observed, accelerating over 15 cm, at a pressure of 0.33 mTorr with a double saddle coil antenna at 200 W RF power and 13.56 MHz. The electron temperature $kT_e \approx 5$ eV at 0.33 mTorr is measured downstream of the acceleration region using an RF-compensated Langmuir probe (LP). Their group also measured beams present in their reactor only for a narrow range of magnetic fields (10 - 30 G), where a large density peak was observed (up to 1.5 x 10^{11} cm^{-3}) at low magnetic fields ($\approx$ 20 G) [39, 40].

Longmier has recently observed ion acceleration in the helicon stage of the VASIMR VX-200i [11] device. The expanding magnetic nozzle region leads to a decaying axial potential profile due to the ambipolar field. Ion speeds up to $v_i/c_s = M \approx 4$ downstream of the magnetic nozzle, corresponding to a 20 eV ion beam in argon. The magnetic field strength is 1.7 kG and RF power up 30 kW is applied to the helicon antenna. The argon flow rate is 840 sccm, which results in a peak electron density of 1×10^{14} cm^{-3} (95% to 100% ionization fraction) and an electron

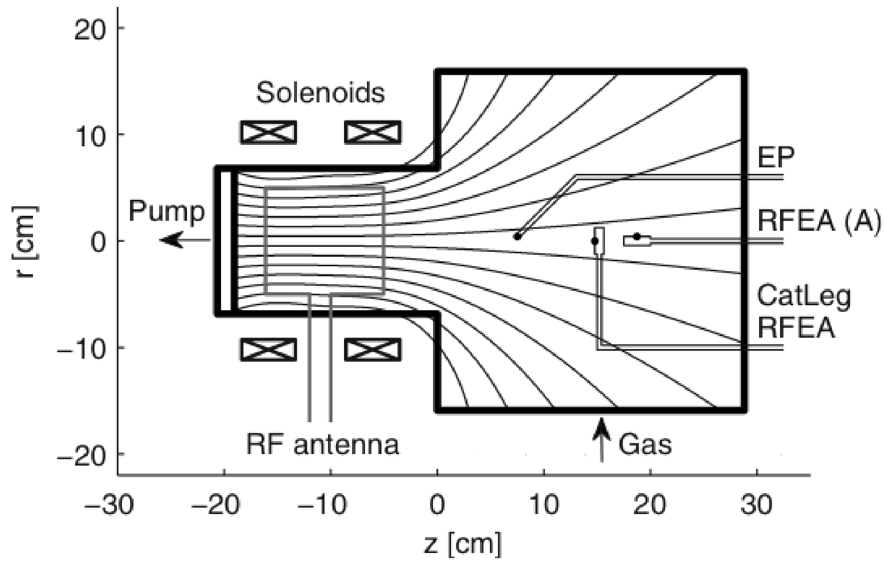

FIGURE 3.9: *Piglet* helicon reactor at ANU [38].

temperature of 9 eV. The potential structure that forms in the exhaust has a similar character to the expanding magnetic field profile. Ion acceleration was observed over 10^4 to 10^5 Debye lengths. In the 150 m^3 expansion chamber, the background electron density is near 10^9 cm^{-3} and the background neutral pressure is 2×10^{-5} Torr. The VX-200i device is shown in Fig. 3.10.

Dunaevsky [41] observed ion acceleration in a capacitive capillary discharge, with energies greater than 100 eV. A molybdenum gas feed, 0.6 mm wide and 18 mm long, acted as the positive electrode, and a ground electrode of copper foil was wrapped around the outside of the 1 mm wide and 10 mm long capillary. Argon gas was fed into the capillary at 2 to 10 sccm, resulting in pressures between 7 to 18 Torr. The discharge was driven with 2 MHz RF with antenna voltages between 210 V and 230 V, or an RF power of 15 - 20 W. Thrust on the order of 0.3 mN for 2 sccm of xenon was estimated and 0.4 mN at 10 sccm with RF power below 20 W. No double layer structures were observed in the plume. This research gives experimental proof that a capacitive discharge could be used to generate thrust. Though not discussed directly in the article, the self-bias effect certainly plays a role in ion acceleration.

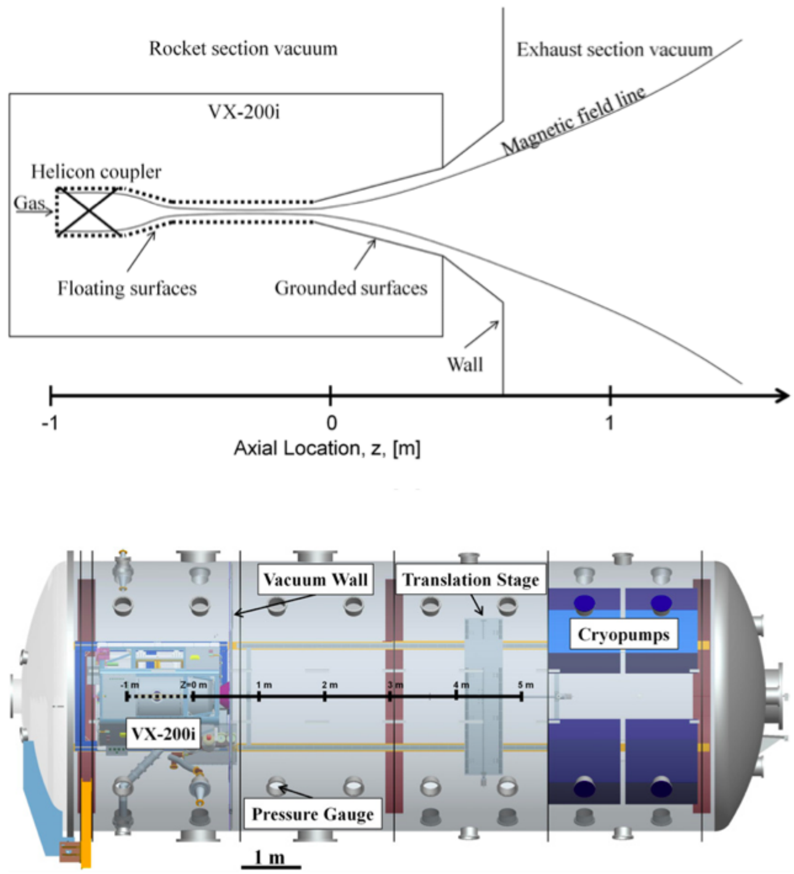

FIGURE 3.10: VX-200i helicon thruster [11].

3.3 Double Layers

In addition to ambipolar expansion, double layers have been observed in the expansion region of helicon plasmas. Double layers are narrow regions of non-neutral plasma, on the order of typical sheath dimensions, that support large potential gradients due to the separation of two adjacent layers of opposite charge. They can form between two plasma regions with differing parameters, such as density or temperature. Double layers have many similarities to sheaths that form at the boundaries of plasmas, but unlike sheaths, they are not connected to plasma boundaries.

Double layers have been shown to be partially responsible for the Northern Lights, or Aurora Borealis, which occurs due to acceleration of solar wind particles into the Earth's atmosphere. They have been investigated in many area of research including geophysics, laser ablation plasmas, materials processing and lab experiments [42] and are important in astrophysical plasmas [43,44]. There has been recent interest in these structures for ion acceleration in helicons and other plasma sources for thrust purposes since they accelerate ions without the use of grids or other lifetime-limiting wear items, making them relevant to the present work.

A double layer is simply an ion-rich layer connected to an electron-rich layer with dimensions on the order of a typical sheath, i.e. on the order of Debye lengths. A double layer has the potential structure shown in Fig. 3.11(a), which results in the ion and electron phase spaces shown in Fig. 3.11(b). There exist four populations of particles, free and trapped electrons and ions. Ions streaming downstream (in the positive x direction) are accelerated. Ions with sufficient energies coming from downstream (right) can make it "over" the potential hill with decreased kinetic energy, and those that cannot overcome the potential barrier are reflected. Ions on the upstream (left) side of the double layer are accelerated by the potential gradient. Only upstream energetic electrons with an energy larger than the potential gradient can make it over the double layer, electrons without sufficient energy are reflected. Downstream electrons are accelerated upstream by the potential. This structure is determined self-consistently by the particles moving in the electric field set up by their net charge distribution [43]. Double layers are considered strong when the potential drop is large compared to the thermal potentials ($\phi_{DL} \gg \frac{kT_i}{e}, \frac{kT_e}{e}$) and weak if the potential drop is on the order of or lower than the thermal potentials.

Double layers can be classified as current carrying, where there is a net current carried through the double layer, or current free, where there is no net current. Current carrying double layers have been studied extensively in several types of devices. Hershkowitz [45] gives a thorough review of double layers seen in laboratory experiments, focusing on current-carrying double layers in Q-machines and double/triple plasma experiments as of 1985, and includes an overview of theory. Q-machine and double/triple plasma devices are ideal for studying double layers since the ionization is occurring at the ends of the device and little ionization occurs in the DL region. They are sustained by DC filament discharges, which are fairly “quiet” devices. There is also a great deal of control over the distribution functions of the particles, providing a great deal of flexibility.

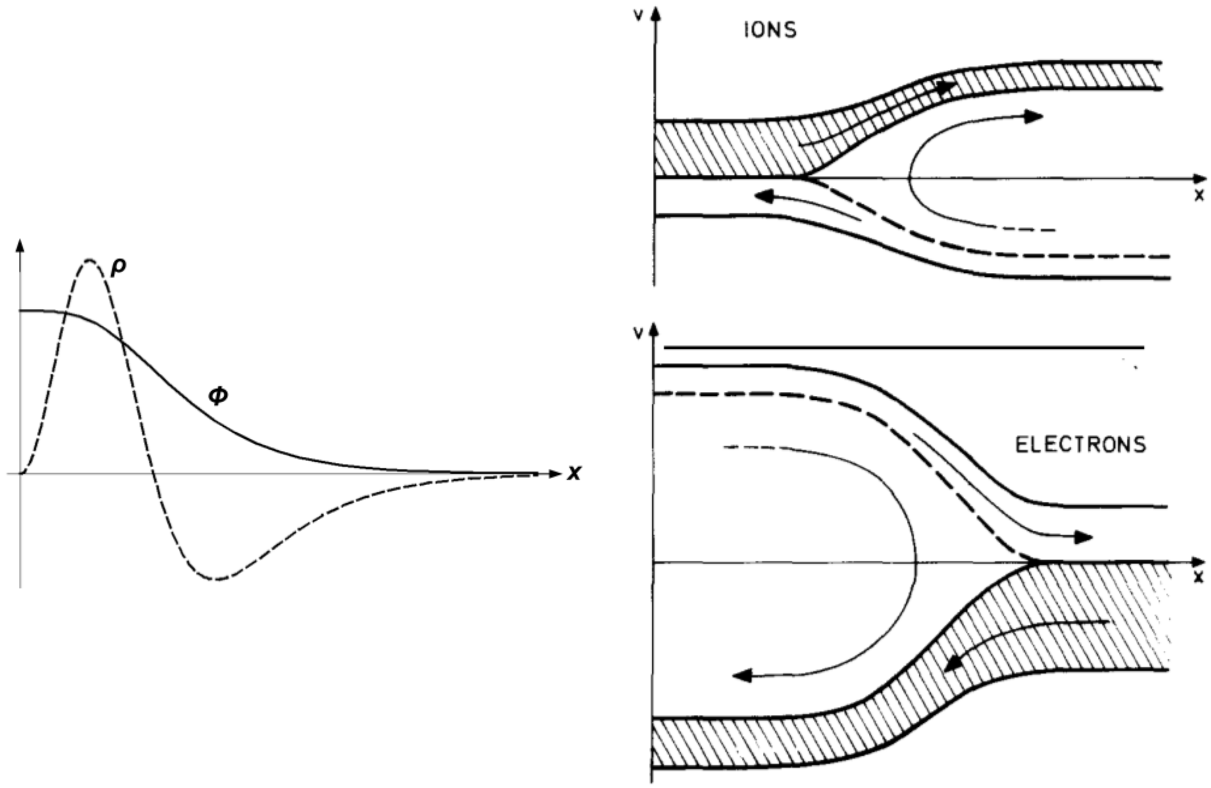

FIGURE 3.11: (a) Potential structure and charge distribution of a double layer. (b) Ion and electron phase space resulting from the double layer potential [43].

Current free double layers were postulated by Perkins [46] as solutions to the Vlasov-Poisson equations exhibiting the following four criteria: (1) an isolated non-quasineutral region of abrupt potential change (2) Maxwellian ions and electrons upstream of the DL (3) Maxwellian electrons on the downstream side but counterstreaming ions so there is no net current and (4) the potential decreases from the upstream to the downstream side. Current free double layers (CFDLs) are attractive because their net energy dissipation ($\vec{E} \cdot \vec{J}$) goes to zero and no mass plasma flow is necessary to sustain them. Also, propulsion devices utilizing a CFDL would not require a separate source of electrons to neutralize the ion flow and avoid spacecraft charging, as typical electron sources are lifetime-limiting.

Recently, CFDLs been found experimentally in an expanding plasma that uses no grids (Fig. 3.12). Devices containing these double layers have a dielectric source chamber and a grounded diffusion or expansion chamber, and an axially expanding magnetic field is imposed. The CFDL is observed at the junction between the two regions. Charles [12] gives a more recent review of double layers focusing on these devices, including scaling of double layers with experimental parameters, and a brief review of experimental evidence of double layers in these types of devices is given in Section 3.3.6.

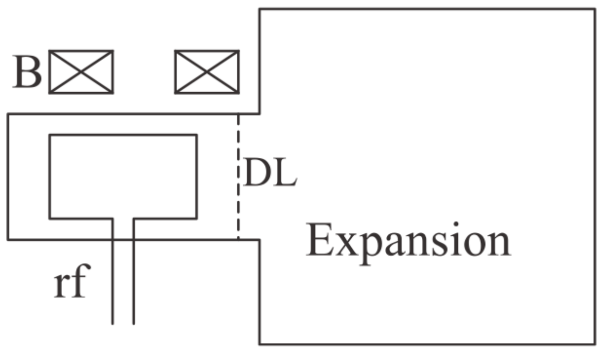

FIGURE 3.12: Geometry of expanding RF plasma source that produces CFDLs [12]. B indicates magnetic field coils, rf indicates the antenna and DL is the location of the double layer formation.

Three prominent models exist for the presence of a CFDL in an expanding plasma such as those seen recently in helicon sources [47]. These models, while not complete, have faithfully described observations in experiments. These models include a thermal ion population upstream and a flowing ion population downstream, as well as a thermal electron population upstream. They differ in their treatment of an additional electron population on the upstream side of the double layer.

Chen Model [48] Chen considers a Maxwellian upstream electron population, with no additional energetic electron population accelerated by the double layer. Some of the upstream electrons are energetic enough to overcome the potential gradient of the double layer, and make it downstream. The plasma expansion is considered to be a simple Boltzmann expansion (see Section 3.2) until the point where quasineutrality breaks down ($n_e/n_{e0} = e^{-1/2}$) and the double layer forms. The double layer potential is self-consistently set such that equal electron and ion fluxes can flow across it, and it is therefore current free. This potential is the floating potential of a probe in the plasma, or $V_s \approx 5.2kT_e/e$ for argon. This theory lacks a mechanism to explain the neutral pressure dependence of the double layer (see Section 3.3.3), which is seen in experiments, since the model is collisionless.

Lieberman Model [49] The Lieberman model also uses the same populations of particles as the Chen model, but it includes a population of electrons that are accelerated from downstream to upstream by the potential gradient of the double layer. This theory is able to predict the neutral pressure dependence of the potential gradient since it is a diffusive model. The additional electron losses at the upstream sheaths due to the accelerated electrons must be balanced by the increased ionization from these electrons. When the neutral pressure is too low, there are not enough electron-neutral ionizing collisions and the double layer collapses. When the neutral pressure is too high, there is no longer a need for ionization by the energetic electrons and the double layer vanishes. The Lieberman model is discussed further in Section 3.3.3.

Ahedo-Sánchez Model [42] The Ahedo-Sánchez model includes the populations of particles as the Chen model as well as a bi-Maxwellian electron population upstream of the double layer. This model is collisionless, so it cannot describe the neutral pressure dependence of the double layer strength. The model derives a parametric region for DL formation, as a function the temperature ratio T_h/T_c of the hot and cold electrons and the ratio of n_h/n_0 of the hot electron density to the total density. For a distribution without hot electrons, the DL cannot form (see Fig. 3.15).

It is important to note that potential drops on the order of 3 - $5kT_e/e$ are also possible under ambipolar expansion as well as with a double layer, but ambipolar expansion occurs on a much longer length scale than the double layer. The potential gradient from ambipolar expansion is set by the magnetic field geometry (expansion ratio), assuming the plasma is tied to the magnetic field lines. Ambipolar expansion also results in a density gradient through the expansion, which is larger than the density gradient through a double layer. This can be used to distinguish a double layer from a simple ambipolar expansion. The qualitative difference between ambipolar expansion and an expansion containing a double layer is shown in Fig. 3.13(a).

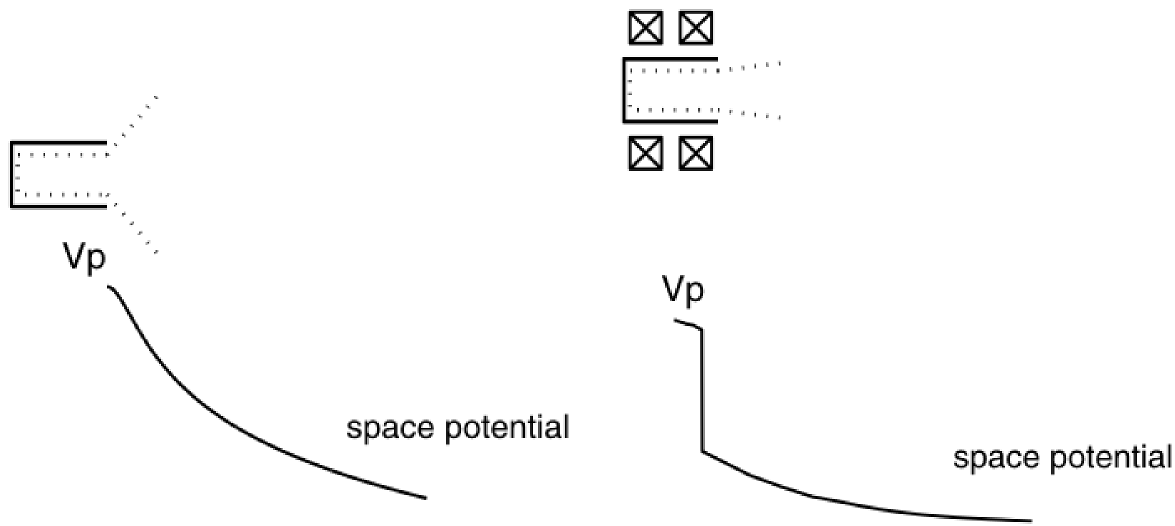

FIGURE 3.13: (a) Plasma potential due to gradual, ambipolar expansion of plasma (b) Plasma potential due to electrostatic shock [8].

3.3.1 Double Layers and P-N Junctions

There are several similarities between a double layer and the depletion region in a p-n junction in a semiconductor diode, and to better understand double layers, the similarities and differences between these two will be explored. Despite the obvious differences between semiconductors and ionized gaseous plasmas, parallels can be drawn to further the understanding of double layers. In fact, circuit models of plasma sheaths typically include a diode to represent the exponential behavior of the electron current on the voltage across the (single) sheath at plasma boundaries [33].

A p-n junction consists of two regions of semiconductor of differing type sandwiched together. The first region, the n-type, is doped with atoms that provide free electrons in the region (donor atoms). The other region, the p-type, is doped with atoms that provide “electron holes”, or vacancies in the atomic lattice, that can accept electrons (acceptor atoms). At the junction of these two types of semiconductors, a depletion region exists where the free electrons from the n-type region can diffuse into the p-type region with extra electron holes due to the finite temperature of the electrons. The electrons and holes in the depletion region recombine, and in the p-type region

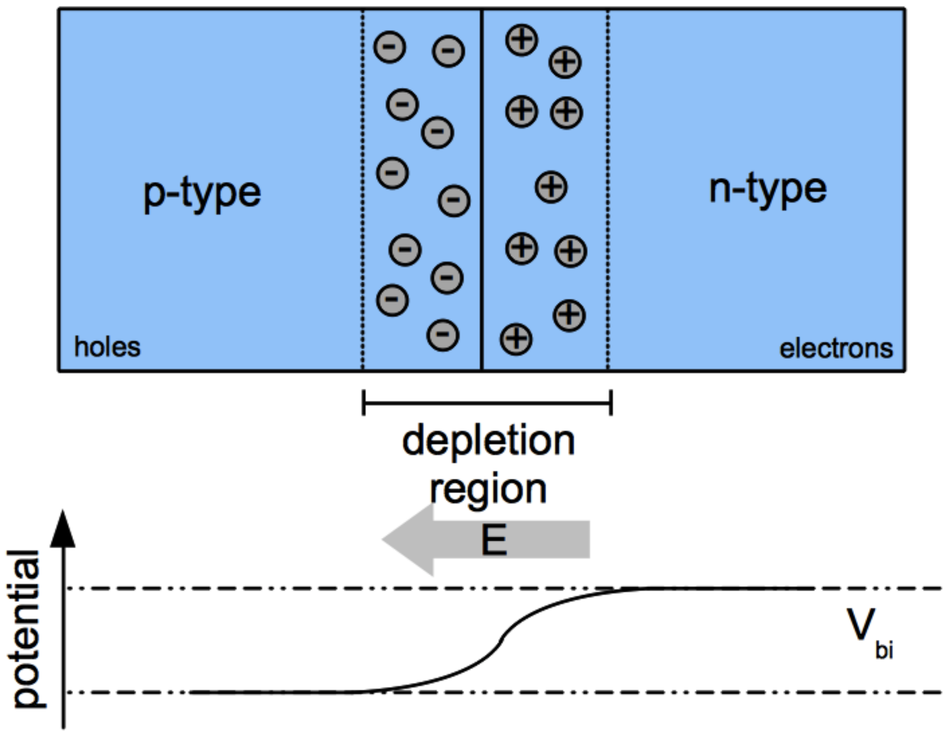

FIGURE 3.14: Diagram of p-n junction. In the depletion region, the recombination of electrons and holes leads to a build up of space charge (+ and - circles) resulting in an electric field and potential gradient. The potential profile is very similar to that of a double layer, as shown in Fig. 3.11(a).

form negative ions and in the n-type region form positive ions. The regions of separated charge formed by the positive and negative ions builds up and retards further electron diffusion as well as causes a drift of the electrons. In equilibrium, the depletion region has a finite width and a potential gradient is formed due to the space charge and resulting electric field, and the drift and diffusion currents of electrons (or holes) are equal. The equilibrium potential drop is called the "built-in voltage", and is given by [50]:

$$V_{bi} = \frac{kT}{e} \ln \left[\frac{N_A N_D}{n_i^2} \right] \tag{3.20}$$

where T is the material temperature (near room temperature, $kT \approx 0.025$ eV), N_A is the number density of acceptor atoms, N_D is the number density of donor atoms and n_i is the intrinsic carrier density, the number of electrons that are thermally excited into the conduction band (a function of temperature, $n_i \approx 10^{10}$ cm^{-3} for silicon at room temperature). If the p-n junction is biased externally, the applied bias will either add to or subtract from the built-in voltage. When the p-n junction is reverse biased (positive potential connected to n-type region), the applied bias *adds* to the built-in voltage, impeding current flow as the conduction electrons see an "uphill" potential profile. If the p-n junction is forward biased (positive potential connected to the p-type region), the applied bias *subtracts* from the built-in voltage. As the applied forward bias surpasses the built-in voltage, current is able to flow through the p-n junction readily and exponentially increases with applied voltage.

Similarities

There are several similarities between double layers and p-n junctions, a few of which are outlined below.

Interface of Two Regions Both p-n junctions and double layers form at the junction of two distinct regions. Double layers can also form via other mechanisms, such as current flow or expansion of a plasma in a divergent magnetic field, but they have been extensively studied in double- and triple-plasma devices at the interface of two plasmas [45].

Temperature Dependence The built-in voltage of a p-n junction is a function of the material temperature. Although the electron temperature in a ionized gaseous plasma is much higher than for conduction electrons in a semiconductor, it has been shown that the potential drop across a double layer is in some cases a dependent on the electron temperature [12].

Potential Profile The potential profile in both double layers and p-n junctions is a result of the separation of charge in space. In a p-n junction, the space charge is a result of positive and negative ions that are present near the depletion region as a result of diffusion of electrons and holes. In a double layer, the space charge separation can be due to several mechanisms, including the diffusion of electrons from a region with higher electron temperature or a laminar shock-type effect. In either case, the potential profile has a region of positive curvature followed by a region of negative curvature as a result of these regions of charge.

Current Flow Both p-n junctions and double layers are affected by the flow of current. Forward biasing a p-n junction results in the exponential conduction of current through the device. Similarly, the electron current through a sheath (single layer) is has an exponential dependence on the sheath voltage. However, the I-V trace of a double layer is not as well understood as for p-n junctions.

Physical Dimensions Depletion region width is dictated by the dopant level (density) and scales with the square root of the bias voltage across the junction (below the built-in voltage) [50]. A double layer is a sheath phenomenon, with dimensions on the order of the Debye length, a function of the electron temperature and density. While the depletion region width is not a direct function of temperature, the built-in voltage is dependent on temperature. The width of a double layer has also been shown to scale with the square root of the potential drop across the double layer [49].

Role of Boltzmann distribution The number of electrons in the conduction band in a p-n junction is a function of the Fermi function and the density of available electron states, whereas the the electron density in a plasma typically follows a Boltzmann relation between the electron density and plasma potential and electron temperature.

Differences

Not including the obvious distinctions of semiconductors and ionized gaseous plasmas (particle densities, sustainment mechanisms, lattice effects, etc.), p-n junctions and double layers also have important differences:

Applied Potential The potential drop across the depletion region in a p-n junction is linearly affected by an applied bias voltage, whereas the potential drop across a double layer, in the presence of an applied potential, will generally not vary linearly with the applied potential. The plasmas surrounding the double layer will be affected nonlinearly by the applied bias, and may lead to the disappearance or growth of the double layer.

Reverse Breakdown In a p-n junction, a very small current flow in the reverse direction is possible until avalanche breakdown occurs. Double layers do not exhibit any breakdown phenomena.

Formation Mechanism The charge separation in a p-n junction is caused by positive and negative lattice ions, whereas the charge separation in a double layer is the result of the separation of electrons and ions in free space by thermal diffusion, flow or other forces.

Particle Motion In electropositive double layers, there are four populations of particles, free and trapped electrons and ions. In a p-n junction, there are also four types particles, two of which are held in the crystal lattice (positive and negative ions) and two are free (the electrons and electron holes). On either side of a double layer, there is quaisneutral plasma consisting of ions and electrons, whereas in a p-n junction there are mainly majority carriers on either side (holes or electrons), and very few minority carriers (electrons or holes).

Magnitude of Potential Drop The built-in voltage in a p-n junction is often less than 1 V (0.7 V for silicon, 0.3 V for germanium). Typical double layer potential drops are at least an order of magnitude higher, due to the larger electron temperature and free energy in ionized gaseous plasmas.

3.3.2 Fast Electron Effects

Hairapetian and Stenzel [51] have examined the effect of a two-temperature electron distribution in a collisionless, weakly divergent plasma formed by a transient DC gas puff system. Detailed experimental measurements of density, potential and distribution functions reveal a high density cold electron (4 eV) population and a low density high energy electron (80 eV) population in the source region. As the plasma expands, the energetic tail electrons electrostatically trap the cold electrons and prevent them from reaching the expansion front, and a double layer forms at the cold electron front. The double layer propagates near the sound speed and then stagnates at a position dependent on the relative populations of electron populations. The fast electron population can make it over the potential hill of the double layer act to neutralize the plume.

Ahedo [42] also gives an analytical model for two temperature distributions expanding in a collisionless plasma in a convergent-divergent nozzle system and shows that current free double layers can form in these systems and includes a parametric range for formation. Fig. 3.15 shows the parameters α, the normalized hot electron component density, and τ, the ratio of the hot electron temperature to the cold electron temperature that allow DL formation. Note that for α = 0 (no hot electron component), the double layer cannot form and there is simple quasineutral expansion.

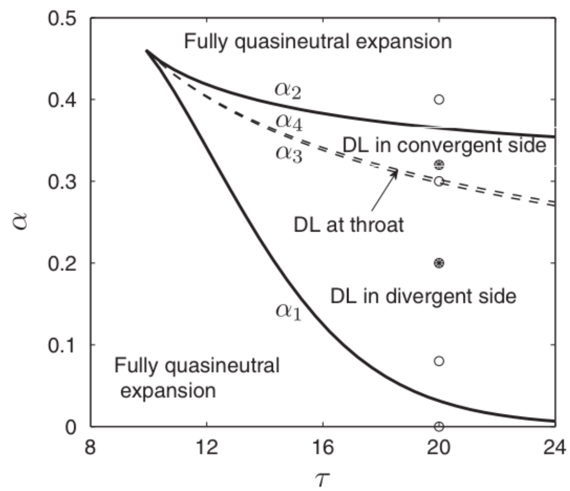

FIGURE 3.15: $\alpha = n_{h0}/n_0$ and $\tau = T_h/T_c$ parameter range for DL formation [42] in a convergent-divergent nozzle system [42].

3.3.3 Pressure Dependence

Lieberman [49, 52] presents a diffusion-controlled model for formation of a CFDL in a low pressure plasma and derives both upper and lower pressure limits for beam formation in the geometry shown in Fig. 3.16(a). The upper limit is reached when the energy relaxation length for ionizing electrons becomes comparable to the system length, and the double layer disappears at low pressures due to a loss of ionization balance between upstream and downstream of the double layer. This explanation assumes a physically expanding system where there are higher surface losses upstream which are compensated for by ionization from the upstream-flowing accelerated electrons. For comparison, experimental data from Charles [53] shows a double layer strength of eV_s/kT_e = 3 for their experiment [53], which is classified as a moderate strength DL. The pressure dependence has been experimentally verified by West [54].

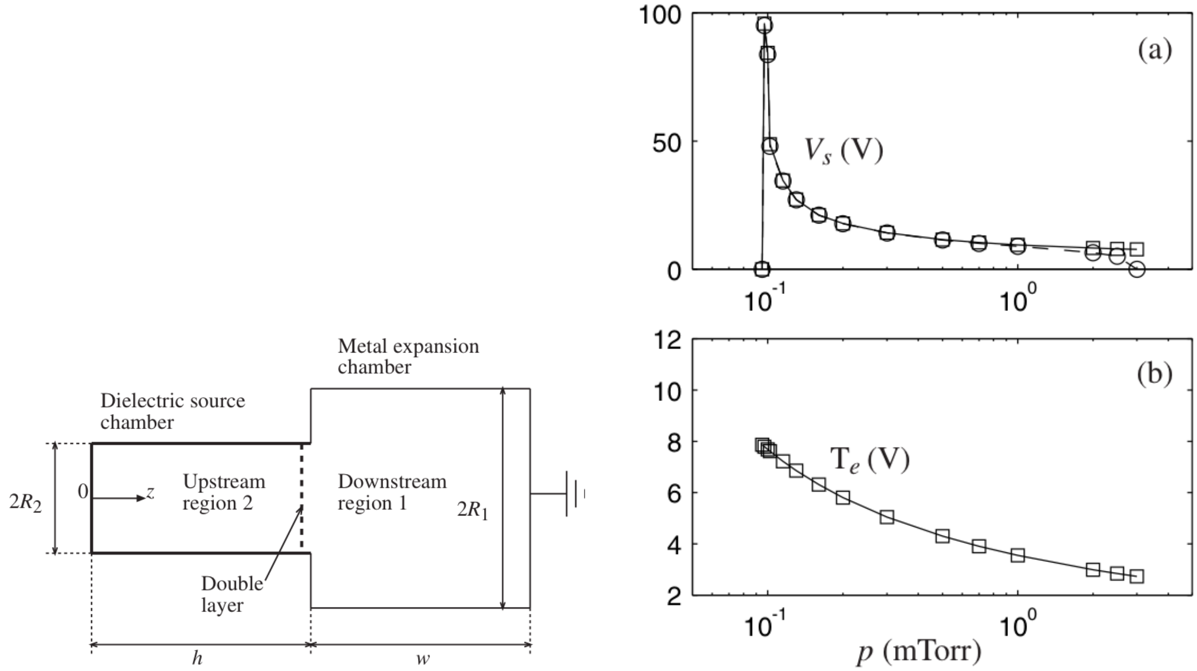

FIGURE 3.16: (a) The system geometry used in Lieberman's theory for formation of CFDLs. (b) The pressure range for formation of CFDLs according to this theory [49].

Lieberman [49] gives an expression for the width of a double layer as a function of the potential drop V_d and the electron temperature T_e:

$$L_{DL} \approx 10\lambda_D \sqrt{\frac{eV_d}{kT_e}} \tag{3.21}$$

where T_e is the electron temperature and λ_D is the Debye length. Note that for most double layers seen in helicon devices (see Section 3.3.6), the width is on the order of tens of Debye lengths, perhaps up to 100 Debye lengths for strong potential drops.

Baalrud [55] derives the pressure limits for the double layer formation based on a 1D kinetic model instead of Lieberman's 3D diffusion-controlled model, although the physical arguments are the same. The low pressure limit is given by:

$$p_{min} \approx \frac{e^{-1/2}\sqrt{2\pi m_e/M_i}}{n_{n0}\sigma_{en}L_s} \tag{3.22}$$

where n_{n0} = 3.25 $\times$ 10^{19} [m^{-3}/mTorr], σ_{en} is the electron-neutral cross section and L_s is the length of the source. For long source tubes, the minimum pressure for DL formation decreases, which results in a larger double layer drop (see Fig. 3.16(b)). The maximum pressure for DL formation is:

$$p_{max} \approx \frac{1}{n_{n0}\sigma_{en}L_d} \tag{3.23}$$

where L_d is the length of the downstream chamber. The DL vanishes when too many electrons are accelerated upstream, and the DL cannot adjust enough to preserve current balance.

3.3.4 Thrust From a Double Layer

Fruchtman claims the net thrust from a double layer must be zero in order for momentum to be conserved [56]. They claim the ion acceleration seen in some devices from CFDLs is due to the magnetic field pressure balancing the plasma pressure rather than the electrostatic pressure from the double layer. The double layer must "push" on the plasma pressure through the magnetic field pressure upstream in order to impart momentum to ions flowing downstream. However, if there is not sufficient magnetic field pressure upstream, the ions “push” on the wall and are lost through the sheaths, an undesired loss mechanism. Charles [8] gives an expression for these losses:

$$P_{loss} = A_{sheath} q n_{sheath} v_i (V_p + \frac{2kT_e}{e}) \tag{3.24}$$

where A_{sheath} is the total sheath area, q is the ion charge, n_{sheath} is the density at the sheath, v_i is the ion velocity into the sheath (the Bohm velocity), V_p is the plasma potential and each ion that leaves take an electron with it and the energy lost is $2kT_e/e$.

3.3.5 Computational Modeling

Several researchers have developed particle-in-cell (PIC) codes to probe the existence of a CFDL in these systems. Meige [57], using a one dimensional (space) and three dimensional (velocity) code observed CFDL formation and ion beams up to 60 eV in a system with geometry similar to that shown in Fig. 3.12. Fig. 3.17 shows the ion velocity distribution vs. z in the computational domain. In order for the DL to be current-free, the upstream source region had to be allowed to charge. If the ends of the domain were at the same potential, a current was observed.

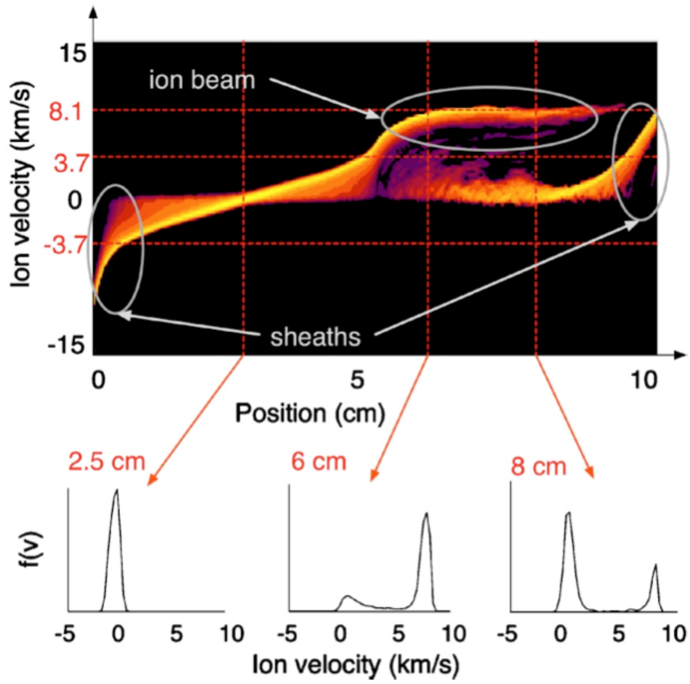

FIGURE 3.17: Result of PIC simulation of a current-free double layer. The ion velocity distribution (top) shows the formation of a beam near 5 cm (the point of physical expansion) with velocity up to 8 km/s. The resulting IVDF at three axial locations are also shown (bottom) [57].

Baalrud et. al. [55], using a code similar to that used by Meige, investigated electron energy distributions in the upstream and downstream regions. They found that the maximum potential drop of the double layer is the floating potential of the system, calculated using the downstream electron temperature, which was always lower than that of the upstream region.

3.3.6 Experimental Evidence

Charles [53, 58–60] was one of the first to observe a current-free double layer in an expanding helicon source with an energy analyzer using their *Chi-Kung* device (see Fig. 3.18). *Chi-Kung* consists of a 20 cm long double-saddle antenna, driven at 13.56 MHz, wrapped around a 15 cm diameter, 30 cm long glass tube which is connected to a 32 cm diameter grounded diffusion chamber. Two solenoids provide a magnetic field up to 250 G. Beam energies up to $E_b = 3kT_e$, or 25 eV, were observed at argon pressures below 0.5 mTorr, which formed over $\approx$ 50 Debye lengths. Higher upstream electron temperatures were observed upstream of the double layer.

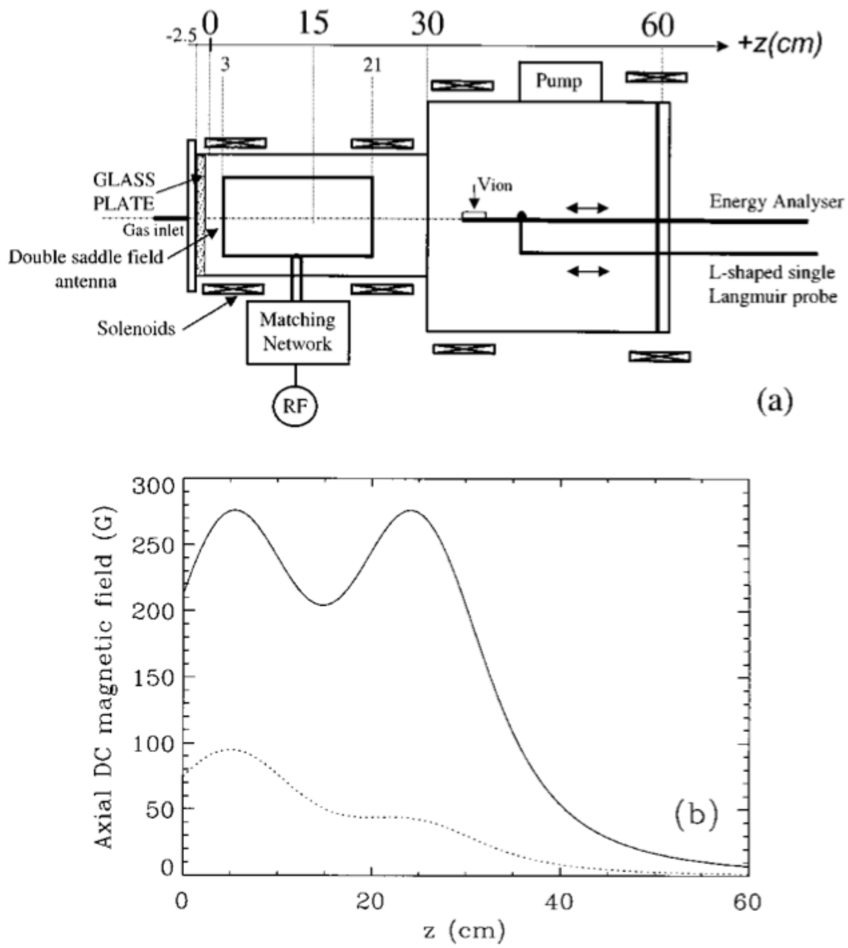

FIGURE 3.18: *Chi-Kung* experimental device [53] including magnetic field profile, diagnostics and vacuum system.

Cohen reported ion acceleration up to 30 eV ($4kT_e$) initially [61] and later [62] to 65 eV (3 to $10kT_e$) in argon using Laser Induced Fluorescence (LIF) in their Magnetic Nozzle Experiment (*MNX*) helicon device with a magnetic nozzle (see Fig. 3.19). *MNX* consists of a 4 cm diameter double-saddle antenna, driven at 26.75 MHz, wrapped around the 30 cm long glass source tube, which is attached to a 20 cm diameter, 45 cm long main chamber. A 1 cm diameter metal aperture separates the main chamber and the 10 cm diameter, 1 m long expansion region (ER), which leads to a drift chamber. Differential pumping and the low conductance aperture provide a large pressure differential (up to a factor of 10) between the main chamber and the ER. Two solenoids and a nozzle coil coincident with the aperture provide a magnetic field of several hundred G with an adjustable peak field up to 1.4 kG. Typical conditions are $P_{RF} \approx 500$ W, $B \approx 575$ G with a 1.4 kG nozzle peak, and pressures of 0.5 mTorr in the main chamber and 0.135 mTorr in the ER. They concluded the ion acceleration is not due to magnetic nozzle acceleration or simple plasma expansion, but is due to a double layer that is induced near the aperture. They also saw evidence [62] of a two-temperature electron distribution downstream of the ion acceleration, with higher tail electron temperatures (0.1% fast electrons), which they claimed may be responsible for the high potential drops (and beam energies) in their system.

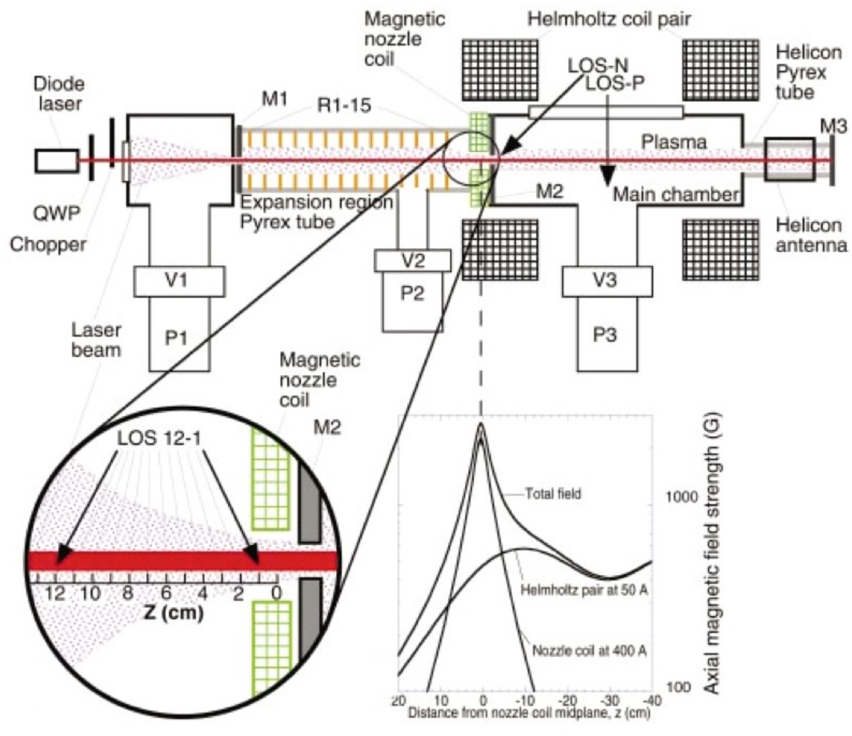

FIGURE 3.19: Magnetic Nozzle Experiment *MNX* experimental device [61] including magnetic field profile, diagnostics and vacuum system. Physical aperture M2 limits the gas flow into the Expansion Region from the Main Chamber.

Sutherland [63] observed double layer formation in the large-volume *WOMBAT* helicon reactor (see Fig. 3.20), up to E_b = 5 - 7kT_e in argon. Gas is fed into the diffusion chamber and the source is fed by diffusion. The reactor consists of a 50 cm long, 20 cm diameter Pyrex tube joined to a 1 m diameter grounded diffusion chamber. Up to 500 W of 7.2 MHz RF power is fed into the double-saddle antenna, and a magnetic field of 250 G is provided by two solenoids. The ion beam forms over $L_d \approx 20$ Debye lengths at argon pressures between 0.09 and 0.3 mTorr, and the DL location was found to be tied to the magnetic field profile, not the location of the physical expansion.

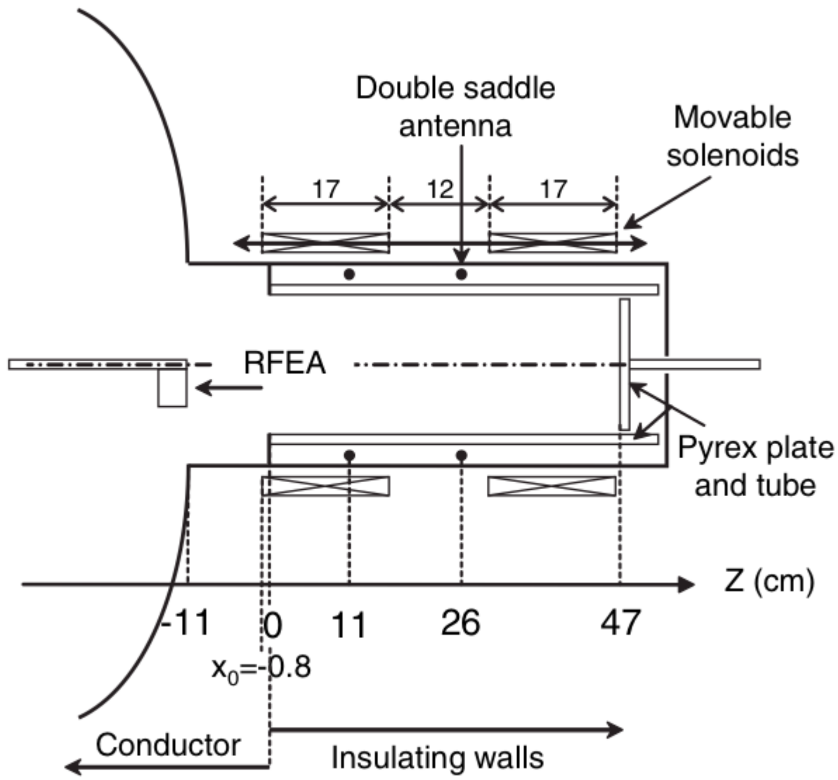

FIGURE 3.20: Waves On Magnetized Beams And Turbulence (*WOMBAT*) experimental device [63] diagnostics and vacuum system. Gas is fed into the diffusion chamber, opposite that of the configuration of MadHeX.

Experiments on the *HELIX/LEIA* device at WVU (see Fig. 3.21) have investigated the time development of the double layer as well as the effect of RF frequency using LIF and energy analyzers [64–66]. The *HELIX/LEIA* device consists of a 10 cm diameter, 61 cm long Pyrex tube connected to a 15 cm diameter, 91 cm long grounded chamber which is then connected to a 2 m diameter, 4.5 m long space chamber. RF power up to 2 kW is coupled to a 19 cm long half-turn double-helix antenna wrapped around the Pyrex tube, and argon pressures are 0.2 mTorr in the source and 0.05 mTorr in the space chamber. Double layer and ion beam formation was observed at RF frequencies above 11.5 MHz, with ion beam energies around 15 eV and spatial extents of tens of Debye lengths, however formation over hundreds of Debye lengths has also been observed on a variant of this system [64]. Figure 3.22 shows the beam evolution vs. axial distance and the results of a particle-in-cell (PIC) calculation showing the ion distribution vs. z through a double layer. They measured low frequency (ion acoustic) instabilities at RF frequencies below 11.5 MHz, which they indicate prevent the DL from forming below the threshold frequency.

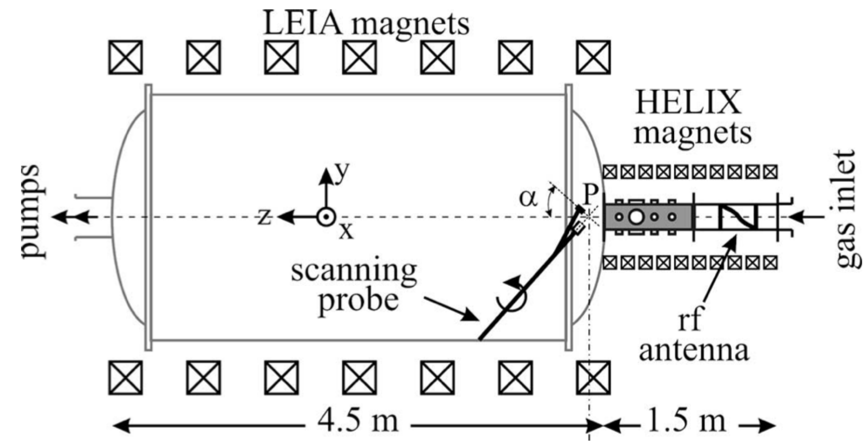

FIGURE 3.21: *HELIX/LEIA* experimental device [65] including vacuum system.

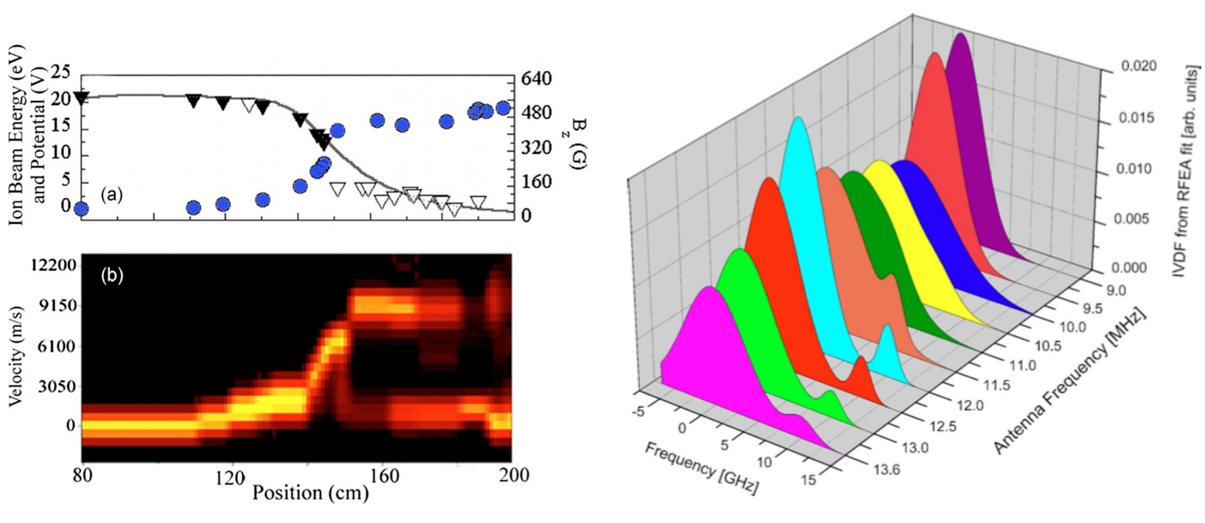

FIGURE 3.22: 3.22(a) Observations of beam energy vs. distance in the *HELIX/LEIA* source (top) and particle-in-cell (PIC) computation of ion energies through a double layer [57] 3.22(b) Ion energy distribution vs. source RF frequency in *HELIX/LEIA* [65].

West et. al. [54, 67] measured DL formation in a helicon source immersed in a vacuum chamber. The source, shown in Fig. 3.23, consists of a 15 cm Pyrex tube, 29 cm long immersed in a vacuum chamber 140 cm long and 100 cm in diameter. Two solenoids provide a magnetic field up to 138 G. A double-saddle antenna, driven at 13.56 MHz at 100 W is wrapped around the Pyrex chamber. A moderate energy beam (up to 30 eV) was measured with an RPA, and the pressure dependence of the Lieberman model was confirmed.

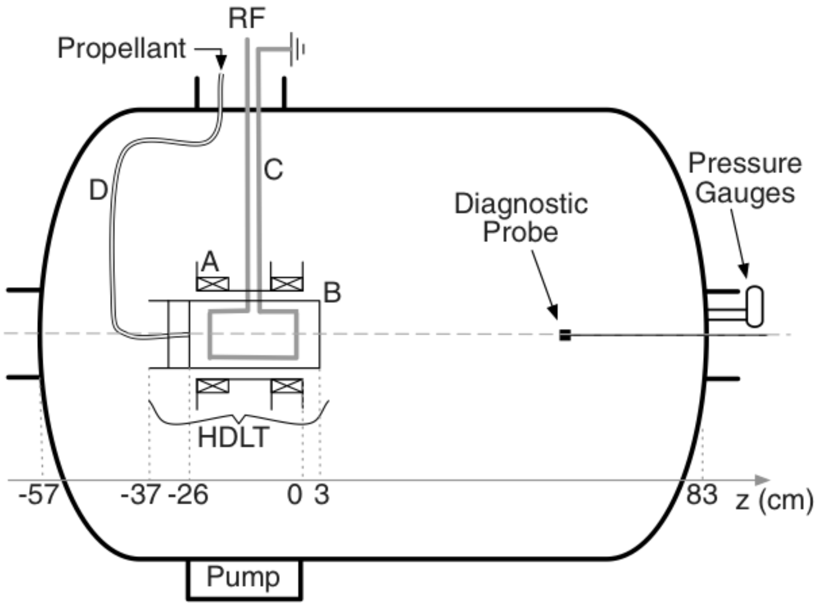

FIGURE 3.23: *HDLT* helicon reactor at ANU [54].

Recently, Virko et. al. [1], using retarding potential analyzers (RPAs), observed ion beams in argon accelerated over several centimeters with energies (E_b = e[V_{beam} - V_{plasma}]) approaching 75 eV in their 4.5 cm diameter quartz helicon system with fixed permanent magnets (see Fig. 3.24). With an axially monotonic magnetic field profile with argon pressures below 1 mTorr, intense pumping was required to achieve ambipolar ion acceleration up to 55 eV, which occurred even at zero magnetic field. With a magnetic cusp, they found that the insulation of high-density source and low-density drift regions created by the cusp led to non-ambipolar ion acceleration due to an extended potential drop (DL) between the two regions, over 5 - 6 centimeters. Ion energies up to 75 eV were observed in this case at 700 W RF power and at pressures near 0.1 mTorr. Emissive probes were used to measure plasma potentials, from 75 V to 110 V, in the source region.

Takahashi [68–70] has observed ion beam formation in argon in the *EMPI* device as well

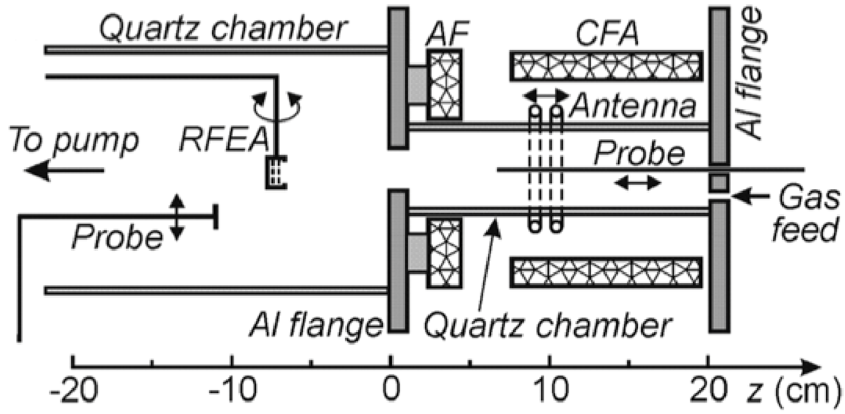

FIGURE 3.24: Helicon reactor used by Virko, et. al. [1].

as the *Chi-Kung* device at ANU used by Charles [53, 58–60]. The *EMPI* device, similar to the *Chi-Kung* device, consists of an insulating source tube, 30 cm long, and a 20.8 cm diameter grounded diffusion chamber (see Fig. 3.25). A triple-turn loop antenna driven at 13.56 MHz is wrapped around the source tube, and up to 200 W RF power is supplied. Typical conditions for beam formation are pressures $p_{Ar} \approx 0.4$ mTorr - 0.6 mTorr, $P_{RF} \approx 200$ W, B $\approx$ 200 - 400 G. By testing different source tube diameters, they found that when the argon ions become magnetized in the source region, the DL and ion beam form. Two-temperature electron distributions were also measured on these devices, with lower tail than bulk electron temperatures.

Fredriksen et. al. [71] and Byhring et. al. [72] have carried out ion beam formation experiments in argon in the *Njord* double-saddle RF device of 13.7 cm diameter (see Fig. 3.26) with source-region plasma potentials around 50 V. They have observed beams of 34 - 40 eV energy with an 8% beam fraction at low flow rates (1.2 - 1.5 sccm) utilizing an RPA, with 400 - 600 W of RF power and magnetic fields in the 110 - 250 G range. They indicate a current free double layer forms 10 cm downstream from the maximum magnetic field gradient in the expansion region. They also added a magnetic coil in the spherical dome region to extend the magnetic field expansion and observed 25 eV argon ion beams which disappear when the extra coil current is high enough such that the plasma is well confined into the downstream region, and the potential drop vanishes.

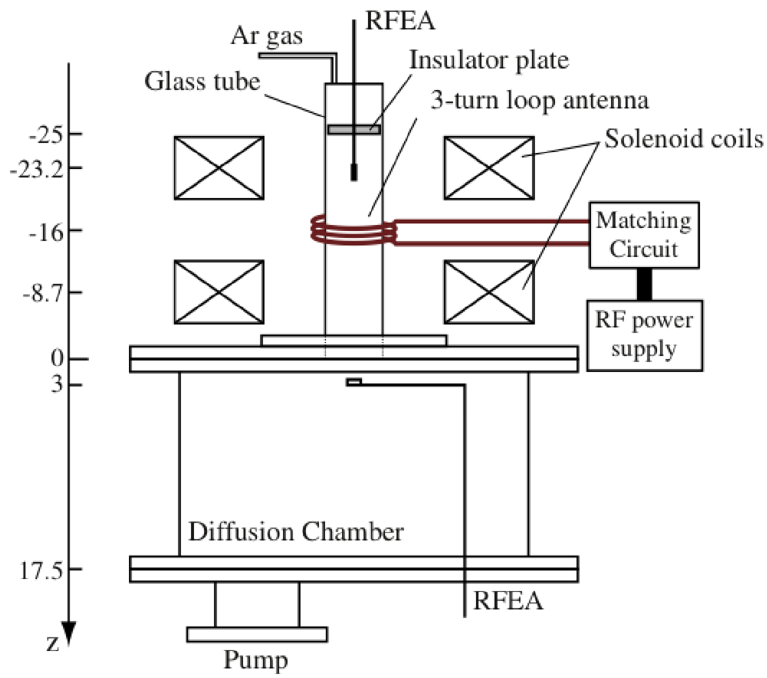

FIGURE 3.25: *EMPI* device at Iwate University [68].

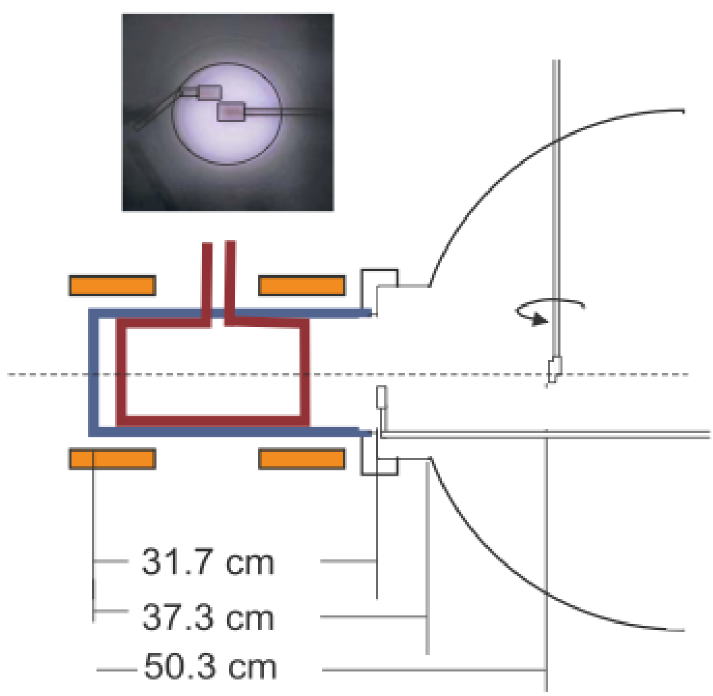

FIGURE 3.26: *Njord* double-saddle device [72].

Summary

Ion acceleration is possible in expanding plasmas, either due to an ambipolar electric field that builds to contain the more mobile electrons, or from a double layer potential structure that due to the separation of charge in free space. Both types of potential structures are observed in expanding plasmas in helicon sources, and their classification can be difficult. RF fluctuation of sheath potentials in capacitively coupled discharges leads to a self-bias voltage, which forms to maintain particle balance in the discharge. The understanding of ion acceleration in RF sources such as helicons must include the RF nature of the source, which has not been thoroughly examined to date.

CHAPTER 4

Madison Helicon Experiment (MadHeX)

4.1 System Description

The Madison Helicon eXperiment (MadHeX), shown in Figs. 4.1 and 4.2, consists of a 10 cm inner-diameter (ID) Pyrex tube, 1.5 m long, joined with a grounded, stainless steel expansion chamber, 45 cm in diameter and 70 cm long. Steel mesh (18 cm diameter) surrounds the Pyrex chamber and is electrically grounded to the expansion chamber. Argon gas flows into the Pyrex tube through a 5 mm inner diameter copper tube through the left (upstream) aluminum endplate, which is electrically grounded to the steel mesh. An 8-inch Varian turbo-molecular pump (550 L/s on N_2) is located at the bottom of the expansion chamber (downstream). MKS 910 DualTrans piezoelectric / Pirani gauges located at the up- and downstream endplates measure the pressure at these locations, which are shown in Fig. 4.3. A Bayard-Alpert ionization gauge measures the base pressure of the system, typically less than 10^{-6} Torr. A half-turn, double-helix antenna, 18 cm long and 13 cm in diameter (pictured in the inset of Fig. 4.1) surrounds the Pyrex chamber. The downstream edge of the antenna denotes z = 0 cm in the system. Positive z is in the direction of the gas flow, from upstream to downstream.

Most helicons flow gas into the system on the same side as it is pumped out, relying on diffusion to bring neutrals to the source region, and thus can starve the source region of neutrals if

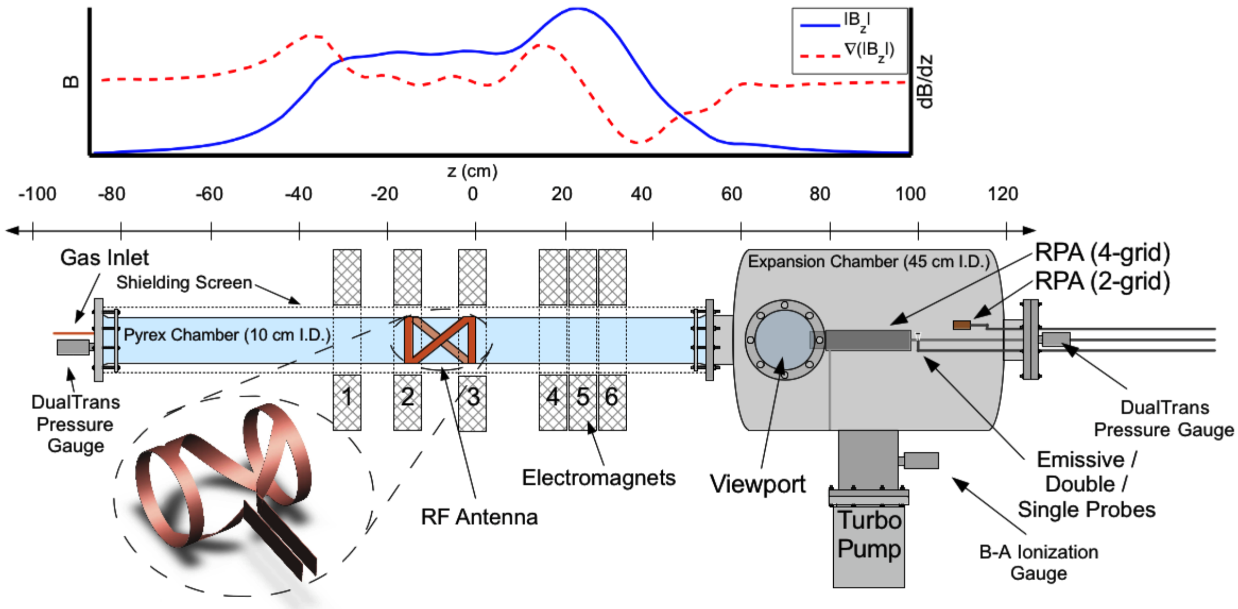

FIGURE 4.1: MadHeX Helicon Facility. The RF antenna is shown in the lower left corner and the static magnetic field value and gradient are shown above the system.

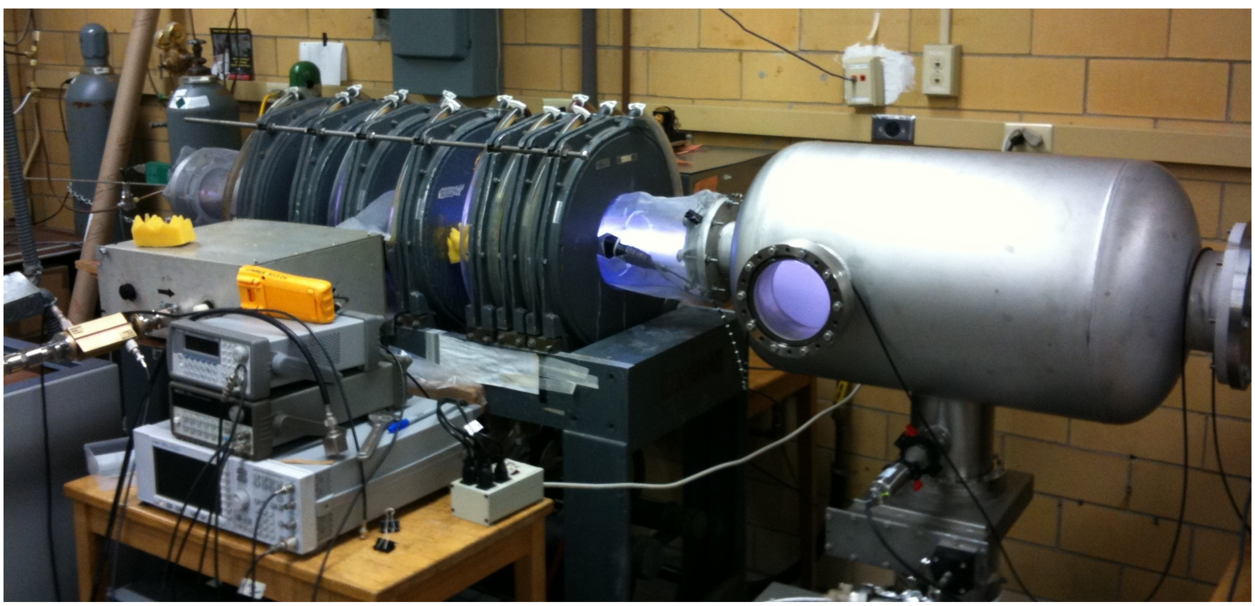

FIGURE 4.2: MadHeX in operation with expansion chamber.

enough ionization occurs. MadHeX is arranged with the gas flowing into the ionization region due to pumping on the downstream side, and this configuration can mitigate density oscillations such as those seen by Degeling [73]. These oscillations are due to a cycle of complete ionization and neutral depletion enhanced transport, resulting in refilling of the source region. These oscillations also occur at very low gas flow rates and are the primary reason the source cannot operate stably when the gas flow and resulting neutral density are below approximately 1 sccm and 0.25 mTorr (upstream), respectively.

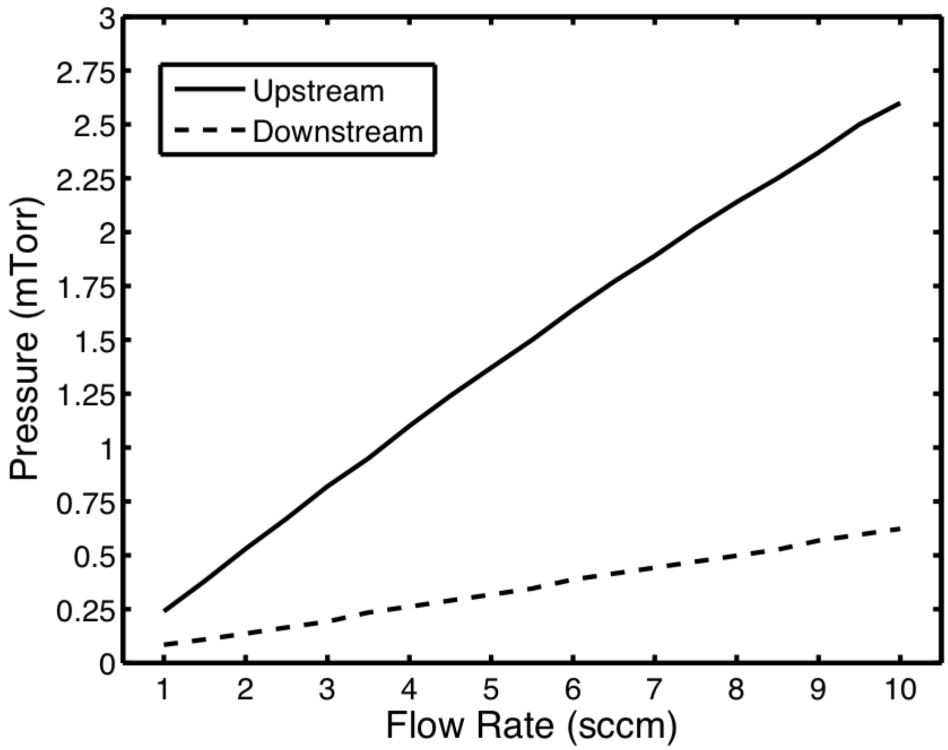

FIGURE 4.3: Pressure vs. argon flow rate measured at the upstream and downstream endplates.

The axial magnetic field is provided by six water-cooled electromagnets, each 7 cm wide with an 18 cm bore. For all the experiments explored here, the magnetic field profile is configured in a “nozzle” profile with a mirror ratio R_m = 1.44, with the peak at z = 28 cm. The system can be configured in a “flat” field configuration without a peak at z = 28 cm. A Sorensen PRO 55-180T DC power supply provides up to 180 A through the series-connected magnets, which corresponds to a field of up to 1.04 kG in the source region. The on-axis B field (B_z) value and gradient are shown in Fig. 4.4 for a magnet current of 60 A. Magnetic field values given below without a specified z position refer to the magnetic field value in the antenna region from z = 0 to z = -18 cm. Computed magnetic field lines for the nozzle field profile are shown in 4.5.

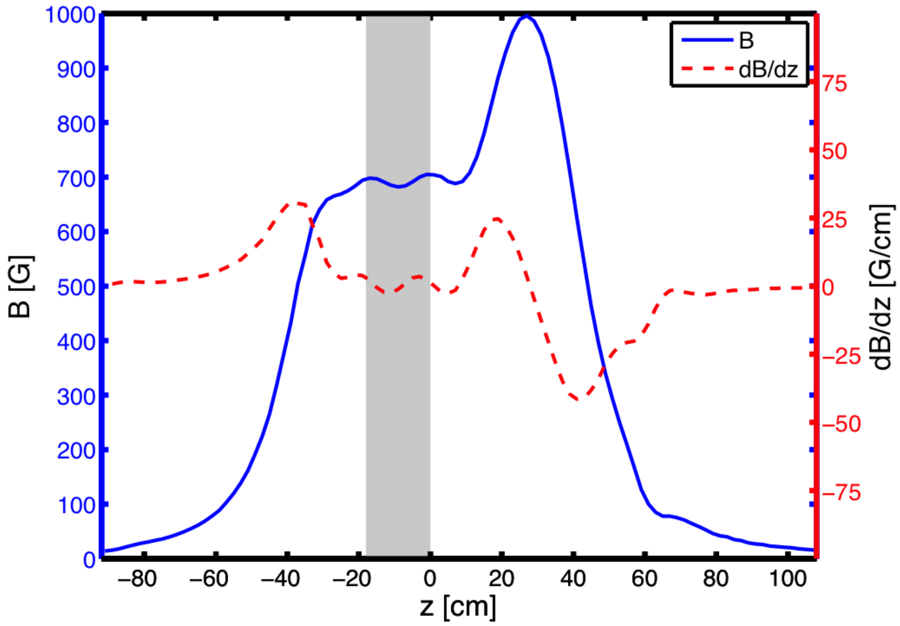

FIGURE 4.4: Axial magnetic field (B_z) and magnetic field gradient (dB_z/dz) vs. z for magnet current I = 60 A. The solid line denotes B_z and the dashed line denotes dB_z/dz. The shaded region shows the extent of the RF antenna.

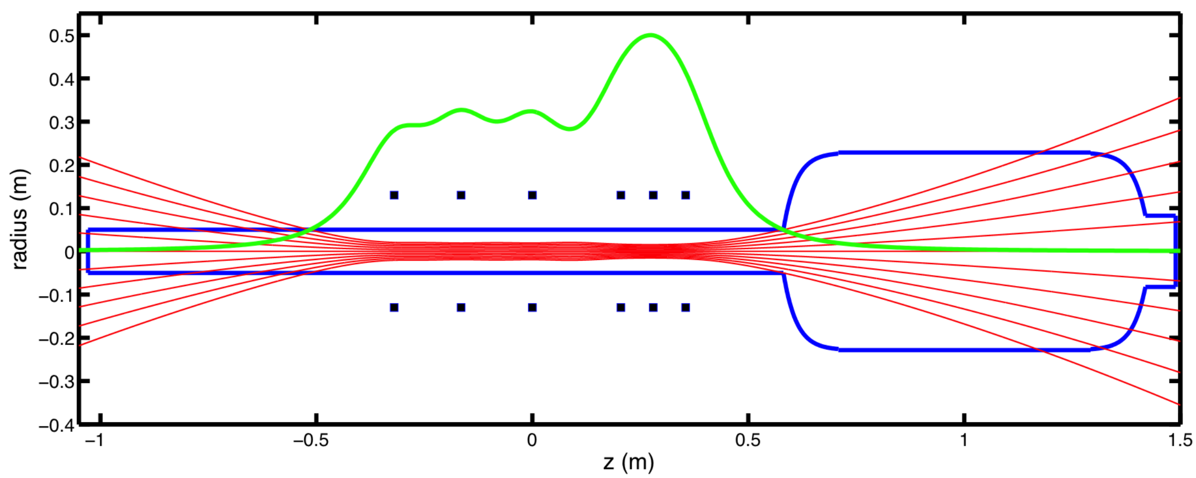

FIGURE 4.5: Computed magnetic field lines for nozzle field profile. Chamber outline (blue), magnet locations (squares) and $|B_z|$ (green) are shown for reference.

4.2 RF Antenna and Matching Network

An RF signal at 13.56 MHz is provided by an HP 33120A function generator, which is then fed to a Comdel CX10KS amplifier, capable of delivering up to 10 kW steady-state. A two-capacitor matching network (shown in Fig. 4.6) is used to match to the antenna impedance, and forward and reflected powers are measured with a Connecticut Microwave directional coupler with calibrated RF diodes. The matchbox is tuned to reduce the steady-state reflected power to below 5% of the incident power in steady-state for all cases shown. Fig. 4.7 shows the forward power vs. matching capacitor values for a given load impedance at the antenna (Z_L = [1.5 + 15j] Ω).

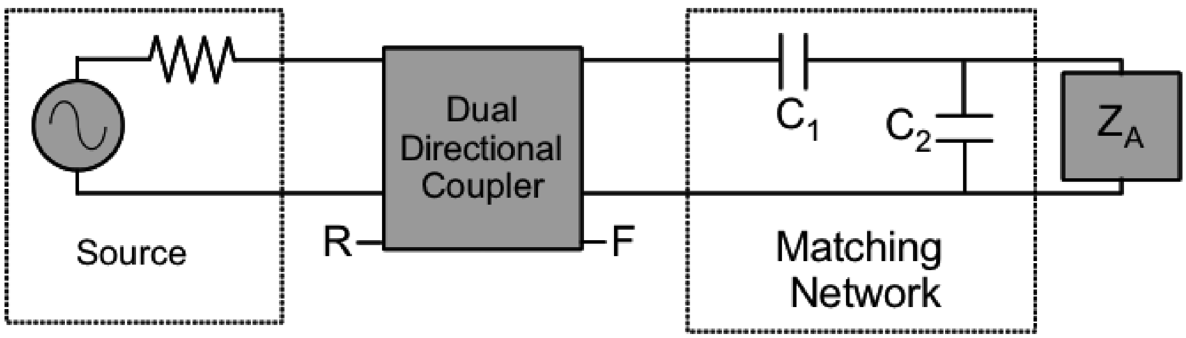

FIGURE 4.6: RF circuit including RF source, dual directional coupler, matching network and antenna load (Z_A).

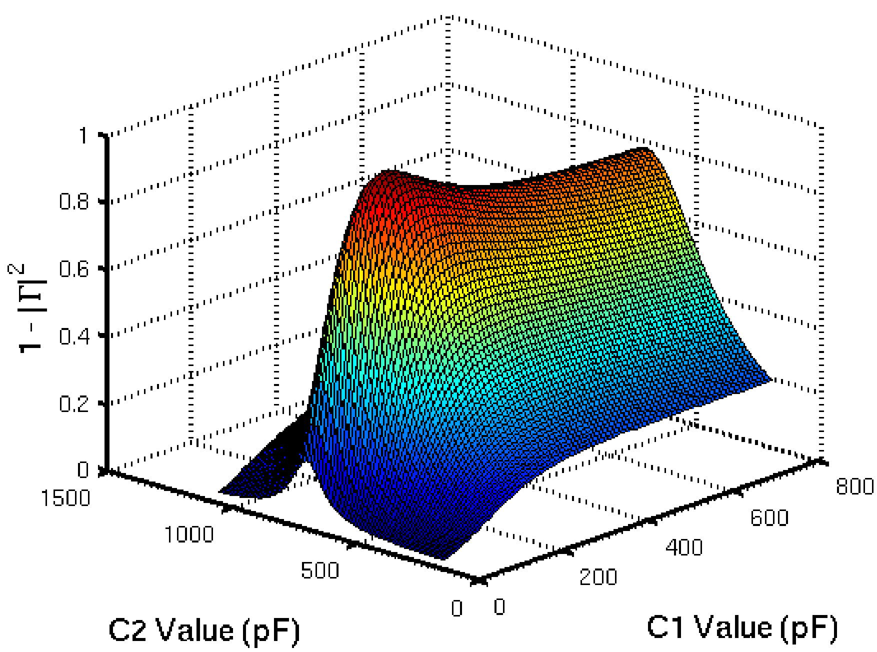

FIGURE 4.7: Forward power coefficient ($1 - |\Gamma|^2$) vs. C_1 and C_2 for a given antenna impedance (Z_L = [1.5 + 15j] Ω).

4.3 Low Pressure Operation

Our recent paper (Wiebold et. al. [74]) describes a technique used to initiate helicon plasmas at low flow rates. Typically, at low pressures ($p < 1$ mTorr), helicon sources can be difficult to start. This is due to the low neutral density in the system and consequently the mean free path for ionization being, on average, longer than the system dimensions, such that ionizing electron-neutral collisions are rare.

This threshold, where the mean free path for ionization is longer than the system length ($\lambda_{mfp} > L$) occurs near Q = 14 sccm in our system. Below this flow rate, our helicon has difficulty starting reliably and sometimes will not start at all. In order to overcome this, it was found that by turning off the static magnetic field, starting the RF supply and getting a glow discharge and then applying the magnetic field could allow operation below 14 sccm reliably. Upon further characterization, it was found that there is a threshold magnetic field for discharge initiation, that is, above a certain static magnetic field, the discharge will not begin reliably. See Fig. 4.8(a).

Below the threshold flow rate, the discharge can no longer be initiated by collisional ionization between background energetic electrons and neutrals, and a resonant multipactor-initiated discharge forms. Multipactor (resonant secondary emission) occurs at the Pyrex chamber boundaries which builds up a sufficient electron density such that a discharge can begin. The static magnetic field significantly affects the multipactor process and can even quench the process all together.

A discharge can be started without the magnetic field at flow rates below 0.1 sccm. Once a discharge is started, the magnetic field can be raised and the discharge may transition from the initial capacitive mode to the inductive and/or helicon modes if the conditions permit. Fig. 4.8(b) shows the magnetic field, electron density and the forward and reflected RF powers during this ramping process.

Evidence for the multipactor process is provided by long-exposure photographs of the experiment at base pressure (no feed gas) in darkness and a simple positively biased Langmuir probe.

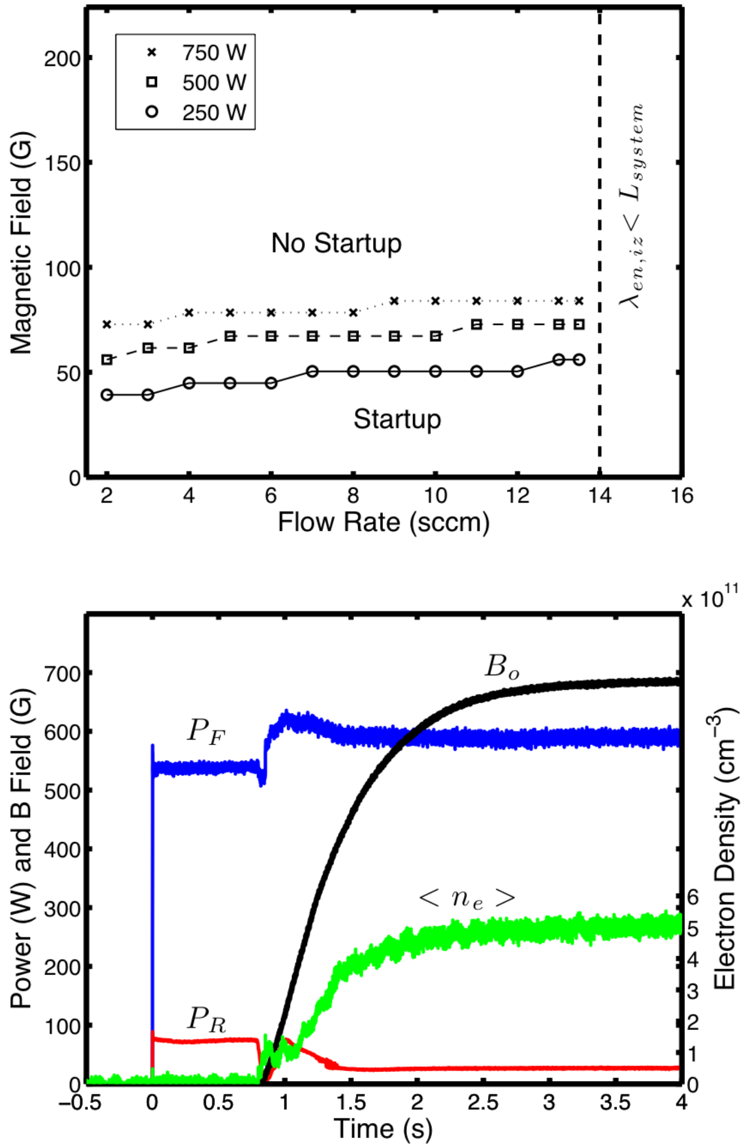

FIGURE 4.8: (a) Magnetic field threshold for discharge initiation in the MadHeX system. (b) The magnetic field ramping technique used to overcome this limitation. Data shown is for 5 sccm, 670 G final magnetic field and 600 W RF power setpoint.

A glow is present in the system and current is detected by the Langmuir probe for magnetic fields below the threshold value for a given power, and the glow and current disappear for fields above the threshold (the multipactor process is quenched). If the magnetic field is decreased from above through the threshold value, the glow and current reappear (see Fig. 4.9). This technique is used throughout the research for initiating discharges.

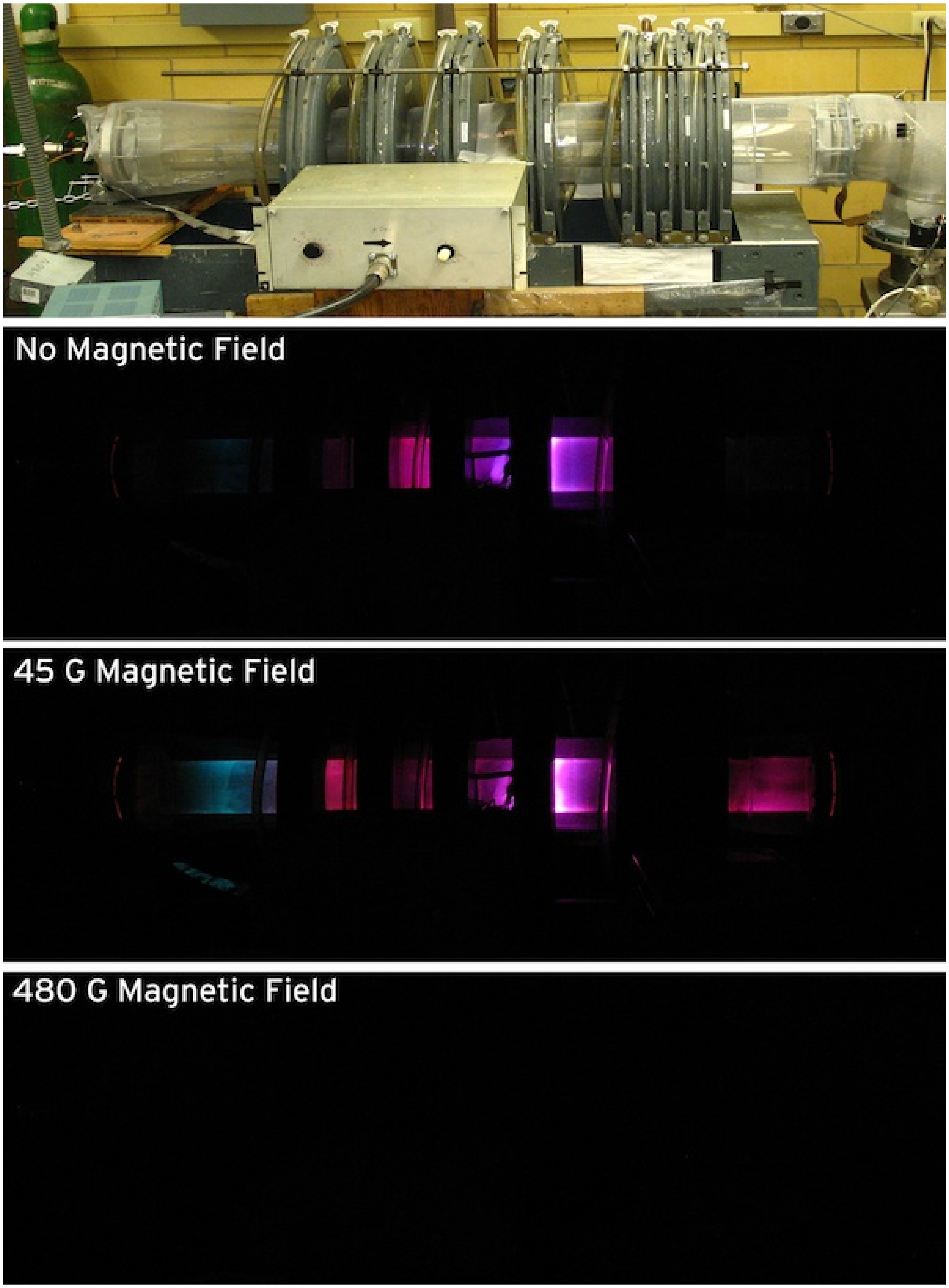

FIGURE 4.9: Multipactor-induced glow is present only for magnetic fields below the threshold field value for a given power level. The exposure time is 8 seconds for the lower three photos, and the experiment in room light is given for reference.

4.4 Georgia Institute of Technology

Collaborative research with Georgia Institute of Technology (Prof. Mitchell Walker and Dr. Alex Kieckhafer) is underway to examine the operation of a mock-up of the UW helicon source in a large vacuum chamber, as well as to directly measure any thrust produced by the device. The mock-up of the source includes identical antenna design, magnetic field profile and geometry, but includes a fully-insulating source region, as opposed to the floating walls but grounded upstream endplate in MadHeX. Figure 4.10(a) is an external photo of the Vacuum Test Facility (VTF) at GT where the helicon mock-up is installed, and Fig. 4.10(b) shows the source before installation into the space chamber. VTF has the capability of up to 600,000 L/s total pumping speed on air. Figure 4.11 is a photo of the source in operation in the space chamber at 13.56 MHz, 500 W RF power, 340 G magnetic field and 1.3 sccm flow rate.

FIGURE 4.10: (a) Vacuum Test Facility (VTF) at Georgia Tech. (b) Mock-up of the UW helicon installed into the VTF.

The results from the work at Georgia Tech will only be briefly discussed in Chapter 6 in order to verify certain results obtained on MadHeX. The majority of the research results at Georgia Tech will be available in a future publication.

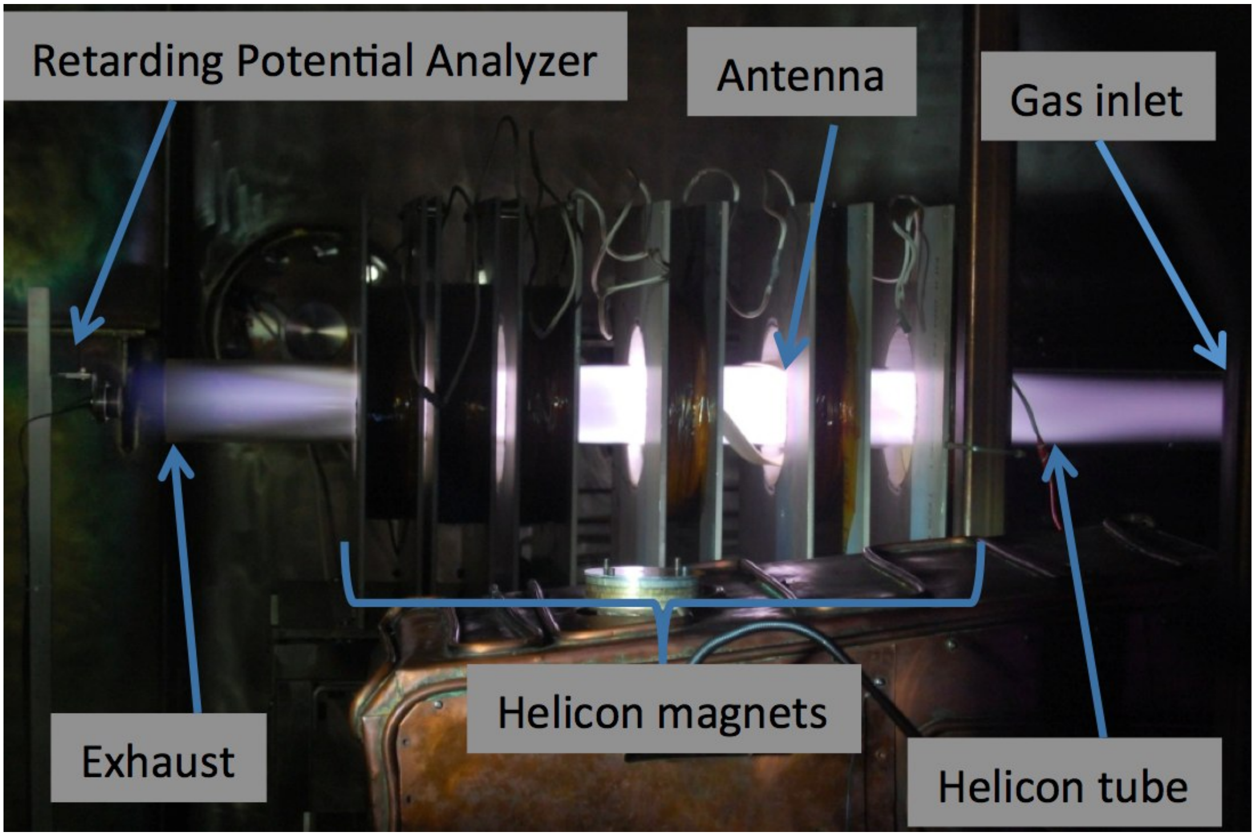

FIGURE 4.11: Operation of the UW helicon mock-up at GT, including the diagnostics and system components. Conditions are P = 500 W, B = 340 G, f = 13.56 MHz and Q = 1.3 sccm.

Summary

The Madison Helicon Experiment (MadHeX) is a high-aspect ratio helicon reactor presently being used to study ion acceleration for use as a thrust source. A capacitive matching network is used to match the RF generator to the antenna load, with up to 10 kW of RF power available. A static magnetic field in a nozzle profile can provide up to 1 kG in the RF antenna region. At low argon gas pressures, a special technique is required to initiate the discharge, which involves temporarily turning off the static magnetic field (which inhibits the multipactor effect that provides the seed electrons for the discharge) and then turning it back on once a discharge initiates.

Chapter 5

Diagnostics

MadHeX has a suite of both invasive (current-collecting) and non-invasive (optical and microwave) diagnostics available. The diagnostics used for detection and observation of potential gradients and ion acceleration as well as electron density and temperature are outlined below. Other diagnostics are available, including broadband spectroscopy and collisional-radiative modeling codes [13], diamagnetic loops and spatio-temporal photon binning [75], which will not be outlined here.

5.1 Retarding Potential Analyzers

Retarding Potential Analyzers (RPAs) or Retarding Field Energy Analyzers (RFEAs) consist of a series of biased or floating grids that selectively allow ions to pass through and be collected by a collector. By varying the potentials on the grids and measuring the current on the collector, the ion energy distribution in the plasma can be obtained.

RPAs have at least one grid and a collector. Some designs have up to four grids plus a collector, and these analyzers have been shown to have very good energy resolution [76]. The grid mesh spacing (distance between wires) must be small enough that the potential that is applied to the grid wires is “seen” by the ions passing through and not shielded by the plasma electrons, negating the effect of the applied potential on the ions. In order for this to be satisfied, the grid mesh spacing must be smaller than two Debye lengths:

$$D_{grid} = 2\lambda_D = \sqrt{\frac{4\epsilon_0 k T_e}{n_e e^2}} \tag{5.1}$$

where T_e is the electron temperature, k is Boltzmann's constant, n_e is the electron density in m^{-3} and e is the fundamental charge. A convenient formula for calculating the Debye length is:

$$\lambda_D\,[\mathrm{cm}] = 743\sqrt{\frac{T_e\,[\mathrm{eV}]}{n_e\,[\mathrm{cm}^{-3}]}} \tag{5.2}$$

where the units for each quantity are given in brackets. If the grid spacing is too small, the transmission factor of the grid will be reduced. This leads to a reduction in collected current, but can also be detrimental to the grids as the ions that are not transmitted impinge on the grid and are collected, which can cause ohmic heating or scatter from the grid and cause grid damage. The grid material is often expensive, due to the manufacturing process required to make the small spacings (often electroforming or etching).

The construction of RPAs is often constrained by size, since a large conducting surface in the system can perturb the plasma and measurement. Therefore, great care is taken in miniaturizing these analyzers, and there is a tradeoff between size and complexity. Typical four-grid (plus collector) analyzers use the following grids [77]:

- **Plasma-facing grid.** This grid is often floated or grounded, and acts as an attenuator. It can also reduce perturbation by the RPA.
- **Electron repeller.** This grid is biased negatively with respect to the plasma potential (often much lower than the plasma potential). It serves to reflect plasma electrons from entering the analyzer and prevent them from reaching the collector and contributing to the measured current.
- **Ion discriminator.** This grid is swept over the range of ion potentials to be measured and acts as a "filter" to selectively collect ions at or below the potential on this grid.

– **Secondary electron repeller.** Ions that strike the collector (below) can be at high energies either from acceleration through the analyzer by potentials on other grids or from beams or high energy ions present in the plasma. When the ions strike the collector, secondary electrons can be ejected depending on the collector material, and this grid prevents them from straying too far from the collector. If these secondaries are "lost", they represent a spurious positive ion current on the collector. This grid is biased negatively with respect to the collector so electrons are returned back to the collector.

– **Collector.** This is often a metal (copper) slug or plate (usually not a grid) that is biased slightly negative (with respect to ground) in order to collect all ions incident on it but not accelerate them such that a significant amount of secondary electrons are emitted. Current collected by the collector is measured as a function of the ion discriminator voltage.

Typical voltages on the grids of a four-grid analyzer are shown in Fig. 5.1. When miniaturizing an RPA, some grids may be omitted to decrease complexity at the expense of energy resolution or operational range. Problems can arise from the lack of these grids, and analysis must include these issues if they are present. Bohm [77] gives an excellent overview of RPA operation and the issues that can arise if grids are omitted.

The current collected by the analyzer is given by [78]:

$$I(V_{d0}) = T^x Ae \int_{V_{d0}}^{+\infty} v_i f(V) \mathrm{d}V \tag{5.3}$$

where V_{d0} is the discriminator voltage, $V = E/e$ represents the ion energy, T is the grid transmission factor, A is the RPA area, v_i is the component of the ion velocity normal to the analyzer, f is the ion distribution and x is the number of grids in the analyzer. An ion in the plasma may have a non-zero kinetic and potential energy:

$$E_i = q\Phi_i + \frac{1}{2}M_i v_i^2 \tag{5.4}$$

where E_i is the total energy of the ion, q is its charge, Φ_i is the potential of the ion with respect

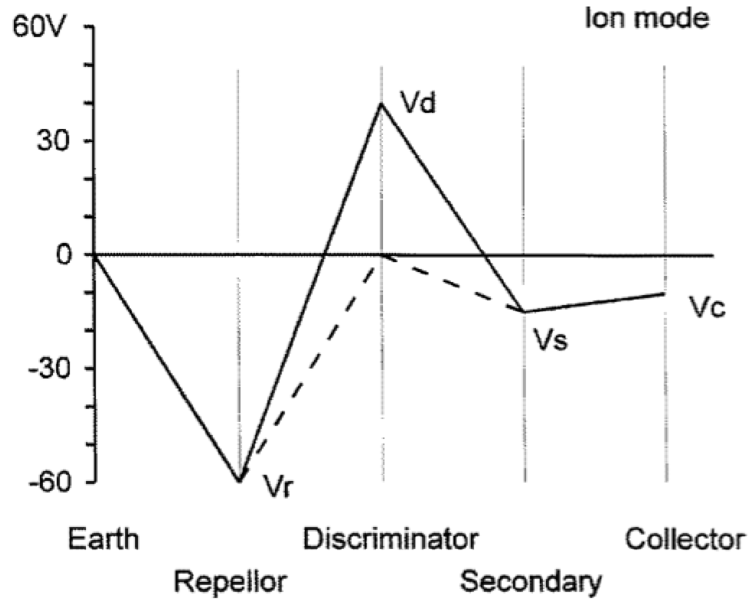

FIGURE 5.1: Typical bias voltages for a four-grid (plus collector) ion energy analyzer (RPA) [76].

to ground, M_i is the ion mass and v_i is the component of the ion velocity normal to the analyzer collector. The RPA gives a measurement of the *total* energy of the ions in the plasma with respect to ground (or the point above which the RPA grids are biased). The physical meaning of Eq. 5.3 is that the RPA collects all ions that have a total energy above the potential of the discriminator grid ($E_i > e\Phi_g$, where Φ_g is the grid potential relative to ground). Ions with a total energy below the grid potential do not have sufficient energy to overcome the grid's potential and are repelled. The ion energy distribution function can be found from the collected current by differentiating the collected current with respect to the ion discriminator grid voltage. The mathematical relationship between the derivative of the collected current and the ion energy distribution is given by [78]:

$$f(V_d) = \frac{1}{e} f(E) = \frac{m}{T^x A e} \frac{1}{v} \frac{\mathrm{d}I}{\mathrm{d}V_d} \tag{5.5}$$

where $f(E)$ is the energy distribution. The derivative of the collector current is actually related to the energy distribution of the ions falling through the sheath in front of the RPA, but is often used in calculating the ion energy distribution function (IEDF) [59]. In this work, the abbreviation 'IEDF' refers to the differentiated collector current, which is proportional to $vf(V_d)$. At a given ion discriminator voltage, the current collected is due to ions that are below that potential. Therefore, at the lowest ion discriminator voltage, ideally all ions are collected. At an ion discriminator voltage that is well above the potential of any ions in the system, the collected current is ideally zero. In reality, any electrons that are present will also be collected, and depending on the analyzer design, the collected current may not return exactly to zero.

In the presence of RF fluctuations of the plasma potential, the plasma ions, if they are able to significantly respond to the fluctuations, will enter the analyzer at a velocity that is dependent on the part of the RF cycle during which the ions enter the sheath in front of the analyzer. This results in a double-peaked distribution of ions, as ions may enter when the plasma potential (relative to the discriminator potential) is a minimum or maximum. If the ions are unable to respond to the fluctuations fully, the plasma potential and therefore electric field strength will oscillate many times as the ion passes through the sheath in front of the analyzer. The ions enter the analyzer with the time-averaged value of the plasma potential, since they feel the effect of the time-averaged electric field in the oscillating sheath. There may be some broadening of the distribution due to the limited oscillations of the ions, which degrades the ability to measure the ion temperature with the analyzer. The ability of the ions to respond to fluctuations in the plasma potential is discussed in Section 3.1.2. The ratio of the ion plasma frequency ω_{pi} to the RF frequency ω_{RF} (or the ion response time $\tau_i = \omega_{pi}^{-1}$ and the RF period τ_{RF}) is used to gauge the ability of the ions to respond to these fluctuations.

Two retarding potential analyzers are used to measure the ion energy distribution in MadHeX. The first, a two-grid (plus collector) design [79], is used as the main diagnostic for the ion beam due to its small size (12 mm diameter, 6.6 mm aperture, 22 mm long), which minimizes perturbations of the plasma when moved axially, especially in the 10 cm diameter source tube region. A second, larger, 50 mm diameter four-grid (plus collector) RPA, of a tested design used in Hall thruster research [80,81], is used to verify the measurements of the first RPA in a region well away from the plasma source. The RPAs cannot be used simultaneously, therefore the vacuum must be turned off and on between measurements. However, extensive operation of this source has shown the plasma characteristics are highly repeatable for a given set of experimental conditions.

For both RPAs, the measured collector current is sampled at 1 MS/s and the data is captured by a LeCroy Waverunner digital storage oscilloscope (DSO). The collector current is processed and numerically differentiated in MATLAB. The MATLAB script reads in the raw binary data from the LeCroy output files and subtracts the background or load line trace (no plasma) collected prior to taking data. The discriminator grid voltage is swept with a triangular waveform, and the oscilloscope captures several periods of the sweeping. The script detects the upwards and downwards sweep end points and averages all upwards and downwards traces separately. These traces are then smoothed using a moving average (window is 0.3% of trace) and numerically differentiated. A Savitsky-Golay filtering and differentiating scheme [82] is not necessary here due to the high sample rates. A manual fitting GUI is called and the resulting IEDF is fitted with either one or the sum of two Gaussian distributions. The IEDF is then normalized if required and plotted.

The LeCroy digital storage oscilloscope has a feature called *ERES* that can be used to increase the vertical resolution of the scope from 8 bits up to an effective 11 bits, at the expense of frequency response. *ERES* uses a low-pass FIR filter to interpolate points in the vertical axis (like a moving average), which results in an increased number of possible y-values (increased vertical resolution). *ERES* has a linear phase response and better passband characteristics than a simple moving-average. At its highest setting, *ERES* limits the signal bandwidth to 1.6% of the Nyquist sample rate. Our scope can sample up to 10 GS/s, which is more than ample for use with the relatively low-frequency signals produced by the RPA sweep. Since the RPA analysis requires plotting the “y values” of two scope channels (discriminator voltage and collector current), better vertical resolution will lead to less noisy measured IEDFs, which must be differentiated. Note that *ERES* does not affect horizontal resolution, which is set by the scope sample rate. The vertical resolution of the scope is further increased by implementing an averaging function on both the discriminator voltage and collector current channels, which averages successive traces. The maximum effective vertical resolution is then 14 bits with *ERES* and averaging enabled.

LC notch filters are used to eliminate DC offsets that can result from rectification of large RF signals often present in the collector current signals by the probe electronics (see Section 5.3).

5.1.1 Two-Grid RPA

The first RPA, shown in Fig. 5.2, has two grids and a collector. The brass body of the RPA is 12 mm in diameter and 22 mm long, and a brass plug forms an aperture, 6.6 mm in diameter, at the entrance of the RPA. The plasma-facing entrance grid is floating, insulated from the other grid and body using mica rings. The discriminator grid is biased with an insulated wire, passed through the inner mica body, which is forced against the discriminator grid holding ring. The copper collector is biased with a second wire passed through the rear of the RPA body. Both grids (discriminator and entrance) are an electroformed nickel mesh, with a 60% transmission factor and 50.8 micron wire spacing (500 wires per inch).

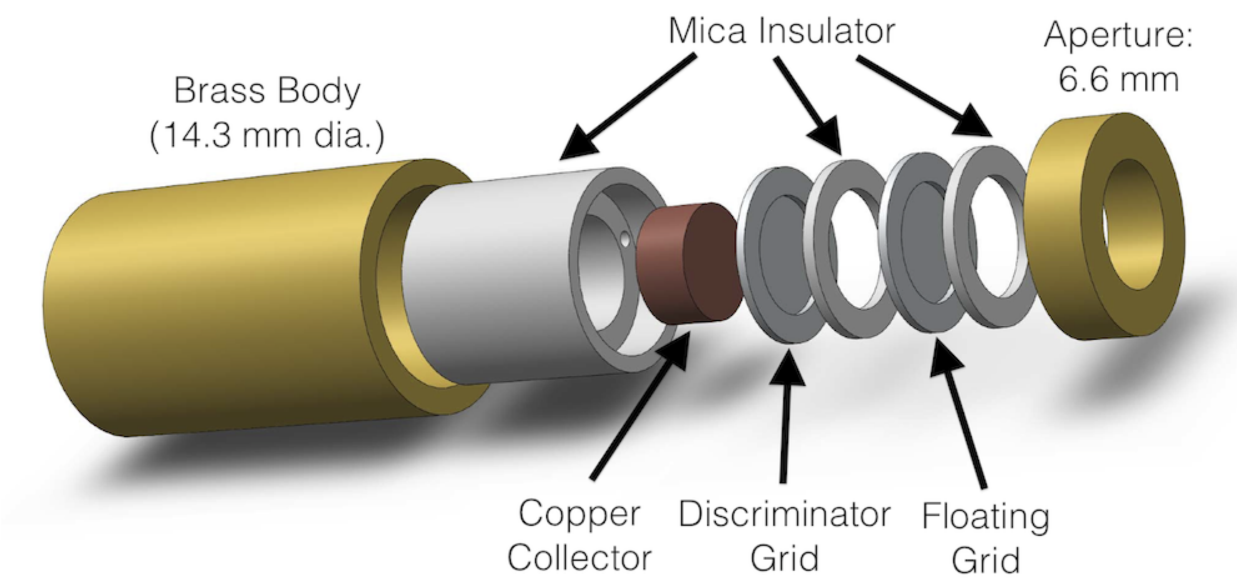

FIGURE 5.2: Two-Grid Retarding Potential Analyzer (RPA) construction.

The RPA is attached and the body is electrically grounded to a 1/4” stainless steel probe shaft which enters the system through the downstream endplate at r = 6 cm. Two 90-degree bends in the probe shaft, 5 cm from the front face of the RPA, align the RPA on-axis at r = 0 cm. This RPA can be swept axially from z = 45 cm to z > 80 cm.

The discriminator grid is biased with a Kepco BOP-500M supply, typically swept between 0 and 300 V. The collector is biased at -9 V using a battery through a 150 kΩ current-measurement

FIGURE 5.3: Two-grid RPA. (a) 2-grid RPA installed on 1/4” stainless shaft, rotated 90° (not facing ion beam) (b) Stainless steel shaft orientation for measurement of beam (’dogleg’).

resistor to chamber ground. An AD620 instrumentation amplifier at unity gain (10 GΩ input impedance) is used to sense the voltage drop across the resistor. The digital storage oscilloscope records both the discriminator voltage, using a 20× voltage divider network, and the output of the current-measurement instrumentation amplifier. An HP 33120A signal generator is used to sweep the Kepco discriminator grid supply at 3 Hz with a triangular waveform, and the recorded waveform is averaged a minimum of 30 times on the DSO. The derivative of the collector current with respect to discriminator voltage ($\mathrm{d}I/\mathrm{d}V \propto$ IEDF) is calculated using a simple differential, and any high-frequency noise is suppressed with smoothing (moving average). The sample rate and vertical resolution are high enough such that more complicated methods (Savitsky-Golay filtering and differentiation) are not necessary.

A typical collector current vs. discriminator voltage trace and the resulting IEDF is shown in Fig. 5.5. There is a single peak at around 100 V, which indicates most of the ions are at this potential, with broadening of the distribution from the convolution of the ions’ true thermal distribution as well as effects of the RPA including grid geometry, sheath and plasma potential fluctuation effects. Energy analyzers such as this two-grid analyzer do not have sufficient resolution to be able to extract an ion temperature, due to the sheaths in front of the analyzer face and grids which result in artificial broadening of the collected current.

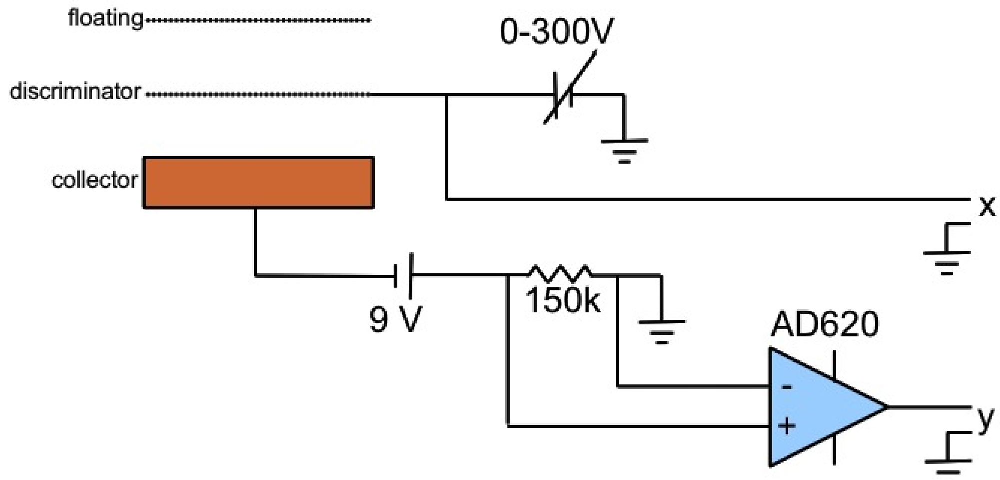

FIGURE 5.4: Biasing circuit used for operation of the 2-grid RPA. The swept 300 V supply is the Kepco BOP-500M and the 9 V source is a battery. The ±15 V supplies for the AD620 instrumentation amplifier are not shown.

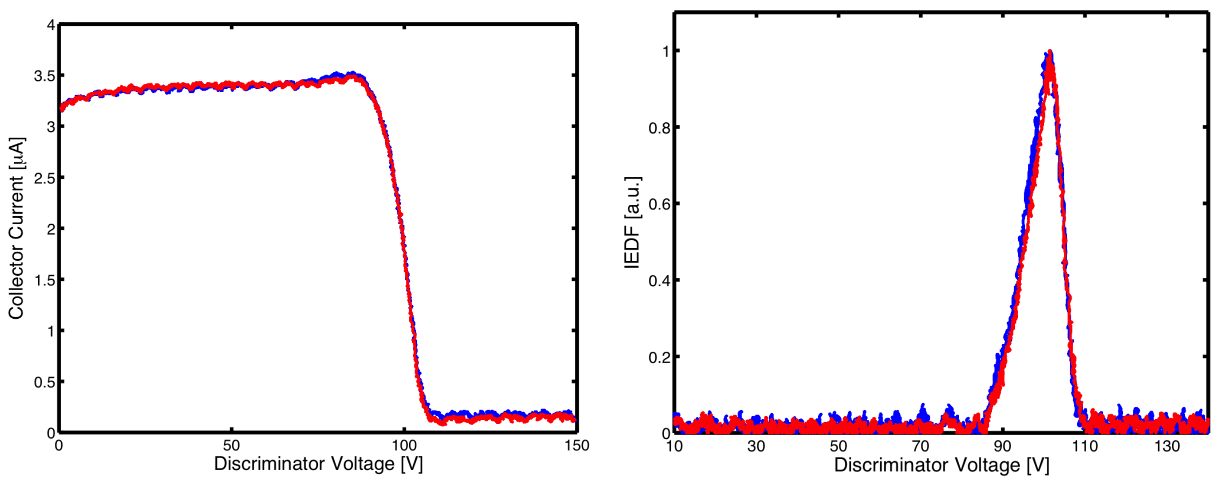

FIGURE 5.5: (a) Typical collector current vs. discriminator voltage trace for the two-grid RPA. (b) Smoothed IEDF calculated from data. The conditions are 2 sccm flow rate, 100 W RF power, 340 G B field and z = 50 cm. Both the up-sweeping (red) and down-sweeping (blue) traces are shown.

5.1.2 Four-Grid RPA

A four-grid (plus collector) RPA, used in Hall Thruster research [80, 81], was used to validate the results of the two-grid RPA under specific conditions. The four-grid RPA is much larger (50 mm diameter); therefore it cannot be used axially along the entire system due to its size limitations and increased plasma perturbation. The four-grid RPA is on loan from Professor Mitchell Walker of Georgia Institute of Technology.

The four-grid RPA is installed in a 50 mm inner-diameter steel tube, 32 cm long, to protect the cabling at the rear of the RPA as well as provide a stable mount for the RPA. The weight of the steel tube and RPA require the use of two stainless steel (1/4") legs at the front of the assembly. The rear of the tube is closed with a steel annulus with a 1/4" port in the center for the stainless steel probe shaft that carries the biasing connections. The probe shaft exits the system through an Ultra-Torr connection at the back of the expansion chamber. The four-grid RPA and mounting tube are shown with the protective cover removed in Fig. 5.6, installed in the protective tube in Fig. 5.7 and photos of the installation are shown in Fig. 5.8.

FIGURE 5.6: Four-grid analyzer with cover removed, showing plasma-facing grid.

The four grids are labeled the plasma-facing grid, the electron repeller, the ion discriminator, and the secondary electron repeller. The grid voltages are tuned to provide the best raw current trace, such that the collector current approaches zero for high bias voltages and the collector

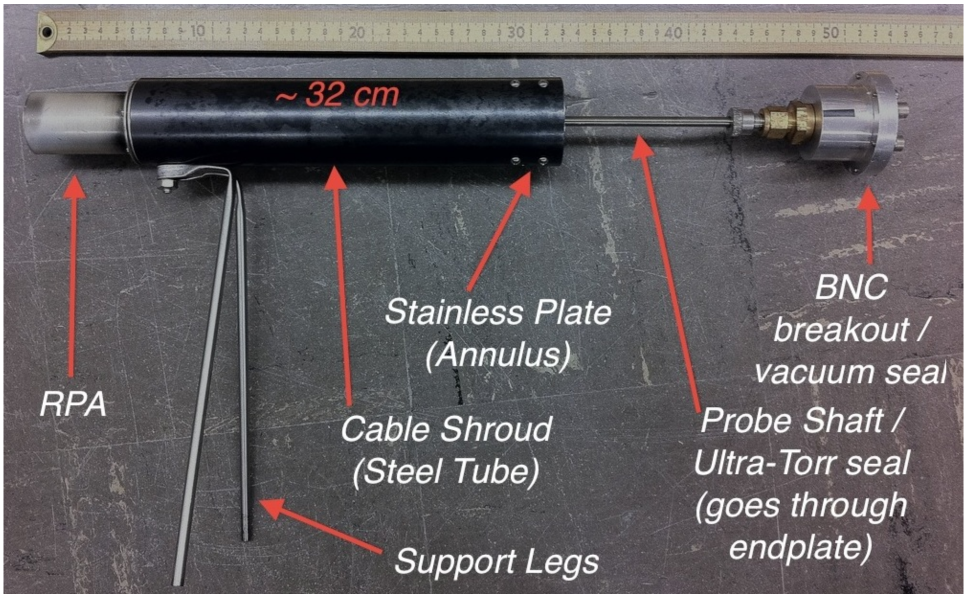

FIGURE 5.7: Four-grid analyzer as installed in the expansion chamber.

FIGURE 5.8: Four-grid RPA. (a) Front of RPA as installed. (b) Rear of RPA as installed, showing probe feedthrough.

current saturates at low bias voltages [76]. The plasma-facing grid is floated, the electron repeller is biased at -120 V, the ion discriminator is swept from 0 - 300 V (using the Kepco BOP-500M supply), and the secondary electron repeller is biased at -83 V via a 9 V battery from the collector [76]. The collector is biased at -74 V with a high voltage battery, and the current is measured through a 150 kΩ resistor to chamber ground, again with an AD620 instrumentation amplifier (see Figure 5.9). The comparison of the two- and four-grid RPAs is given in Section 6.1.

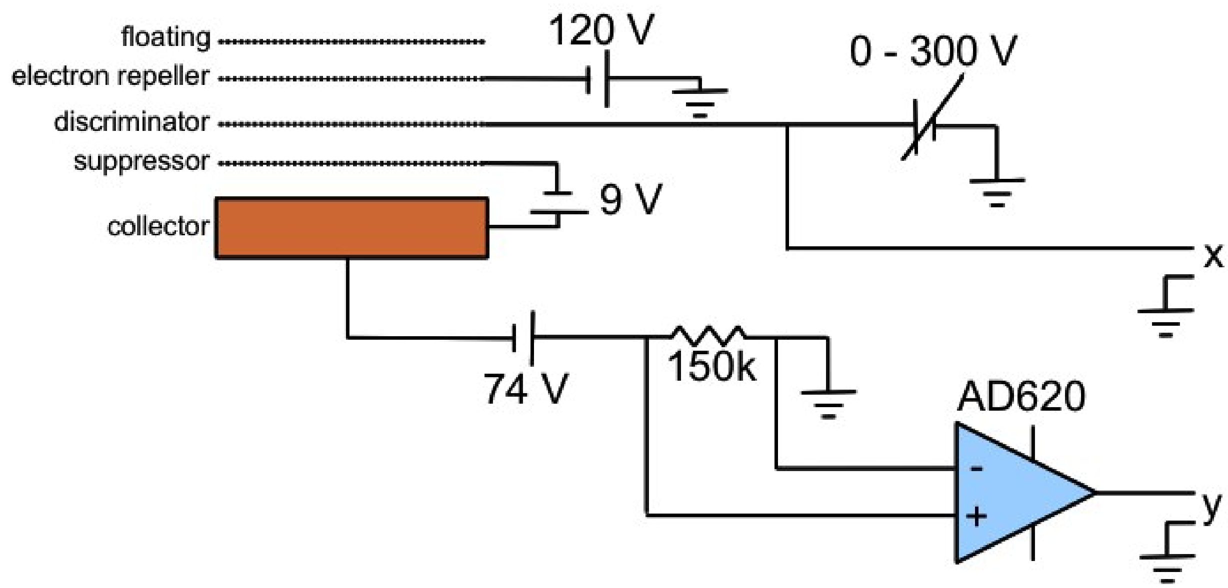

FIGURE 5.9: Four-grid analyzer bias circuit. The 120 V source is provided through two bench supplies in series, the swept 300 V supply is the Kepco BOP-500M, the 74 V and 9 V source are batteries. The ±15 V supplies for the AD620 isolation amplifier are not shown.

5.2 Emissive Probe

Emissive probes are current-collecting (or floating) probes that consist of a filament that is heated to thermionically emit electrons, often by passing a current through the filament [83], but laser [84] and other heating methods have been used. Tungsten or thoriated tungsten are often used as filaments due to their high melting point, with wire thicknesses from 25 microns up to a few hundred microns being common. The potential of the filament can be swept similar to a Langmuir probe, or the floating potential of the cold (not emitting) and hot (emitting) filament can be measured.

Emissive probes can be used to very accurately measure the local plasma potential, to within kT_w/e where T_w is the temperature of the filament. When the filament is thermionically emitting, the emitted electrons essentially "neutralize" the ion sheath that forms around the filament and, if not directly biased, the filament will float at or near the plasma potential (typically within a few kT_e/e) [85]. However, in RF or magnetized plasmas, the floating potential of the emitting probe may not necessarily indicate the true plasma potential [27, 86–88]. When there are strong RF plasma potential fluctuations present, a strongly emitting probe can float to the maximum value of the RF fluctuations, which is not necessarily the plasma potential [27]. However, floating emissive probes offer several advantages over cold probes or swept emissive probes for plasma potential measurement, including less perturbation and simplicity [86]. Since the floating emissive probe draws no current, there is less perturbation of the plasma by the measurement. Also, the measurement is simple; a DC voltage is measured and no sweeping or biasing electronics or further analysis are required.

The emissive probe potential can also be swept similar to a Langmuir probe, and the collected current measured versus bias voltage. Using the inflection point method, the plasma potential can be found [89] with excellent accuracy. When the probe is not emitting (cold), it will act as a simple Langmuir probe. As filament current (also wire temperature T_w and electron emission) is increased, the inflection point (peak in first derivative) of the I-V trace will approach the plasma potential, assuming no RF modulation of the plasma potential is present. Typically, the true plasma potential is calculated in the limit of zero emission. This is done by plotting the filament current versus the inflection point voltage, and a straight line fit is used to extrapolate to zero emission current, which is interpreted as the plasma potential. Fig. 5.10(a) shows typical emissive probe I-V traces as filament current (T_w) is increased, and Fig. 5.10(b) shows the calculation of the plasma potential using the limit of zero emission method.

In the presence of RF plasma potential fluctuations, two or more peaks in the first derivative of the I-V trace may occur, depending on the number of significant harmonics of the RF are present [90, 91]. Figs. 5.11 and 5.12 show the effect of a fluctuating plasma potential on emissive probe analysis. In the absence of fluctuations of the plasma potential, the emitted electron current from

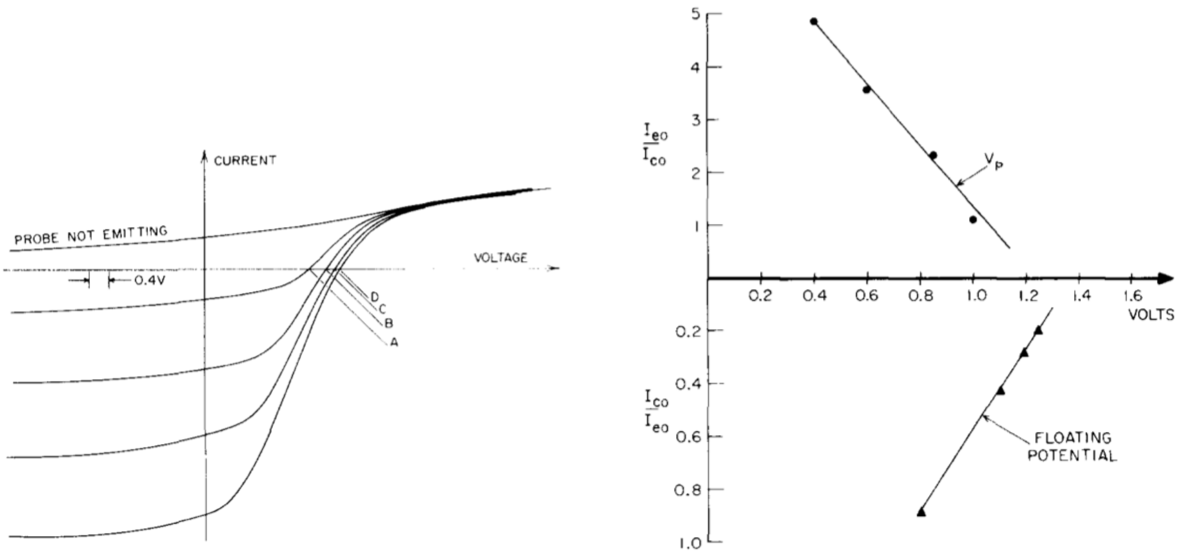

FIGURE 5.10: (a) Emissive probe I-V trace showing the effect of increasing filament current (T_w) (b) Limit of zero emission method, showing the inflection point and floating potential vs. filament current [89].

the heated probe is ideally zero when the probe bias is above the plasma potential and non-zero when the probe bias is below the plasma potential. The finite temperature of the filament and emitted electrons leads to a somewhat smoothed onset of emission. Figure 5.11(a) shows the emitted current versus probe bias voltage with a plasma potential V_b = 15 V that is constant in time. The emitted electron current is plotted as a negative current as is typically done in Langmuir probe I-V traces. The derivative of the probe current with respect to the probe bias voltage is plotted in Fig. 5.11(b), which reveals a sharp peak at the plasma potential with some broadening due to the finite temperature of the filament. In the presence of RF fluctuations of the plasma potential, the instantaneous collected current will oscillate at the RF frequency and possibly its harmonics. The black dashed lines in Fig. 5.12(a) denote the maximum excursions of the collected current, a result of a modulation of the plasma potential with a V_{RF} = 5 V amplitude. The blue, solid line indicates the time-averaged value of the emitted current. If the probe and associated electronics are able to respond on the timescale of the fluctuations, the probe will be able to "follow" these fluctuations and the instantaneous plasma potential can be measured. However, if the probe is unable to follow the fluctuations due to stray or inherent impedances of the probe and electronics, the probe will measure the time-averaged value of the collected current, and two peaks will appear in the derivative of the probe current, as shown in Fig. 5.12(b). The bias voltages of the inflection points (peaks) represent the maximum excursions of the plasma potential.

The first derivative curve also represents a “binning” or histogram of the values of the plasma potential averaged over many RF cycles, showing the relative amount of time spent at each value. For a purely sinusoidal fluctuation, the peaks in the histogram are symmetric about the unweighted mean of the peak locations and are the same magnitude, as shown in Fig. 5.13(a). If the fluctuations are not sinusoidal, the peaks in the histogram will not necessarily be of the same magnitude and will likely not be centered around the unweighted mean of the peak locations, as shown in 5.13(b). In this case, the *weighted* mean of the histogram reveals the time-averaged value of the fluctuations. As will be shown in Chapter 6, in our system there are asymmetric inflection points in the emissive I-V curve, representing asymmetric RF plasma potential fluctuations, but the time-averaged plasma potential can be calculated from the first derivative of the emissive I-V curves using a weighted mean.

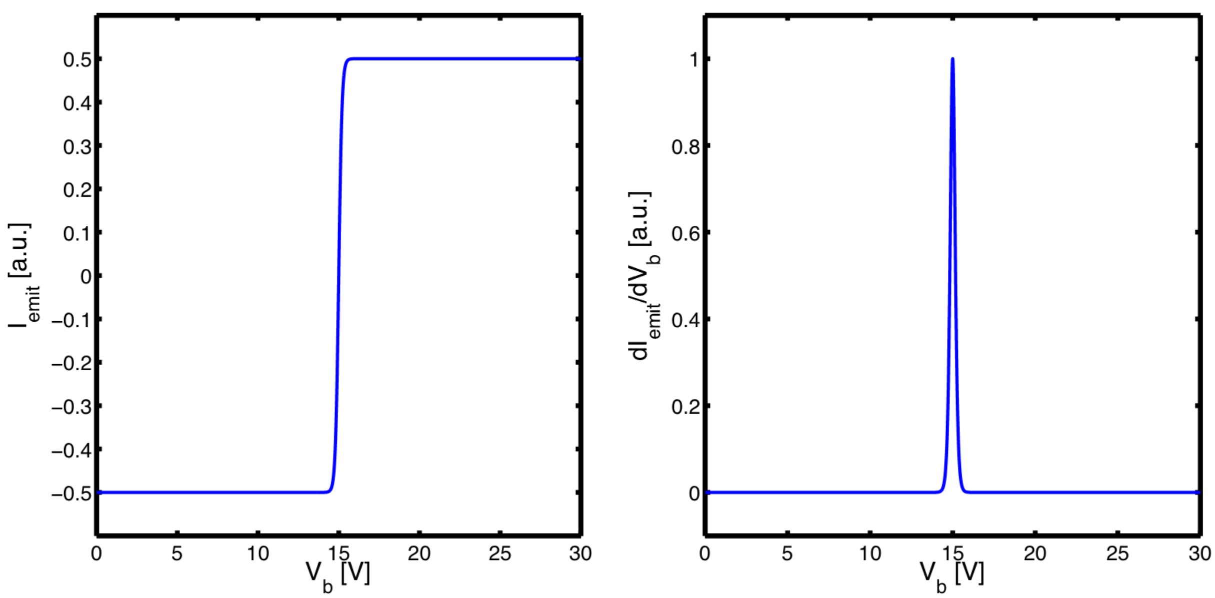

FIGURE 5.11: (a) Emitted electron current plotted against probe bias voltage in the absence of fluctuations of the plasma potential. (b) Resulting first derivative, showing the presence of a single peak at the plasma potential (V_p = 15 V).

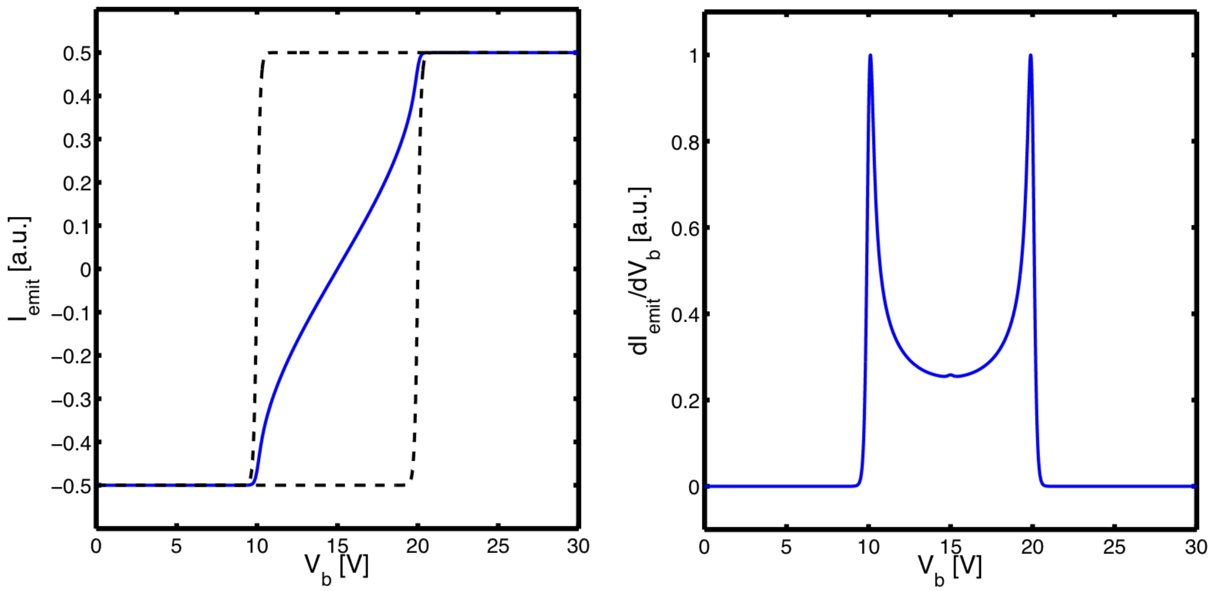

FIGURE 5.12: (a) Emitted electron current plotted against probe bias voltage in the presence of modulation of the plasma potential with an amplitude V_{RF} = 5 V. The black dashed lines indicate the instantaneous I-V trace at the maximum excursions of the plasma potential in time, and the blue, solid line indicates the time-averaged value of the emitted current. (b) Resulting first derivative, showing the presence of two peaks at the maximum excursions of the plasma potential.

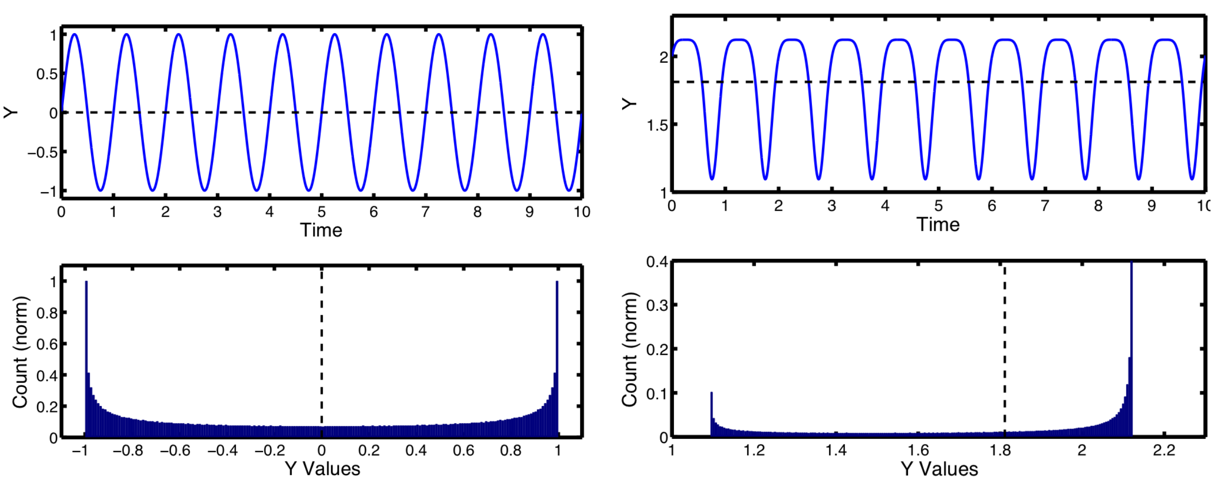

FIGURE 5.13: (a) $y = \sin \omega t$ and a histogram of y values. (b) $y = \frac{1}{3} \exp(-\sin \omega t) \sin \omega t + 2$ and a histogram of y values. The dashed lines indicate the mean y value.

The emissive probe used in MadHeX consists of a thoriated tungsten filament, 25 μm in diameter and 6.8 mm long, which is spot-welded between two 3 cm long gold-plated nickel wires coated entirely in Sauereisen No. 31 ceramic cement. The last 25 cm (from the tungsten filament) of the probe shaft is made of alumina tubing to minimize the effect of the grounded stainless steel probe shaft on the system. The probe enters the system through the downstream endplate, and a 90-degree joint at then end of the probe shaft puts the filament on-axis (r = 0 cm) in the system, oriented perpendicular to the B field.

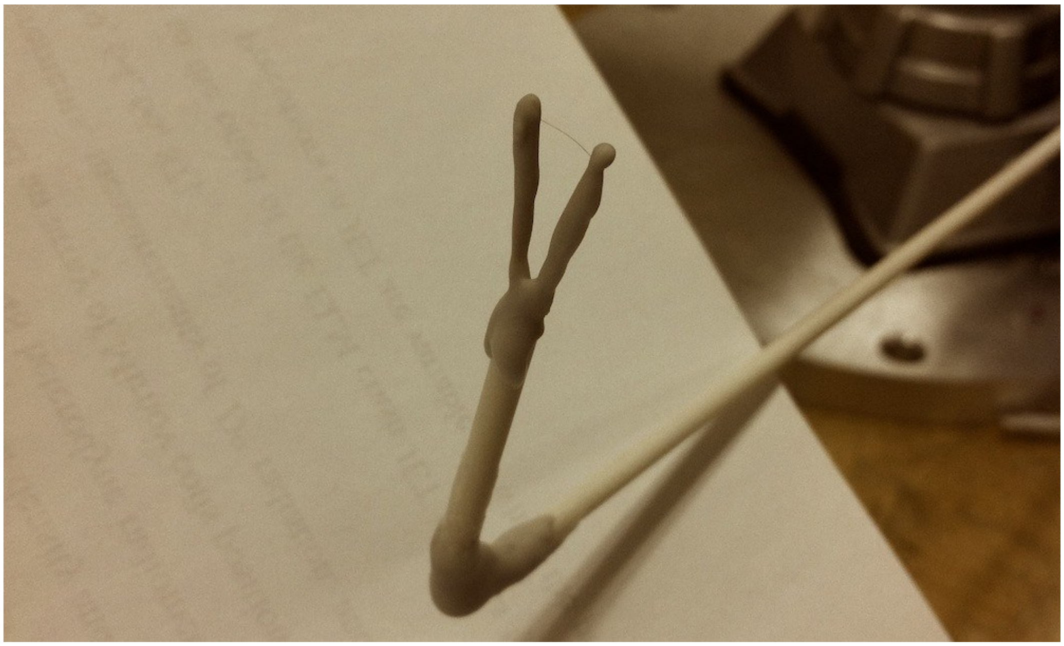

FIGURE 5.14: Emissive probe construction.

For floating potential measurements, a Fluke 179 DMM, with an input impedance greater than 10 MΩ, is used to measure the floating potential of the emissive probe in steady-state. A 6 V lantern battery provides the filament current through a low-resistance potentiometer which allows the filament current to be adjusted, shown in Fig. 5.15. The filament current is increased until the measured floating potential saturates. For the 25 micron filament, the required filament heating current is around I_{fil} = 210 mA.

For swept emissive probe measurements, the custom-built probe supply detailed below is used to bias the filament heating circuit relative to chamber ground. The probe supply is driven with a 3 Hz triangle wave signal and a MATLAB script is used to display the I-V trace and its first derivative.

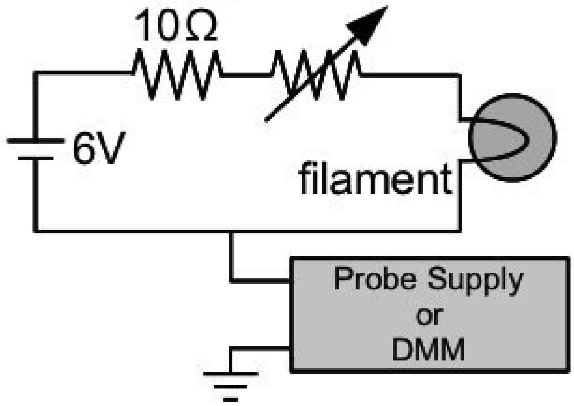

FIGURE 5.15: Emissive probe bias circuit.

5.3 Single and Double Probes

Probes are one of the simplest plasma diagnostics to use, but can be the most difficult to properly analyze. Single (Langmuir) probes consist of a simple electrode that is inserted into the plasma, biased relative to ground. The current collected by the probe is measured and plotted against the bias voltage, and the resulting I-V trace can reveal the plasma potential, electron density and temperature as well as the electron energy distribution function (EEDF).

Double probes consist of two electrodes, biased relative to each other but electrically floating from ground. Since both electrodes are floating, they draw no net current from the plasma. The current drawn through one electrode returns through the other electrode, and is therefore limited to the maximum current that can be drawn from either electrode, the ion saturation current. For this reason, double probes can be less perturbative compared to single probes. However, double probes also float to the floating potential in the plasma, and therefore can only sample the electron distribution near the floating potential, and the full EEDF cannot be measured, as it can with single probes.

The probe used in MadHeX is a planar double probe, shown in Fig. 5.16, and is constructed from two 2.4 mm tantalum discs spot-welded to gold plated nickel wires, spaced 6 mm apart. The probes are coated with Sauereisen No. 31 cement except for the front-facing surfaces of the discs (facing the gas flow, -z direction). The front-facing surfaces of the probes are aligned such that the normal to the probe surface is parallel to B_z. The probe can also be used as a single probe by biasing one disc relative to ground, instead of both discs relative to each other when used as a double probe. A single probe similar in construction was used previously on this facility in high-pressure helicon experiments [92].

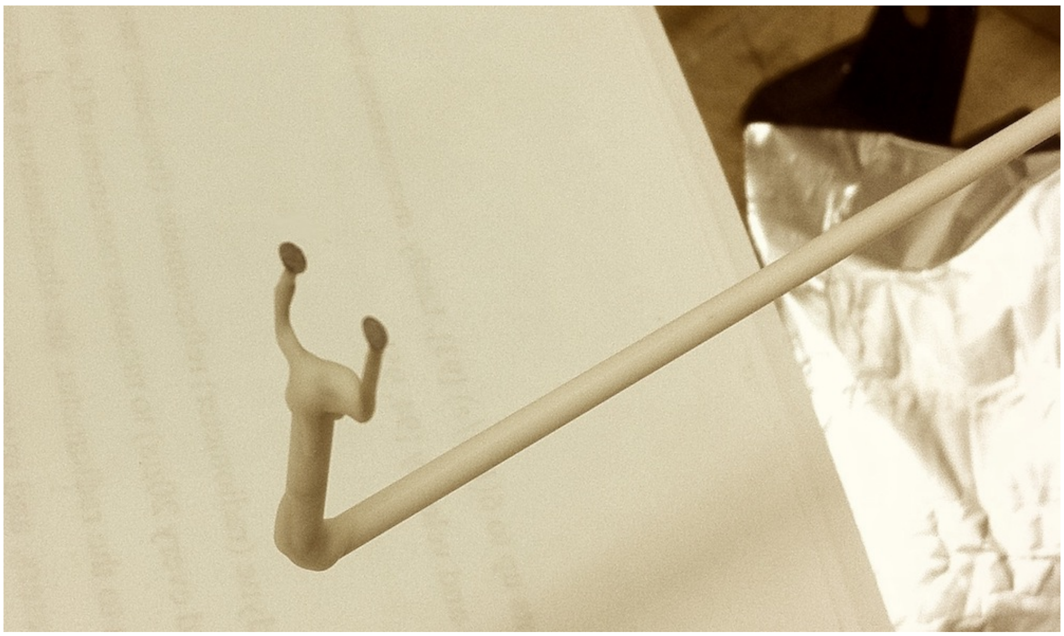

FIGURE 5.16: Tantalum double probe used in MadHeX.

The probe(s) are biased using a custom-built double probe supply. The probe circuit is based around the PA241 high voltage op-amp from Cirrus Logic. It is capable of delivering up to 60 mA of current in steady state and up to 120 mA peak, at up to $\pm$175 V. It is powered by an isolated DC bipolar supply from Acopian with dual outputs at $\pm$150 V. The entire PA241 circuit is isolated from ground through AD210 magnetically-coupled isolation amplifiers. The input sweep signal is buffered and clamped to $\pm$10 V with Zener diodes to protect the expensive AD210 input amplifier. The overall gain of the amplifier is 30 V/V. The probe current is measured through a selectable current-measurement resistor whose voltage drop is measured with another AD210 isolation amplifier. The probe voltage is measured through a high impedance voltage divider network with a 20$\times$ divider ratio, using a third AD210 isolation amplifier. Both the current and voltage measurement outputs are buffered, again to protect the AD210 isolation amplifiers. The supply can be used to drive a single probe by simply connecting one of the probe outputs (signal ground) to the stainless steel expansion chamber (chamber/earth ground). For large current-sense resistors used for detecting small currents, the load line (background) contribution can be a significant portion of the current output waveform. An adjustable subtraction circuit built from LM741 op-amps can be enabled, which subtracts a scaled copy of the probe voltage signal from the current output. This removes a significant portion of the load line in-circuit so the full dynamic range of the DSO can be used. An internal photo of the supply is shown in Fig. 5.17, and the full schematic is given Appendix A.

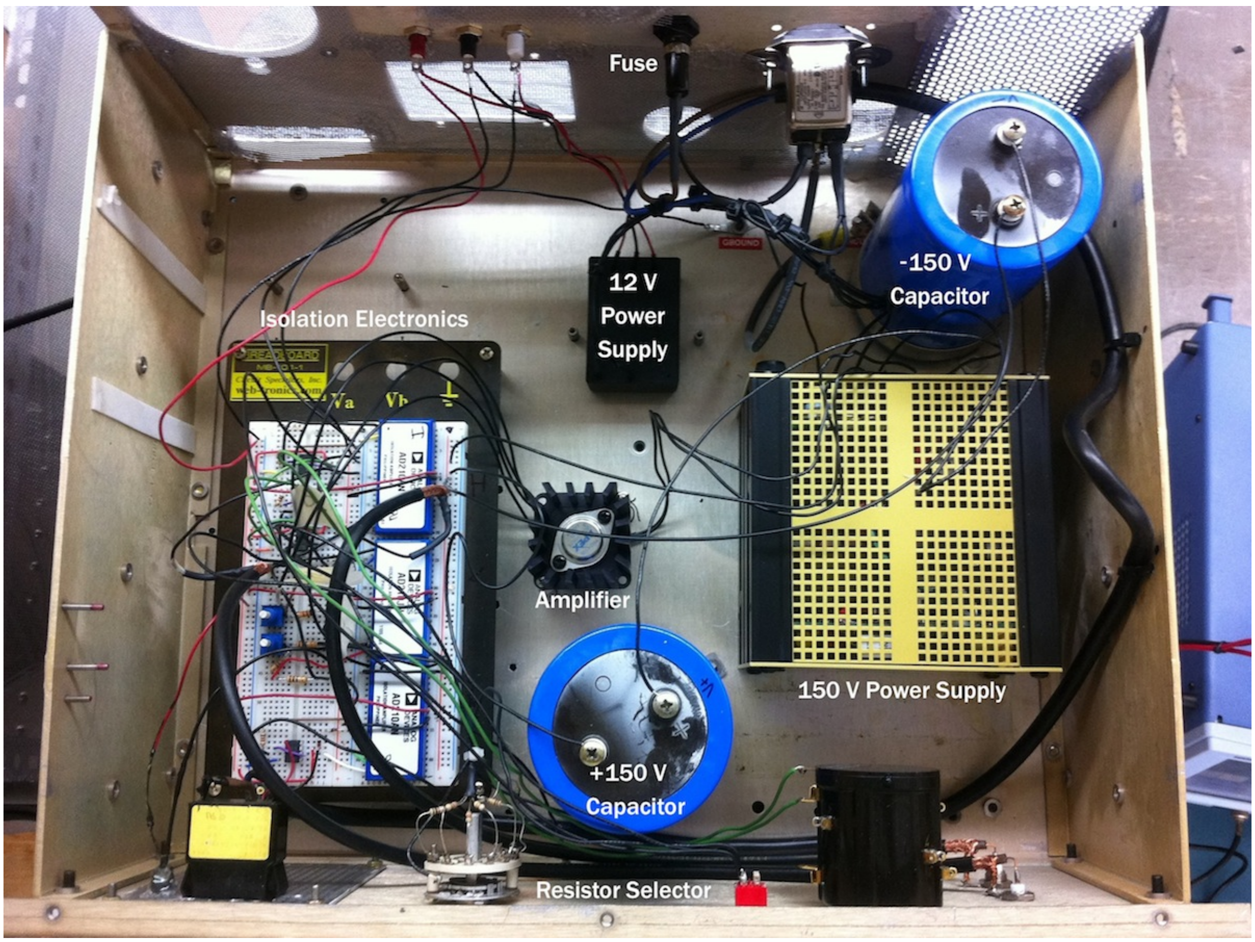

FIGURE 5.17: Single and double probe supply.

RF fluctuations in the plasma potential can adversely affect the collected current, making it difficult to extract the electron energy distribution function. Typically, without significant RF fluctuations or with a well-compensated probe (e.g. [70, 93, 94]), the EEDF (and EEPF) can be calculated from the collected current vs. voltage trace by simply looking at its first derivative. The zero (reference) voltage is set to the plasma potential, where the collected electron current deviates from an exponential (the “knee”). By plotting the collected electron current (subtracting the ion current from the collected current) on a logarithmic scale, a Maxwellian electron probability function will manifest itself as a straight line. The electron energy distribution function (EEDF), if necessary, can then be calculated from the electron energy probability function (EEPF) by $g_P(E) = E^{-1/2} g_D(E)$ where $g_P(E)$ is the EEPF and $g_D(E)$ is the EEDF. If there is a population of electrons that have a different temperature than the bulk, there will be two distinct slopes visible, equating to two separate temperatures.

In the presence of RF plasma potential fluctuations, the collected electron current will be strongly affected by the fluctuations, particularly in the region used to determine the electron temperature from the slope of the I-V trace [94]. However, it has been shown that it is possible to extract an electron temperature using the straight-line fitting method using an uncompensated probe in the presence of RF fluctuations, as long as the technique is done properly. Oksuz [95] showed that in the presence of RF fluctuations, since the distribution, assumed to be Maxwellian, is simply fluctuating in time, fitting to the linear region of the distribution is simply “sampling” the distribution when the plasma potential is at its lowest value, as shown in Fig. 5.18. It is akin to measuring the diameter of a ball held by someone swinging on a playground swing. Measuring the diameter with a ruler as they swing past you would be difficult – but a measurement may be possible if made at the edge of the swing’s (and ball’s) travel, if assumptions are made about the shape of the ball. It should be noted that the electron temperature extracted in this way will be representative of the "tail" of the distribution, since the electrons furthest from the plasma potential are being sampled. This does not mean the tail electron temperature is different from the bulk electron temperature, simply that the electrons that are sampled are from the tail of the distribution. The electron temperatures obtained in the presence of RF fluctuations must be regarded as indicators of the electron temperature, and should ideally be confirmed with other diagnostics such as optical emission spectroscopy (OES), discussed in Chapter 8.

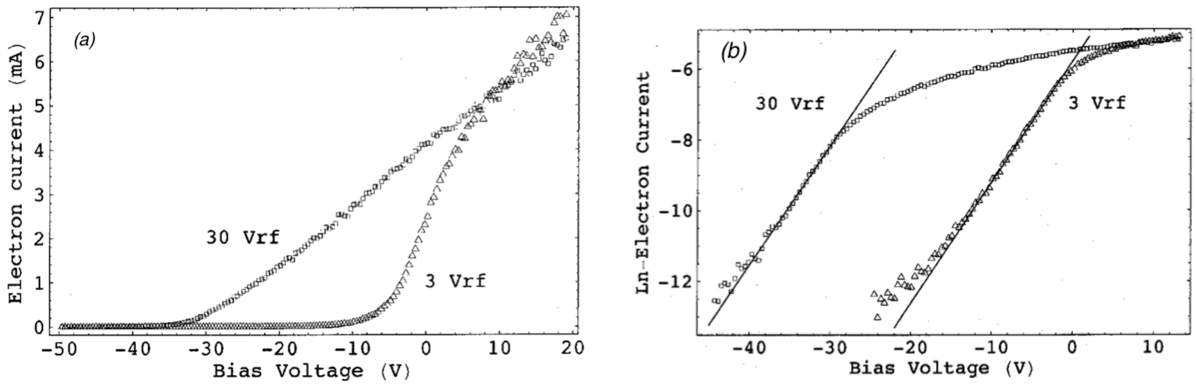

FIGURE 5.18: (a) I-V trace showing the effects of RF fluctuations for two levels of fluctuation. (b) Electron current plotted on a log scale for two different levels of RF fluctuation [95].

Because of the large RF fluctuations present in our source in some cases (see Chapter 6), a RF LC notch filter network is used to suppress any large RF components of the measured probe currents. This does not serve to RF compensate the probe well enough to be able to measure the EEPF or EEDF (as done in [93, 94]), but will remove any RF that could affect the measurement electronics. For instance, instrumentation amplifiers can rectify out-of-band signals (high frequencies), and when amplifying small value signals (such as those across the current measurement resistor for small currents) this rectification can result in a DC offset. Compensation circuits can be included in the measurement circuitry, but it must be well designed and may not cope well with differing input impedances. For this reason, the LC notch filters are used. The filter has $Q = f_0/\Delta f$ of 56, 51 and 48 at the fundamental, second and third harmonics, respectively. The frequency response is shown in 5.19 and the effect of the filter on real-world signals is shown in 5.20. When RF effects need to be measured in an experiment, or when filtering them would have detrimental side effects, the filters are not used. At all other times, the filters are used to avoid DC offsets in the sensitive, low voltage ($\approx$ mV) measurements. Note that despite the use of the three-pole filters, when the emissive probe is swept, RF fluctuations of the plasma potential still affect the probe traces, and it is still possible to extract the fluctuation magnitude from the inflection points. The emissive probe is still unable to follow the RF fluctuations and the probe measures the time-averaged current at each bias voltage.

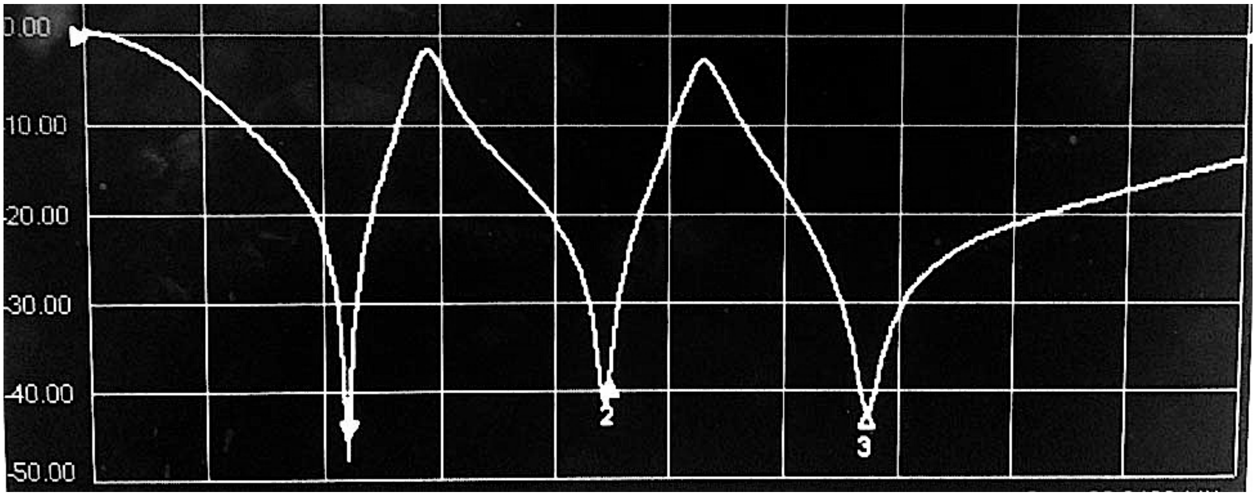

FIGURE 5.19: Frequency response of the LC filter used with the planar single probe. The horizontal axis scaling is not shown but represents 300 kHz - 60 MHz. The vertical axis is logarithmic and has units of dB.

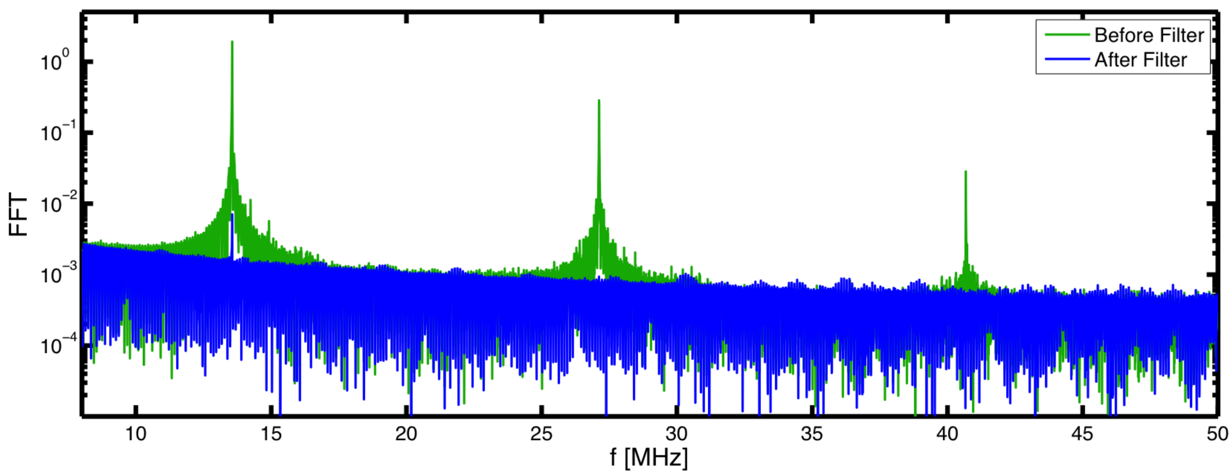

FIGURE 5.20: FFT of recorded waveforms before and after the RF filter, with the single-ended double probe supply sweeping at 3 Hz. There is a marked decrease in the first, second and third harmonic.

In order to accurately measure the electron energy distribution in the presence of RF plasma potential fluctuations, the probe tip must be able to "follow" the plasma potential fluctuations. This allows the probe to sample the distribution *with* the fluctuations, similar to making some measurement while *sitting* on a swing instead of trying to make the same measurement while watching the swing from a stationary position. In order for the probe to follow the fluctuations, the probe tip must be able to "float" and therefore have a high impedance to ground at the RF frequency such that it can easily follow the fluctuations and is not "tied" to ground. However, it must be able to be biased at some voltage with respect to the plasma potential and therefore have a low impedance to ground at lower frequencies. Mathematically, the probe filter system must satisfy the following requirements [93]:

$$|Z_{pr}/Z_f| \leq (0.3 - 0.5)\frac{kT_e}{eV_{prf}} \tag{5.6}$$

where Z_{pr} is the impedance between the probe and the plasma (through the sheaths), Z_f is the filter impedance and V_{prf} is the RMS value of the fluctuations with respect to ground. For a worst-case scenario, the electron temperature in our system is $kT_e \approx 8$ eV and the plasma potential fluctuations can exceed 120 V in some cases. In order for the above equation to be satisfied, the filter impedance Z_f must be at least ≈ 50 times Z_{pr}, which can be difficult to satisfy since the filter impedance is typically set by the Q of the network, which can be low for both LC and choke (single L) filters. For this reason, it was not attempted to construct a well-compensated probe to measure the EEDF or EEPF due to the very large RF fluctuations measured in the source (see Chapter 6). Instead, optical emission spectroscopy (OES) could be used [96], which is discussed in Section 8.2.1.

Single Probe Analysis

MATLAB scripts are used for analysis of both single and double probe data. The single probe data is captured with the DSO with *ERES* enabled and a sample rate of at least 1 MS/s. Similar to the RPA data analysis, the single probe is swept with a triangle waveform. Both the up- and downwards sweeps are recorded and averaged, and both are plotted to check for any hysteresis.

Fitting is done in a MATLAB GUI written for single probe analysis, shown in Fig. 5.21. The ion saturation current is subtracted from the measured current using a least-squares linear fit to the ion saturation portion of the curve (large, negative bias voltages). The ion saturation current fit is subtracted from the measured current, and the start and end points for the least-squares fit can also be adjusted in the GUI to minimize the electron current at low probe bias voltages, and the plotted data in the GUI is updated in real time when the fitting values are changed. The electron current (measured current with ion current subtracted) is plotted on a logarithmic scale. Least-squares linear fits (signifying a single or bi-Maxwellian distribution) are calculated for the straight-line regions of the electron current. The slope of the linear fit is proportional to the inverse of the electron temperature, and is displayed on the GUI. In the presence of strong RF fluctuations of the plasma potential, the farthest-negative edge of the I-V trace is used for the electron temperature fit.

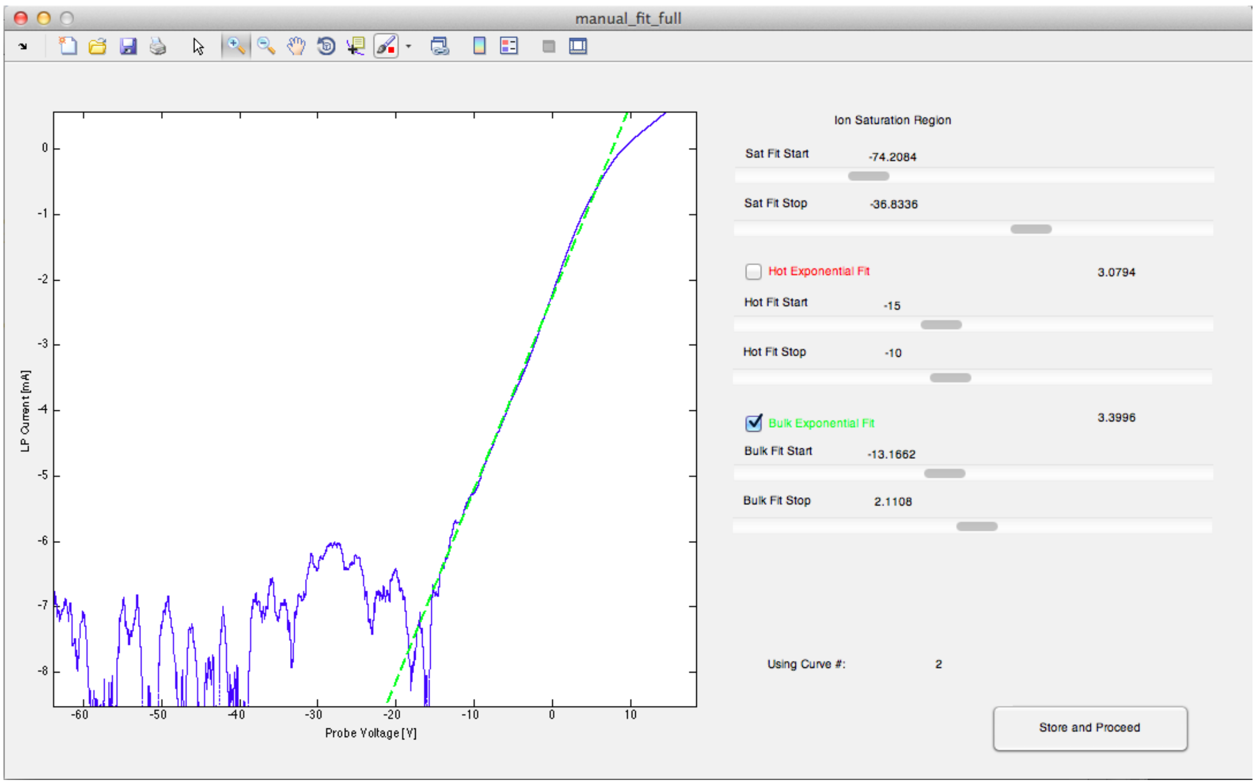

FIGURE 5.21: MATLAB GUI used to fit single probe traces.

The ion density is calculated from the ion saturation current using [23]:

$$n_i = \frac{I_{sat}}{0.6eA_s\sqrt{\frac{kT_e}{M_{Ar}}}} \tag{5.7}$$

where I_{sat} is the ion saturation current, e is the elemental charge, A_s is the physical probe area, T_e is the electron temperature and M_{Ar} is the mass of argon. Bulk electron temperatures used in the density calculation are calculated with the above MATLAB GUI near the floating potential.

Figure 5.22 shows a typical result from the fitting method. A fit to the electron saturation region is included to aid in calculating the plasma potential (where the green and red solid lines cross). Here, due to the RF fluctuations, the plasma potential predicted by this method (6 V) is lower than the actual plasma potential (31 V).

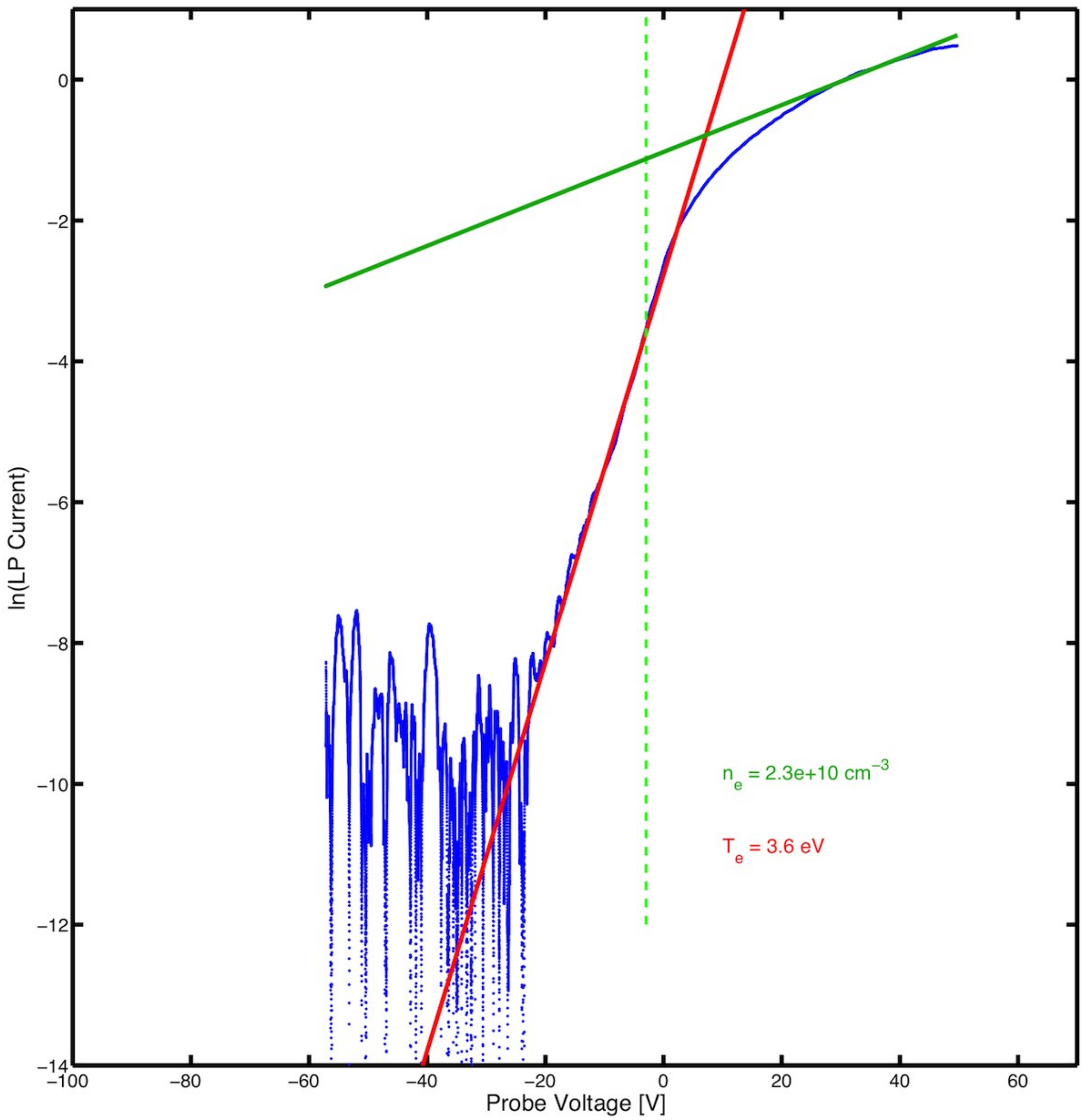

FIGURE 5.22: Typical result from the Langmuir Probe analysis. The red solid line denotes the Maxwellian fit (a good approximation here) and the green solid line denotes the fit to the electron saturation region, used only to find the “knee” of the trace (the plasma potential). The dashed green line denotes the measured floating potential. The experimental conditions are 10 sccm flow rate, 100 W, 340 G magnetic field at z = 50 cm.

Double Probe Analysis

Double probe I-V traces are fitted to a hyperbolic tangent plus a linear rise due to sheath expansion [97, 98]:

$$I(V) = I_{sat}\tanh\left[\frac{eV}{2kT_e}\right] + \frac{V}{S} \tag{5.8}$$

where I_{sat} is the ion saturation current, e is the elemental charge, k is the Boltzmann constant, T_e is the electron temperature and S is a sheath expansion factor. The ion saturation current I_{sat}, bulk electron temperature T_e and the sheath expansion factor S are used as fitting parameters. It should be noted that a double probe samples the electron distribution at or near the floating potential [97], and therefore the calculated electron temperature is taken at the floating potential and the fit assumes a Maxwellian distribution, which may not hold in our source at lower pressures [70].

The fitting to Eq. 5.8 is done in MATLAB using the function `fminsearch`, which finds the minimum of an unconstrained multivariable function using the derivative-free method. The fit function is defined in a separate function and starting values are passed to that function. The mean squared error (difference between fit and real data) is calculated and minimized with `fminsearch`, which adjusts the fit parameters until a tolerance has been reached. The final fit values are returned and the fit is plotted with the data.

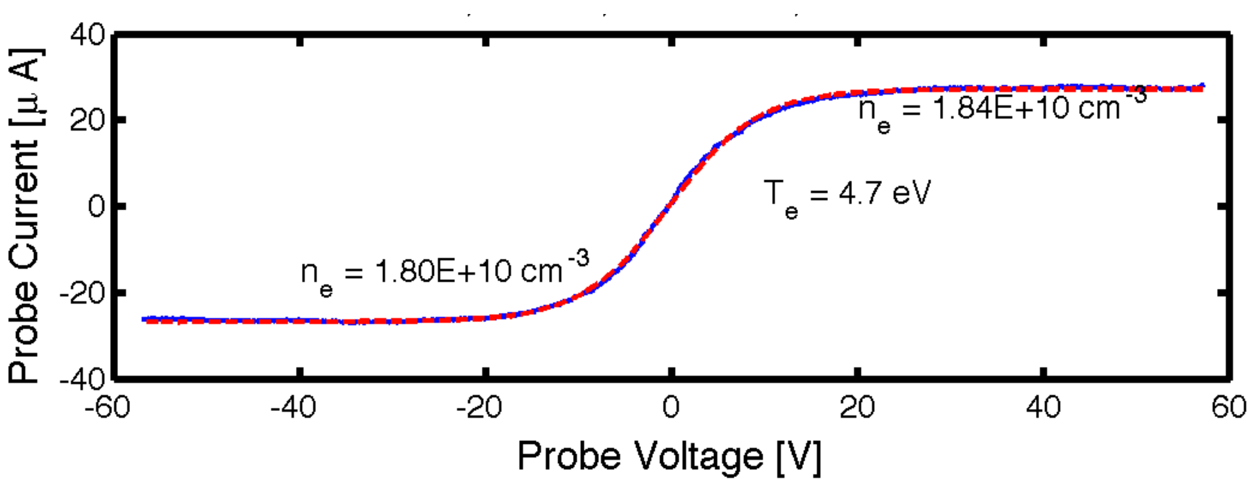

FIGURE 5.23: Example of double probe I-V trace and fit from Eq. 5.8 with linear rise from sheath expansion subtracted.

Figure 5.23 shows a typical double probe I-V trace (blue) and the fit from Eq. 5.8 (red), both after the linear rise has been subtracted. The density (in cm^{-3}) is shown for each corresponding saturation current and the bulk electron temperature also shown.

5.4 Antenna Impedance Measurement

The impedance of the RF antenna can useful in deducing the operating mode of the helicon source. Using the dual directional coupler installed at the input of the impedance matching network and the known or estimated values of the matching capacitors, the vacuum and plasma-loaded impedance of the antenna can be calculated. The RF circuit is shown in Fig. 5.24, including the dual directional coupler, which directly measures $\widetilde{V}_{ref}$ and $\widetilde{V}_{forw}$ with -40 dB and -50 dB coupling factors, respectively. The complex reflection coefficient $\widetilde{\Gamma}$ looking into the matching network from the generator (at the directional coupler) can then be calculated:

$$\widetilde{\Gamma} = \frac{\widetilde{V}_{ref}}{\widetilde{V}_{forw}} = \frac{Z_T - Z_0}{Z_T + Z_0} \tag{5.9}$$

where Z_T is the total impedance of the matching network and antenna, and Z_0 is the transmission line and generator impedance (50 Ω). The total (complex) impedance Z_T is equal to:

$$Z_T = Z_{C1} + \frac{Z_{C2} Z_A}{Z_{C2} + Z_A} \tag{5.10}$$

solving for Z_A and including $Z_T = Z_0 \frac{1+\widetilde{\Gamma}}{1-\widetilde{\Gamma}}$:

$$Z_A = \frac{Z_{C2}[Z_0 \frac{1+\widetilde{\Gamma}}{1-\widetilde{\Gamma}} - Z_{C1}]}{Z_{C2} - Z_0 \frac{1+\widetilde{\Gamma}}{1-\widetilde{\Gamma}} + Z_{C1}} \tag{5.11}$$

Therefore, if the capacitor values $C1$ and $C2$ are known, Z_A is only a function of the complex reflection coefficient $\widetilde{\Gamma}$. This simple circuit model does not take into account other parasitic impedances of the circuit elements, including capacitances and resistive losses of the intercon-

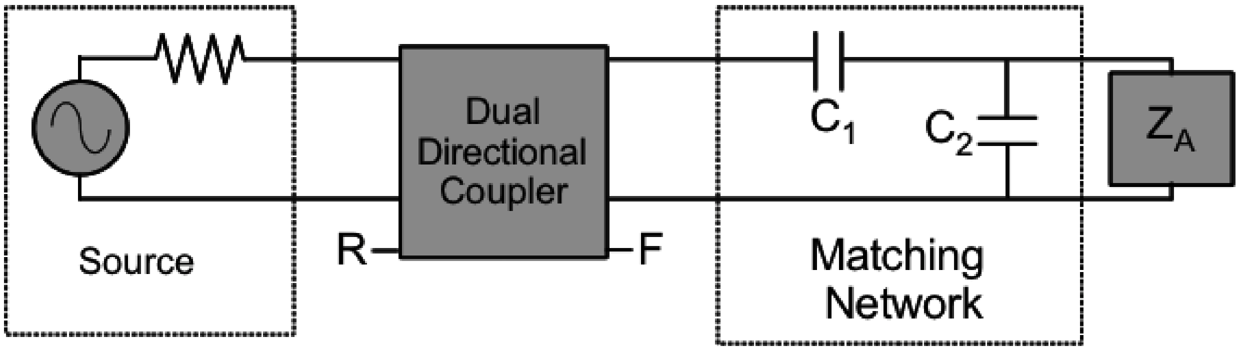

FIGURE 5.24: Circuit diagram of RF matching system, including dual directional coupler. The directional coupler is the measurement point of the reflection coefficient $\widetilde{\Gamma}$, looking right.

nects in the matching network. In addition, the exact values of the capacitances are not known (since they are tuned for the lowest power for each case). For these reasons, this simple model is only used to measure *relative* changes in the plasma-loaded antenna impedance, and the calculated impedances are not necessarily the correct absolute value. However, if the capacitor values are not changed, the relative change in the plasma-loaded antenna impedance Z_A can be extracted.

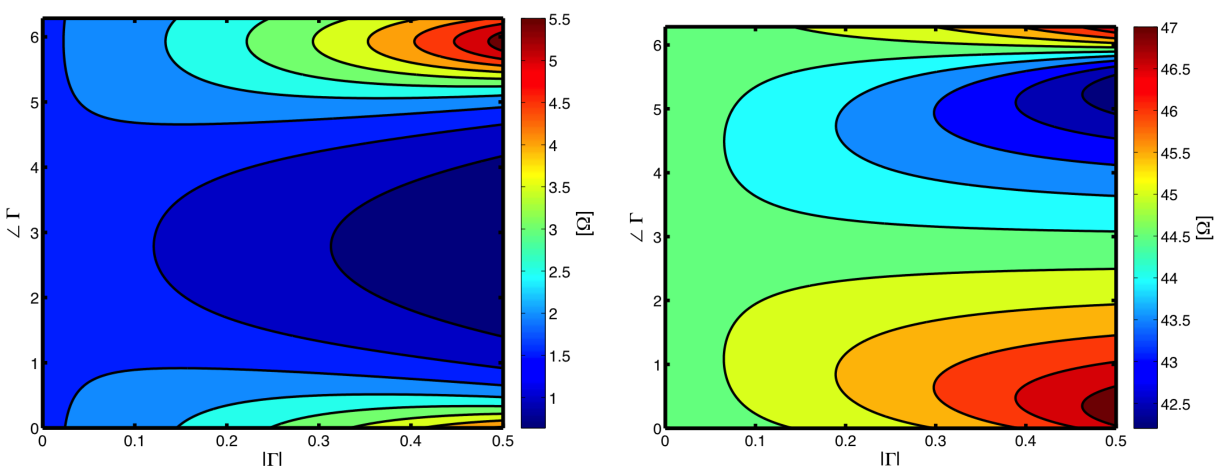

FIGURE 5.25: Resistive (a) and reactive (a) parts of the antenna impedance vs. the magnitude and phase of the complex reflection coefficient $\widetilde{\Gamma}$ for a typical set of matching capacitor values.

Figs. 5.25(a) and 5.25(b) show the dependence of Z_A on the magnitude and phase of the complex reflection coefficient $\widetilde{\Gamma}$ for a typical set of matching circuit capacitor values. The voltages at the directional coupler are measured with the DSO using a 50 Ω input impedance with a 10 GS/s sample rate. A MATLAB script is used to extract the magnitude and phase of the forward and reflected voltages at the fundamental RF frequency (13.56 MHz) and calculate the plasma-loaded or vacuum antenna impedance Z_A. The fast Fourier transform (FFT) of both the incident and reflected signals is calculated, and the complex value of the FFT is extracted at the fundamental harmonic of the RF signal (13.56 MHz). The phase shift θ between the incident and reflected signals is the difference in the angle of the complex FFT:

$$\theta = \angle\mathcal{F}_{ref}(f_0) - \angle\mathcal{F}_{inc}(f_0) \tag{5.12}$$

where $\mathcal{F}$ denotes the FFT of either the incident or reflected signal, and f_0 is the fundamental RF frequency. The complex reflection coefficient is then calculated from $\tilde{\Gamma} = |\Gamma|\exp(j\theta)$ where $|\Gamma| = |V_{ref}|/|V_{inc}|$.

The impedance of the antenna can be used to signal changes in the coupling mode to the plasma [99, 100]. As the plasma density increases, the energy extracted from the antenna increases. This manifests as an increase in the real part of the antenna load. The reactive part of the antenna load decreases as a result of the increased induced current in the plasma, which opposes the antenna current. The induced current results in a drop in the magnetic flux and therefore the coil inductance, and the reactance of the antenna drops [99].

Summary

Several diagnostics are available to characterize the potential gradients and associated ion acceleration in the MadHeX system. Two-grid and four-grid Retarding Potential Analyzers (RPAs) are used to measure the ion energy distribution, with the larger four-grid unit used to cross-check the smaller two-grid unit, which can be used with less perturbation to the plasma. Emissive probes are used to measure the plasma potential and RF fluctuations in the plasma potential. Single and double probes are used to measure the electron temperature and density, but extraction of the electron energy distribution, typically calculated from the single probe I-V curve, is not reliable due to the large RF fluctuations. Probe compensation for the large RF fluctuations measured is not practical, and other methods will need to be used to measure the distribution function of the electrons. A directional coupler is used to estimate the change in plasma-loaded antenna impedance to detect mode changes in the source.

CHAPTER 6

Results

6.1 Two-Grid RPA Validation

Since the performance of the two-grid RPA hadn't been previously investigated, it was necessary to compare its performance to the well-tested [80, 81] four-grid RPA. Both were used under the same conditions and the measured IEDFs compared, which are shown in Fig. 6.1. For the comparison, the flow rate Q = 1.3 sccm, RF power P = 100 W, and the magnetic field B = 340 G in the source region. For the validation, both analyzers' collectors were placed at the same z location (z = 64 cm). The grid spacing for the four-grid RPA is larger than that of the two-grid RPA, meaning the front-facing grids of the analyzers were offset by 2 cm. In Fig. 6.1, there is a slight difference between the measured potentials and widths of the bulk and the beam ions between the two analyzers, however the beam energies (differences between the bulk and beam potentials) are within 10 V (10 %). The differences between the two RPAs is likely due to spatial averaging resulting from the larger grid area of the four-grid RPA as well as increased perturbation introduced by the four-grid RPA's larger physical size (50 mm diameter, 40 cm long compared to 12 mm diameter and 2 cm long. From the subsequent investigation of the beam characteristics, it was observed the two-grid RPA provides the best agreement with the swept emissive probe data, and also introduces less perturbation on the source operation than the four-grid RPA. For the rest of the experimental results below, the smaller (12 mm diameter) two-grid RPA is used unless noted.

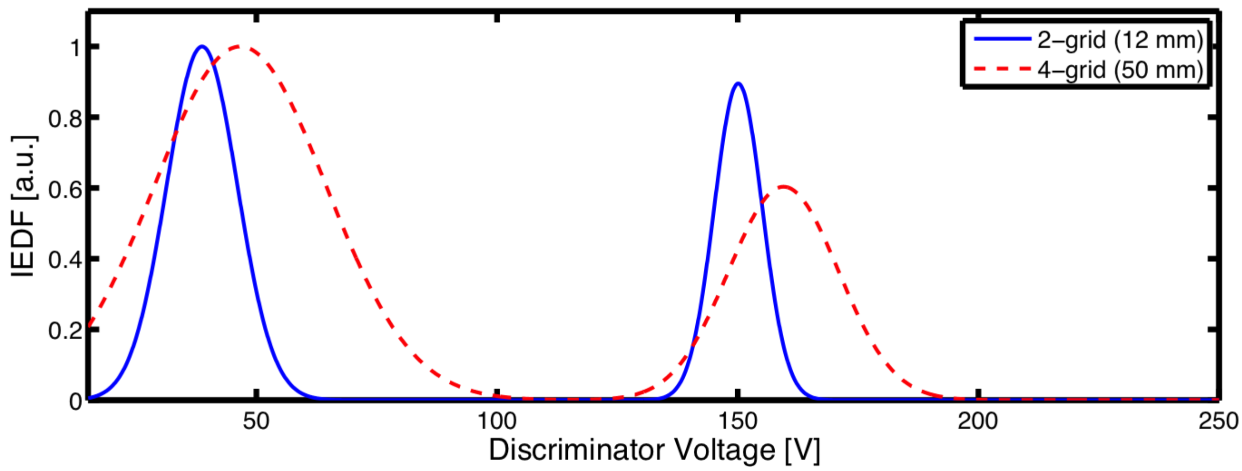

FIGURE 6.1: Comparison of four-grid (red dashed) and two-grid RPA (blue solid) measurements. Conditions are Q = 1.3 sccm, B = 340 G, P = 100 W.

In an RF-driven plasma, it is possible to observe a double-peaked ion distribution using an RPA as a result of the ions following any RF fluctuation of the plasma potential. The fluctuating plasma potential in time results in a time-varying potential gradient from the bulk plasma to the analyzer. If the ion transit time through the sheath is shorter than or comparable to the RF time period ($\tau_i \lesssim \tau_{RF}$), ions can transit a large portion of the sheath during an RF cycle and are affected by the rapidly changing potential gradient in front of the analyzer. Ions enter the sheath in front of the analyzer at different parts of the RF cycle and arrive at the analyzer with a distribution of energies. This double-peaked distribution can be easily mistaken for an accelerated population of ions or a beam, but there is no time-averaged energetic ion population present. However, if the ion response time is longer than the RF period ($\tau_i \gg \tau_{RF}$), the ions only respond to the time-averaged value of the gradient in the potential from the bulk plasma to the analyzer (the time-averaged electric field) and arrive at the analyzer at or near a single energy, even though the plasma potential is rapidly changing in time. As will be shown later in Chapter 7, for the conditions examined in Fig. 6.1 (and most plasmas when the source is operating in the capacitive mode), the ion plasma frequency is much lower than the RF frequency (equivalent to $\tau_i \gg \tau_{RF}$), and any double-peaked distribution is evidence of an accelerated ion population, not RF modulation of the ion energy distribution function. In order to verify that the observed double-peaked ion energy distribution is not from RF fluctuations of the plasma potential, the two-grid RPA was installed into the helicon system with the plasma-facing grid facing the walls of the expansion chamber (perpendicular to the direction of the measured ion beam). If the double-peaked distribution is no longer present with the analyzer facing the wall, the double-peaked distribution observed when the analyzer is facing in the z direction is evidence of an accelerated ion population. The ion distribution function with the RPA in this configuration, for the same plasma conditions in Fig. 6.1, was single-peaked at the background, time-averaged plasma potential, indicating negligible RF influence on the RPA for that case. This is a common method used to verify that RF perturbations are not causing false beam indications [40, 71].

6.2 Plasma Potential and Ion Energy Evolution

The axial dependence of the total ion energy, electron density and electron temperature were examined for source parameters that provide a well-defined accelerated ion population. The flow rate for this "test case" is Q = 2 sccm (0.53 mTorr at the upstream endplate, 0.16 mTorr at the downstream endplate), the RF power is P = 100 W and the magnetic field is B = 340 G in the source region under the antenna near z = 0 cm. Figure 6.2 shows the two-grid RPA-measured, Gaussian-fitted ion energy distribution with respect to chamber ground as a function of axial distance, with color indicating the height of the distribution (red is highest, with the data normalized to the maximum overall). The color map has been compressed (lowest peak height is shifted higher in the color domain) to keep the data visible throughout the z domain due to the large spatial variation of the ion density (see Fig. 6.4 below, a decrease by a factor of 36). The observed accelerated-ion potential (relative to chamber ground) is 110 V, and the bulk-ion potential varies from 110 V to 45 V as the RPA is moved axially over 25 cm into the expansion chamber. It is interesting to note that the total energy of the ions in the accelerated population is conserved, as evidenced by the invariance of the potential of the peak in the accelerated ion population in Fig. 6.2, as expected. While the total energy remains the same, the kinetic energy of the ions increases, which is equal to the difference between the accelerated ion potential and the bulk ion (plasma) potential ($E_i = e[V_{beam} - V_{plasma}]$). The kinetic energy increases from the bulk, background flow around z = 50 cm up to 65 eV at z = 70 cm. The IEDF, shifted such that the plasma potential is at E_i = 0, is plotted in Figure 6.3. The increase in kinetic energy of the ions is visible, as well as the decay in the density of the accelerated population of ions. The beam density decreases into the expansion chamber due to radial expansion and ion-neutral charge-exchange collisions, and the beam decays over its 25 cm axial extent and vanishes by z = 78 cm as the fast ions collide with neutrals and produce slow (thermal) ions. The beam decay due to charge-exchange collisions is discussed further in Chapter 7. It is interesting to note that the accelerated ion population does not last much longer than the extent of the acceleration region (z = 45 cm to z = 70 cm). However, in the mock-up of our experiment placed in a much larger vacuum chamber at Georgia Tech shows that the beam persists much longer (up to 1 m) with a lower background neutral pressure in the expansion chamber (see Fig. 6.23). Additionally, a comparison of the RPA-measured ion potential with emissive probe data is given in Fig. 6.19.

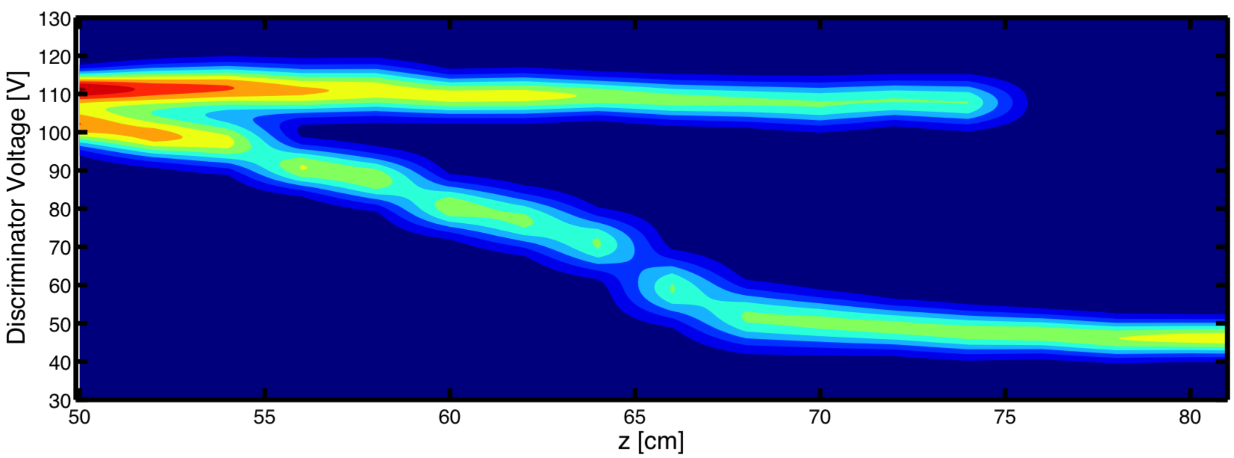

FIGURE 6.2: Ion Energy Distribution Function (IEDF) from z = 50 - 80 cm measured by the two-grid RPA and fitted with one or two Gaussian distributions. The conditions are Q = 2 sccm, P = 100 W, and B = 340 G. Color indicates the height of the distribution and the color map has been compressed in order to keep the data visible throughout the z domain.

The electron density and electron temperature are shown in Fig. 6.4 for the same spatial domain and source conditions in Fig. 6.2. The ion (and electron) density, measured with the single (Langmuir) probe biased in ion saturation (large negative bias), decreases rapidly through the ion acceleration region (z = 50 cm to z = 65 cm) from 8.8×10^9 cm^{-3} to 2.4×10^8 cm^{-3} (a factor of $\approx$ 36) from z = 50 cm to z = 65 cm, and then rises slowly to 7×10^8 cm^{-3} from z = 65 cm to z = 80 cm. The bulk electron temperature obtained from the single probe remains near kT_e = 8 - 10 eV

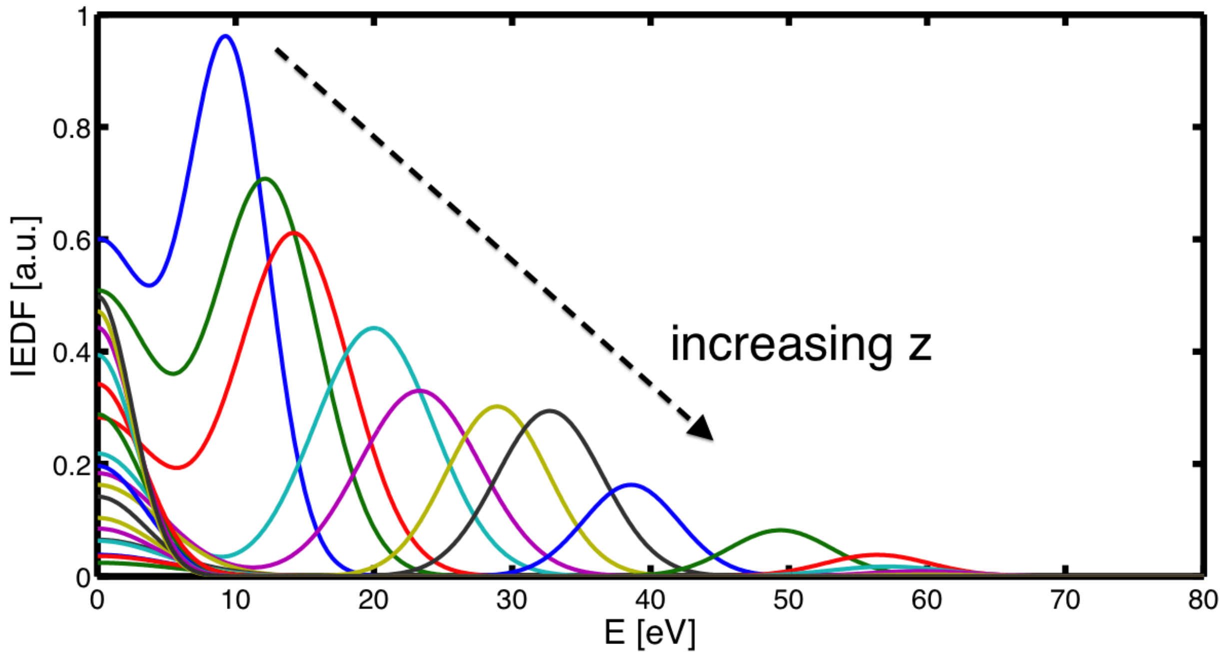

FIGURE 6.3: Ion energy distribution (IEDF), shifted such that the plasma potential is at $E_i = 0$, showing the increasing kinetic energy of the ions in z as well as the decay of the accelerated population.

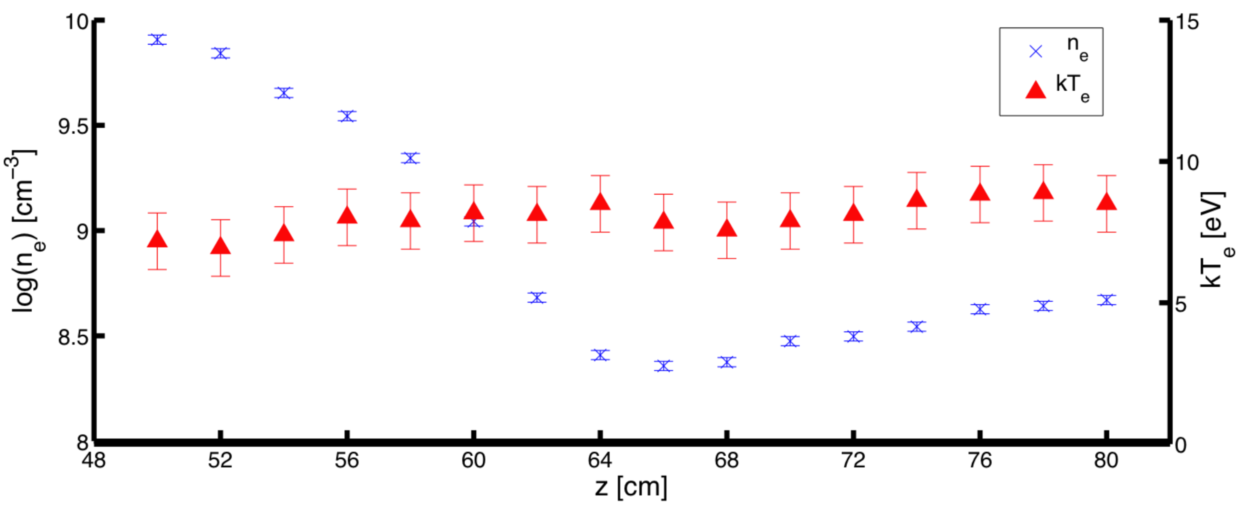

FIGURE 6.4: Electron density and electron temperature measured with single probe for the same conditions and spatial domain shown in Fig. 6.2.

throughout the acceleration region, with no statistically significant change.

The axial extent of the potential gradient is an important parameter in determining the physics of the potential gradient. For the conditions in Fig. 6.2, the potential gradient occurs over roughly

15 - 20 cm. The Debye length, calculated using the upstream density and temperature (n_e = 8.8×10^9 cm^{-3} and kT_e = 9 eV) is $\lambda_D \approx 0.2$ mm, therefore the acceleration region is roughly 1000 Debye lengths long. As discussed in Chapter 3, a classical double layer has much shorter dimensions (tens to a few hundred Debye lengths) than that observed in our experiment. However, longer double layers have been observed, up to 500 λ_D in some cases [64].

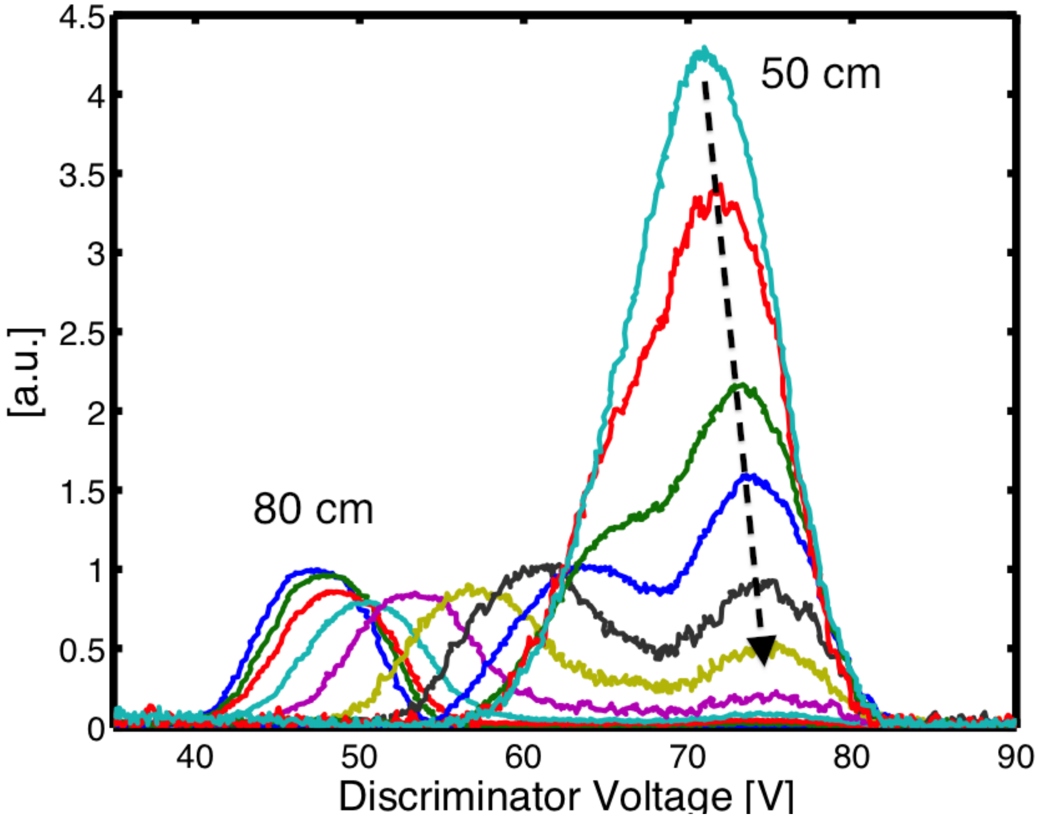

FIGURE 6.5: Detailed behavior of the ion energy distribution function measured with the 12 mm RPA from z = 50 to z = 80 cm for flow rate of 4 sccm, 100 W RF power, 670 G source magnetic field. The data shown is unfitted.

The unfitted ion energy distribution, measured with the two-grid RPA, is shown in Fig. 6.5 for several z positions as the plasma flows into the expansion chamber, for Q = 4 sccm, P = 100 W, and B = 670 G. The higher flow rate (and pressure) and magnetic field than for the data shown in Figs. 6.2 and 6.4 result in a lower potential drop with a shorter axial extent, which provides a full view of the evolution from a single-peaked distribution at z = 50 cm to a bimodal distribution and back to a single-peaked distribution at z = 80 cm. The peak in the upstream (z $<$ 60 cm) distribution appears to increase slightly in energy as the RPA is moved downstream. However, as Byhring [72] noted, the distribution remains "inside" the initial distribution and the apparent increase appears because the lower energy ions in the beam are preferentially lost due to the energy dependence of the charge-exchange cross section.

The radial profile of the ion energy distribution is shown in Fig. 6.6, for the same conditions as in Fig. 6.2. At radii larger than the source tube radius, the ion energy is equal to the plasma potential in the expansion chamber. At smaller radii, the local plasma potential increases from $V_p \approx 38$ V to $V_p \approx 60$ V, and there is evidence of formation of an accelerated population with a potential $V_i \approx 105$ V.

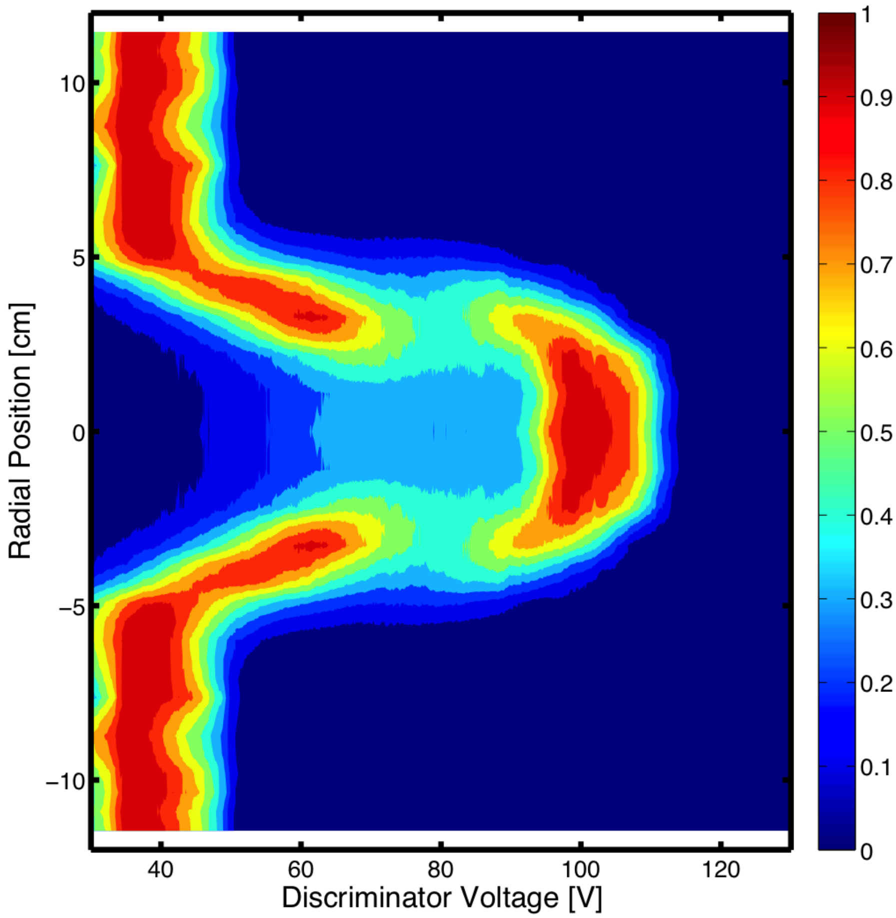

FIGURE 6.6: Radial beam profile for Q = 2 sccm, P = 100 W, B = 340 G and z = 64 cm.

Operation of the source for extended periods with the four-grid RPA installed led to a change in appearance of the front surface of the four-grid RPA. Two photos, before and after operation, are shown in Appendix B. An iridescent coating formed on the beam-facing surface of the RPA, whereas the sides of the RPA remained uncoated, suggesting an energetic population was impinging on the RPA front surface and not on the sides. In addition, a similar effect was observed on the four-grid RPA installed in the Georgia Tech helicon source, where instead the RPA front-facing surface turned hazy and dull after extended operation. An "after" photo for the four-grid RPA is shown in Appendix C.

6.3 Mode Transitions

Two distinct mode transitions have been observed in this source, the capacitive to inductive (E-H) and inductive to helicon (H-W) transitions. The theory of these transitions is described in Chapter 2. The impedance of the plasma-loaded antenna is used as an indicator of a mode transition, since it is a "global" diagnostic that gives an overall picture of the plasma condition. These mode hops are further characterized via density measurements, and the dependence of the potential difference across the mode transitions is measured. Particular attention is paid to the capacitive mode, where the highest potential gradients are measured, the result of a self-biasing effect which will be further discussed in Chapter 7.

6.3.1 Capacitive - Inductive (E-H) Mode Transition

The RF power level at which the capacitive to inductive (E-H) transition occurs is a function of both the magnetic field and flow rate (pressure). To explore the nature of the transition, the magnetic field is fixed at 340 G in the source region and the flow rate is 2 sccm (0.53 mTorr at the upstream endplate, 0.16 mTorr at the downstream endplate), the same conditions used in the "test case" shown in Fig. 6.2, and the RF power is scanned. Figure 6.8 shows the real and reactive parts of the loaded antenna impedance as a function of the RF power for these conditions. As stated in the description of the impedance diagnostic in Chapter 5, the relative *change* in the real and reactive parts of the antenna load are the important result of this diagnostic, not necessarily the absolute values of each, which are sensitive to the value of the matching capacitors (as well as the assumptions of the circuit model). For the following calculations, the capacitor values were not adjusted for the best match, since the invariance of the capacitors is assumed for the calculation of the antenna impedance from the reflection coefficient. The capacitor values used in the analysis of the directional coupler data are C_1 = 52.5 pF and C_2 = 211.8 pF, based on measurements with a Stanford Research Systems LCR meter. As a check of the antenna impedance calculated from this model, the antenna impedance was calculated for the test case (Q = 2 sccm, P = 100 W and B = 340 G) using the measured RMS voltage across the antenna (V_{0-p} = 600 V, V_{RMS} = 424 V using a Tektronix P6015A high voltage probe) and the real power dissipated into the antenna (assumed to be the RF amplifier output power with an approximate 5% losses subtracted, P_{diss} = 95 W). The dissipated power is the real part of the complex power:

$$P_{diss} = \text{Re}\,(\widetilde{V}\widetilde{I}^{*}) = \text{Re}\left[\frac{\widetilde{V}\widetilde{V}^{*}}{\widetilde{Z}^{*}}\right] = \text{Re}\left[\frac{\widetilde{V}\widetilde{V}^{*}}{R - jX}\right] = R\frac{V^2}{R^2 + X^2} \tag{6.1}$$

where V is the RMS voltage and R and X are the real and complex part of the antenna impedance Z. Solving for the reactive part of the antenna impedance, X:

$$X = \sqrt{\frac{RV^2 - P_{diss}R^2}{P_{diss}}} \tag{6.2}$$

therefore the relationship between the real and reactive parts of the antenna load are known if the dissipated power in the antenna P_{diss} and the RMS voltage across the antenna V are known. In order to fully solve for the antenna impedance, measurement of the antenna current (magnitude and phase) is necessary. However, the relationship in Eq. 6.2 gives some insight into the antenna impedance. For the test case, the relationship between R and X from Eq. 6.2 is shown in Fig. 6.7, which means the actual antenna impedance must lie on this line, assuming the model and measured values are correct. The impedance of the antenna calculated using the directional coupler data is also shown in Fig. 6.7 as an $\times$ for the same conditions. The difference between the two diagnostics is due to errors in the estimates of the matching capacitor values as well as the parasitic impedances not accounted for in the matching circuit model. This illustrates that the *changes* in the directional-coupler measured impedance of the plasma-loaded antenna can be used to detect mode transitions, but the absolute value of the calculated impedances may not be exact.

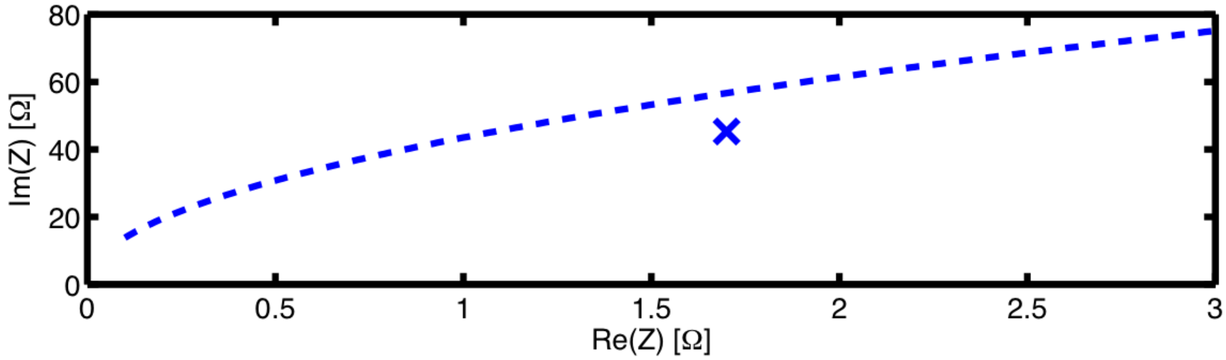

FIGURE 6.7: Relationship between the real (R) and reactive (X) part of the plasma-loaded antenna impedance, as calculated using Eq. 6.2. The actual impedance of the antenna must lie on this line (assuming the model and measured values are correct). The impedance measured with the directional coupler data is shown as an $\times$.

In Fig. 6.8, there is a marked increase in the real part of the antenna load from P = 200 W to P = 220 W, and a slight decrease in the reactive part at the same power level. The increased real (resistive) part of the loaded antenna impedance corresponds to an increase in the overall plasma density, as the increased energy transfer to the plasma appears as an increased resistance of the antenna. The slight decrease in the reactive part of the loaded antenna impedance is a result of the load on the antenna becoming *more* inductive, as described in Section 5.4.

To verify the increase in density predicted by the data in Fig. 6.8, the ion (and electron) density was measured with the double probe for the same conditions (B = 340 G, Q = 2 sccm) at z = 50 cm as the RF power was increased, as shown in Fig. 6.9. Error bars shown are the standard deviation of the set of four points: the up-sweep and down-sweep positive and negative ion saturation (ion density) measurements. Between P = 200 W and P = 220 W, there is an increase in the ion density from 7×10^{9} cm^{-3} to 1.5×10^{10} cm^{-3}. Also shown in Fig. 6.9 is the bulk electron temperature kT_e from the double probe, which remains near 10 eV and does not show a dramatic change across the mode transition.

In addition to an increase in density, there is a drastic change in the overall appearance of the plasma across the mode transition as the plasma coupling changes, as shown earlier in Fig. 2.4

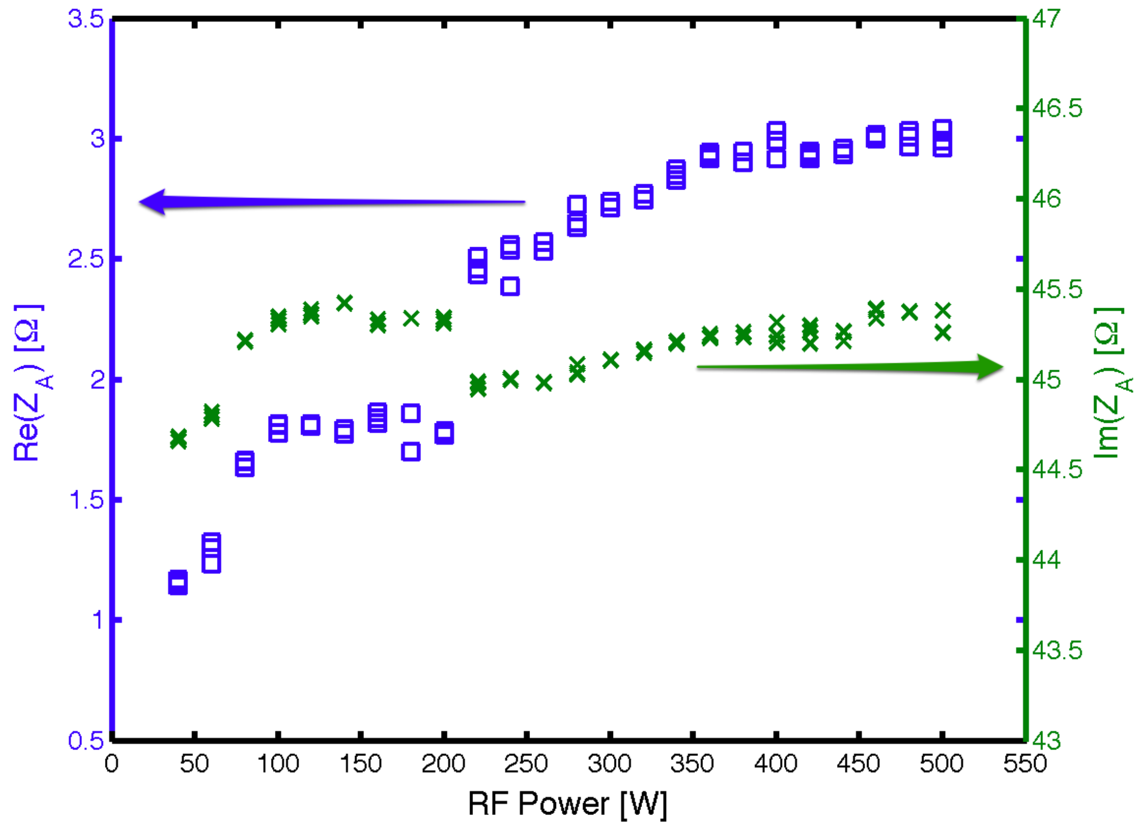

FIGURE 6.8: Real (Re(Z_A) – left, open blue squares) and reactive (Im(Z_A) – right, green $\times$s) component of plasma-loaded antenna impedance estimated with matching circuit model given in Section 5.4, for Q = 2 sccm and B = 340 G. The absolute values of the components of the impedance are sensitive to the measured capacitor values, therefore the relative change in the impedance is the important characteristic. Error bars are not shown, but are represented by the clustering of data points.

as a part of Chapter 2. Before the transition, the plasma has a diffuse, pale pink appearance and after the transition, the overall light output increases and the plasma becomes brighter pink color.

The discontinuous increase in plasma density, change in plasma-loaded antenna impedance and the shift in light output between P = 200 W and P = 220 W are all evidence of the capacitive (E) to inductive (H) transition described in Chapter 2. There are several indicators that this is indeed the E-H transition and not the inductive to helicon (H-W) transition. First, if this was the H-W transition, there would be a distinct blue core in the plasma, a feature of “true” helicon wave coupling. Second, as will be shown below, there are significant RF fluctuations of the plasma potential before the transition, a feature of capacitive coupling, which are reduced after the transition. Lastly,

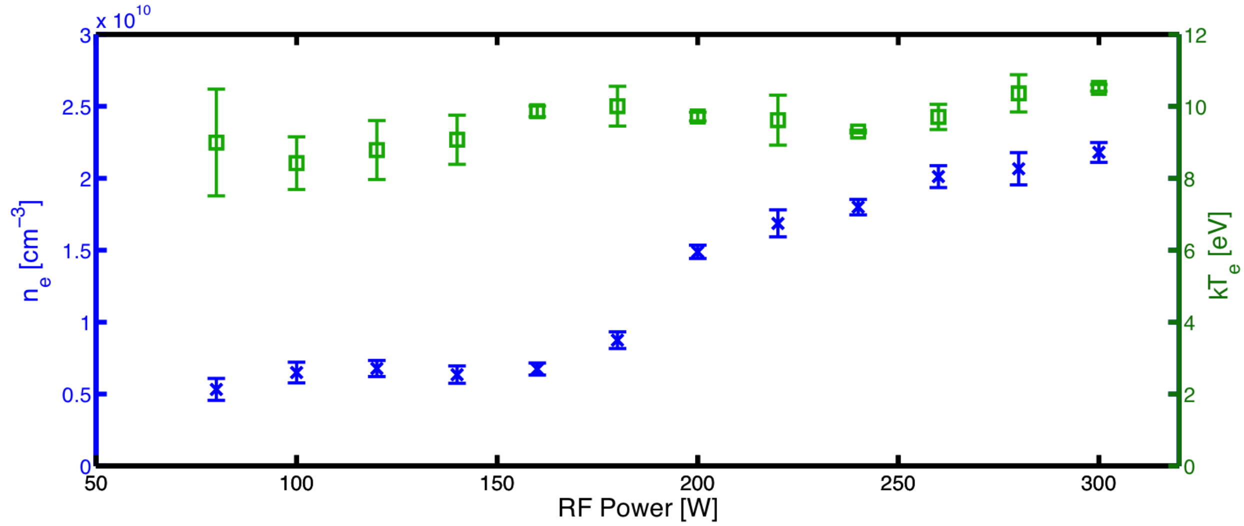

FIGURE 6.9: Electron (and ion) density (blue ×s, left axis) and electron temperature (green open squares, right axis) measured with the double probe for B = 340 G, Q = 2 sccm, and z = 50 cm as a function of RF forward power. Error bars denote the standard deviation of the values measured, four points for the density and two for the electron temperature.

the plasma densities before and after the transition (a few 10^9 cm^{-3} to 10^{10} cm^{-3}) are characteristic of the capacitive and inductive mode, and are much too low to be the helicon mode.

It is important to note that for magnetic fields lower than B = 340 G at Q = 2 sccm and P = 100 W, it is possible to create a plasma but it remains localized under the RF antenna and does not propagate or flow to the expansion chamber. This same phenomenon occurs when the argon flow rate is decreased (see Section 6.4). In this case, the plasma density in the expansion chamber is very low, below the threshold of measurement with the current diagnostics. It is expected that the plasma is produced capacitively under the antenna, only between the two antenna leads. This will be further discussed in Chapter 7. In addition, there is also some hysteresis present in the E-H mode transition, which is not shown. The data in Fig. 6.8 was taken as the RF power was increased from 40 W to 500 W, and the mode transition occurs at 200 W. If the power is instead decreased from 500 W to 40 W, the mode transition point occurs (from H-E) at a lower power, around 160 W. This hysteresis is discussed in Chapter 2.

The two-grid RPA was used to measure the bulk ion potential difference between the source and expansion chambers and subsequent accelerated ion population across the E-H transition, which is shown in Fig. 6.10. The potential drop is calculated from the difference between the upstream plasma potential (at z = 50 cm) and the downstream plasma potential (at z = 90 cm). Also shown is the collector current at a discriminator voltage V_D = 0, which is indicative of the ion density (see Section 7.1 for a rigorous treatment), at z = 50 cm. There is a distinct jump in the potential drop from the E mode to the H mode, from $\Delta V = 72 \pm 2$ V at P = 200 W to $\Delta V = 54 \pm 2$ V at P = 220 W. In the E mode (P < 200 W), the potential drop increases with RF power, from $\Delta V = 45 \pm 2$ V at P = 40 W to $\Delta V = 72 \pm 2$ V at P = 200 W, right before the mode transition. In the H mode, the potential drop magnitude varies much less, with a slight decrease (about 5 V) from P = 220 W to P = 400 W. The error in the RPA potential measurements arises from the manual fitting used to determine the peak in the ion distribution.

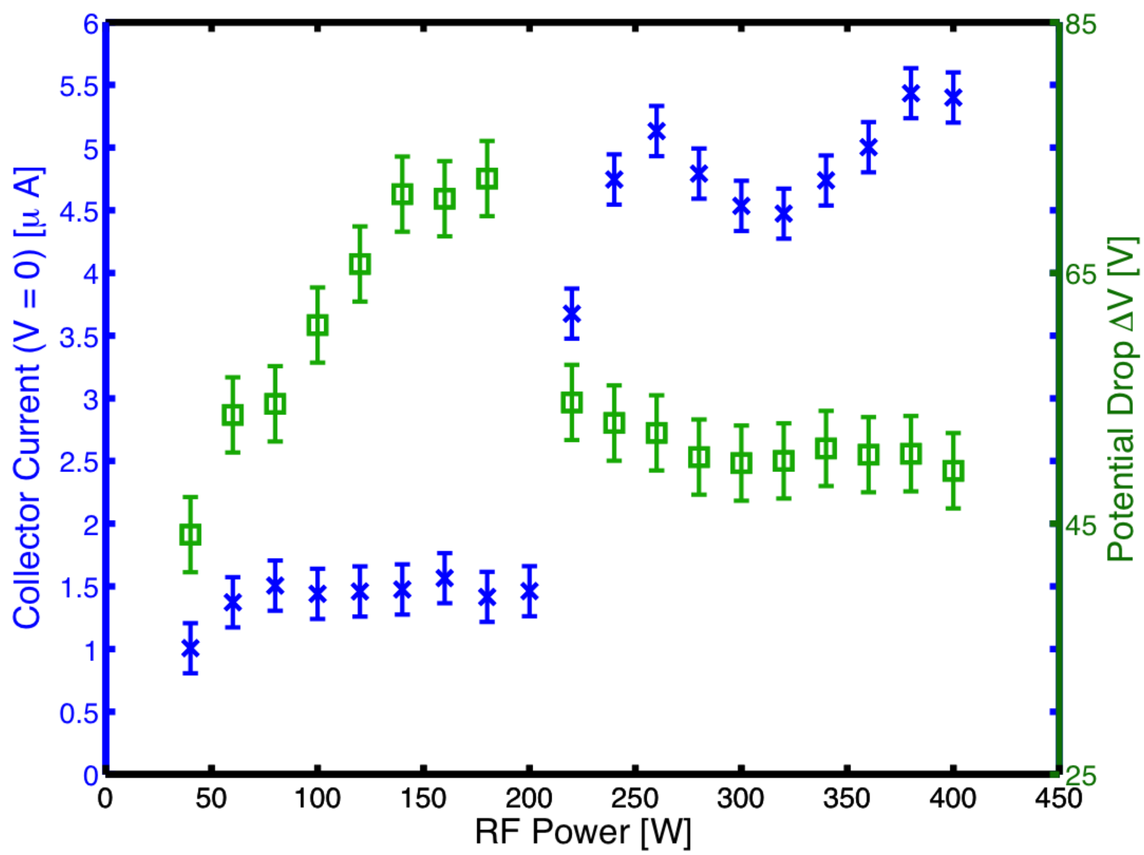

FIGURE 6.10: Collector current at V_D = 0 (left, blue ×s) and potential drop ΔV (right, green open squares) vs. RF power across the E-H transition for Q = 2 sccm, B = 340 G. The potential drop ΔV is calculated from the upstream (z = 50 cm) and downstream (z = 90 cm) bulk ion potentials, and the collector current is measured at z = 50 cm.

6.3.2 Inductive - Helicon (H-W) Mode Transition

A second mode transition occurs at much higher neutral pressures and RF powers, which will be shown to be the inductive-helicon (H-W) transition. Figure 6.11 shows the real and reactive components of the plasma-loaded antenna impedance vs. RF power for a flow rate Q = 20 sccm and B = 340 G. A clear mode transition occurs between P = 700 W and P = 800 W, with an increase in the real (resistive) component and a decrease in the reactive component. It is important to note that the H-W transition only occurs at higher neutral pressures, flow rates and magnetic fields, since there is a threshold electron density for the helicon wave dispersion relation to be satisfied with a given antenna spectrum (geometry). The ion density for the same conditions, measured with the double probe, is shown in Fig. 6.12. There is a sharp jump from $n_e = 6 \times 10^{11}$ cm^{-3} to $n_e = 1.2 \times 10^{12}$ cm^{-3} from P = 700 W to P = 800 W.

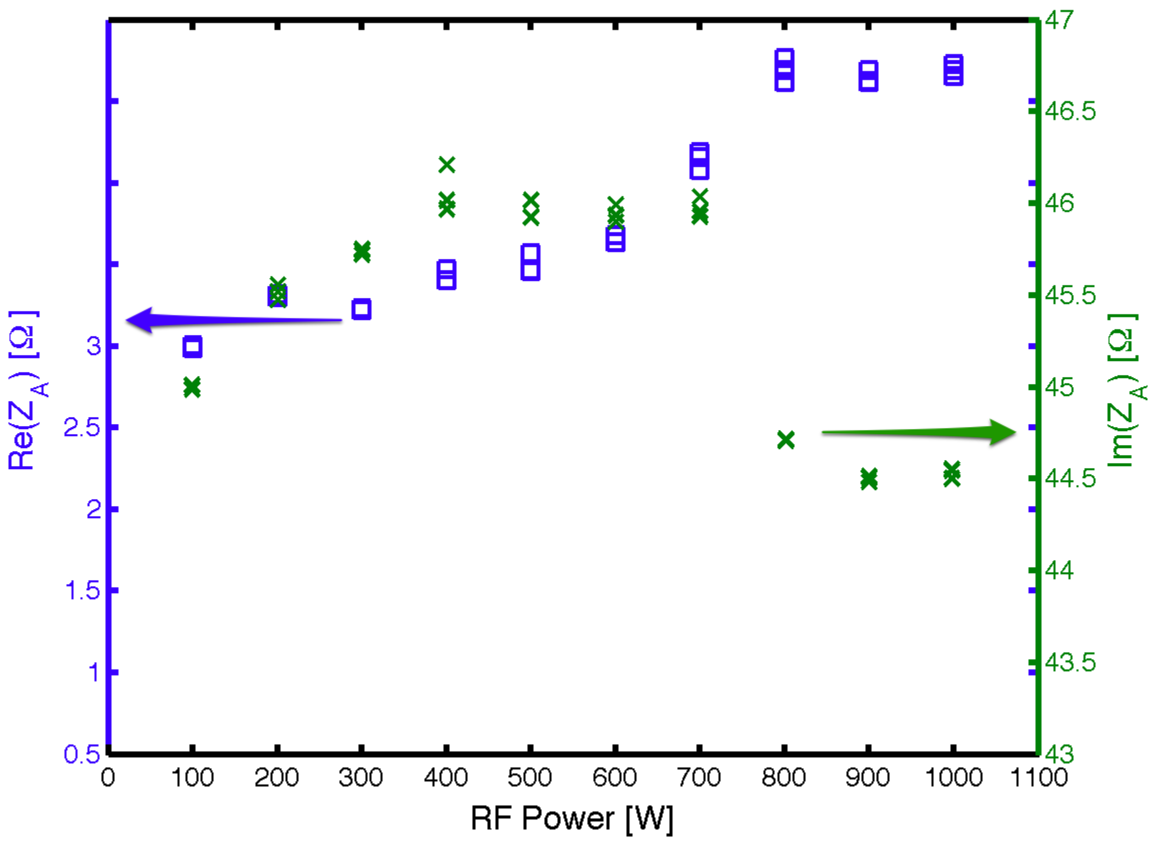

FIGURE 6.11: Real (Re(Z_A) – left, open blue squares) and reactive (Im(Z_A) – right, green $\times$s) components of loaded antenna impedance vs. RF power for the H-W transition for Q = 20 sccm and B = 340 G, measured with the antenna impedance diagnostic.

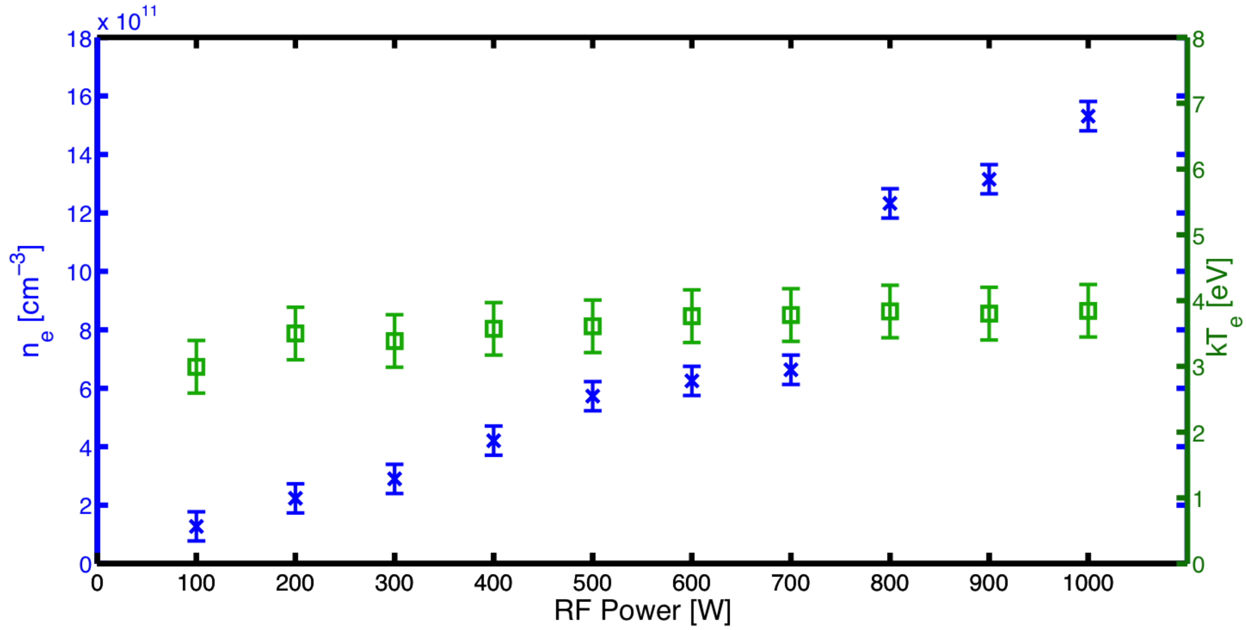

FIGURE 6.12: Electron (and ion) density (blue $\times$s, left) and electron temperature (green open squares, right) measured with the double probe for B = 340 G, Q = 20 sccm, and z = 50 cm as a function of RF forward power.

The primary indicator that this transition is the H-W transition is the appearance of a bright, blue core in the center of the discharge just downstream of the antenna, characteristic of helicon wave coupling. Previous work in our group has shown in the presence of the blue core in this device, measurements of the RF magnetic fields are consistent with the helicon mode, therefore the blue core can be used as a basic indicator of the presence of the helicon mode [28]. For the purposes of this work, it is important to note that the helicon mode cannot be obtained for the same parameters that give large potential gradients.

Again the two-grid RPA was used to measure the potential drop between the source and expansion chambers for the H-W transition, shown in Fig. 6.13. Overall, the potential drops are much lower than for the E-H transition. A potential drop $\Delta V = 5 \pm 1$ V, which is fairly insensitive to RF power, is observed from 100 W to 700 W, and a jump to a potential drop $\Delta V = 8 \pm 1$ V is observed past 800 W in the helicon mode. The collector current at zero discriminator voltage is also shown, and a sharp rise is observed across the H-W transition point, indicative of a density jump.

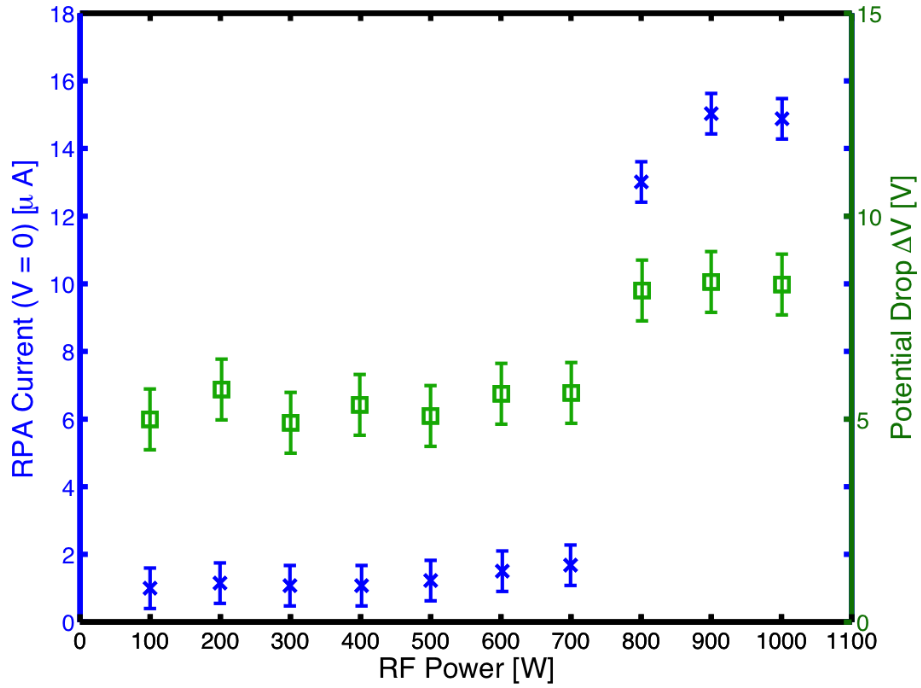

FIGURE 6.13: Collector current at V_D = 0 (left, blue $\times$s) and potential drop ΔV (right, green open squares) vs. RF power across the H-W transition for Q = 20 sccm, B = 340 G. The potential drop ΔV is calculated from the upstream (z = 50 cm) and downstream (z = 90 cm) plasma potentials and the collector current is measured at z = 70 cm.

6.4 Scaling of Potential Gradient

The parametric scaling of the potential difference between the source and expansion chambers is investigated, including variation with flow rate, RF power and magnetic field strength.

Flow Rate

Figure 6.14 shows the potential drop magnitude (difference between upstream plasma potential at z = 50 cm and the expansion chamber plasma potential at z = 80 cm) as a function of argon flow rate at P = 100 W and B = 340 G. As flow rate is decreased, an increase in the potential drop is observed from ΔV = 35 V at 4 sccm to over ΔV = 110 V at 1.3 sccm. Below 1.3 sccm, the source operation changes abruptly and no significant plasma extension is observed into the expansion chamber and there is no signal observed on the two-grid RPA at z = 50 cm. As the flow rate is decreased further, a diffuse discharge is observed under the antenna until the source becomes unstable [60] and steady state operation is not possible, with oscillations in visible light likely due to neutral starvation and replenishing as seen by Degeling [101] and previously on this source by Wiebold [74].

The source is operating in the capacitive mode below a flow rate of Q = 2.5 sccm, and the inductive mode beyond that flow rate. There is a slight change in the inflection of the curve at this flow rate threshold as evidence of the transition. The potential difference does not abruptly change at this point due to the decreasing self-bias voltage at the transition (see Section 6.5.1 below and Chapter 7). The density is increasing with increasing flow rate, further reducing the RF fields in the bulk plasma. At the transition, the density is such that the electrostatic RF fields are significantly screened and the self-bias effect is reduced and gradually decreases with decreasing modulation of the plasma potential. A potential difference between the upstream and downstream regions still exists due to the ambipolar expansion of the plasma.

After operating the source for several months, it was noted that the lowest flow rate that gave stable operation significant plasma extension into the expansion chamber (and a detectable accelerated population in the expansion chamber) increased. For example, observation of an accelerated population at flow rates down to Q = 1.3 sccm was possible after initially installing the expansion chamber, but several months later, operation was only possible down to Q = 1.9 sccm. This is believed to be a result of an impurity coating or sputtering onto the stainless steel expansion chamber walls, resulting in a reduced “quality” of the grounded boundary condition there. This will be further discussed in Chapter 7 in the context of the self-biasing effect.

Magnetic Field Strength

Figure 6.15 shows the behavior of the potential drop as a function of the source region magnetic field, for a flow rate Q = 2 sccm and P = 100 W. The potential drop has been calculated from individual z scans with the two-grid RPA using the upstream (z = 50 cm) ion potential and the downstream (z = 90 cm) ion potential, and is therefore not dependent on z. The potential drop monotonically decreases with increasing magnetic field, from ΔV = 65 $\pm$ 3 V at 340 G to

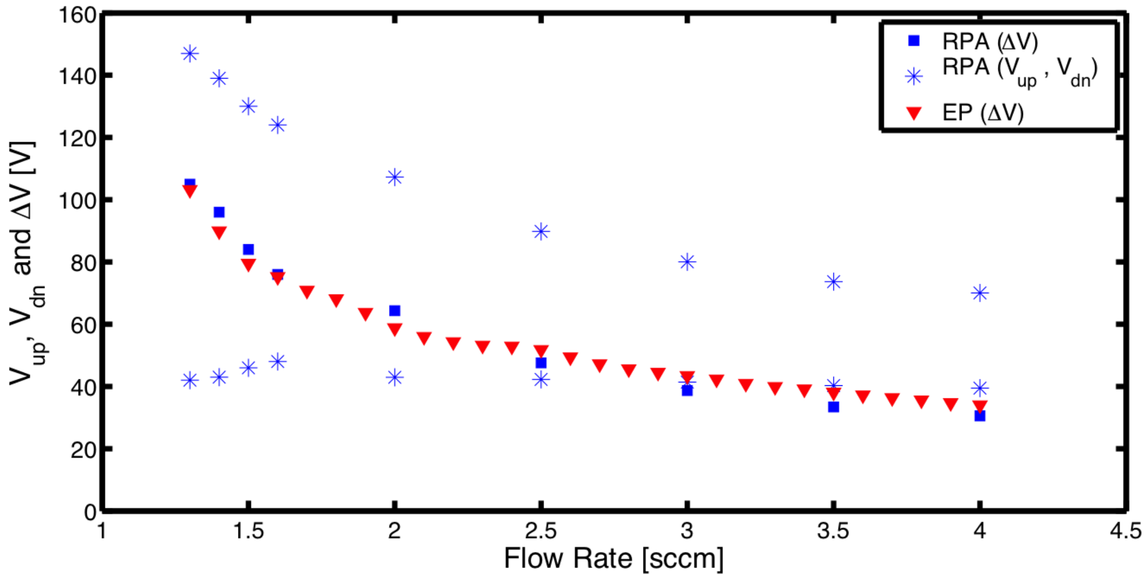

FIGURE 6.14: Potential drop (ΔV) and up- and downstream potentials (V_{up}, V_{dn}) vs. flow rate for 100 W RF power and 340 G magnetic field. The stars represent the higher, upstream (z = 50 cm) and lower, downstream (z = 80 cm) potentials measured with the two-grid RPA. The potential drop is calculated using the difference between the upstream and downstream ion potentials as measured by both the small (two-grid) RPA (squares) and emissive probe (triangles). Error bars are not shown here for clarity, but are on the order of $\pm$ 2 V.

ΔV = 27 $\pm$ 3 V at 1000 G. Also shown in Fig. 6.15 is the z extent of the potential gradient, which decreases in length and moves further into the expansion chamber with increasing magnetic field. The E-H mode transition occurs near B $\approx$ 600 G.

RF Power

The energy of the accelerated ion population was also measured as a function of the RF coupled power. For each power level, the reflected power measured with the directional coupler was minimized (< 5%). Figure 6.16 shows the difference in potential between the background and accelerated ion populations, (E_i = e[V_{accel} - V_{back}]) at z = 64 cm as a function of RF input power for a flow rate of 1.3 sccm and magnetic field of 340 G in the source region, measured with the four-grid RPA. The energy of the accelerated population increases from 110 $\pm$ 4 eV at 1.3 sccm, in agreement with the two-grid RPA data shown in Fig. 6.14, to 165 $\pm$ 5 eV at P = 500 W.

It is interesting to note that the source is operating in the capacitive (E) mode for the data

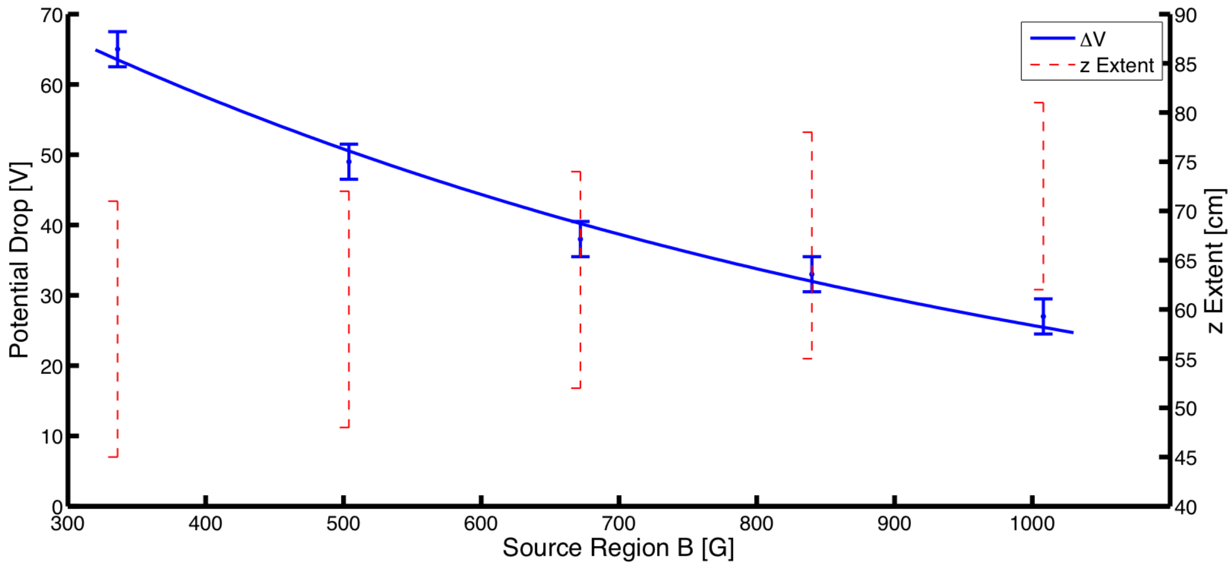

FIGURE 6.15: Potential drop (ΔV) vs. source region magnetic field value (field profile does not change) for flow rate Q = 2 sccm, RF power P = 100 W. Also shown is the z extent (cm) of the potential drop structure taken from individual axial scans of the ion distribution with the two-grid RPA.

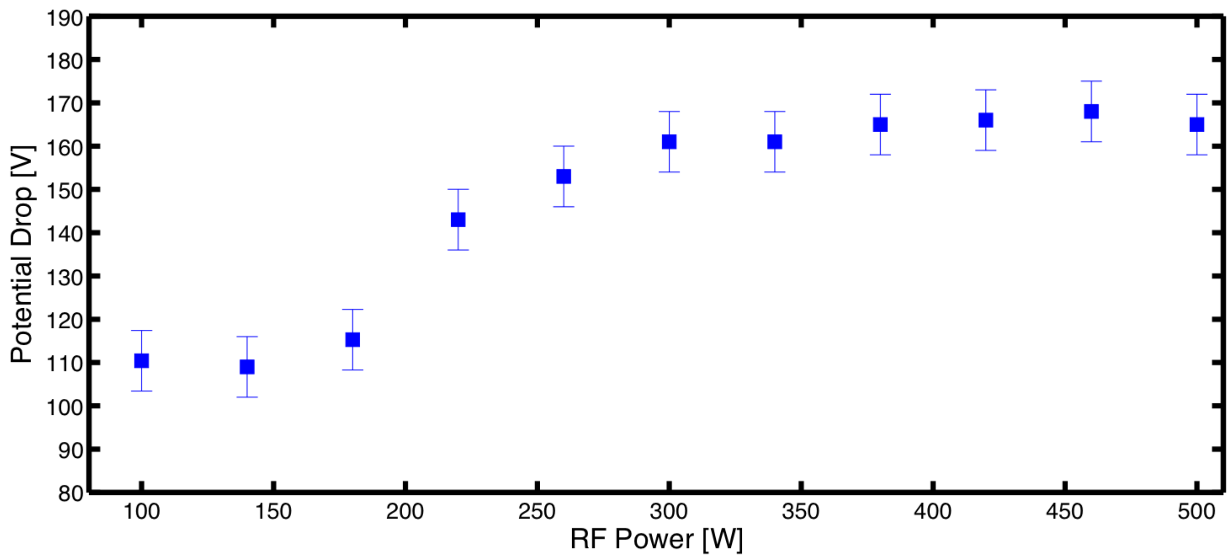

FIGURE 6.16: Difference between accelerated ion potential and local plasma potential as measured with the four-grid RPA vs. RF power for Q = 1.3 sccm, B = 340 G and z = 64 cm.

shown in Fig. 6.16, since the flow rate is low enough to keep the source in the capacitive mode up to P = 500 W. Above 500 W, the source transitions to the inductive (H) mode and the accelerated population energy drops, which is not shown in Fig. 6.16.

6.5 RF Plasma Potential Fluctuations

The high potential differences from the source to expansion chamber measured in the capacitive mode (up to 165 V) led to a further investigation of the capacitive mode to determine their cause. It was found that in the capacitive mode, there are significant fluctuations of the plasma potential resulting from the significant capacitive coupling of the antenna and the plasma's inability to shield out the antenna's fields. As will be shown below, the potential gradients are too large to be explained by ambipolar plasma expansion or static double layer formation (see Chapter 3).

6.5.1 Capacitive (E) Mode

As detailed in Chapter 5, the first derivative of the I-V trace from an emissive probe can be used to measure the plasma potential quite accurately (the inflection point method in the limit of zero emission). In the presence of RF fluctuations of the plasma potential, two or more peaks appear in the first derivative of the I-V trace. Figure 6.17 shows the first derivative of the collected current with respect to the bias voltage as a function of the bias voltage as the filament (heating) current is increased for Q = 2 sccm, P = 100W, B = 340 G and z = 80 cm (the same conditions as in Fig. 6.2), in the grounded expansion chamber. Two distinct peaks appear as the filament current is increased, which is evidence of RF fluctuations of the plasma potential. Here, the potential fluctuations are nearly symmetric about the center-point of the two peaks, but this is not always the case. The first derivative gives a measure of the relative amount of time the plasma potential spends at each voltage, and the weighted mean of the fluctuations (see Chapter 5) gives the time-averaged plasma potential. Although not directly measured with the emissive probe, time-resolved measurements of the floating potential of a cold probe show potential fluctuations at the fundamental and higher harmonics of the RF frequency, leading us to believe the observed fluctuations in Fig. 6.17 are of similar harmonic content (the RF frequency and its harmonics). Time-resolving the fluctuations accurately requires a probe and electronics with adequate frequency response like that required for accurately measuring the EEDF in a plasma with plasma potential fluctuations (RF compensation). A measurement of the separation in inflection points, such as that shown in

Fig. 6.17, is sufficient as a measure of the level of RF potential fluctuations.

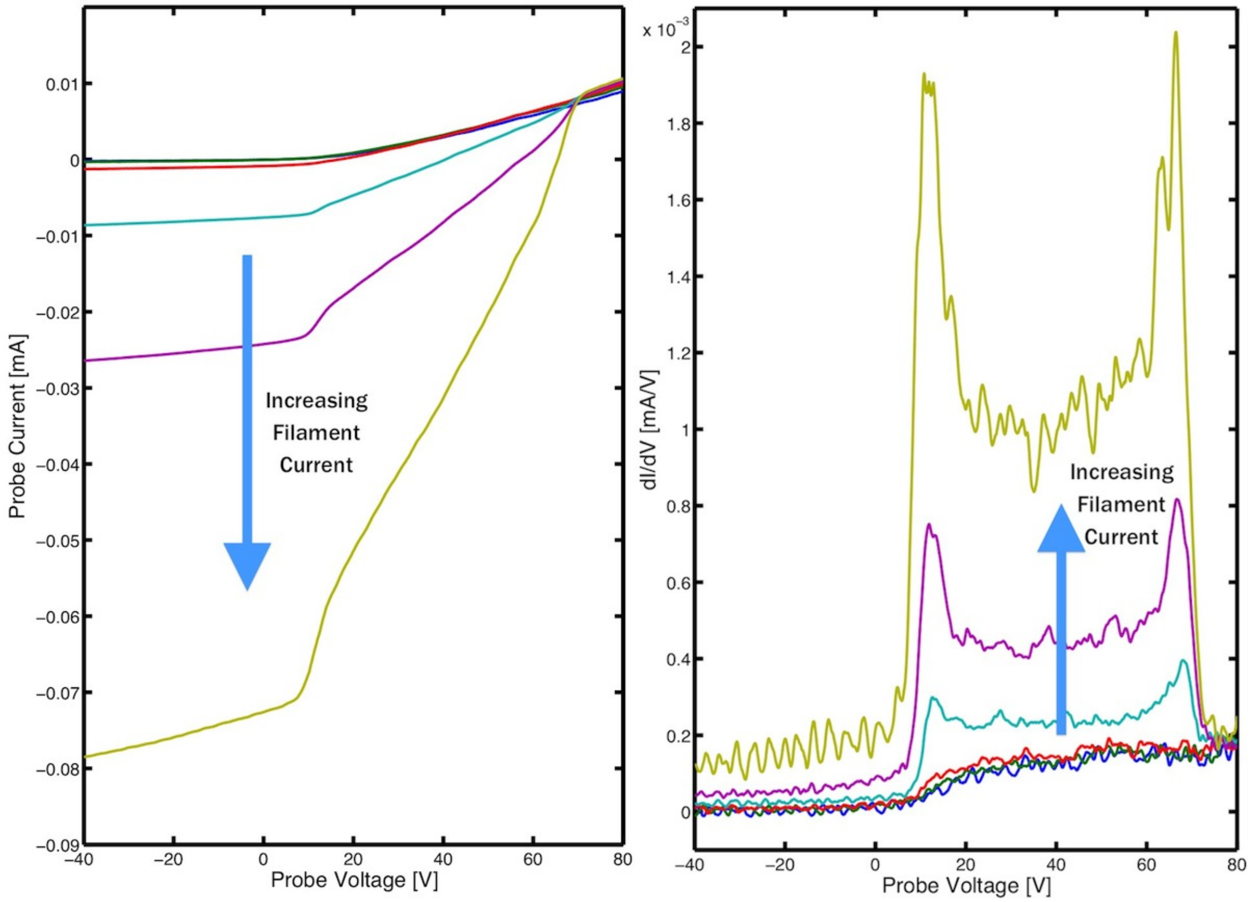

FIGURE 6.17: First derivative of collected current with respect to the bias voltage from emissive probe as filament (heating) current is increased for Q = 2 sccm, P = 100 W, B = 340 G and z = 80 cm.

At a closer z position to the antenna, the fluctuations become asymmetric and increase in magnitude considerably. Figure 6.18 shows the raw I-V trace and first derivative for the emissive probe when strongly emitting for z = 50 cm, Q = 2 sccm, P = 100 W and B = 340 G. Also shown are the weighed mean of the fluctuations (brown dashed arrow) and the ion potential measured with the two-grid RPA (red dashed arrow), which agree within experimental uncertainty. The black arrows denote the extent of the potential fluctuations as determined from the first derivative. The fact that the ion potential and the weighted mean of the plasma potential fluctuations are nearly the same potential is a result of the ions' inability to respond to the high-frequency fluctuations. The ion plasma frequency ω_{pi} is equal to the RF frequency (13.56 MHz) when the ion density

$n_i \approx 1.67 \times 10^{11}$ cm^{-3}. As shown in Fig. 6.9, the ion density for the conditions in Fig. 6.18 is $n_i \approx 8.8 \times 10^{9}$ cm^{-3}, such that the condition $\omega_{pi}^2 \ll \omega_{RF}^2$ holds and the ions are not able to fully respond to the fluctuations.

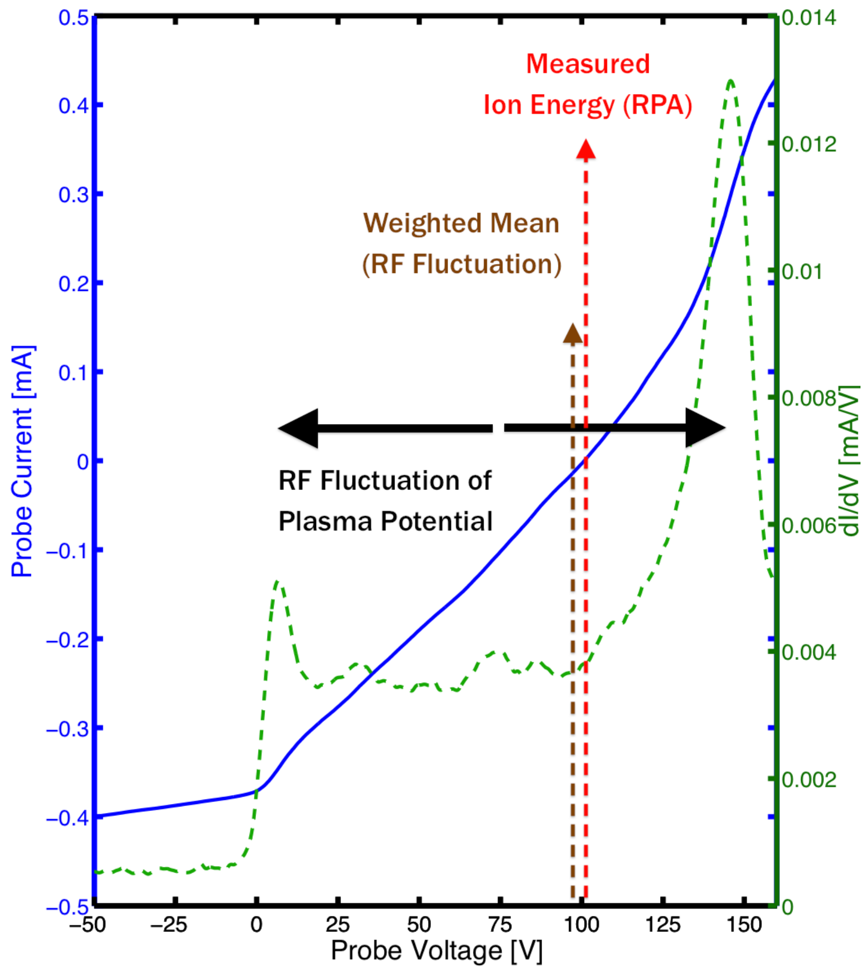

FIGURE 6.18: Emissive probe I-V trace (blue, solid line) and first derivative (dashed, green line) at z = 50 cm for P = 100 W, Q = 2 sccm and B = 340 G. The brown dashed arrow indicates the weighted mean of the potential fluctuations, and the red dashed arrow denotes the ion potential measured with the two-grid RPA. The black arrows indicate the extent of the RF fluctuations.

The full z dependence of the fluctuation limits as well as the weighted mean of the RF plasma potential fluctuations are shown in Fig. 6.19. The blue and red lines show the limits of the fluctuations and the weighted mean, respectively. Also shown (black $\times$s) is the potential of the background population of ions measured with the two-grid RPA. As in Fig. 6.18, the time-averaged plasma potential is the same as the bulk ion potential measured with the RPA. It is interesting to note that there must be a part of the RF cycle when the instantaneous plasma potential gradient is much smaller than the time-averaged plasma potential gradient. The electrons, which are able to fully respond to the instantaneous plasma potential profile, can easily transit the "acceleration region" between the upstream and downstream regions in an RF cycle. The ions, however, cannot respond as quickly and feel the effects of the *time averaged* plasma potential gradient. The differing response of the electrons and ions is the basis of the self-bias effect, as will be discussed in Chapter 7.

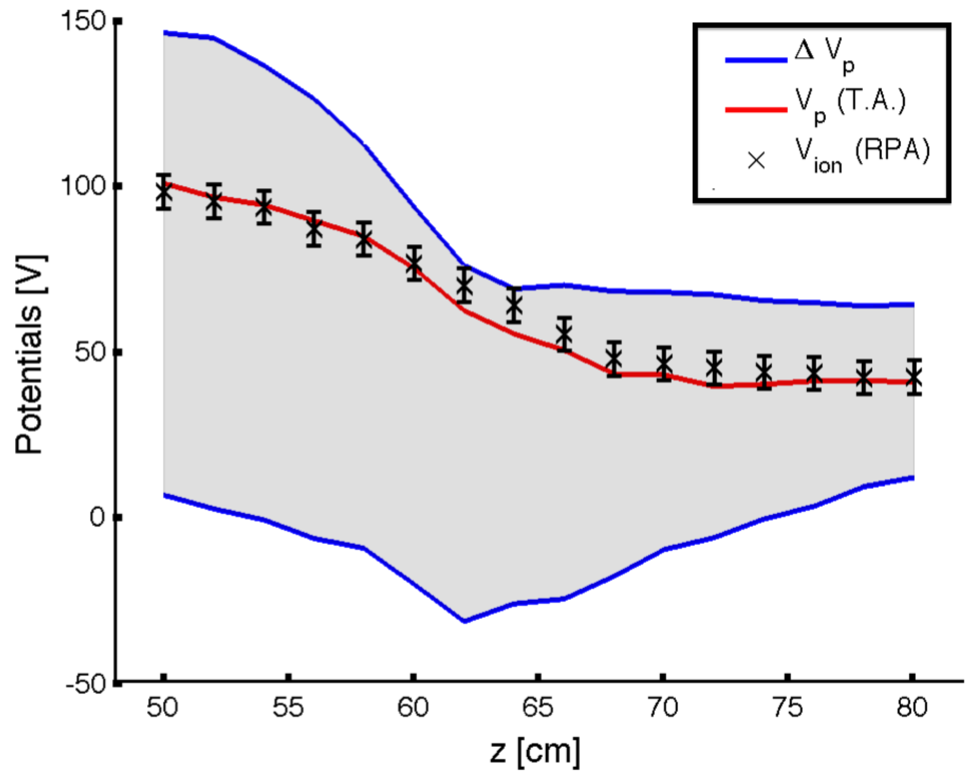

FIGURE 6.19: Upper and lower limits (blue lines) and weighted mean (red line) of RF plasma potential fluctuations as measured with the emissive probe for Q = 2 sccm, P = 100 W and B = 340 G. Also shown is the bulk ion potential measured with the two-grid RPA (black $\times$s).

6.5.2 Inductive (H) and Helicon (W) Modes

In the inductive mode, the amplitude of the RF plasma potential fluctuations is decreased compared to the capacitive mode. For Q = 2 sccm, P = 300 W, B = 340 G and z = 80 cm (H mode), the RF plasma potential fluctuation amplitude is approximately $\pm$ 12 V, whereas for the capacitive (E) mode the fluctuation amplitude is approximately $\pm$ 30 V.

A direct measurement of the fluctuation amplitude with the emissive probe was not possible in the W mode, due to increased heating of the filament from the collected current at higher plasma densities. As the probe is swept, the filament emission (and visible light output) varies with the sweep voltage as the probe draws more electron current at higher bias voltages, resulting in additional filament heating and distortion of the I-V trace. A probe heating scheme with a feedback loop is necessary to control the filament heating during the sweep.

While not a direct measurement of the fluctuations, the difference between the Langmuir-probe-measured plasma potential and the two-grid RPA-measured ion potential offers an indication that the fluctuations are greatly reduced in the W mode. The Langmuir probe is strongly affected by fluctuations in the plasma potential (see Section 5.3), and the potential at which the electron current deviates from an exponential (roughly the plasma potential in the absence of plasma potential fluctuations) becomes more negative than the time-averaged plasma potential, assuming a value close to the lower end of the fluctuation extent. In the W mode, the plasma potential as measured with the Langmuir probe is V_p = 26 $\pm$ 2 V (shown in Fig. 6.20), and the ion potential measured with the two-grid RPA is V_p = 31 $\pm$ 2 V. Since the ion potential (the time-averaged plasma potential) is within a few volts of the Langmuir-probe measured plasma potential (the lower end of the fluctuations), it can be inferred that the fluctuation magnitude is only a few volts, much lower than in the H and especially the E mode.

A second way to measure the RF fluctuations of the plasma potential in the helicon mode is to examine the RPA-measured IEDFs. Since the density in the W mode is larger than 1.6 $\times$ 10^{11} cm^{-3} (the frequency for which the ion plasma frequency ω_{pi} is equal to the RF frequency ω_{RF}), the plasma ions are able to better respond to fluctuations in the plasma potential. The IEDF becomes double-peaked as the ions follow the fluctuations in the plasma potential, which are much lower in magnitude ($\Delta V \approx \pm$ 1.7 V) than in the E or H modes. Figure 6.21 shows the IEDF for Q = 20 sccm, P = 800 W and B = 340 G at z = 50 cm. The IEDF is double peaked due to RF fluctuations in the plasma potential, not due to the presence of an accelerated population.

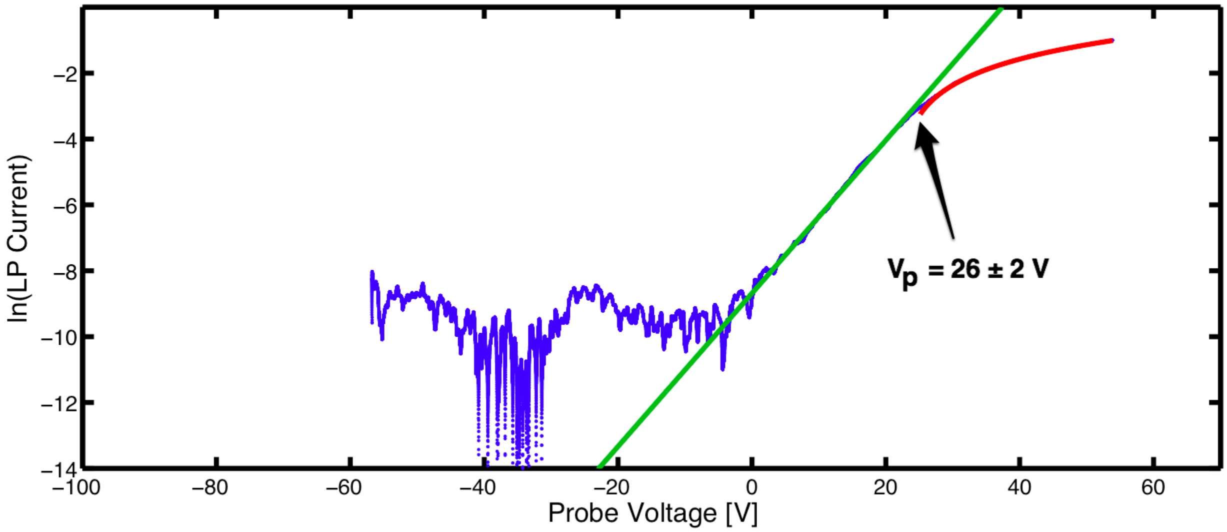

FIGURE 6.20: Langmuir probe I-V trace for Q = 20 sccm, P = 100 W, B = 340 G at z = 80 cm, plotted on a logarithmic scale with the ion saturation current subtracted. The green solid line shows an exponential (Maxwellian) fit to the bulk electrons and the red solid line shows a linear fit to the electron saturation region.

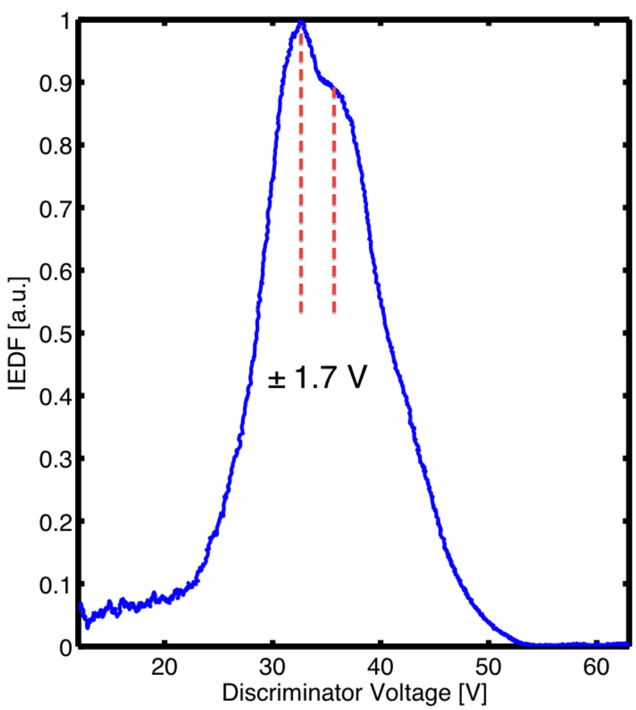

FIGURE 6.21: Broadened IEDF for W mode, measured with Q = 20 sccm, P = 800 W, B = 340 G at z = 50 cm. The double-peaked distribution is a consequence of RF fluctuations of the plasma potential, not due to the formation of an accelerated population.

6.6 Upstream Boundary Condition

In order to ensure current-free flow of the plasma from the source tube into the expansion chamber, as would be required for spacecraft to avoid charging, any return paths for current to the upstream end of the source must be removed. To that end, the upstream endplate, which is grounded in the experiments outlined above, was insulated from ground using 1/8" PTFE sheets to verify that a potential gradient still occurred. Figure 6.22 shows the magnitude of the potential difference ΔV from z = 50 cm to z = 80 cm versus flow rate for both the grounded and floating (insulated) upstream endplate. There is an overall decrease in the magnitude of the potential difference when the upstream endplate is floated, a consequence of the reduced electron loss area for the source region in steady state. Most importantly, there is still a significant potential drop when the upstream endplate is floated.

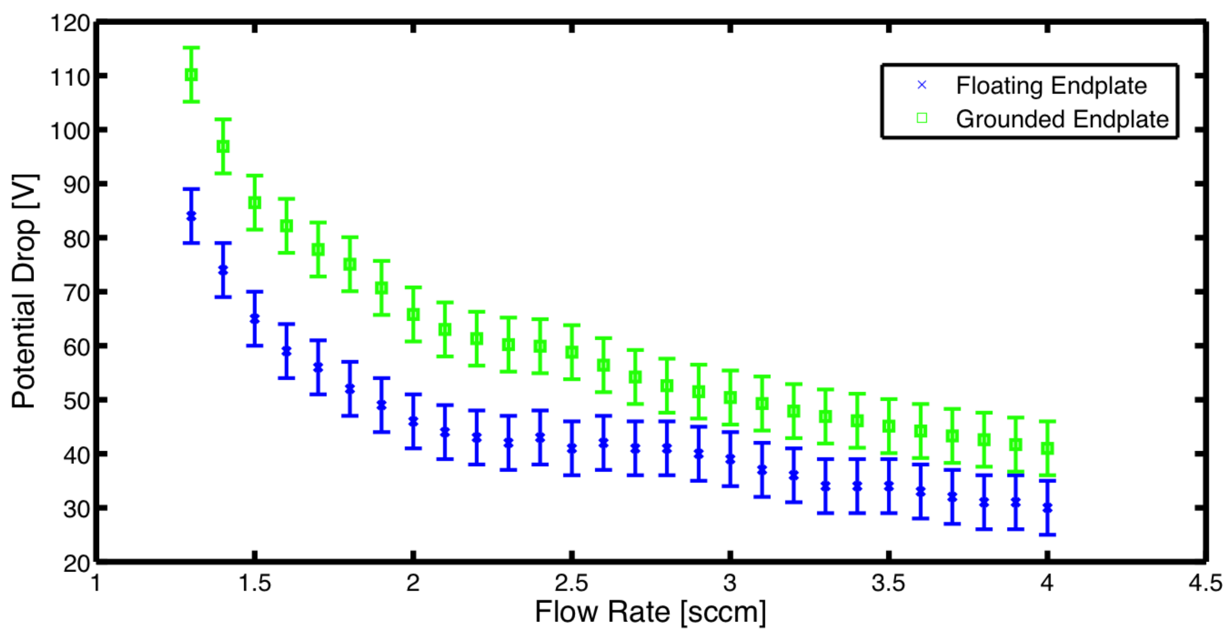

FIGURE 6.22: Potential drop vs. argon flow rate for a grounded (green squares) and floating (blue $\times$s) for P = 100 W, B = 340 G. The potential drop is calculated from the difference between the two-grid RPA-measured ion potentials at z = 50 cm and z = 80 cm.

In addition to floating the upstream endplate, the DC current to the endplate when grounded was measured with a simple DMM. A net DC current flow into the plate from ground (or net electron current out of the plasma to ground) was measured for Q = 2 sccm, P = 100 W and B = 340 G, showing that the grounded upstream endplate does cause a net current flow through the source. This will be further discussed in Chapter 7.

6.7 Georgia Institute of Technology

The accelerated ion population shown in Fig. 6.2 persists for roughly the axial extent of the potential gradient itself. The ions are being accelerated through the potential gradient, but no significant accelerated population persists far beyond the potential gradient as the ions in the accelerated population are charge-exchanging with the neutral argon population in the expansion region. However, a mock-up of our experiment, installed in a large space chamber at Georgia Tech (see Section 4.4), has shown a significant population of ions up to 1 meter from the end of the source chamber. Fig. 6.23 shows the ion energy distribution function, shifted such that E_i = 0 eV corresponds to the local plasma potential. A broad distribution of ions is visible at E_i = 135 eV. The decay of the beam population due to charge exchange will be discussed further in Chapter 7.

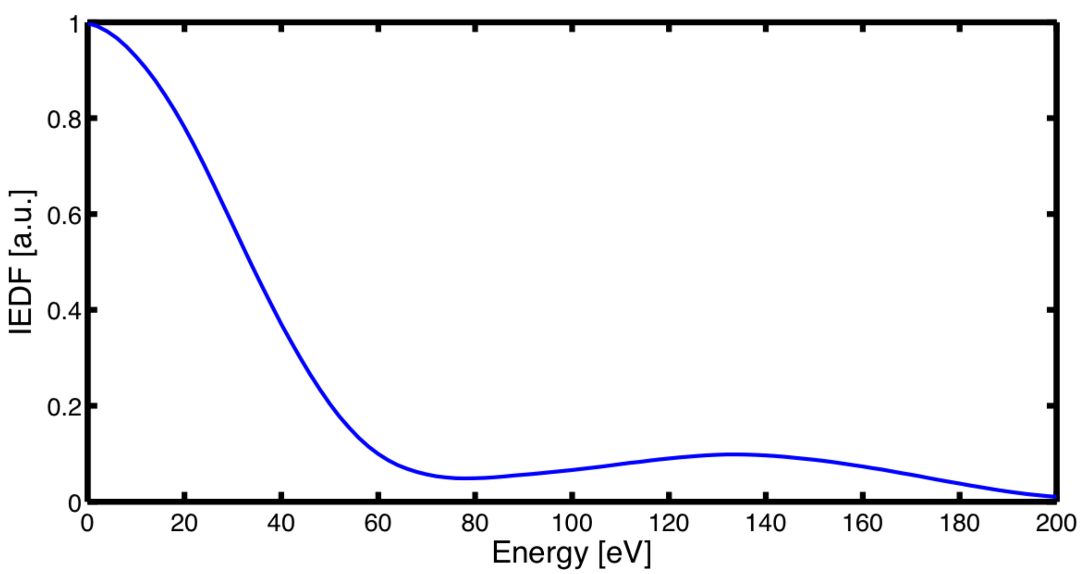

FIGURE 6.23: Ion energy distribution function measured with a four-grid RPA in the UW helicon mock-up at Georgia Tech, for Q = 1.3 sccm, P = 500 W and B = 100 G at a z position 1 meter from the end of the source tube. The IEDF is normalized and shifted such that E_i = 0 corresponds to the local plasma potential.

Summary

Large potential differences are observed in the expansion region (between the source and expansion chambers) of the MadHeX system. The potential drops, up to ΔV = 165 V for a flow rate Q = 1.3 sccm, RF power P = 500 W and magnetic field B = 340 G, lead to an accelerated ion population that decays via charge-exchange collisions into the expansion chamber. Two distinct mode hops are observed, the capacitive to inductive (E-H) and inductive to helicon (H-W) mode transitions. The potential gradients are the largest in the capacitive mode, and significant plasma potential fluctuations at the RF frequency are also measured in the capacitive mode. In the inductive mode, both the potential gradients and fluctuation amplitude of the plasma potential are lower. The scaling of the potential drop magnitude in the capacitive mode with the argon flow rate, magnetic field and RF power has been quantified. The initial observation of the accelerated population of ions as well as the scaling study has been published in our recent paper [102].

Chapter 7

Discussion

As shown in Chapter 6, potential differences exceeding 100 V are observed between the source chamber to the expansion chamber over several hundred to a few thousand Debye lengths for certain experimental conditions. It is important to distinguish the physical mechanism for the formation of these substantial potential gradients. As will be shown below, the potential differences observed in the capacitive mode cannot be understood solely in terms of ambipolar plasma expansion or static double layer formation, discussed in Chapter 3. Instead, a self-biasing of the upstream plasma in the insulating chamber occurs relative to the downstream plasma in the grounded expansion chamber as a result of the reduction in confinement of plasma electrons upstream for all times during an RF cycle brought upon by significant, rapid fluctuations in the plasma potential. The upstream, time-averaged plasma potential increases to equalize the global time-averaged electron and ion fluxes.

Figure 7.1 is a system diagram including the labeled regions that will be used throughout the discussion of the research results. The upstream and downstream regions are delineated and the the region of the observed potential drops are shown.

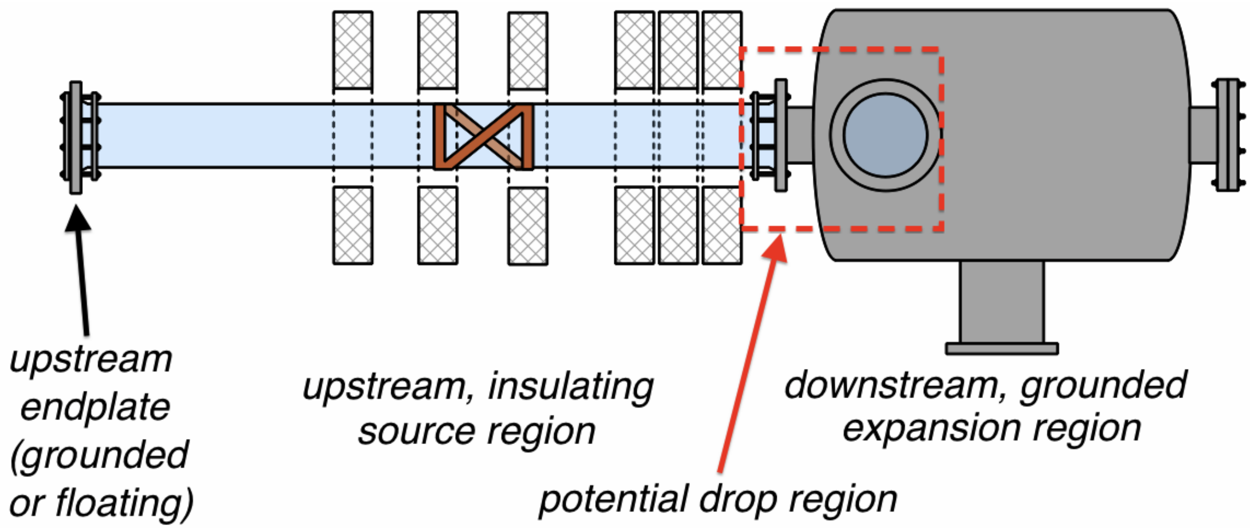

FIGURE 7.1: System diagram for reference during discussion of results. The upstream and downstream regions are shown, as well as the region of the observed potential drops (red dashed box). The upstream endplate is also noted, which can be floated or grounded.

7.1 Ambipolar Plasma Expansion

Ambipolar (Boltzmann) plasma expansion is characterized by the balance between the gradient in the electron pressure ($p_e = n_e k T_e$) and an ambipolar electric field that forms. The ambipolar field retards electrons and accelerates ions to maintain neutrality [23]. It is important to note that the electrons and ions both remain at the (DC) plasma potential, determined by the Boltzmann relation:

$$n_e(z) = n_{e0} \exp\left[\frac{e(V_p(z) - V_{p0})}{kT_e}\right] \tag{7.1}$$

where $V_p(z)$ is the local potential, V_{p0} is the initial potential, $n_e(z)$ is the electron density profile, n_{e0} is the initial electron density and T_e is the electron temperature under the assumption of a Maxwellian distribution. Equation 7.1 can be solved for the potential profile as a function of the electron density $n_e(z)$:

$$V(z) = V_0 + \frac{kT_e}{e} \ln\left[\frac{n_e(z)}{n_{e0}}\right] \tag{7.2}$$

If the electron density $n_e(z)/n_{e0}$ is plotted versus the potential $V_p(z) - V_{p0}$, the electron temperature can be determined from a fit to the resulting curve. MATLAB's `cftool` was used to perform a least-squares fit on the time-averaged plasma potential and ion density (assumed equal to the electron density) data to Eq. 7.1, and the result is plotted on a semi-log scale. For a given set of experimental conditions, if the calculated (Maxwellian) electron temperature from the fit matches the measured electron temperature, it is assumed that the expansion is following the Boltzmann relation.

It should be noted that the method used to measure the electron temperature with the single and double probes can be affected by fluctuations in the plasma potential. In the presence of significant fluctuations (in the capacitive mode, for example), a straight-line fit was applied to the tail region of the measured electron current (total collected current with ion saturation current subtracted with a linear fit) that is "outside" of the extent of the fluctuations in an effort to avoid the effects of the fluctuations. Since the probe is unable to fully respond to the fluctuations at the RF frequency, the time-averaged collected current is measured instead of the instantaneous collected current, which will result in a poor estimate of the electron temperature. However, this method does not measure the full EEDF and only offers an estimate of the true electron temperature (and distribution), which may be changing on an RF timescale and may not be Maxwellian. In order to more accurately measure the EEDF, a non-invasive method such as optical emission spectroscopy (OES) or a fully compensated probe must be constructed. However, the large magnitude of the fluctuations makes the use of a compensated probe impractical. These issues should be kept in mind when interpreting the results below. Chapter 8 details the use of OES for EEDF measurement.

7.1.1 Capacitive (E) Mode

For the data shown in Figs. 6.2 and 6.4, taken with Q = 2 sccm, P = 100 W and B = 340 G, the source is operating in the capacitive mode as shown in Section 6.3.1. The ion density $n_i(z) = n_e(z)$ from the single probe is plotted versus the bulk ion potential $V(z)$ obtained from the two-grid RPA and shown in Fig. 7.2. The right-hand side of the plot corresponds to z = 50 cm (the highest density and potential) and the left-hand side corresponds to z = 80 cm. It was shown previously in Chapter 6 that the RPA-measured bulk ion potential and the emissive probe measured time-averaged plasma potential are quite close (Fig. 6.19), therefore either result can be used in this calculation. In addition, the ion density is assumed to be equal to the electron density, as is assumed in ambipolar expansion. Also shown in Fig. 7.2 is the fit to Eq. 7.1 (black dashed line). Since the data is plotted in a logarithmic scale, the data points at lower densities (the left-hand side of the plot) appear to not fit the equation as well as at higher densities, but the fit is performed on a linear scale to avoid weighting points unequally as would occur if the data were fit to a straight line with a least-squares fit on a logarithmic scale.

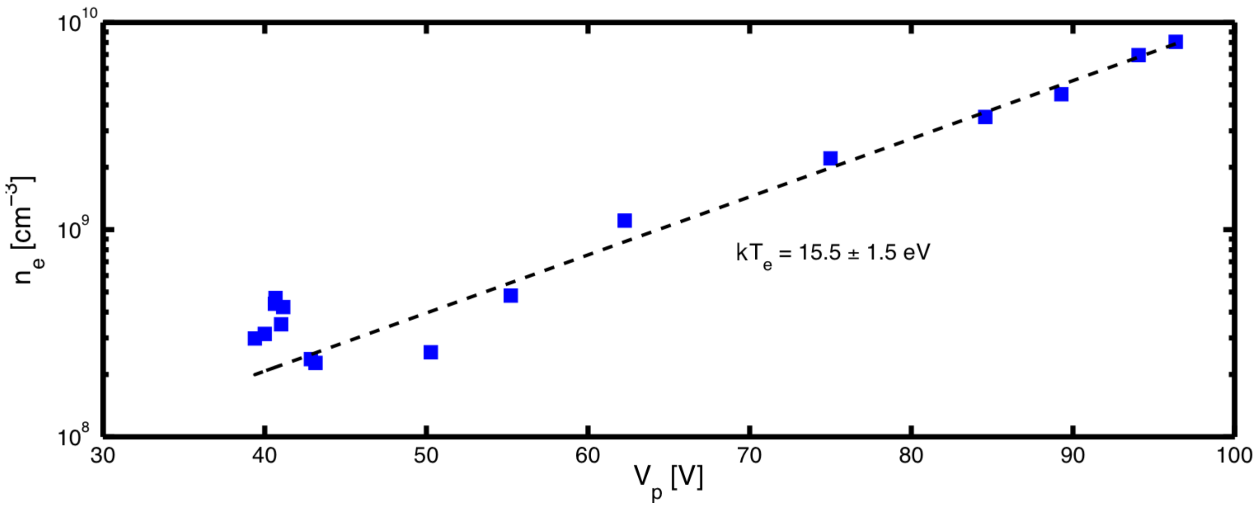

FIGURE 7.2: Electron density (single probe) plotted versus the bulk ion potential from the two-grid RPA for Q = 2 sccm, P = 100 W and B = 340 G. A least-squares fit to Eq. 7.1, calculated on a linear scale, is also shown (black dashed line) as well as the resulting electron temperature from the fit.

The calculated electron temperature kT_e = 15.5 $\pm$ 1.5 eV is substantially higher than that measured with the single probe (shown in Fig. 6.4) of kT_e = 9.0 $\pm$ 1.1 eV at z = 50 cm, therefore the expansion for this case is likely not following a Boltzmann relation. Of course, the significant plasma potential fluctuations measured in the capacitive mode (shown in Fig. 6.19) are proof that the electrons and ions will respond differently, so it is not expected that an ambipolar expansion applies. The electrons, which can follow the rapid fluctuations in the plasma potential, obey a Boltzmann relation relation in response to the time-dependent plasma potential profile, but the time-dependent electron density is difficult to measure experimentally. The ions, which respond only to the time-averaged plasma potential, do not follow a Boltzmann relation.

Since the density profile has been measured, the model given in Section 3.2, which assumes a density profile based on the magnetic field profile, is not necessary for calculating the potential profile and the resulting required electron temperature for Boltzmann expansion. However, the model should produce the same result using the measured magnetic field profile. For an area expansion ratio of roughly $B_1/B_2 = A_2/A_1 \approx 10$ for z = 48 cm to z = 70 cm (the potential gradient region in Fig. 6.2, see Fig. 4.4), the predicted potential drop is $e\Delta V/kT_e \approx 3.3$. For the measured temperature of $kT_e = 9 \pm 1$ eV for these conditions, the model-predicted potential drop is $\Delta V = 29.7 \pm 3.3$ V, much lower than the observed $\Delta V \approx 65$ V. Looking at it in a different way, for the measured potential drop of $\Delta V \approx 65$ V, the required electron temperature $kT_e \approx 19.7$ eV, much higher than the measured $kT_e = 9 \pm 1$ eV. The magnetic field ratio used in the above calculation is approximate and varies depending on which z locations are chosen as the "upstream" and "downstream" points, leading to the difference between the electron temperature calculated in Fig. 7.2 and the above calculation. In addition, the density profile has been measured, not assumed.

While the electron density was not directly measured with the single or double probe for a lower flow rate Q = 1.3 sccm with P = 100 W and B = 340 G, the two-grid RPA collector current at V_D = 0 can be used as an indicator of the total ion density. Charles [78] gives an expression for the density as a function of the collector current at $V_D = 0$:

$$n_i = \frac{I(V_D = 0)}{T^2 A q \langle v \rangle} \tag{7.3}$$

where $I(V_D = 0)$ is the collector current at $V_D = 0$, T is the grid transmission factor (for two grids), A is the RPA area, q is the ion charge and $\langle v \rangle$ is the average velocity of the ions entering the RPA, calculated using:

$$\langle v \rangle = \frac{\int_0^\infty v f(v) \mathrm{d}v}{\int_0^\infty f(v) \mathrm{d}v} \tag{7.4}$$

Since T, A and q do not change, plotting $I(V_D = 0)/\langle v \rangle$ is indicative of the ion density. The average ion velocity $\langle v \rangle$ is calculated experimentally from the IEDF. In Fig. 7.3, $I(V_D = 0)/\langle v \rangle$ is plotted versus the bulk ion potential, also from the two-grid RPA, on a logarithmic scale. The resulting fit from Eq. 7.1 gives an electron temperature of $kT_e = 23.8 \pm 3.1$ eV, much higher than expected for these conditions. The ion density and electron temperature were not directly measured for Q = 1.3 sccm due to the increase in minimum operating pressure observed over several months (discussed previously in Section 6.4). The single and double probe diagnostic was not utilized until after the minimum operating flow rate (pressure) had increased beyond Q = 1.3 sccm (to approximately 1.8 sccm).

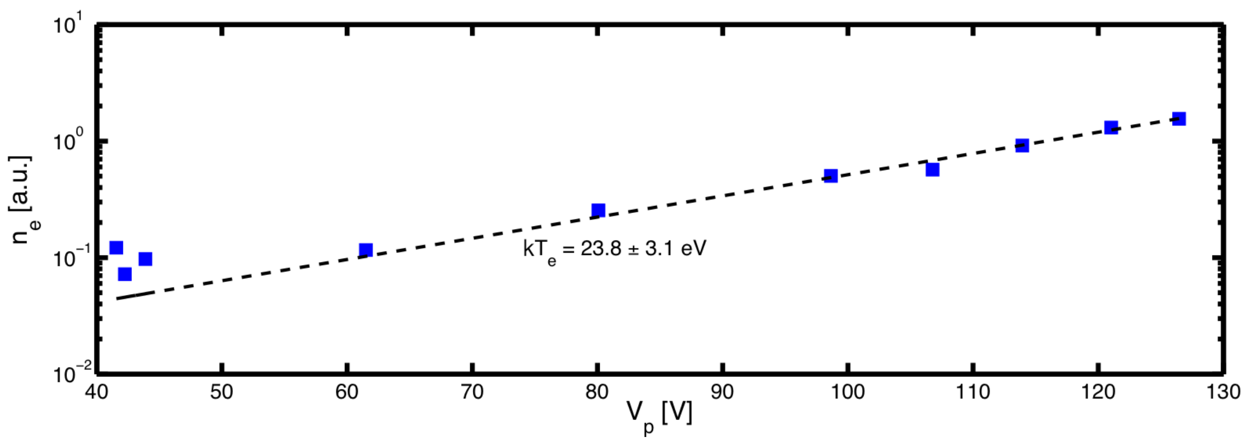

FIGURE 7.3: Electron density (single probe) plotted versus the bulk ion potential from the two-grid RPA for Q = 1.3 sccm, P = 100 W and B = 340 G. A least-squares fit to Eq. 7.1, calculated on a linear scale, is also shown (black dashed line) as well as the resulting electron temperature from the fit.

The above calculations are based on data taken with the upstream endplate of the system grounded, creating the possibility of a net current flow through the source region. If the upstream endplate is instead floated, enforcing a zero net current from the source region to the expansion chamber, a potential difference is still present and remains higher than that predicted by ambipolar expansion. For a grounded endplate, the potential drop for Q = 2 sccm, P = 100 W and B = 340 G is $\Delta V \approx 65$ V. For the floating endplate under the same conditions, the potential drop was measured to be $\Delta V \approx 46$ V. Figure 7.4 shows the electron density, measured using the two-grid RPA collector current at a discriminator voltage $V_D = 0$ versus the bulk ion potential as well as a fit calculated from Eq. 7.1. The required electron temperature to satisfy a Boltzmann relation is $kT_e = 11.7 \pm 0.8$ eV, and the temperature measured with the double probe at z = 50 cm for the same conditions is $kT_e = 7.6 \pm 0.5$ eV. Since the temperature for ambipolar expansion in this case is larger than that measured, the expansion is likely not ambipolar.

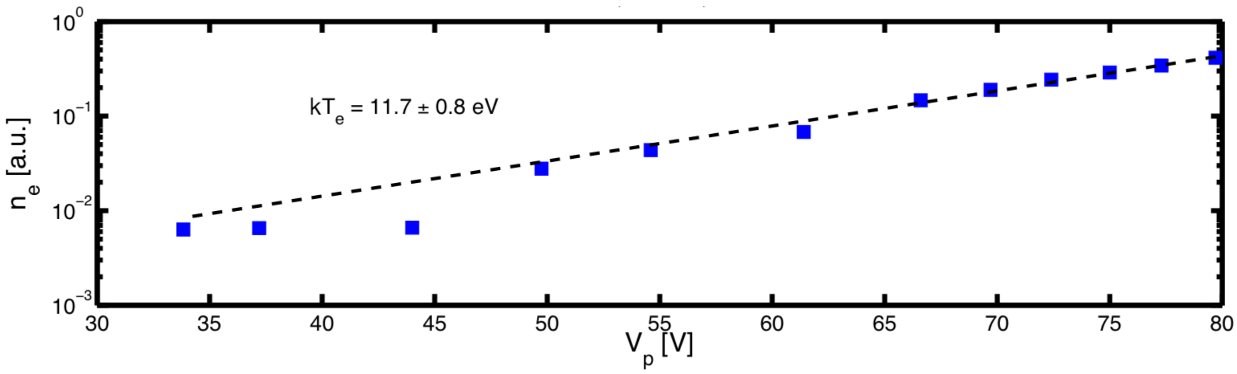

FIGURE 7.4: Electron density (single probe) plotted versus the bulk ion potential from the two-grid RPA for Q = 2 sccm, P = 100 W and B = 340 G with the upstream endplate floated. A least-squares fit to Eq. 7.1, calculated on a linear scale, is also shown (black dashed line) as well as the resulting electron temperature from the fit.

It is worthwhile to note that in the presence of an energetic tail population of electrons, the ambipolar potential will increase as the energetic electrons can more readily escape the upstream region. The effect of the energetic electrons can be quantified using a bi-Maxwellian distribution with an effective temperature T_{eff} [103]:

$$g_p(E) = \frac{2n_{e0}}{\sqrt{\pi}}\left[\frac{1-\beta}{kT_1^{3/2}}\exp(-E/kT_1) + \frac{\beta}{kT_2^{3/2}}\exp(-E/kT_2)\right] \tag{7.5}$$

where $g_p(E)$ is the EEPF, n_{e0} is the electron density and T_1 and T_2 are the temperatures of the bulk and energetic distributions, expressed in eV. The effective temperature is defined as $T_{eff} = (1-\beta)T_1 + \beta T_2$. While it was not possible to measure the time-dependent electron energy distribution (EEDF) accurately with the current set of diagnostics, there is no indication that a significant population of energetic electrons exists using the single probe. A significant fraction of energetic electrons would need to be present for the effective temperature T_{eff} to equal the predicted electron temperature for the expansion. For example, to attain an effective temperature kT_{eff} = 15.5 eV as in the expansion observed in the capacitive mode (above), a 30 % fraction (β = 0.3) of 31 eV electrons would be required, using the measured $kT_e = kT_1$ = 9 eV. This large an energetic population would likely appear on even an uncompensated single probe. Measurements of the EEDF using RF-compensated probes in discharges similar to ours have not shown the presence of energetic electrons in a helicon system where ion acceleration is observed (see [69,70,104] for example). Instead, the electron energy distribution is depleted past an energy equal to the potential drop observed. For this reason, it is not believed an energetic population is responsible for the larger-than-ambipolar potential difference, especially in light of the RF fluctuations and the self-bias effect well known in capacitive discharges (see Sections 3.1.3 and 7.3). Optical emission spectroscopy (OES) could be a valuable tool in extracting the EEDF, which will be used on this experiment in the future (see Chapter 8).

7.1.2 Inductive (H) Mode

In the inductive mode, it was observed that the potential fluctuations were reduced, a result of the increased inductive coupling of the antenna to the plasma. Some non-zero capacitive coupling to the plasma remains and potential fluctuations are still observed. The same analysis of the electron density vs. bulk ion potential was carried out for two cases in the inductive mode. In the first case, the RF power is increased from the case shown in Fig. 7.2 from 100 W to 500 W, such that the source transitions to the H mode (see Fig. 6.9) with the flow rate Q = 2 sccm and magnetic field B = 340 G kept the same. The result is shown in Fig. 7.5, including the Boltzmann fit (black dashed line). The required electron temperature to satisfy a Boltzmann expansion for this case is kT_e = 11.5 $\pm$ 2 eV, quite close to the measured value of kT_e = 11.0 $\pm$ 0.8 eV with the double probe (not shown, but see Fig. 6.9). Therefore, it is likely that Boltzmann plasma expansion is responsible for the potential difference for these conditions.

In addition, the same analysis was carried out for another set of conditions that lead to inductive operation of the source. Instead of increasing the RF power from that in Fig. 7.2, the flow rate was increased from Q = 2 sccm to Q = 4 sccm and the power kept at P = 100 W and magnetic field at B = 340 G. The result and the fit are shown in Fig. 7.6. The electron temperature required for Boltzmann expansion in the case is kT_e = 4.7 $\pm$ 0.8 eV, well within the measured electron temperature of kT_e = 4.5 $\pm$ 0.6 eV with the double probe for these conditions (not shown). For this case, it also appears the expansion obeys the Boltzmann relation.

Despite the presence of the RF fluctuations of the plasma potential ($\Delta V/V \approx 20\%$), the ex-

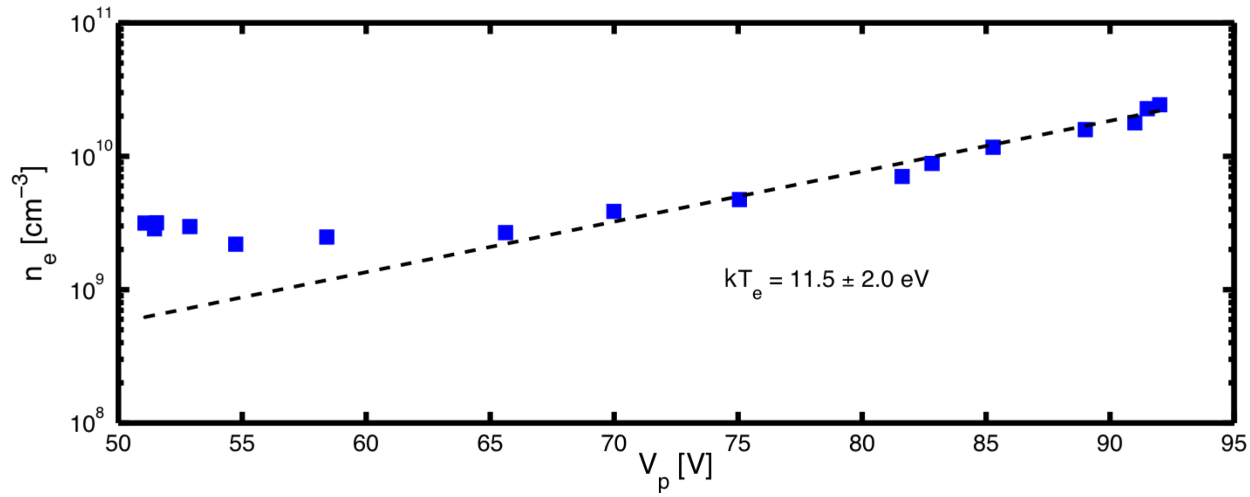

FIGURE 7.5: Electron density (single probe) plotted versus the bulk ion potential from the two-grid RPA for Q = 2 sccm, P = 500 W and B = 340 G. A least-squares fit to Eq. 7.1, calculated on a linear scale, is also shown (black dashed line) as well as the resulting electron temperature from the fit.

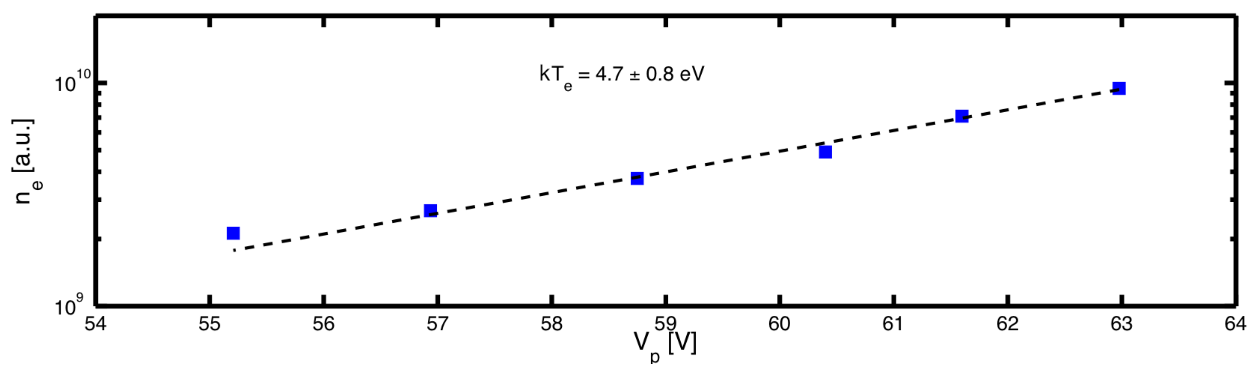

FIGURE 7.6: Electron density (single probe) plotted versus the bulk ion potential from the two-grid RPA for Q = 4 sccm, P = 100 W and B = 340 G. A least-squares fit to Eq. 7.1, calculated on a linear scale, is also shown (black dashed line) as well as the resulting electron temperature from the fit.

pansion for these two cases in the inductive mode follows the Boltzmann relation.

7.1.3 Helicon (W) Mode

In the helicon mode, the expansion also obeys the Boltzmann relation, just as for the inductive mode. The RPA was used to measure the potential drop between z = 50 cm and z = 80 cm for Q = 20 sccm, P = 800 W and B = 340 G. A decrease in the potential difference from ΔV = 35 $\pm$ 1 V to ΔV = 27 $\pm$ 1 V is observed (a difference of $\approx$ 8 V) and a density drop from n_i = 3.5 $\times$ 10^{11} cm^{-3}

to n_i = 3 $\times$ 10^{10} cm^{-3}, a factor of $\approx$ 12, using the double probe at the same axial locations. The required electron temperature for this density and potential gradient is $kT_e \approx$ 3.3 eV, close to the measured electron temperature of kT_e = 3.5 $\pm$ 0.3 eV, measured with the double probe at z = 50 cm. Therefore, the expansion in the helicon mode is likely an ambipolar expansion.

7.2 Axial Evolution

Decay of Accelerated Population

Regardless of operating mode, the accelerated ion population decays due to ion-neutral collisions, in particular charge-exchange (CX) collisions. The mean free path for these interactions is given by:

$$\lambda_{cx} = \frac{1}{n_g \sigma_{cx}} \tag{7.6}$$

where n_g [cm^{-3}] = 3.25 $\times$ $10^{13}p$ [mTorr] and σ_{cx} is the total ion collisional cross section and is a function of the incident argon ion energy. The cross section σ_{cx} varies from 8 $\times$ 10^{-15} cm^2 at low ($E_i \approx$ 4 eV) energies and decreases to 4 $\times$ 10^{-15} cm^2 at higher ($E_i >$ 300 eV) energies [23]. Using the Gaussian-fitted data from the two-grid RPA for Q = 2 sccm, P = 100 W and B = 340 G (shown in Fig. 6.2, the characteristic decay length for the accelerated ion population can be calculated using an exponential decay fit. The current collected by the RPA that is due to the accelerated ion population is equal to:

$$I_{accel} = q n_{accel} v_{accel} A_{RPA} \tag{7.7}$$

where I_{accel} is the current collected by the RPA when the discriminator voltage is $V_D = V_{accel}$, the potential of the peak in the accelerated voltage, n_{accel} is the density in the accelerated population, A_{RPA} is the collecting area of the RPA, q is the ion charge and v_{accel} is the accelerated ion velocity. The current collected by the RPA that is due to the beam can be calculated from the integral of the distribution of the accelerated population [58, 72]:

$$I_{accel} \propto \int_0^{+\infty} v f_{accel}(V) dV \tag{7.8}$$

which is from Eq. 5.5 and $f_{accel}(V)$ is *only* the accelerated part of the distribution. The Gaussian fitting described in Chapter 5 separates the accelerated- and bulk-ion portions of the IEDF, allowing an analysis of just the accelerated population. It is important to note that the axial profile of the density n_{accel} will include the effects of both charge-exchange collisions as well as any radial divergence of the plume. There will be non-zero radial divergence of the accelerated population due to the diverging magnetic field and non-zero radial potential gradients (see Fig. 6.6). The radial profile of the beam as a function of axial distance was not characterized, but an estimate can be made using the magnetic field profile. The axial profile of the density decay, which is appropriate for use in calculating the charge-exchange mean free path, can then be calculated by compensating for the expansion of the plasma, since only the effect of the charge-exchange collisions should be included in a calculation of the charge-exchange mean free path. In the absence of any charge-exchange collisions that would depopulate the accelerated population, the flux of ions in the accelerated population will be conserved. If there is any decrease in the flux of the accelerated population (that is not due to expansion or acceleration), it is assumed to be a result of charge-exchange collisions. With this in mind, the density of the accelerated population n_{accel} from Eq. 7.7 can be written as:

$$n_{accel} = n_b \frac{v_0 A_0}{v_{accel} A_b} \tag{7.9}$$

where v_0 and A_0 are the initial ion velocity and area of the beam before the acceleration, A_b is the area of the plume at the point where n_{accel} and v_{accel} are measured, and n_b is the density of the accelerated population, which is “compensated” for any radial expansion. If there are no charge-exchange collision losses, $n_{accel} = n_b$. Inserting Eq. 7.9 into Eq. 7.7 and solving for n_b:

$$n_b = \frac{I_{accel}}{q v_0 A_{RPA}} \frac{A_b}{A_0} \tag{7.10}$$

The velocity of the accelerated population does not appear in Eq. 7.10, since the RPA measures an increasing flux from the increasing ion velocity, but the density n_{accel} is also decreasing by the same amount due to the acceleration. The area ratio remains, however, since the area of the RPA is not changing. Physically, this can be interpreted using the assumption that the plasma is tied to the magnetic field lines (although this is not critical for the calculation). The RPA is intercepting some bundle of flux lines in the upstream region, and in order to make a fair comparison between the measured fluxes at two points, the area of the RPA would have to increase or decrease such that it intercepts the same bundle of flux lines at every measurement location. Since the collection area of the RPA is constant, the measured flux at a given location must be adjusted to fairly make a comparison to another location. It is also important to mention that this sort of compensation does not need to be carried out for the calculations performed in Section 7.1, since the Boltzmann relation depends on the measured density, *including* any radial expansion of the plasma.

The normalized density n_b is shown versus axial distance z in Fig. 7.7, including the fit to an exponential decay, compensated using the measured magnetic field profile. The decay constant, equal to the mean free path λ_i, has a value of 7.8 $\pm$ 1.1 cm. The estimated neutral pressure in the potential drop region is some value in between the measured upstream (0.53 mTorr) and downstream (0.16 mTorr) gauges, most likely near 0.3 - 0.4 mTorr. For a cross section $\sigma_{cx} = 6 \times 10^{-15}$ cm^2, the predicted mean free path is $\lambda_i \approx 13$ cm, longer than that calculated from the fit. In terms of neutral pressure, the calculated n_g using Eq. 7.6 and the measured λ_i = 7.8 $\pm$ 1.1 cm is approximately $n_g \approx 0.65$ mTorr. While there is some error from the energy dependence of the cross section (the energy of the charge-exchanging ions is a function of z and therefore σ_{cx} is as well), the mean free path is shorter than expected for the estimated neutral pressure in the potential drop region. This could also be due to an inaccurate measurement of the pressure, an increase in the local neutral pressure due to neutral recycling or due to a higher neutral pressure in the RPA, which is not differentially pumped.

The duplicate of the MadHeX source in the space chamber at Georgia Tech (see Section 4.4) has produced accelerated ions that persist for much longer distances, up to 1 meter from the exhaust of the source tube. The background neutral pressure in the expansion chamber is held at $\sim 10^{-5}$ Torr as a result of a high pumping rate (six diffusion pumps, up to 600,000 L/s on air total pumping speed) in the space chamber. The result of the same analysis as in Fig. 7.7 for this data is shown in Fig. 7.8, using the four-grid RPA with Q = 1.3 sccm, P = 500 W and B = 100 G. The

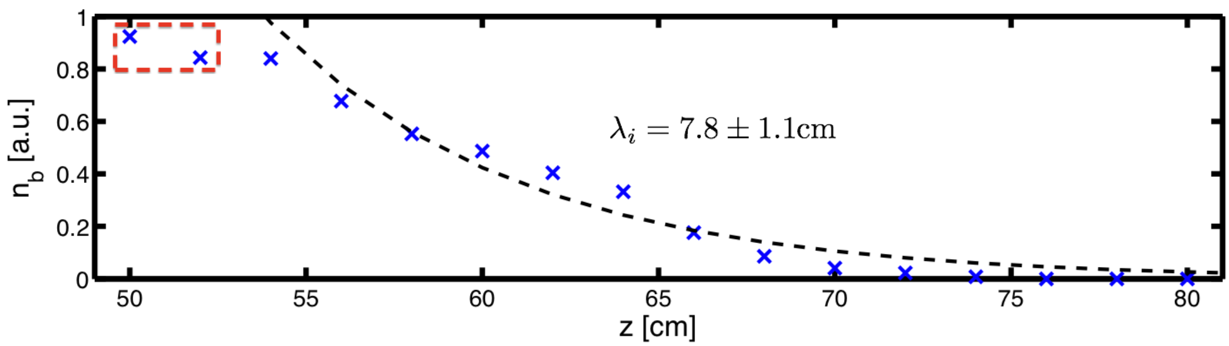

FIGURE 7.7: Density of the accelerated ion population calculated from Eq. 7.10 versus axial distance including the result of an exponential decay fit. The conditions are Q = 2 sccm, P = 100 W and B = 340 G, the same conditions as in Fig. 6.2. The data points outlined in the red dashed box are not included in the computation of the fit, since they are very near the formation point of the accelerated population where it is not well defined yet.

resulting mean free path λ_i = 22.5 $\pm$ 2.5 cm. In this case, for λ_i = 22.5 cm, the predicted neutral pressure in the acceleration region is $p_n \approx$ 0.2 mTorr, again higher than background pressure in the space chamber, possibly a result of a higher neutral pressure inside the four-grid RPA. Note that this fit does not include the same compensation for radial expansion as in Fig. 7.7, and the actual mean free path could be longer.

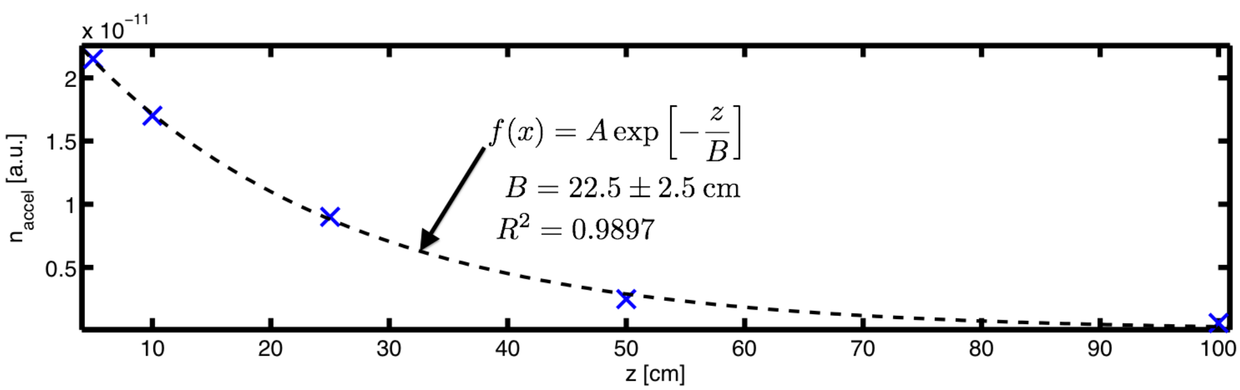

FIGURE 7.8: Density of the accelerated ion population calculated from Eq. 7.7 versus axial distance including the result of an exponential decay fit, taken in the experimental mock-up in a space chamber at Georgia Tech. The conditions are Q = 1.3 sccm, P = 500 W and B = 100 G.

As a side note, the electron-neutral cross section σ_{en} is much smaller than σ_{cx}, roughly 3 to 8 $\times$ 10^{-16} cm^2 for kT$_e$ $\approx$ 5-8 eV [105], therefore the electron-neutral mean free path $\lambda_{en} \geq$ 90 cm is substantially longer than λ_{cx}, hence the ion acceleration region is electron-neutral collisionless.

Fraction of Ions in Accelerated Population

The fraction of ions in the accelerated population can be calculated using Eq. 7.7 for the bulk and accelerated populations. Here, the compensation for the radial expansion of the plasma is not necessary, as the compensation factor (A_b/A_0) would cancel out of the ratio. The fraction of the ions in the accelerated population can be calculated using:

$$\frac{n_{\text{accel}}}{n_{\text{bulk}} + n_{\text{accel}}} = \frac{\frac{I_{\text{accel}}}{v_{\text{accel}}}}{\frac{I_{\text{bulk}}}{c_s} + \frac{I_{\text{accel}}}{v_{\text{accel}}}} \tag{7.11}$$

where n_{accel} is the beam ion density, n_{accel} is the bulk ion density, c_s is the ion sound speed calculated using the measured electron temperature from the single probe, v_{accel} is the beam velocity and I_{accel} and I_{bulk} denote the currents collected by the 2-grid RPA for the beam and the bulk distributions, respectively, calculated from the integrated fits to the IEDF. It is assumed that the bulk ions enter the analyzer at the Bohm speed c_s. For Q = 2 sccm at P = 100 W and B = 340 G, the calculated fraction in the accelerated population is $\approx$ 50% at z = 62 cm, and for Q = 1.3 sccm at P = 100 W and B = 340 G, the beam fraction is $\approx$ 60%, also at z = 62 cm.

It should be noted that the neutral pressure gradient that exists in the system is not a significant source of ion acceleration. The Knudsen number, which relates the argon neutral-neutral mean free path to the chamber diameter, is given by:

$$\text{Kn} = \frac{\lambda_{\text{mfp}}}{D} = \frac{1}{\sqrt{2} D \pi d_o^2 n_g} \tag{7.12}$$

where D is the characteristic dimension of the system, d_0 is the hard-sphere diameter of argon and n_g is the gas density [106]. For the pressures measured in our system, the Knudsen number Kn $\gtrsim$ 1, such that the flow is approaching free-molecular. The average neutral velocity in free-molecular flow $v_{av} = \sqrt{\frac{8kT}{\pi M_{Ar}}}$ is the characteristic velocity of the flow, which for room temperature is $\approx$ 400 m/s. Even with neutral heating, (neutrals in thermal equilibrium with the plasma ions, roughly 0.1 eV [107]), $v_{av} \approx$ 800 m/s. The measured ion beam velocities are in the range of 13 - 28 km/s, therefore the background neutral velocities are much smaller than the ion beam velocities.

7.3 Self-Bias Effect

In light of the conclusions of Section 7.1, it is of interest to determine the reason the potential differences exceed that predicted by ambipolar or Boltzmann plasma expansion when the source is operating in the capacitive mode. The large RF fluctuations of the plasma potential observed in the capacitive mode offer insight into the mechanism; the upstream plasma is "self-biasing" relative to the plasma in the grounded expansion chamber.

The plasma electrons' characteristic time scale $\tau_e = \omega_{pe}^{-1}$ is less than a few percent of the RF period for densities characteristic of the capacitive mode. For instance, the electron density at z = 50 cm for Q = 2 sccm, B = 340 G and P_{RF} = 100 W is $n_e = 8.8 \times 10^9$ cm^{-3}, therefore $\tau_e^2/\tau_{RF}^2 = \omega_{RF}^2/\omega_{pe}^2 \approx 0.03\%$. The electrons are easily able to transit the scale length of the acceleration region and possibly the length of the system in an RF period. The plasma ions, however, whose characteristic time scale $\tau_i = \omega_{pi}^{-1}$ is several times the RF period for the same electron density, are unable to respond to the rapid changes in the plasma potential and its gradient in an RF cycle. Instead, the ions respond to the time-averaged plasma potential profile as indicated in Fig. 6.19. The electrons can easily flow from the upstream region during an RF cycle, whereas the ions cannot, and there is an imbalance of flux. This imbalance is short-lived, as the steady state fluxes of electrons and ions must balance over an RF cycle (assuming no net current flow). A time-averaged (DC) potential difference builds to retard electron flux and increase ion flux, and this increase is the self-bias voltage described in Eq. 3.13. For an electron density of 1.6×10^{11} cm^{-3}, $\omega_{pi} = \omega_{RF}$ and the ions will be better able to follow the fluctuations. However, at these densities, the source is operating in such a mode where the plasma potential fluctuations are much reduced, either in the inductive or helicon mode. The higher electron density better shields the RF antenna fields as the skin depth $\delta_p = c/\omega_{pe}$ decreases, for instance $\delta_p \approx 1.3$ cm for low collisionality ($\nu_{en} \ll \omega_{RF}$) at $n_e = 1.6 \times 10^{11}$ cm^{-3}. The self-bias effect occurs exactly in the mode with the highest plasma potential fluctuations. When the ion density is high enough such that they can follow the fluctuations, the magnitude of the fluctuations is reduced in the source.

In the case of ambipolar expansion, the ambipolar (retarding) electric field increases until enough electrons are confined such that the ion and electron fluxes are equal from the source region. The electron diffusion over the ambipolar potential gradient is directly related to the number of electrons in the distribution with sufficient energy to overcome the ambipolar field, which can be calculated from the electron temperature in a Maxwellian electron distribution. For this reason, the ambipolar electric field and potential profile is a function of the electron temperature. However, in the present case, the plasma potential is rapidly fluctuating due to the capacitive coupling of the antenna to the plasma, and the resulting electric field that forms (which the electrons can respond to) is not necessarily dictated strictly by the electron temperature or distribution, but the field instead adjusts such that electron and ion fluxes through the potential gradient are equal. The electron temperature still plays a role in the system equilibrium and the self-bias effect (see Eq. 3.13), but the potential difference between the source and expansion regions is not necessarily limited by the ambipolar potential, set by the density gradient and electron temperature. The resulting electric field (and potential gradient) is a result of the self-bias effect. Typically, the self-bias effect is studied in a plasma processing system, where a floating substrate self-biases negatively with respect to the bulk plasma (and ground) because of the extra electron flux to the substrate (see Eq. 3.13). The bulk plasma potential is held at some positive potential due to the grounded walls confining it, but the substrate is allowed to charge negatively.

In the present case, the time-averaged plasma potential in the expansion chamber is held at roughly the DC floating potential ($\approx 5kT_e/e \sim$ 40-50 V) by the grounded walls (see Section 3.1). The upstream plasma, inside an insulating chamber, is able to charge relative to the downstream plasma. The insulating walls do not provide an “anchor” for the plasma potential in the source region, since they are allowed to float. However, the transition region between the source and expansion chambers, which would normally support a potential gradient equal to that predicted by simple ambipolar expansion, supports a much larger potential difference due to the increased electron flux from the source region due to the RF timescale plasma potential fluctuations. Of course, the situation is always self-consistent, such that the global electron and ion losses from the plasma are equal in steady state (no net current drawn from the plasma as a whole). The upstream boundary condition, explored below in Section 7.3.1, establishes the distribution of the losses in the system and the restriction on current flow through the source region. In the case of the floating endplate, the plasma in the upstream source region self-biases relative to the downstream plasma in the expansion chamber such that the time-averaged electron and ion fluxes from the upstream source to the downstream chamber are equal. When the upstream endplate is grounded, the same occurs, except equality of the *net* electron and ion fluxes from the upstream region (to the endplate as well as to the downstream chamber) is satisfied.

It is possible to estimate the magnitude of the expected self-bias voltage using Eq. 3.13, where the additional self-bias voltage due to the plasma potential fluctuations is given by:

$$V_{fl-RF} - V_{fl-DC} = V_{SB} = \frac{kT_e}{e} \ln\left[I_0\left(\frac{eV_1}{kT_e}\right)\right] \tag{7.13}$$

where V_{SB} is the increase in the floating potential due to the plasma potential fluctuations, V_1 is the amplitude of the fluctuations and T_e is the electron temperature. From Fig. 6.19, the amplitude of the fluctuations at z = 50 cm is $V_1 \approx 70$ V for Q = 2 sccm, P = 100 W and B = 340 G. The electron temperature $kT_e \approx 9$ eV from Fig. 6.4 for these conditions, therefore the predicted self-bias voltage is $V_{SB} \approx 53$ V. The measured potential drop from z = 50 cm to z = 80 cm for the same conditions is $\Delta V \approx 65$ V, higher than that predicted. However, the fact that the time-average of the fluctuations is not equal to the midpoint between the maximum and minimum plasma potential is evidence that there are multiple harmonics of the fundamental RF frequency present. As discussed in Chabert [33], additional harmonics increase the self-bias voltage, with each harmonic contributing an extra factor $\ln[I_0(a_i)]$ where a_i is the contribution of the ith harmonic, if the harmonics are in phase. The contribution of additional harmonics can be estimated by assuming a form of the plasma potential fluctuations and using the maximum, minimum and time-averaged values of the plasma potential (all known) to find the necessary coefficients. The assumed form of the fluctuations is:

$$V(t) = B \exp\left[-A \sin(\omega t)\right] + C \tag{7.14}$$

where ω is the RF frequency. The assumed plasma potential $V_p(t)$ for Q = 2 sccm, P = 100 W B = 340 G at z = 50 cm is shown in Fig. 7.9, and the time-average is shown as a dashed line.

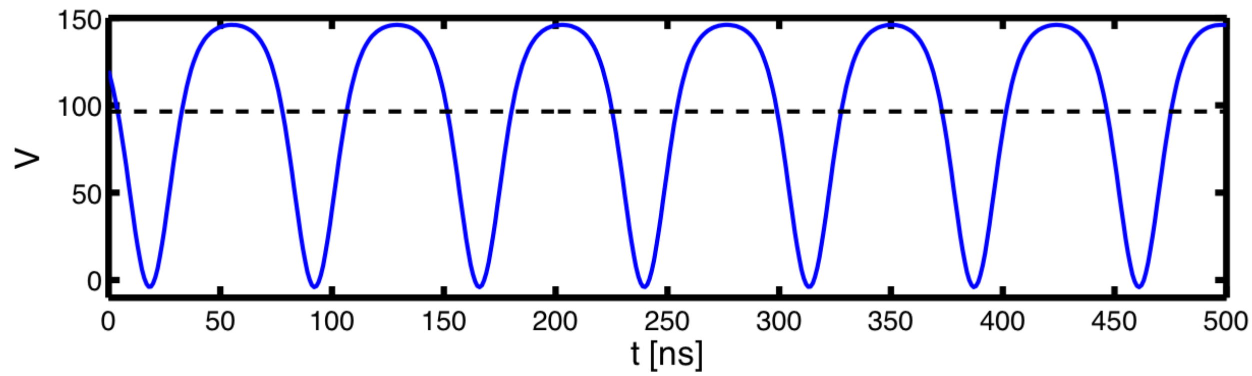

FIGURE 7.9: Waveform of plasma potential fluctuations using an assumed form $V(t) = B\exp[-A\sin(\omega t)] + C$, where the coefficients are calculated from the measured minimum, maximum and time-averaged plasma potentials. The time-average of the waveform is shown as a dashed line.

The contribution of the second, third and fourth harmonics in the waveform in Fig. 7.9 are 35%, 10% and 2%, respectively. This results in an increase in the estimated self-bias voltage to V_{SB} = 72 V. The measured potential drop for these conditions is ΔV = 65 V, between the estimated self bias voltage for a single harmonic (V_{SB} = 53 V) and including four harmonics (V_{SB} = 72 V). The potential fluctuations in the downstream chamber are lower than that in the upstream region, but still nonzero. In Fig. 6.19, at z = 80 cm the fluctuations are still V_1 = 30 V, however the time averaged plasma potential in the chamber is most likely set by the fluctuations closer to the chamber walls, which are presumably much lower. For the same conditions, the emissive probe was rotated such that the probe tip was within a few centimeters of the grounded wall, and the measured fluctuations were $V_1 \approx 10$ V. The self-bias voltage in the expansion chamber is much lower than that in the source region, $V_{SB} \approx 3$ V. Therefore, the time-averaged plasma potential remains near the DC floating potential, roughly $\overline{V_p} \approx 5\ kT_e/e \approx 45$ V in the expansion chamber.

The additional potential difference from the self-bias effect results in additional ion acceleration resulting in a decrease in the ion density as a result of the conservation of ion flux. However, as explained in Section 7.1, the density and potential gradients do not follow a Boltzmann relation. For example, at Q = 2 sccm, P = 100 W and B = 340 G (the capacitive mode), the ion density measured with the single probe decreases by a factor of ≈ 36 through the potential drop. The ion velocity, assuming the ions are moving at the sound speed c_s before the acceleration, increases by a factor of ≈ 3.6. Assuming the plasma is tied to the magnetic field lines, the cross sectional area of the plasma increases by a factor of roughly ≈ 10. The ratio of the ion flux upstream and downstream of the potential gradient is approximately unity:

$$\frac{\Gamma_u}{\Gamma_d} = \frac{n_u v_u A_u}{n_d v_d A_d} \approx 1 \tag{7.15}$$

where u and d denote upstream and downstream quantities. The ion flux is conserved, but the ions' potential and density do not obey a Boltzmann relation. Although not a rigorous calculation, it demonstrates that the ion flux is conserved even through the potential and density are not related by a Boltzmann expression.

It is interesting to discuss the role of the grounded walls of the expansion chamber. There is always some non-zero capacitive coupling of the RF antenna fields to the plasma, with the highest levels in the capacitive mode. The grounded expansion chamber walls act as a grounded electrode in the RF circuit. Some capacitive coupling is always present between the grounded and driven ends of the RF antenna (as the RF voltage is dropped across the antenna), but it is possible to also support RF coupling and current between the antenna and the grounded walls of the expansion chamber (though no DC current flows), similar to that in a processing reactor. The RF electric field between the antenna and the grounded chamber walls is not sufficient to produce breakdown or plasma initiation, but once a plasma is created under the antenna the coupling between the antenna and the chamber walls can lead to extension of the plasma from the source region to the chamber, perhaps through electrostatic wave propagation such as Trivelpiece-Gould modes. During operation of the source, a coating forms and builds on the chamber walls, which reduces the "quality" of the ground provided by the grounded walls of the expansion chamber over time. The reduced quality of the ground has several ramifications. First, the magnitude (difference between upper and lower limits) in the expansion chamber has decreased over time, from $\pm$ 30 V to $\pm$ 24 V for the same experimental conditions. Second, the time-averaged plasma potential in the source region has decreased slightly, from 110 V to 103 V for the same experimental conditions. Lastly, there is a gradual increase of the lower neutral pressure limit for which accelerated populations are observed. In the context of this lower neutral pressure limit, the reduced quality of the ground requires a higher background electron density (a function of neutral pressure) to attain enough electrostatic RF coupling to the grounded downstream chamber walls and resulting extension of the plasma. A similar lower limit for appearance of the accelerated ion population is seen with the magnetic field, but this is primarily a result of the loss of electron confinement at reduced magnetic fields, and this limit is not significantly affected by the reduced quality of the ground in the expansion chamber. The coating build-up over time serves to reduce the amount of capacitive coupling and the magnitude of the self-bias effect, which will need to be addressed for future experiments (see Chapter 8).

As an aside, at the lowest flow rate of Q = 1.3 sccm, it is possible to keep the source in the capacitive (E) mode for RF powers up to P = 500 W. The potential differences, measured with the four-grid RPA, exceed ΔV = 160 V at these higher powers. With this in mind, experimental observation of accelerated ions in other expanding helicon sources operated at similar parameters (low pressure, low or modest powers and modest magnetic fields [8]) could possibly have significant capacitive coupling producing large RF fluctuations of the plasma potential, leading to the self-bias effect. Ion acceleration in a high-pressure (several Torr) capillary capacitive discharge was investigated by Dunaevsky [41] and it was found that significant ion acceleration is possible, up to energies near eV_{RF} where V_{RF} is the RF voltage of the source. While the self-bias effect was not explicitly mentioned, it certainly the mechanism at work in their case.

In general, the idea of the self-bias effect and equality of particle loss rates is similar to the global diffusion-based model of a current-free double layer in an expanding helicon source proposed by Lieberman and discussed in Chapter 3. However, in the present case, the loss rates are affected by the plasma potential fluctuations, which are not present in the Lieberman model, leading to a larger potential difference between the source and expansion chambers due to the self-bias effect. It is not believed a “classical” static double layer is observed in our system, at least not a double layer that can be described by present models. The presence of plasma potential oscillations indicate if the potential difference and ion acceleration were due to a double layer, it would be an RF-modulated double layer that may serve to extend the physical length of the acceleration region. Annatarone [108] has observed formation of RF-timescale double layers as a result of plasma sheath resonance, such that large RF currents are present in their system. The strong RF currents led to large RF field gradients and weak ($eV_d \approx kT_e$) double layer formation. The distinction between a double layer and ambipolar expansion is the presence of charge separation that leads to the observed electric field. In ambipolar expansion, there is no charge separation and the electric field forms to balance the gradient in the electron pressure, whereas in a double layer, significant charge separation in space is present. The observation of significant plasma potential fluctuations, which the plasma electrons can follow but the plasma ions cannot, is evidence of charge separation in time and almost certainly in space. It has been established above that the self-bias effect is responsible for the observed plasma potential gradient, however the intricate details of the evolution of the time-dependent plasma potential has not been measured (and cannot be accurately measured with the present diagnostics) in the potential drop region. The profile of the plasma potential excursions shown in Fig. 6.19 is evidence that a strong plasma potential gradient exists ($\approx$ 70 V over 12 cm) for some time during the RF cycle (the profile of the upper limit of the plasma potential) which would require a significant density gradient if it were ambipolar, a factor of $\approx 10^5$ for kT_e = 10 eV. Assuming the electron density is the same as the ion density at the upstream edge of this potential gradient, the width of the potential drop region is roughly $L_d \approx 500\ \lambda_D$, longer than that of typical double layers but not unreasonable. The self-bias effect is responsible for the potential gradient, and it may be possible that a time-dependent double layer forms for some part of the RF cycle to connect the upstream and downstream time-dependent plasma potentials.

Due to the presence of the static magnetic field, it is also possible for propagating electrostatic waves to propagate in the plasma column, including Trivelpiece-Gould modes. These waves could lead to increased extent of the plasma and are likely present in not only the capacitive (E) mode but also the inductive and helicon modes. In fact, Trivelpiece-Gould modes have been suggested as a mechanism for the efficient operation of helicon sources [109]. The effects of any propagating electrostatic waves are beyond the scope of the present work, but may be of interest for further investigation of the self-bias effect.

7.3.1 Upstream Boundary Condition

When the upstream endplate is grounded, there is an additional electron flux from the upstream region, and there are two ways for the plasma to compensate. First, the time-averaged plasma potential upstream could increase to try and equalize the overall particle fluxes from the plasma. If the upstream time-averaged plasma potential increased enough alone to compensate for the extra electron losses, there would be no net current to the upstream plate and the acceleration due to the downstream potential gradient would be current-free, and the global net electron and ion losses would be equal. On the other hand, it is possible to support a net current flow through the upstream endplate, which would act to equalize overall electron and ion losses globally in the system. In reality, both an increase of the upstream plasma potential of roughly 20 V and a net positive current flowing from ground into the endplate (or a net negative (electron) current flowing from the plasma to the endplate) are observed. The (negative) electron current flows into the upstream endplate, through ground and back into the plasma through the downstream chamber. There cannot be an overall net current flow out of or into the plasma or infinite charging of the plasma would occur. When the upstream endplate is isolated from ground (floated), there can be no net current to or from the plate in steady state. Since the upstream endplate's potential is not held at any particular value, it can charge with respect to the plasma such that the net ion and electron currents to the plate are zero in steady state. Most importantly, the potential difference between the source and expansion chambers cannot be described by ambipolar plasma expansion alone, when the endplate is either grounded or floated, and is a result of the self-bias effect.

7.4 Scaling of Potential Gradient

The scaling of the potential difference between the upstream source region and the expansion chamber is mainly controlled by the time-averaged plasma potential in the upstream region, since the potential in the grounded expansion chamber changes relatively little. For these scaling studies, the upstream endplate is grounded, and the source is operating in the E mode unless noted.

7.4.1 Argon Flow Rate

As the argon flow rate is decreased, a near-exponential increase in the potential drop from the source to expansion chambers is observed. The increase in the potential drop is a result of the rising time-averaged value of the upstream plasma potential (the self-bias) as flow rate is reduced. As the flow rate is reduced, the ionization rate decreases as a result of the lengthening mean free path for electron-neutral ionizing collisions, leading to a decreased bulk electron density. As the density decreases, the shielding of the RF electrostatic antenna fields from the plasma becomes less effective as the skin depth δ_p increases. The increased RF modulation of the plasma potential results in a larger self-bias effect and a larger potential difference between the source region and expansion chamber. When the flow rate is dropped below a certain threshold, there is not enough ionization to maintain a discharge in both the source and expansion chambers, and a weak capacitive discharge forms directly under the antenna but does not extend into the expansion chamber. This could also be due to the lack of a propagating electrostatic mode, but more investigation of these modes is required. This threshold flow rate was shown to rise with increased operation time, a result of the reduced quality of the ground condition in the chamber (discussed above). There is also evidence of the E-H transition in the middle of the flow rate scan presented in Fig. 6.14, as an inflection point near 2.5 sccm. The transition is not as abrupt as observed in the RF power scans (Fig. 6.8 for example) since as the neutral pressure is increased, the electron density increases gradually and the plasma shielding of the RF antenna fields becomes more effective. At the E-H transition, the density is such that bulk RF electric fields in the plasma are greatly reduced (compared to lower neutral pressures), leading to lower fluctuation magnitudes of the plasma potential. Induced fields in the plasma become the primary mechanism for plasma sustainment and the self-bias effect is greatly reduced or eliminated.

7.4.2 Magnetic Field

The magnetic field has an effect on the confinement of the electrons, and to a lesser extent the ions. As B is increased, the potential difference between the source and expansion regions decreases. With the model of ambipolar expansion of Section 3.2 in mind, the profile of the magnetic field does not change with the magnetic field strength, so the potential gradient predicted by the model (a function of the ratio of magnetic field strengths) does not change drastically, only if the *location* of the expansion changes. In the region of the expansion, the B field profile has a negative slope whose magnitude decreases with increasing z, therefore if the expansion moves further in z, the predicted potential drop from the model will also decrease. A shift in the z location of the expansion to larger z values is observed with increasing magnetic field, but this is not the primary reason for the decreased potential drop. The increased magnetic field confines the plasma electrons, which only diffuse radially due to collisions (which become increasingly rare at lower pressures). The improved radial confinement at higher magnetic fields results in reduced overall losses from the upstream region, leading to a higher electron density, as seen previously in this experiment [28]. The increased electron density results in a shorter skin depth, leading to lower penetration of the RF antenna fields and reduced fluctuation in the plasma potential at the RF frequency as discussed above, which produces a lower self-bias effect. The axial extent of the potential gradient also shifts further into the expansion chamber, a result of increased radial plasma confinement further into the chamber at higher magnetic fields. The ion gyroradius is approximately $r_L \approx 4$ mm at z = 45 cm for the B = 340 G coil current to $r_L \approx 5$ cm at z = 80 cm. The potential gradient onset starts when the ion gyroradius is $r_L \approx 0.4$ - 0.8 cm, suggesting the ion magnetization may play a role in the the location of the potential gradient.

7.4.3 RF Power

An increase in the RF coupled power to the antenna leads to an increase in the voltage across the antenna. There is also a rise in the electron density with increasing power, but it is not significant in the potential gradient region, so there isn't a significant increase in the shielding of the RF fields as the RF power is increased. The increased antenna voltage leads to increased RF electric fields inside the plasma, larger fluctuations of the plasma potential and therefore a larger self-bias effect. Once the plasma density near the antenna passes the threshold, the capacitive to inductive transition occurs. In the inductive mode, the antenna coupling is more efficient, leading to higher electron densities and increased shielding of the antenna's RF electric fields as well as a vanishing self-bias effect.

7.5 Analysis as a Thrust Source

Although this research is primarily aimed at understanding the fundamental mechanisms behind the acceleration of ions from an expanding helicon source, it is of interest to perform some initial calculations of the propulsion metrics explored in Section 1.1. Of course, the further development of this source for use as a thruster would require detailed measurement and optimization of these parameters. The research at Georgia Tech is aimed more at the real-world performance of the helicon source in a space environment, including measurements of actual thrust developed using an null-type inverted pendulum thrust stand inside the space chamber. Measurements of thrust have been performed on other helicon sources inside large vacuum chambers (see Williams [110] for example), but without consideration of the self-bias effect.

Considering the low plasma densities measured in the capacitive mode, a low thrust would be expected but the high ion energies will result in a fairly large specific impulse. Using the quantities measured for the test case of Q = 2 sccm, P = 100 W and B = 340 G, the thrust, defined as:

$$T = I_b\sqrt{\frac{2Vm_i}{q}} \tag{7.16}$$

is approximately 0.5 mN, assuming the beam density is $n_b = 5.3 \times 10^9$ cm^{-3} calculated using the upstream ion density and 50% fraction of ions in the accelerated population, a 4 cm radius of the accelerated population (smaller than the source chamber radius), and a beam energy of 65 eV. The specific impulse $I_{sp} = v_b/g \approx 1800$ seconds, and the power efficiency $\eta = P_b/P_{in} \approx 4\%$ using P_{in} = 100 W. Using the highest ion energy measured in the source, E_i = 160 eV, the specific impulse $I_{sp} \approx 2800$ seconds. In the inductive mode, the density is several times higher that in the capacitive mode but the potential gradients are lower, resulting in larger thrust (scales linearly with both ion energy and beam density), but lower specific impulse (scales with the square root of the ion energy). The beam density is even higher in the helicon mode, but the potential gradients are the lowest of any mode.

The RF plasma potential fluctuations in the capacitive mode lead to larger time-averaged electron fluxes to the walls than would occur in the absence of the fluctuations. The extra time-averaged electron flux, balanced by an increased ion flux, leads to increased power loss to the walls and a reduction in overall power efficiency. To minimize the losses in the source, the surface area of the source region should be minimized as much as possible without affecting the operation of the source. In its present configuration, the source tube has a large aspect ratio (L/R) and the surface area is likely larger than necessary to develop the requisite self-bias and could be reduced, resulting in an increased power efficiency.

Experiments on the VASIMR helicon section [11] have shown large thrusts ($\gtrsim$ 100 mN) as a result of mid-level ion energies ($\approx$ 20 eV) but significant plasma densities (up to 10^{14} cm^{-3}). Up to 30 kW of RF power is suppled to the source, which is operating in the helicon mode. This research on the VASIMR source provides evidence that a helicon source can be used to develop significant thrust, even in the absence of a double layer.

The appearance of a self-bias effect in the capacitive mode could be used in conjunction with the high power, helicon-mode operation of a helicon source as an additional operating regime with low thrust but high specific impulse and efficient propellant utilization. The design of the thruster could also be optimized to increase the capacitive coupling and self-bias voltage.

Summary

The presence of a high-energy accelerated ion population in the capacitive mode in a helicon source is the result of a self-bias effect. Ions, unable to follow RF fluctuations of the plasma potential and associated electric field, remain near the time-averaged plasma potential, while electrons are able to follow the fluctuations. This leads to an increased initial electron flux from the source region as the electrons are not well confined for all times during the RF cycle. A self-consistent electric field (and potential gradient) builds to accelerate ions from the source to equalize the net flux from the insulating source region. The self-bias effect is only significant in the capacitive mode, and the plasma expansion in the inductive and helicon modes can be well described by ambipolar expansion. The scaling of the potential difference with source parameters is dictated by the parameters' effect on the magnitude of the plasma potential fluctuations in the source region and the overall particle balance. As a thruster, in its present form the calculated thrust is quite low but the specific impulse is on the order of other ion thruster technologies. The self-bias effect in the capacitive mode could be used as a low thrust, high specific impulse (mass utilization efficiency) mode in a high-power helicon thruster such as VASIMR.

Chapter 8

Conclusions and Future Work

8.1 Conclusion

A full discussion of the results of the research is found in Chapters 6 and 7, and a brief summary of qualitative results follows. The initial observation of the accelerated population as well as the scaling analysis has been published in our recent paper [102].

- ▷ Potential gradients and accelerated ion energies larger than those seen in other comparable helicon experiments are observed in the expanding, exhaust region of the Madison Helicon Experiment, with ΔV exceeding 100 V when the source is operating in the capacitive mode.
- ▷ These potential gradients occur over several hundreds to thousands of Debye lengths, with a potential drop magnitude ΔV larger than that predicted for ambipolar expansion, for certain experimental conditions.
- ▷ The magnitude of the potential difference is dependent on the coupling mode of the antenna.
    - ⇒ Three modes of coupling are observed in the source; capacitive (E), inductive (H) and helicon (W) mode.
    - ⇒ The highest potential gradients are observed in the capacitive mode, slightly lower in the inductive mode and are the lowest in the helicon mode.

- ▷ Plasma potential fluctuations on the RF timescale are observed in the source, with the largest amplitude fluctuations in the capacitive mode.
  - ⇒ The large fluctuations in the plasma potential are due to the inability of the plasma to shield out the RF electrostatic antenna fields, with the highest penetration in the capacitive mode and less so in the inductive and helicon modes.
  - ⇒ The plasma electrons are able to fully follow to these rapid changes in the plasma potential and associated electric field, while the ions cannot, due to their significantly longer characteristic time scale compared to the RF period (for the operating conditions in the capacitive mode). The ions remain near the time-averaged value of the fluctuating plasma potential.
- ▷ The high potential differences observed in our system in the capacitive (E) mode are a result of a self-bias effect commonly seen in RF capacitive discharges, but not studied or considered in ion acceleration in expanding helicon sources to date.
  - ⇒ The mobile plasma electrons can easily flow from the upstream region during an RF cycle, whereas the more massive ions cannot, and there is an imbalance of flux. This imbalance is short-lived, as the steady-state fluxes of electrons and ions must balance over an RF cycle (assuming no net current flow). A time-averaged (DC) potential difference builds to retard electron flux and increase ion flux, and this increase known as the self-bias voltage.
  - ⇒ The potential difference in the case of ambipolar expansion (and double layer formation) is directly related to the electron distribution function. However, the self-bias effect depends only weakly on the electron temperature and is a much stronger function of the magnitude of the fluctuations. This results in ion acceleration that is not as strongly dependent on the electron temperature.
- ▷ The plasma in the dielectric (insulating) source region self-biases with respect to the downstream plasma potential, resulting in a potential difference between the two regions that is larger than that predicted by ambipolar plasma expansion.

- ⇒ The time-averaged plasma potential in the expansion chamber is held at or near the floating potential in argon ($\overline{V_p} \approx 5kT_e/e$) since the chamber walls are grounded. Relatively low RF fluctuations slightly increase the floating potential in the expansion chamber (less than kT_e/e).
- ⇒ The electrons in the upstream region can escape the plasma axially to the downstream expansion chamber when the time-dependent plasma potential profile permits. A self-bias voltage develops between the upstream and downstream time-averaged plasma potentials. The downstream plasma potential acts as the reference point due to its connection to ground through the chamber walls, and the upstream plasma potential increases above the downstream plasma potential by the self-bias voltage. The magnitude of the self-bias voltage agrees with theory for RF modulated sheaths.
- ⇒ Grounding the upstream metal endplate (as is the case for much of the experimental work) increases the electron loss from the source region. As a consequence, the self-bias voltage increases and a net electron current is drawn through the upstream endplate, and the ground provides current closure. The self-bias increase and net ion current happen self-consistently to equalize global net particle fluxes from the plasma in steady state. A potential gradient larger than predicted by ambipolar expansion is still observed when the upstream endplate is floated.

▷ The self-bias effect is most pronounced in the capacitive mode, where the RF plasma potential fluctuations are most severe. In the inductive and helicon modes, the plasma expansion more closely follows that of an ambipolar expansion as a result of reduced plasma potential fluctuations from increased electron density in these modes.

▷ The plasma is also expanding from the source chamber into the expansion chamber, which will result in a distributed potential gradient due to ambipolar expansion, in the absence of any fluctuations in the plasma potential. However, due to the self-bias effect, the magnitude of the observed potential drop is larger than that predicted by ambipolar expansion. A self-bias voltage appears if necessary, such that the total potential drop will self-consistently equalize time-averaged fluxes from the upstream, source region to the expansion chamber (if the upstream endplate is floated) or the total current from the plasma (if the upstream endplate is grounded).

▷ Ions are accelerated by the potential gradient between the upstream and downstream regions, and the accelerated population decays due to charge-exchange collisions in the expansion chamber. After accounting for the radial expansion of the accelerated population, the calculated mean free path is consistent with that predicted by charge exchange collisions.

▷ The scaling of the potential drop with argon flow rate, magnetic field and RF power in the capacitive mode is shown to be controlled by the magnitude of the RF fluctuations in the source region as the parameters are scanned. A lower electron density leads to increased penetration of the RF electric fields and therefore a larger self-bias voltage.

▷ Similar large potential gradients as well as ion acceleration have also been observed in a mock-up of our experiment installed in a space-simulation chamber by a collaborating group at Georgia Institute of Technology (Georgia Tech). Accelerated ions persist further in the experiment at Georgia Tech (up to 1 meter) due to the much larger, lower pressure ($p_n < 1 \times 10^{-5}$ Torr) space chamber.

8.1.1 Implications

The study of potential gradients in similar expanding helicon sources has been an active area of research as of late, with many researchers ascribing significant potential gradients to the presence of a double layer in the expansion region (see Section 3.3.6). The present work suggests a possible mechanism to explain these significant potential gradients in the context of the RF nature of the source, which has not been considered in most studies.

The current-free acceleration of ions to high energies without the use of grids is attractive for use in a thruster. The large potential gradients in the capacitive mode could be used as part of a helicon thruster system, offering a high specific impulse, low thrust mode (capacitive coupling) in addition to higher thrust, lower specific impulse modes (inductive or helicon wave coupling) [11]. Ion acceleration in a capillary at high pressures (several Torr) using a capacitive discharge has been demonstrated [41], and this mechanism would be an extension of that concept. However, optimization of the capacitive coupling and determination of the effects of the boundary conditions would need to be carried out. Because of the RF-timescale fluctuations of the plasma potential, the natural limit on the magnitude of the potential drop is no longer directly a function of the electron temperature, as is the case for ambipolar expansion [23] (see Section 3.2) and for current-free double layers [12] (see Section 3.3).

8.2 Future Work

8.2.1 Optical Emission Spectroscopy

Knowledge of the precise electron energy distribution (EEDF) is crucial to fully understanding most plasma phenomena. Current-collecting probes offer a seemingly simple method to extract the EEDF, but in reality the technique is very sensitive to the design of the probe and electronics, especially when the plasma potential is fluctuating in time, as is the case in our experiment. In addition, current-collecting probes perturb the plasma since an object must be inserted in the plasma, which collects current itself but also presents a large metal surface (the probe shaft, often metal and grounded).

It is possible to extract the electron energy distribution (EEDF), or certain aspects of it, by observing the optical emission of the plasma using optical emission spectroscopy (OES). A model based on the relevant atomic physics is developed, and the inputs to the model are adjusted until the predicted plasma emission matches the observed plasma emission. The model can be as simple as a line-ratio measurement, where the ratio of two emission lines is correlated to the electron temperature, assuming a Maxwellian distribution of electrons [111]. On the other hand, complex models including several emission mechanisms have been developed to fully measure the EEDF [96]. One of the more appealing aspects of OES is the non-perturbing nature of the diagnostic, especially in smaller systems where current-collecting probe size is not negligible.

The electron density determines the processes that dominate the thermodynamic equilibrium of a plasma, and two regimes exist based on the electron density. At low electron densities

($n_e < 10^{10}$ cm^{-3}), the populations of excited states is controlled mainly by radiative decay or excitation, since collisional processes are negligible. This is called Coronal Equilibrium. At high densities ($n_e > 10^{18}$ cm^{-3}), collisional processes control the equilibrium population densities, which is called Local Thermodynamic Equilibrium. In our system the electron densities lie between these two extremes, therefore the models used to predict population densities must include the contributions of both radiative and collisional excitation and decay.

Our group currently uses two collisional-radiative models for comparison to experimental results [13]. The first, the *ADAS* CR model, is used to determine the electron temperature T_e assuming the electron density n_e is known, and examines transitions in singly-ionized argon. This code uses pre-calculated, tabulated data from a model that solves a set of differential equations relating the populations of excited states grouped into 35 level parents, or sets of transitions that share the same electronic configuration. The tabulated data was pre-calculated assuming a Maxwellian EEDF. The second, the *Vlček* CR model, is used to determine the neutral density n_0 given a n_e and T_e. This code solves a set of 65 differential equations for transitions from four level parents, and can include non-Maxwellian EEDFs. Both of these codes have been used to measure T_e and n_0 in argon plasmas in the helicon mode with densities greater than 10^{11} cm^{-3}. A absolutely-calibrated broadband spectrometer is used to measure the excited state population densities, and unknown variable (T_e or n_0) is adjusted in either model until the measured population densities match the calculated population densities.

In principle, the Vlček model can be used to extract the EEDF, assuming n_e, and n_0 are known, since the EEDF could be adjusted until the measured and calculated population densities converge just as with the electron temperature. In principle, however, the neutral density n_0 is not well known as a function of z, leading to large uncertainties in the calculated EEDF. Work has begun already in our group to adapt the Vlček model for this use to examine if the uncertainty in the neutral density is too large to get meaningful results.

Work by Boffard and Prof. Amy Wendt at UW-Madison [96] using a verified collisional-radiative model has also shown promising results for measurement of the EEDF in an inductive source.

8.2.2 Laser Induced Fluorescence

A major component of the research is measuring the ion energy distribution. Retarding potential analyzers have several drawbacks, including perturbation of the plasma and complications with extracting the true ion energy distribution (in the midst of sheath, grid and geometry effects). Laser Induced Fluorescence (LIF) offers a non-perturbing way to measure the ion energy distribution without inserting anything into the plasma. MadHeX currently has an LIF setup, but it is optimized for use in high density ($n_e \approx 10^{12}$ cm^{-3}) plasmas. Measurements have been carried out investigating the bulk ion flow speed at higher flow rates and powers, but the system will need to be modified to operate well at the low electron densities observed in the capacitive mode, roughly $n_e \approx 10^9$ cm^{-3} - 10^{10} cm^{-3}.

Using LIF to measure the ion energy distribution in double layers and expanding helicon plasmas is a well-studied topic. Work at West Virginia University (Thakur [66] and Scime [65] and references therein), working at moderate electron densities ($n_e \approx 10^{11}$ cm^{-3}) has looked extensively at the time dependence and parameter (frequency in particular) dependence of accelerated ion populations using LIF. However, ion energies encountered in such systems are much lower than those measured in our experiment, and the self-bias effect has not been explored in those systems. It would be of great interest to verify the axial dependence of the ion energy non-invasively.

Laser Induced Fluorescence uses a tunable laser to excite an atomic transition and detect the Doppler shift in the radiation from that transition. The laser is typically modulated and lock-in amplifiers are used to extract the signal in the presence of very low signal to noise ratios. From the Doppler shift, the velocity distribution of the ions can be extracted by removing artificial broadening mechanisms, including natural, Stark and Doppler broadening and Zeeman and hyperfine splitting. The transition used in our system (in argon) is shown in 8.1.

A newly-acquired Master Oscillator Power Amplifier (MOPA) system has greatly increased the laser power output and therefore the range of parameters that can be investigated. A MOPA system consists of two components: a master tuneable diode laser that can output slightly around 20 mW at 668.6 nm is used as a source for a tapered amplifier which boosts the laser output power to greater than 600 mW. The full system is shown in Fig. 8.2. A Faraday cage surrounds the sensitive electronics to mitigate RF interference.

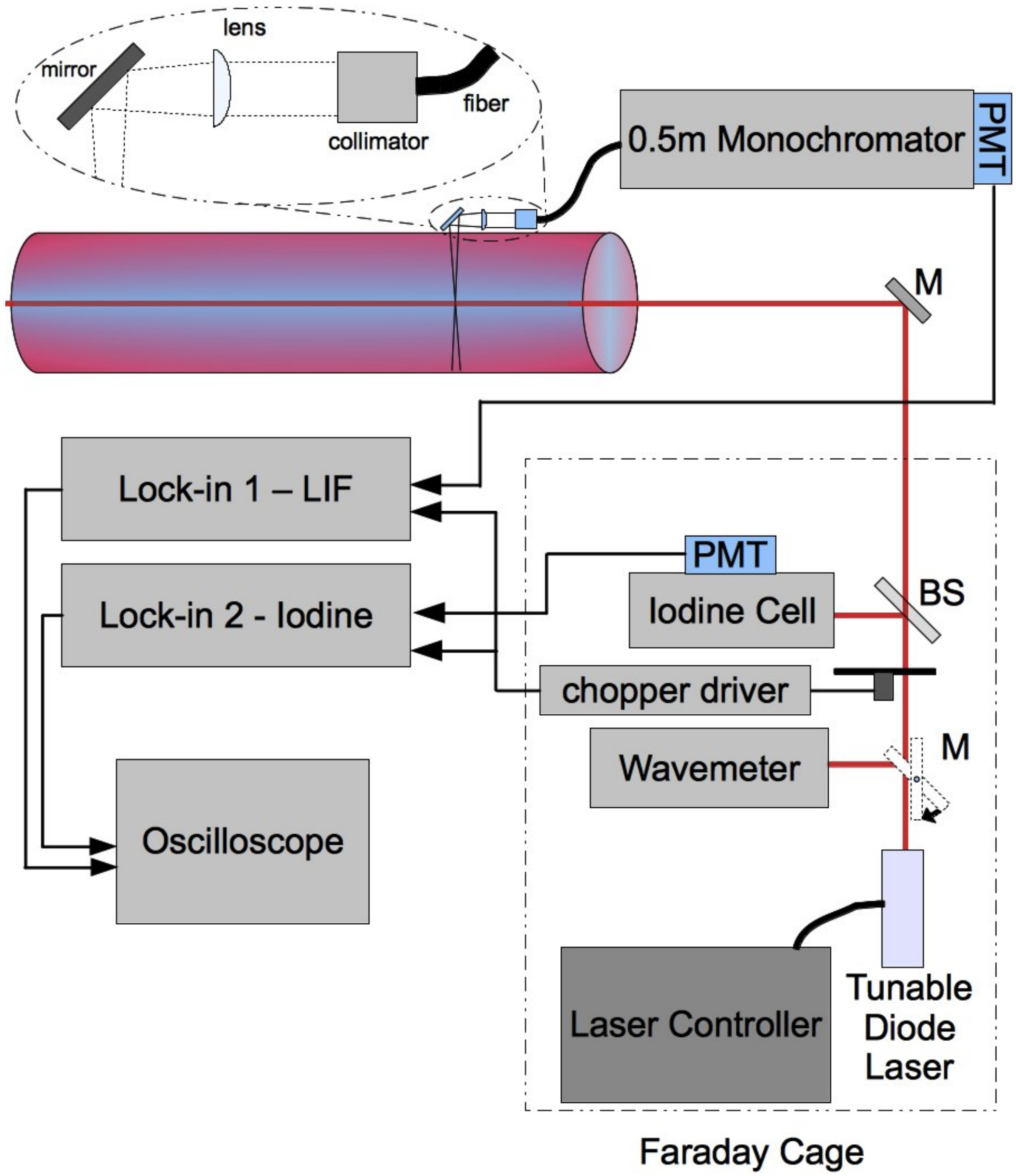

FIGURE 8.2: LIF system diagram.

An iodine cell, fed by a 10% beam splitter, is used to calibrate the wavelength measurement as the laser wavelength is swept. The current system uses a collimator and optics mounted in a lens tube affixed externally to the clear Pyrex tube to collect the laser-induced emission. In order to make measurements in the expansion chamber, a new optical system will have to be designed that can be either used inside the expansion chamber (similar to that used in [65]) or that can be used externally and focused through the viewport on the side of the chamber. Such a design is shown in Fig. 8.3.

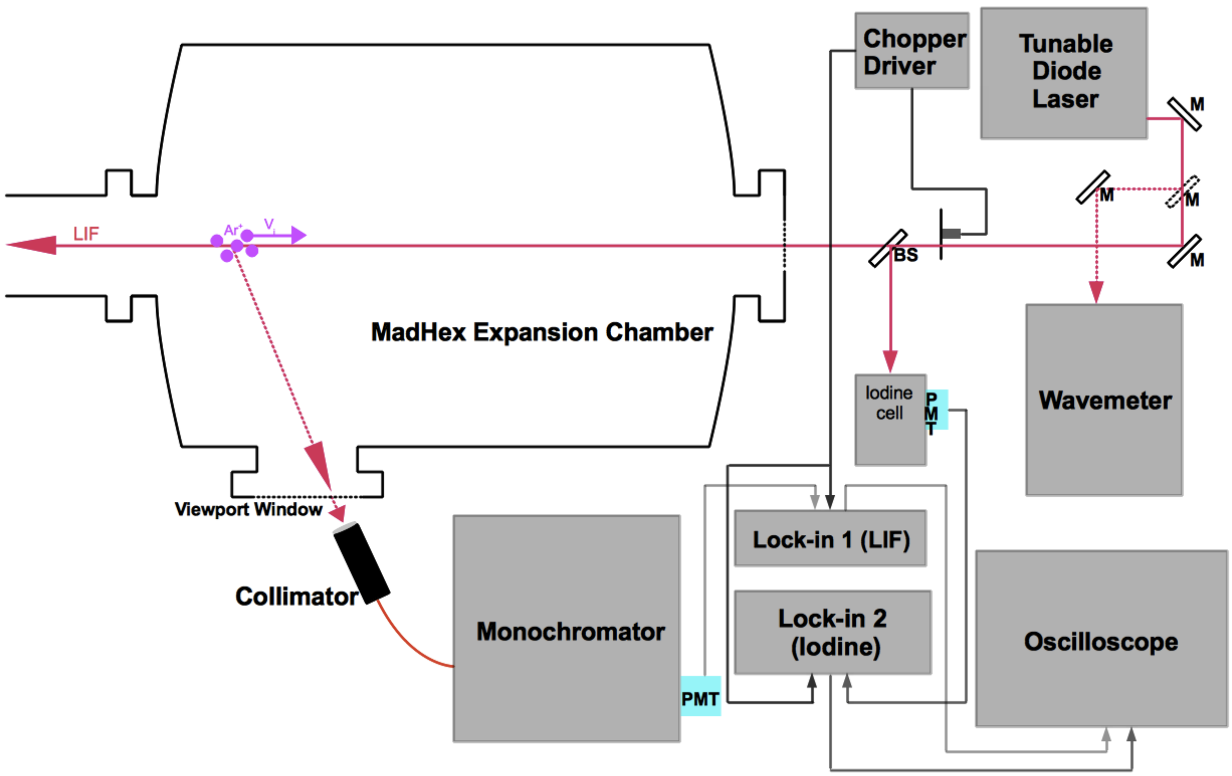

FIGURE 8.3: New optics for LIF system.

LIF, while time-consuming, is one of the most accurate measurements of the ion distribution, and would greatly improve the accuracy of ion velocity measurements. It would be used primarily to corroborate simpler diagnostics such as the RPA or emissive probes. Work is underway to modify the collection optics to operate at lower argon flow rates (lower electron densities) where the total optical emission from laser-excited argon ions is reduced.

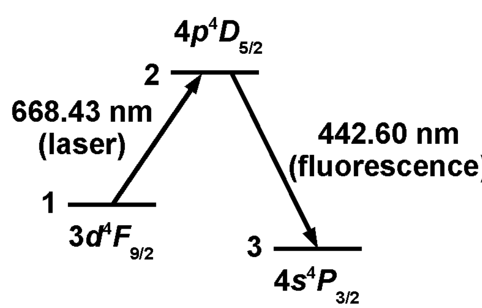

FIGURE 8.1: LIF transition of interest.

8.2.3 Boundary Conditions

It was observed that the minimum flow rate for observation of the accelerated population increased with operating time. This is likely due to a coating that is formed on the grounded expansion chamber walls as discussed in Chapters 6 and 7. The Pyrex chamber was replaced in an attempt to restore the original operation of the source, but had no effect on the lower flow rate threshold for the observation of an accelerated population, suggesting the ground condition in the expansion chamber is to blame for the performance degradation. Aanesland [112] showed that in a helicon source immersed in a vacuum chamber, a sputtered coating of copper in the source tube resulting from ion bombardment due to the formation of a negative self-bias on the floating RF antenna adversely affected the operation of a helicon source over time. In order to fully understand the formation of the potential gradient, the effect of the downstream (as well as upstream) boundary conditions should be further investigated. If the source is to be used in a space environment, the degradation of performance over time would need to be understood and mitigated. A thorough cleaning of the grounded walls of the expansion chamber is required to restore the original operation of the source. In addition, the very presence of the grounded boundary condition will also affect the operation of the source. The grounded chamber acts as an electrode and a "reference" for the plasma in the chamber. Without the ground provided by the chamber, as would occur under space conditions, the self bias effect may be reduced. In fact, the increasing lower threshold for observation of an accelerated population with increasing experiment run-time may support this conclusion. The coating on the walls that has formed may serve to insulate the chamber walls and reduce the effectiveness of the ground presented by the chamber walls, and further insulation will likely lead to even higher threshold flow rates. In the limit of a complete removal of the ground, capacitive operation and self-biasing of the upstream plasma may vanish. The effect of the downstream ground condition needs to be further investigated.

In the present work, the effect of the upstream endplate was only briefly explored. For operation in space, the current-free condition is necessary to avoid charging of the spacecraft and the resulting limitation of thrust. Further characterization of the operation of the source with a zero-net-current condition enforced would be of interest for development of this source for thrust applications. The helicon system at Georgia Tech includes a fully insulating upstream boundary condition, since the main goal of the research at Georgia Tech is aimed at understanding the use of a helicon as a thruster.

8.2.4 Self-Bias Effect

It may be possible to optimize the present system to exploit or eliminate the RF fluctuations of the plasma potential and self-bias as a result of the capacitive coupling of the antenna. This could be achieved by adjusting the amount of capacitive coupling to the plasma either with a Faraday screen and the present antenna or by designing a new or separate antenna that has enhances capacitive coupling.

As stated by Chabert [33], if the plasma potential fluctuations are comprised of several harmonics, the floating potential discussed in Section 3.1.3 (Eq. 3.13) increases in magnitude by approximately $\ln[I_0(a_i)]$, where a_i is the relative contribution of the ith harmonic, assuming all harmonics are in phase. Any phase difference between the harmonics decreases the relative contribution of that harmonic. Therefore, it may be possible to increase the self-bias effect if the driving waveform is non-sinusoidal, for instance a square wave. Chabert [33] examines the increase in self-bias for a square waveform (compared to a sinusoidal waveform), and the result is shown in Fig. 8.4. The increase in magnitude of the floating potential, normalized to the electron temperature, is plotted with respect to the magnitude of the fluctuation ($V_1 \sin \omega t$ or $V_1 \mathrm{sgn}[\sin \omega t]$), also normalized to the electron temperature. The increase in floating potential (the self-bias) could lead to larger potential gradients for a given input power. There is naturally harmonic generation from rectification of the sinusoidal voltage across the sheaths (this can be seen in the non-sinusoidal or asymmetric potential fluctuations in Fig. 6.18 for example), but a square wave or other non-sinusoidal driving voltage may lead to larger contributions of higher harmonics. However, the broad harmonic content of a square waveform would be difficult to reproduce and amplify unless a broadband RF amplifier was used.

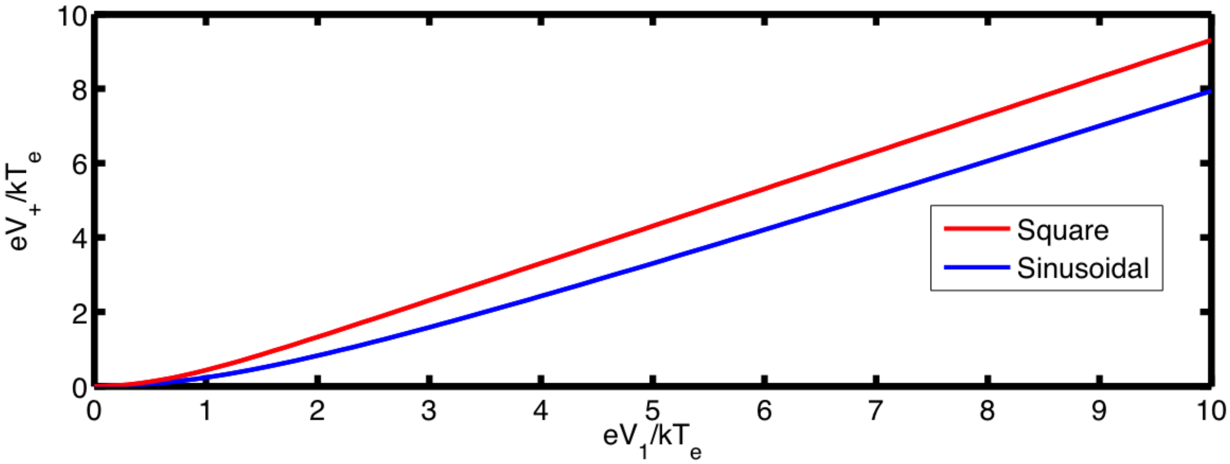

FIGURE 8.4: Addition to DC floating potential (eV_+/kT_e) vs. fluctuation magnitude (eV_1/kT_e), for sinusoidal and square fluctuation waveforms.

8.2.5 Georgia Tech

Measurements in the UW helicon mock-up at Georgia Tech in the large space chamber have shown potential gradients and ion acceleration of similar nature to that in MadHeX. Most work at Georgia Tech has focused on the installation and measurement of vacuum parameters (no plasma), including the evolution of the neutral pressure with z, RF metrology for maximum power transfer to the helicon antenna in vacuum and optimization of the inverted pendulum thrust stand [113]. The fully insulating source region in the Georgia Tech mock-up enforces current-free operation, and acceleration up to E_i = 160 eV has been observed with accelerated ions persisting over 1 meter from the source. Further characterization of the source is required, including measurement of the thrust using the thrust stand as well as measurements of the beam divergence, efficiencies and specific impulse.

Summary

Non-invasive diagnostics, previously used on MadHeX in a higher neutral pressure and RF power regime, can be adapted for use in the low density, low power plasmas in which high energy ions are observed. Optical emission spectroscopy (OES) can be used to measure the electron energy distribution function (EEDF), a key parameter in understanding the acceleration of ions in our source, which is difficult to measure by conventional means due to the large fluctuations in the plasma potential observed in our source. The current Laser Induced Fluorescence (LIF) system, a very powerful diagnostic for measuring the IEDF, must be modified to operate at the low argon ion densities observed in our system and new collection optics must be designed for use in the opaque expansion chamber.

References

[1] V. F. Virko, Y. V. Virko, V. M. Slobodyan, and K. P. Shamrai, "The effect of magnetic configuration on ion acceleration from a compact helicon source with permanent magnets," *Plasma Sources Science and Technology*, vol. 19, no. 1, p. 015004, 2010.

[2] NASA, "Ground ignition weights," http://history.nasa.gov/SP-4029/Apollo_18-19_Ground_Ignition_Weights.htm.

[3] D. M. Goebel and I. Katz, *Fundamentals of Electric Propulsion*. John Wiley and Sons, 2008.

[4] R. McKay, M. Macdonald, F. B. de Frescheville, M. Vasile, C. McInnes, and J. Briggs, "Non-Keplerian orbits using low thrust, high I_{sp} propulsion systems." International Aerospace Congress, IAC-09 C1.2.8, 2009.

[5] T. W. Glover, F. R. C. Diaz, J. P. Squire, V. P. Jacobson, D. G. Chavers, and M. D. Carter, "Principal VASIMR results and present objectives," *Space Technology and Applications International Forum (STAIF)*, 2005.

[6] R. Coppinger, "NASA to test plasma engine on space station," Online - http://www.flightglobal.com/articles/2008/08/05/226329/nasa-to-test-plasma-engine-on-space-station.html, 2008.

[7] NASA JPL, "Ion propulsion," Online - http://dawn.jpl.nasa.gov/mission/ion_prop.asp.

[8] C. Charles, "Plasmas for spacecraft propulsion," *Journal of Physics D: Applied Physics*, vol. 42, no. 16, p. 163001, 2009.

[9] Ad Astra Rocket Company, "VASIMR," Online - http://www.adastrarocket.com/VASIMR.html.

[10] J. P. Squire, F. R. Chang-Diaz, M. D. Carter, L. D. Cassady, W. J. Chancery, T. W. Glover, V. T. Jacobson, G. E. McCaskill, R. D. Bengtson, E. A. Bering, and C. A. Deline, "High power VASIMR experiments using deuterium, neon and argon," *IEPC Proceedings, 30th IEPC - Florence, Italy*, 2007.

[11] B. W. Longmier, E. A. B. III, M. D. Carter, L. D. Cassady, W. J. Chancery, F. R. C. Diaz, T. W. Glover, N. Hershkowitz, A. V. Ilin, G. E. McCaskill, C. S. Olsen, and J. P. Squire, "Ambipolar ion acceleration in an expanding magnetic nozzle," *Plasma Sources Science and Technology*, vol. 20, no. 1, p. 015007, 2011.

[12] C. Charles, "A review of recent laboratory double layer experiments," *Plasma Sources Science and Technology*, vol. 16, pp. 1–25, 2007.

[13] C. M. Denning, M. Wiebold, and J. E. Scharer, "Observations of neutral depletion and plasma acceleration in a flowing high-power argon helicon plasma," *Physics of Plasmas*, vol. 15, no. 7, p. 072115, 2008.

[14] F. F. Chen, "Physics of helicon discharges," *Physics of Plasmas*, vol. 3, no. 5, pp. 1783–1793, 1996.

[15] A. J. Perry, D. Vender, and R. W. Boswell, "The application of the helicon source to plasma processing," vol. 9, no. 2. American Vacuum Society, 1991, pp. 310–317.

[16] P. Chabert, N. Proust, J. Perrin, and R. W. Boswell, "High rate etching of ^{4}H–SiC using a SF_6/O_2 helicon plasma," *Applied Physics Letters*, vol. 76, no. 16, pp. 2310–2312, 2000.

[17] H. D. Jung, M. J. Park, S. H. Kim, and Y. S. Hwang, "Development of a compact helicon ion source for neutron generators," *Review of Scientific Instruments*, vol. 75, no. 5, pp. 1878–1880, 2004.

[18] T. Ziemba, J. Slough, and R. Winglee, "High power helicon propulsion experiments," *Space Technology and Applications International Forum (STAIF)*, vol. 746, no. 1, pp. 965–975, 2005.

[19] Y. Mouzouris and J. E. Scharer, "Wave propagation and absorption simulations for helicon sources," *Physics of Plasmas*, vol. 5, no. 12, pp. 4253–4261, 1998.

[20] P. K. Loewenhardt, B. D. Blackwell, R. W. Boswell, G. D. Conway, and S. M. Hamberger, "Plasma production in a toroidal heliac by helicon waves," *Physical Review Letters*, vol. 67, no. 20, pp. 2792–2794, 1991.

[21] M. Yano and M. L. R. Walker, "Plasma ionization by annularly bounded helicon waves," *Physics of Plasmas*, vol. 13, no. 6, p. 063501, 2006.

[22] S. Shinohara, K. P. Shamrai, and S. Shinohara, "Direct comparison of experimental and theoretical results on the antenna loading and density jumps in a high pressure helicon source ," *Plasma Physics and Controlled Fusion*, vol. 42, pp. 865–880, 2000.

[23] M. Lieberman and A. Lichtenberg, *Principles of Plasma Discharges and Materials Processing*, 2nd ed. John Wiley and Sons, 2005.

[24] Lieberman, M. A. and Boswell, R. W., "Modeling the transitions from capacitive to inductive to wave-sustained RF discharges," *Journal of Physics IV France*, vol. 08, no. PR7, pp. 145–164, 1998.

[25] A. R. Ellingboe and R. W. Boswell, "Capacitive, inductive and helicon-wave modes of operation of a helicon plasma source," *Physics of Plasmas*, vol. 3, no. 7, pp. 2797–2804, 1996.

[26] A. W. Degeling, C. O. Jung, R. W. Boswell, and A. R. Ellingboe, "Plasma production from helicon waves," *Physics of Plasmas*, vol. 3, no. 7, pp. 2788–2796, 1996.

[27] A. Perry, G. Conway, R. Boswell, and H. Persing, "Modulated plasma potentials and cross field diffusion in a helicon plasma," *Physics of Plasmas*, vol. 9, no. 7, pp. 3171–3177, 2002.

[28] S. M. Tysk, C. M. Denning, J. E. Scharer, and K. Akhtar, "Optical, wave measurements, and modeling of helicon plasmas for a wide range of magnetic fields," *Physics of Plasmas*, vol. 11, no. 3, pp. 878–887, 2004.

[29] C. M. Franck, O. Grulke, and T. Klinger, "Mode transitions in helicon discharges," *Physics of Plasmas*, vol. 10, no. 1, pp. 323–325, 2003.

[30] F. F. Chen, "Plasma ionization by helicon waves," *Plasma Physics and Controlled Fusion*, vol. 33, no. 4, p. 339, 1991.

[31] W. Manheimer and R. Fernsler, "Plasma acceleration by area expansion," *IEEE Transactions on Plasma Science*, vol. 29, no. 1, pp. 75–84, 2001.

[32] V. A. Godyak and N. Sternberg, "Dynamic model of the electrode sheaths in symmetrically driven RF discharges," *Physical Review A*, vol. 42, no. 4, pp. 2299–2312, 1990.

[33] P. Chabert and N. Braithewaite, *Physics of Radio-Frequency Plasmas*. Cambridge University Press, 2011.

[34] Y. Raizer, M. Schnieder, and N. Yatsenko, *Radio-Frequency Capacitive Discharges*. CRC Press, 1995.

[35] K. Kohler, J. W. Coburn, D. E. Horne, E. Kay, and J. H. Keller, "Plasma potentials of 13.56 MHz RF argon glow discharges in a planar system," *Journal of Applied Physics*, vol. 57, no. 1, pp. 59–66, 1985.

[36] C. S. Corr, J. Zanger, R. W. Boswell, and C. Charles, "Ion beam formation in a low-pressure geometrically expanding argon plasma," *Applied Physics Letters*, vol. 91, no. 241501, 2007.

[37] C. S. Corr, R. W. Boswell, C. Charles, and J. Zanger, "Spatial evolution of an ion beam created by a geometrically expanding low-pressure argon plasma," *Applied Physics Letters*, vol. 92, no. 22, p. 221508, 2008.

[38] T. Lafleur, C. Charles, and R. W. Boswell, "Detailed plasma potential measurements in a radio-frequency expanding plasma obtained from various electrostatic probes," *Physics of Plasmas*, vol. 16, no. 4, p. 044510, 2009.

[39] J. Ling, M. D. West, T. Lafleur, C. Charles, and R. W. Boswell, "Thrust measurements in a low-magnetic field high-density mode in the helicon double layer thruster," *Journal of Physics D: Applied Physics*, vol. 43, no. 30, p. 305203, 2010.

[40] T. Lafleur, C. Charles, and R. W. Boswell, "Ion beam formation in a very low magnetic field expanding helicon discharge," *Physics of Plasmas*, vol. 17, no. 4, p. 043505, 2010.

[41] A. Dunaevsky, Y. Raitses, and N. J. Fisch, "Plasma acceleration from radio-frequency discharge in dielectric capillary," *Applied Physics Letters*, vol. 88, no. 25, p. 251502, 2006.

[42] E. Ahedo and M. M. Sanchez, "Theory of a stationary current-free double layer in a collisonless plasma," *Physical Review Letters*, vol. 103, no. 135002, 2009.

[43] M. Raadu, "The physics of double layers and their role in astrophysics," *Physics Reports - Review Section of Physics Letters*, vol. 178, no. 2, pp. 25–97, 1989.

[44] R. E. Ergun, L. Andersson, D. Main, Y.-J. Su, D. L. Newman, M. V. Goldman, C. W. Carlson, A. J. Hull, J. P. McFadden, and F. S. Mozer, "Auroral particle acceleration by double layers: The upward current region," *Journal of Geophysical Research*, vol. 109, no. A12220, 2004.

[45] N. Hershkowitz, "Review of recent laboratory double layer experiments," *Space Science Reviews*, vol. 41, pp. 351–391, 1985.

[46] F. W. Perkins and Y. C. Sun, "Double layers without current," *Physical Review Letters*, vol. 46, no. 2, 1981.

[47] S. D. Baalrud, "Current-free double layers for spacecraft propulsion," Proposal for NSF EASPI Program.

[48] F. F. Chen, "Physical mechanism of current-free double layers," *Physics of Plasmas*, vol. 13, no. 3, p. 034502, 2006.

[49] M. A. Lieberman, C. Charles, and R. W. Boswell, "A theory for formation of a low pressure current-free double layer," *Journal of Physics D: Applied Physics*, vol. 39, pp. 3294–3304, 2006.

[50] R. F. Pierret, *Semiconductor Device Fundamentals*. Addison-Wesley Publishing Company, 1996.

[51] G. Hairapetian and R. L. Stenzel, "Particle dynamics and current free double layers in an expanding collisionless two electron population plasma," *Physics of Fluids*, vol. 3, no. 4, 1991.

[52] M. A. Lieberman and C. Charles, “Theory for formation of a low-pressure, current-free double layer,” *Physical Review Letters*, vol. 97, no. 4, p. 045003, 2006.

[53] C. Charles and R. Boswell, “Current free double layer formation in a high-density helicon discharge,” *Applied Physics Letters*, vol. 82, no. 9, 2003.

[54] M. D. West, C. Charles, , and R. W. Boswell, “Testing a helicon double layer thruster immersed in a space-simulation chamber,” *Journal of Propulsion and Power*, vol. 24, no. 1, 2008.

[55] S. D. Baalrud, T. Lafleur, R. W. Boswell, and C. Charles, “Particle-in-cell simulations of a current-free double layer,” *Physics of Plasmas*, vol. 18, no. 6, p. 063502, 2011.

[56] A. Fruchtman, “Electric field in a double layer and the imparted momentum,” *Physical Review Letters*, vol. 96, no. 6, p. 065002, 2006.

[57] A. Meige, R. W. Boswell, C. Charles, and M. M. Turner, “One-dimensional particle-in-cell simulation of a current-free double layer in an expanding plasma,” *Physics of Plasmas*, vol. 12, no. 5, p. 052317, 2005.

[58] C. Charles and R. W. Boswell, “Laboratory evidence of a supersonic ion beam generated by a current-free “helicon” double-layer,” *Physics of Plasmas*, vol. 11, no. 4, pp. 1706–1714, 2004.

[59] ——, “Time development of a current-free double-layer,” *Physics of Plasmas*, vol. 11, no. 8, pp. 3808–3812, 2004.

[60] C. Charles, “High source potential upstream of a current-free electric double layer,” *Physics of Plasmas*, vol. 12, no. 4, p. 044508, 2005.

[61] S. A. Cohen, N. S. Siefert, S. Stange, R. F. Boivin, E. E. Scime, and F. M. Levinton, “Ion acceleration in plasmas emerging from a helicon-heated magnetic-mirror device,” *Physics of Plasmas*, vol. 10, no. 6, pp. 2593–2598, 2003.

[62] S. Cohen, X. Sun, N. Ferraro, E. Scime, M. Miah, S. Stange, N. Siefert, and R. Boivin, “On collisionless ion and electron populations in the magnetic nozzle experiment (MNX),” *IEEE Transactions on Plasma Science*, vol. 34, no. 3, pp. 792 –803, 2006.

[63] O. Sutherland, C. Charles, N. Plihon, and R. W. Boswell, “Experimental evidence of a double layer in a large volume helicon reactor,” *Physical Review Letters*, vol. 95, no. 20, p. 205002, 2005.

[64] X. Sun, A. M. Keesee, C. Biloiu, E. E. Scime, A. Meige, C. Charles, and R. W. Boswell, “Observations of ion-beam formation in a current-free double layer,” *Physical Review Letters*, vol. 95, no. 2, p. 025004, 2005.

[65] E. E. Scime, I. A. Biloiu, J. J. Carr, S. C. Thakur, M. Galante, A. Hansen, S. Houshmandyar, A. M. Keesee, D. McCarren, S. Sears, C. Biloiu, and X. Sun, “Time-resolved measurements of double layer evolution in expanding plasma,” *Physics of Plasmas*, vol. 17, no. 5, p. 055701, 2010.

[66] S. C. Thakur, Z. Harvey, I. A. Biloiu, A. Hansen, R. A. Hardin, W. S. Przybysz, and E. E. Scime, “Increased upstream ionization due to formation of a double layer,” *Physical Review Letters*, vol. 102, no. 3, p. 035004, 2009.

[67] M. D. West, C. Charles, and R. W. Boswell, “High density mode in xenon produced by a helicon double layer thruster,” *Journal of Physics D: Applied Physics*, vol. 42, no. 24, p. 245201, 2009.

[68] K. Takahashi, C. Charles, R. W. Boswell, and T. Fujiwara, “Double-layer ion acceleration triggered by ion magnetization in expanding radiofrequency plasma sources,” *Applied Physics Letters*, vol. 97, no. 14, p. 141503, 2010.

[69] K. Takahashi, C. Charles, R. Boswell, and R. Hatakeyama, “Radial characterization of the electron energy distribution in a helicon source terminated by a double layer,” *Physics of Plasmas*, vol. 15, no. 7, p. 074505, 2008.

[70] K. Takahashi, C. Charles, R. W. Boswell, T. Kaneko, and R. Hatakeyama, "Measurement of the energy distribution of trapped and free electrons in a current-free double layer," *Physics of Plasmas*, vol. 14, no. 11, p. 114503, 2007.

[71] Ã. Fredriksen, L. N. Mishra, and H. S. Byhring, "The effects of downstream magnetic field on current-free double layers and beam formation in the Njord helicon plasma device," *Plasma Sources Science and Technology*, vol. 19, no. 3, p. 034009, 2010.

[72] H. S. Byhring, C. Charles, A. Fredriksen, and R. W. Boswell, "Double layer in an expanding plasma: Simultaneous upstream and downstream measurements," *Physics of Plasmas*, vol. 15, no. 10, p. 102113, 2008.

[73] A. W. Degeling, T. E. Sheridan, and R. W. Boswell, "Model for relaxation oscillations in a helicon discharge," *Physics of Plasmas*, vol. 6, no. 5, pp. 1641–1648, 1999.

[74] M. Wiebold, H. Ren, J. E. Scharer, and C. M. Denning, "Low pressure helicon discharge initiation via magnetic field ramping," *IEEE Transactions on Plasma Science*, vol. 37, no. 11, 2009.

[75] J. Scharer, A. Degeling, G. Borg, and R. Boswell, "Measurements of helicon wave propagation and ArII emission," *Physics of Plasmas*, vol. 9, no. 9, pp. 3734–3742, 2002.

[76] G. D. Conway, A. J. Perry, and R. W. Boswell, "Evolution of ion and electron energy distributions in pulsed helicon plasma discharges," *Plasma Sources Science and Technology*, vol. 7, no. 3, p. 337, 1998.

[77] C. Bohm and J. Perrin, "Retarding-field analyzer for measurements of ion energy distributions and secondary electron emission coefficients in low-pressure radio frequency discharges," *Review of Scientific Instruments*, vol. 64, no. 1, pp. 31–44, 1993.

[78] C. Charles, R. W. Boswell, and R. K. Porteous, "Measurement and modeling of ion energy distribution functions in a low pressure argon plasma diffusing from a 13.56 MHz helicon source," *Journal of Vacuum Science and Technology*, vol. 10, no. 2, pp. 398–403, 1992.

[79] A. Y. Wong, *Introduction to Experimental Plasma Physics*. University of California at Los Angeles, 1977.

[80] B. E. Beal, "Clustering of hall effect thrusters for high-power electric propulsion applications," Ph.D. dissertation, The University of Michigan, 2004.

[81] D. L. Brown, "Investigation of low discharge voltage hall thruster characteristics and evaluation of loss mechanisms," Ph.D. dissertation, The University of Michigan, 2009.

[82] S. A. and M. J. E. Golay, "Smoothing and differentiation of data by simplified least squares procedures," *Analytical Chemistry*, vol. 36, no. 8, pp. 1627–1639, 1964.

[83] R. F. Kemp and J. J. M. Sellen, "Plasma potential measurements by electron emissive probes," *Review of Scientific Instruments*, vol. 37, no. 4, pp. 455–461, 1966.

[84] M. Mizumura, S. Uotsu, S. Matsumura, and S. Teii, "Probe system with bias compensation using a laser heated emissive probe for rf discharge plasma diagnostics," *Journal of Physics D: Applied Physics*, vol. 25, no. 12, p. 1744, 1992.

[85] J. P. Sheehan, Y. Raitses, N. Hershkowitz, I. Kaganovich, and N. J. Fisch, "A comparison of emissive probe techniques for electric potential measurements in a complex plasma," *Physics of Plasmas*, vol. 18, no. 7, p. 073501, 2011.

[86] H. Fujita, S. Nowak, B. A. Hoegger, and H. Schneider, "Potential measurements by an emissive probe in a magnetized plasma," *Physics Letters A*, vol. 78, pp. 263–265, 1980.

[87] J. Kang, R. N. Carlile, and J. F. O'Hanlon, "A radio frequency compensated emissive probe," *Review of Scientific Instruments*, vol. 67, pp. 1818–1821, 1996.

[88] E. Y. Wang, N. Hershkowitz, T. Intrator, and C. Forest, “Techniques for using emitting probes for potential measurement in rf plasmas,” *Review of Scientific Instruments*, vol. 57, no. 10, pp. 2425–2431, 1986.

[89] J. R. Smith, N. Hershkowitz, and P. Coakley, “Inflection-point method of interpreting emissive probe characteristics,” *Review of Scientific Instruments*, vol. 50, pp. 210–218, 1979.

[90] T. Lho, N. Hershkowitz, and G.-H. Kim, “Effect of harmonic rf fields on the emissive probe characteristics,” *Review of Scientific Instruments*, vol. 71, pp. 403–405, 2000.

[91] T. Lho, N. Hershkowitz, G. H. Kim, W. Steer, and J. Miller, “Asymmetric plasma potential fluctuation in an inductive plasma source,” *Plasma Sources Science and Technology*, vol. 9, no. 1, p. 5, 2000.

[92] X. M. Guo, J. Scharer, Y. Mouzouris, and L. Louis, “Helicon experiments and simulations in nonuniform magnetic field configurations,” *Physics of Plasmas*, vol. 6, no. 8, pp. 3400–3407, 1999.

[93] V. A. Godyak and V. I. Demidov, “Probe measurements of electron-energy distributions in plasmas: what can we measure and how can we achieve reliable results?” *Journal of Physics D: Applied Physics*, vol. 44, no. 23, p. 233001, 2011.

[94] A. E. Wendt, “Passive external radio frequency filter for Langmuir probes,” *Review of Scientific Instruments*, vol. 72, no. 7, pp. 2926–2930, 2001.

[95] L. Oksuz, F. Soberon, and A. R. Ellingboe, “Analysis of uncompensated Langmuir probe characteristics in radio-frequency discharges revisited,” *Journal of Applied Physics*, vol. 99, no. 1, p. 013304, 2006.

[96] J. B. Boffard, R. O. Jung, C. C. Lin, and A. E. Wendt, “Optical emission measurements of electron energy distributions in low-pressure argon inductively coupled plasmas,” *Plasma Sources Science and Technology*, vol. 19, no. 6, p. 065001, 2010.

[97] Young-chul. Ghim(Kim) and N. Hershkowitz, “Improved double planar probe data analysis technique,” *Review of Scientific Instruments*, vol. 80, no. 3, p. 033502, 2009.

[98] E. O. Johnson and L. Malter, “A floating double probe method for measurements in gas discharges,” *Physical Review*, vol. 80, no. 1, pp. 58–68, 1950.

[99] S.-H. Seo, C. Chung, and H.-Y. Chang, “Review of heating mechanism in inductively coupled plasma,” *Surface and Coatings Technology*, vol. 131, no. 1-3, pp. 1 – 11, 2000.

[100] M. A. Razzak, S. Takamura, and Y. Uesugi, “Effects of radio-frequency driving power, gas pressure, and nitrogen seeding on the transition dynamics in argon inductively coupled plasmas,” *Journal of Applied Physics*, vol. 96, no. 9, pp. 4771–4776, 2004.

[101] A. W. Degeling, T. E. Sheridan, and R. W. Boswell, “Model for relaxation oscillations in a helicon discharge,” *Physics of Plasmas*, vol. 6, no. 5, pp. 1641–1648, 1999.

[102] M. Wiebold, Y.-T. Sung, and J. E. Scharer, “Experimental observation of ion beams in the Madison Helicon eXperiment,” *Physics of Plasmas*, vol. 18, no. 6, p. 063501, 2011.

[103] J. Y. Bang and C. W. Chung, “Experimental investigation of the Boltzmann relation for a bi-Maxwellian distribution in inductively coupled plasmas,” *Physics of Plasmas*, vol. 16, no. 9, p. 093502, 2009.

[104] K. Takahashi, C. Charles, R. Boswell, and R. Hatakeyama, “Radial characterization of the electron energy distribution in a helicon source terminated by a double layer,” *Physics of Plasmas*, vol. 15, no. 7, p. 074505, 2008.

[105] A. Zecca, G. P. Karwasz, and R. Brusa, “One century of experiments on electron-atom and molecule scattering: A critical review of integral cross-sections,” *La Rivista Del Nuovo Cimento*, vol. 19, no. 3, pp. 1–146, March 1996.

[106] J. O'Hanlon, *A User's Guide to Vacuum Technology*, 3rd ed. Wiley, 2003.

[107] R. F. Boivin and E. E. Scime, "Laser induced fluorescence in ar and he plasmas with a tunable diode laser," *Review of Scientific Instruments*, vol. 74, no. 10, pp. 4352–4360, 2003.

[108] B. M. Annaratone and J. E. Allen, "Radiofrequency sustained double layer in a plasma reactor," *Journal of Applied Physics*, vol. 91, no. 10, pp. 6321–6324, 2002.

[109] D. D. Blackwell, T. G. Madziwa, D. Arnush, and F. F. Chen, "Evidence for Trivelpiece-Gould modes in a helicon discharge," *Physical Review Letters*, vol. 88, p. 145002, Mar 2002.

[110] L. Williams and M. L. R. Walker, "Thrust measurements of a helicon plasma source," *AIAA/ASME/SAE/ASEE Joint Propulsion Conference & Exhibit*, pp. San Diego, CA, 2011.

[111] R. F. Boivin, J. L. Kline, and E. E. Scime, "Electron temperature measurement by a helium line intensity ratio method in helicon plasmas," *Physics of Plasmas*, vol. 8, no. 12, pp. 5303–5314, 2001.

[112] A. Aanesland, C. Charles, R. W. Boswell, and Å Fredriksen, "Sputtering effects in a helicon plasma with an additional immersed antenna," *Plasma Sources Science and Technology*, vol. 12, no. 1, p. 85, 2003.

[113] A. W. Kieckhafer and M. L. R. Walker, "RF power system for thrust measurements of a helicon plasma source," *Review of Scientific Instruments*, vol. 81, no. 7, p. 075106, 2010.

Appendices

A Double Probe Supply Schematic

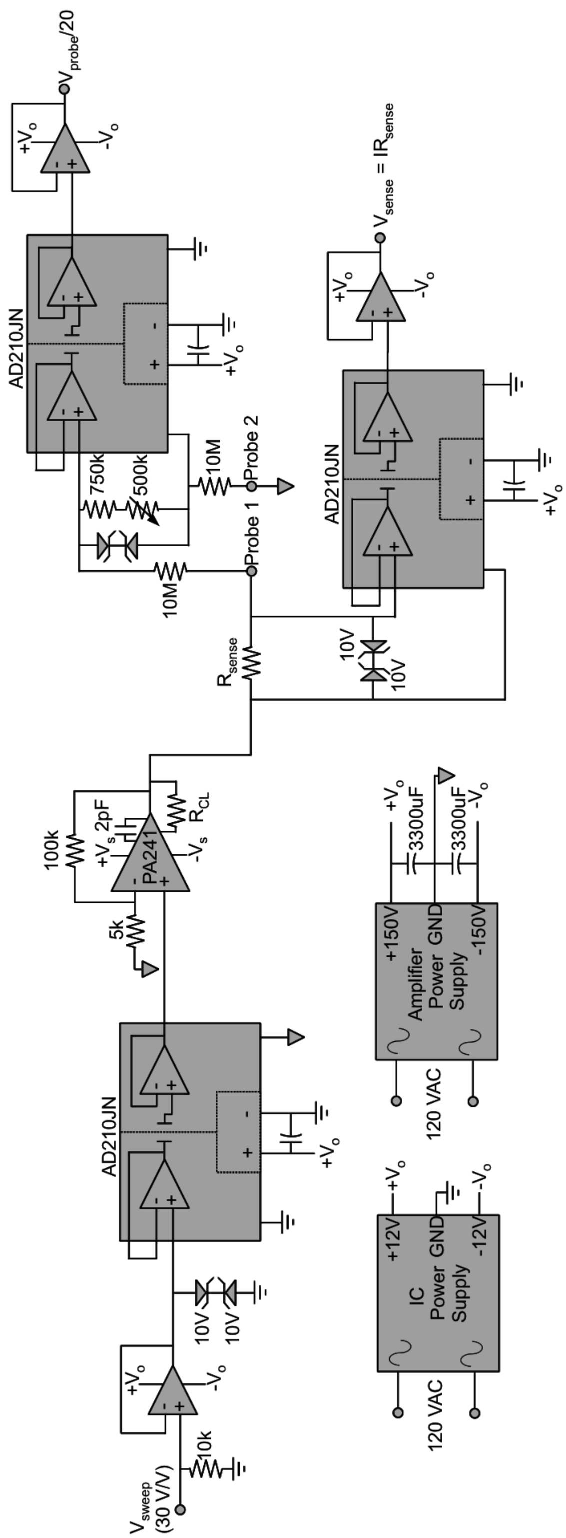

B RPA Appearance – UW Experiment

C RPA Appearance – GT Experiment